Top Mass Determination using Effective Field Theories

by

Aditya Pathak

Submitted to the Department of Physics
in partial fulfillment of the requirements for the degree of

Doctor of Philosophy

at the

MASSACHUSETTS INSTITUTE OF TECHNOLOGY

September 2017

Signature redacted

Author .....

Department of Physics
August 17, 2017

Signature redacted

Certified by .....

Iain Stewart
Professor of Physics
Thesis Supervisor

Signature redacted

Accepted by .....

Scott Hughes
Associate Department Head

Top Mass Determination using Effective Field Theories

by

Aditya Pathak

Submitted to the Department of Physics
on August 17, 2017, in partial fulfillment of the
requirements for the degree of
Doctor of Philosophy

Abstract

The top quark mass is one of the most important Standard Model parameters and its mass has been measured at sub-percent precision by the Tevatron and LHC using Monte Carlo (MC) based methods. The resulting MC top mass parameter suffers from $\mathcal{O}(1\text{ GeV})$ uncertainty due to lack of specification of a precise field theoretic definition. Here a kinematic extraction method for obtaining a precisely defined short distance top mass at the LHC is proposed. A formula for factorized top jet mass cross section in the peak region is derived using methods of Effective Field Theory (EFT). It can then be used for direct comparison with data or for calibrating Monte Carlo simulations. Result for hard matching coefficient at two loops at the top mass scale is presented that enables N^{3}LL logarithmic resumamtion of the cross section for top-jets in e^+e^- collisions. An effective theory setup for top mass extraction with soft drop grooming is derived, and is used to derive a factorization formula for the groomed jet mass distribution. Constraints from power counting in EFT limit the strength of groomers to "light grooming region". Studies with PYTHIA demonstrate that application of soft drop, even when restricted to light grooming, shows remarkable improvements in resilience to contamination from the underlying event (UE), has vastly reduced dependence the jet radius, and makes the top jet mass spectrum from pp collisions look like that of e^+e^- collisions as predicted. Modifications to the peaked spectrum from hadronization and UE for groomed top jets are suppressed and can be handled reliably. Using our factorization theorem results, a preliminary calibration study of Pythia top mass parameter is performed that yeilds results consistent with earlier calibrations for e^+e^- colliders.

Thesis Supervisor: Iain Stewart
Title: Professor of Physics

Acknowledgments

I am grateful to a number of people who have helped me immensely in their own special way during my graduate student life at MIT. It is through their unending support that I have been able to achieve my goals. I have had the opportunity to meet a lot of amazing people in the physics community and share their inspiring company. In particular, I have had the privilege of collaborating with Andre Hoang, Sonny Mantry, Piotr Pietrulewicz, Brad Bachu, Moritz Preißer, Ira Rothstien, and Duff Neill. I express my deepest gratitude for Iain Stewart for being an excellent collaborator, and an amazing mentor, providing me constant guidance throughout my graduate career. I cannot thank Iain more for opening before me so many opportunities to travel and be introduced to a number of amazing physicists in our field, around the world. I also thank Ian Moult for being a very supportive colleague ever since we met at the start of the graduate program.

I send special thanks to the MIT Junior Lab staff, instructors, and the talented students of the course 8.13, with whom I had a lot of fun learning experimental physics. They include Janet Conrad, Sean Robinson, Anna Jungbluth, Kay Lowden, Matt Hodel, Charles Bosse, Matt Lindsay, Dave Pritchard, and many others. I have been very fortunate to be surrounded with so many supportive friends at MIT. I would like to acknowledge all the support from the MIT medical staff. I am thankful to the MIT-India MISTI program coordinators for providing me financial support for my trips to India where I had the opportunity to share my work at a number of research institutions and universities, start new collaborations, and also visit family and friends. Graduate student life at MIT has been a great growing experience for me thanks to all the people who help foster love and mutual respect among all the members of MIT community, across various cultures and nationalities.

I have been very fortunate to be a part of a beautiful culture around MIT, in Boston and Cambridge, and further beyond all over the United States, that upholds and honors artistic and musical pursuits. My interests outside of physics in art and music have not only connected me to a bigger community but have also continued to

inspire me to work towards making physics ever more accessible and enjoyable to non-physicists, just like art and music, and have also helped me find creative solutions to physics problems. I am immensely grateful to all the amazing artists and musicians, that I met both in and outside of MIT, and all the friends who have supported me in pursuing these dreams, for helping me discover and develop my expression through painting, singing, playing piano and guitar. Of these people, I would like to acknowledge in particular Anupama Pattabiraman, Luanne Off, Nicole Teriverdian, Catherine Modica, Frederick Frank, Julie Matheson, Greg Kieffer, Sonja Tengbald, Jaime Lynn Hart, Jacob Scharffman, Keren Porat, Will Lunden, Geoff Bartley and Tim Lukas.

I am also very thankful to the Sidney Pacific Graduate Dorm Community where I had a chance to engage in fun volunteering activities for over four years. I thank immensely Poh Lim for being the best Tai-Kwan-Do teacher ever and teaching me lots of martial arts. I am grateful to Steven Bloomberg for working so hard with me on improving my English speaking skills. And, finally, I owe everything in my life to my parents who have been supportive and encouraging more than I could have ever asked for.

Contents

List of Figures

List of Tables

Chapter 1

Introduction

This thesis is about precision measurement of the mass of the heaviest elementary particle that we know of, the top quark. This work falls under the theme of the quest for precision measurement of properties of subatomic particles that we have discovered over the course of last century. In this thesis we aim to broaden our understanding of the various theoretical and experimental challenges that we face in this pursuit, and how they have led us to develop unique and powerful tools. The introduction section is aimed at non-physicists, and can be followed by anyone with modest interest in particle physics. The rest of the thesis contains advanced material.

Let us first recall how the mass of macroscopic objects is measured. An ant weighs about 2-5 milligrams, an average human about 70 kilograms. The mass of the earth is 5.9×10^{24} kg and that of the sun is 1.9×10^{30} kg. This is a wide range of masses but the common feature in their measurement is that we use the force of gravity to measure the mass. On the other hand, consider a hydrogen atom: given the extremely small mass of 1.6×10^{-27} kg, the force of gravity between an atom and anything macroscopic is undetectable. The state of art measurement of gravity is limited up to dielectric microspheres with diameters $\gtrsim 1$ μm [101], which is still far from being able to weigh much smaller atoms.

However, it is still possible to measure the masses of subatomic particles. The key ideas that enable this are as follows:

1. The known fundamental matter particles that have mass interact with each other, not just through gravity, but also through some or all of the three other forces of interaction that are much stronger than gravity: the 'weak', electromagnetic, and the strong force (the 'weak' force still being much stronger than gravity). With the exception of the electromagnetic force, the strong and the weak forces manifest themselves only at subatomic distances.

2. Einstein's relation $E = mc^2$ tells us that the mass of a particle is equivalent to a certain amount of energy, and that matter and energy are inter-convertible. As a consequence, through these forces of interactions, the particles can not only influence each other in the way they move in each others' vicinity, they can also completely transform or decay into other particle(s).

3. Such transformations happen in a way that energy and momentum is conserved throughout the process.

Thus if it happens that a parent particle with an unknown property transforms into daughter particles with known properties that can be experimentally measured then we have found a way to learn something about the parent particle. In particular, by measuring the energy and momentum of these known daughter particles we can calculate the mass of the parent particle.[1] Furthermore, the parent particle can itself be produced by smashing together known particles at high enough energies. As an example, a neutral pion, represented by π^0, mostly decays into two photons. By measuring the momentum of these photons we can calculate the mass of π^0.

In this introductory part we first discuss in Sec. 1.1 some of the interesting features of the strong force that are relevant to top mass measurement. We then consider the challenges imposed by the nature of the experiment in Sec. 1.2, and by the theory in Sec. 1.3. We conclude with an overview of the theoretical tools of Effective Field Theory description in Sec. 1.4 that has made it possible to overcome these challenges developing a promising method to precisely measure the top mass.

[1]This is also the reason why it is so hard to determine properties of dark matter, whose only yet known interaction with normal matter is gravitational.

1.1 The Standard Model

The physics at the shortest subatomic distances is described by the Standard Model (SM) of particle physics. We learned about the very first Standard Model particle to be discovered, the electron, over hundred years ago, and since then, through the use of particle colliders and studying cosmic rays, we have come a long way towards identifying the elementary particles that are the building blocks of nature. By smashing particles at higher and higher energies in a particle colliders we can create heavier and unstable particles that do not make up bulk the stable matter that macroscopic objects are composed of.

During the 1970s came the first experimental confirmation of the existence of a class of particles called quarks, which make up the protons and neutrons and are held together by the strong nuclear force [26]. Over the course of following decade we found, one after another, different types of quarks, each of them heavier than the ones already known. In 1995 we discovered the sixth quark, the top quark [4]. It is the heaviest elementary particle that we know so far. Its mass alone is about the same as that of a gold nucleus that contains about 185 protons and neutrons. The next heaviest quark, the bottom quark is about forty times lighter than the top quark. We refer to the five other quarks collectively as "lighter" quarks.

The second half of the twentieth century was also the time when the properties of the strong nuclear force were being understood and a theoretical framework for calculations involving the strong force was being developed. We learned that the strong force is quite different from the electromagnetic force. The electromagnetic force between two charged particles decreases as they move further apart, but the strong force behaves rather like a rubber band: the further the rubber band is stretched the more tension is created, whereas an unstretched rubber band is slack and there is no tension. This different nature of the strong force gives rise to very interesting phenomenon in nature.

A consequence of this behavior is that (lighter) quarks exist only in bound combinations with other quarks, held together by gluons, particles that mediate the strong

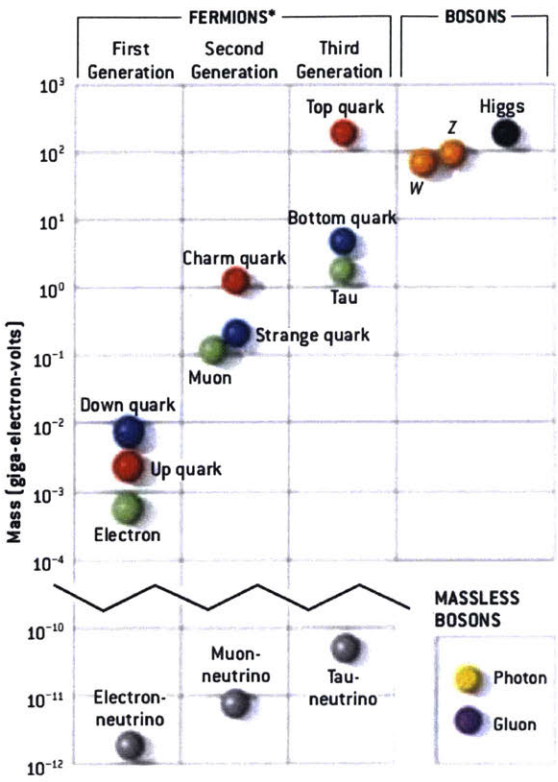

Figure 1-1: Masses of various elementary particles in Standard Model [81].

force. Protons and neutrons are examples of such bound configurations consisting of three valence quarks, but many more such composite particles called hadrons have been discovered. There have been even recent observations of hadrons consisting of exotic combinations of more than three quarks [3]. Just like all the electromagnetically interacting particles carry the (regular) charge, quarks are also charged under the strong force. This charge is referred to as the color charge. Bare quarks carrying color charge thus combine to form color neutral hadrons.

All the hadrons need roughly the same amount of time to form starting from bare quarks. This time scale is set by the dynamics of strong interaction. However, the top has a unique property that it has a shorter lifetime, and hence, it decays into lighter particles before it can bind into a hadron.

In Fig. 1-1 we show masses of various elementary particles in Standard Model. This is expressed in units of GeV where 1 GeV corresponds roughly to the mass of a hydrogen atom. The heaviest is the top quark with a mass of about 173 GeV and

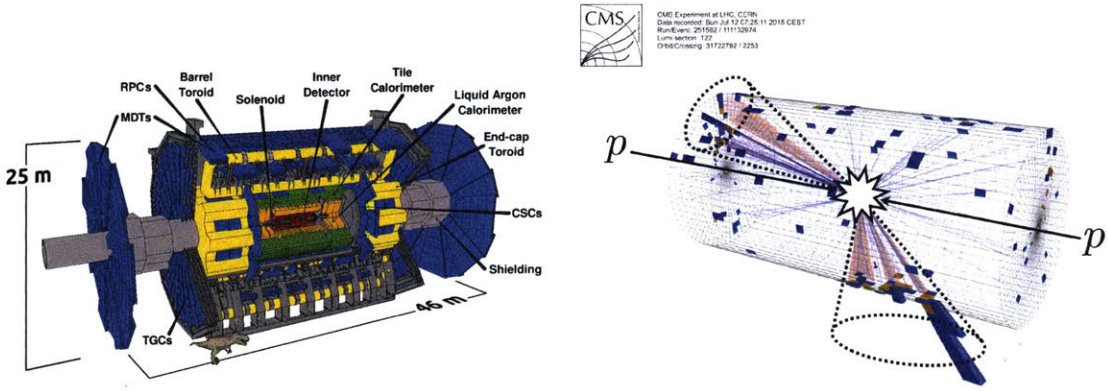

Figure 1-2: Shown on the left is a schematic of the ATLAS detector at the LHC [9]. Shown on the right is an event display of top anti-top pair production at the CMS experiment with identifiable 3-prong substructure from the t and $\bar{t}$ decays [39].

the lightest particles are the neutrinos, about a factor of 10^{14} times lighter. It is a big open puzzle in physics as to why we have such variety of elementary particles with such different masses. Here we limit ourselves to a much less ambitious, but still quite exciting, problem: given these particles with their specific properties, how can we accurately measure their masses, and in particular, measure the top mass?

1.2 The Large Hadron Collider

We show a schematic of the ATLAS detector of the Large Hadron Collider(LHC) in Fig. 1-2. Two oppositely directed beams of protons collide at the center of the barrel shaped detector. The particles produced from the collision stream through the surrounding detectors while depositing their energy. The electronic signals thus generated allow us to reconstruct the energy and momenta of these particles. The top quark can be produced at such high energy proton-proton collisions. An event display of top and anti-top pair production at the CMS detector of LHC is shown in the right panel of Fig. 1-2. The top quark is an unstable particle that decays before it reaches the detectors, which precludes direct mass measurement. Its mass must be measured through measurement of the energy and momentum of the decay products

The measurement of the top mass requires a sample of top quark events. One

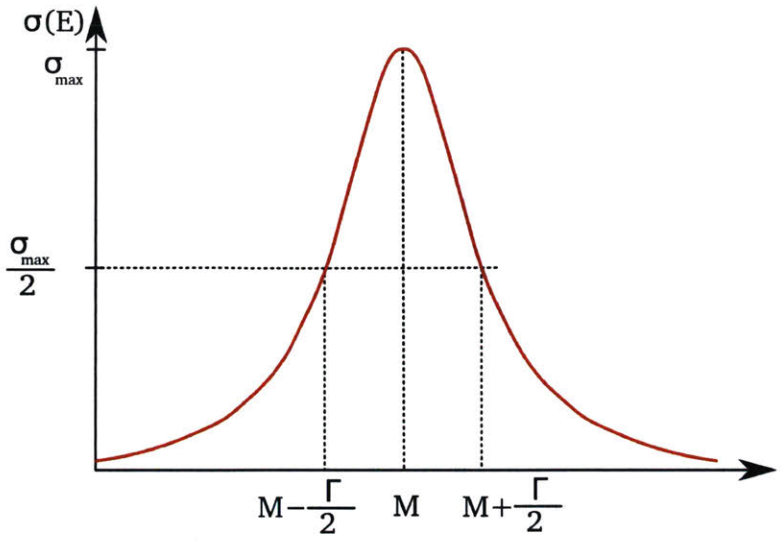

Figure 1-3: The Breit-Wigner distribution. The width Γ is inversely related to the lifetime of the unstable particle with mass M.

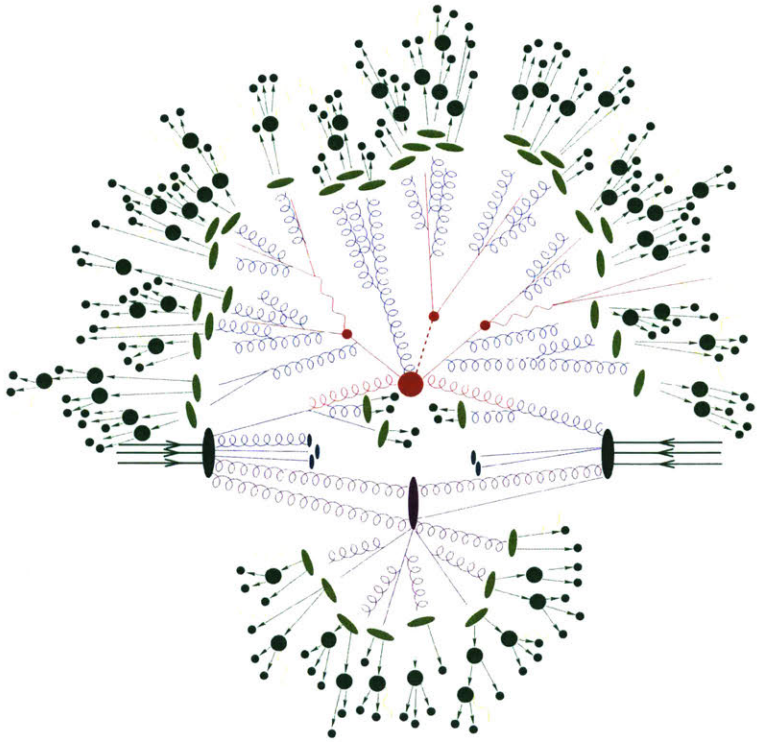

Figure 1-4: A schematic of components of an LHC collision, showing the hard collision, shower, hadronization, as well as multiple particle interactions [87].

reconstructs the top mass through the decay products for every event and bins it in a histogram. Fig. 1-3 shows is how an idealized spectrum of reconstructed top

mass would look like. One might argue that given the fact that the top mass is a single valued number we should always obtain the same value of mass every time we reconstruct it using top decay products. Rather, we instead see a probability distribution that peaks at a certain value and has certain width to it. This is because the decay of a particle is a quantum phenomenon. For an unstable particle, which only lasts a finite amount of time, Heisenberg's Uncertainty principle comes into play. According to this principle there is an inherent uncertainty in the energy (or mass) of an unstable particle inversely proportional to its lifetime. This leads to a specific probability distribution of the top mass called the Breit-Wigner (BW) shape shown in Fig. 1-3 with a small width of about 1.4 GeV. This uncertainty is represented by the width of the spectrum. Hence, top mass measurement effectively corresponds to measurement of the peak position of the distribution.

Top quarks are produced in colliders in a much more complex environment. Shown above in Fig. 1-4 is a representation of what a typical collision event at the LHC looks like. We find that in addition to top quark production there are several other processes going on which change the shape and the location of the original BW distribution. An example of such modifications is shown in Fig. 1-5. The modifications correspond to a shifting of the peak and smearing of the original BW shape to yield a wider distribution. In order to be able to extract the top mass from the LHC data, we must have a good understanding of these extraneous effects and how they shift the mass distribution. Many of these processes cause contamination in the top mass measurement and they need to be understood and controlled.

We can understand some of the features of these additional processes by considering the behavior of the strong force. Going back to the rubber band analogy, we can distinguish between two scenarios when the rubber band is slack and not stretched vs. when it is stretched and has tension in it. Top production and decay happens at such short distances where decay product quarks are relatively free, or when the "rubber band" is still slack. As the decay products propagate, the strong force between them gets significant, and after they move far enough apart the energy of interaction gets transformed into creating more and more quark-antiquark pairs. This is the stage

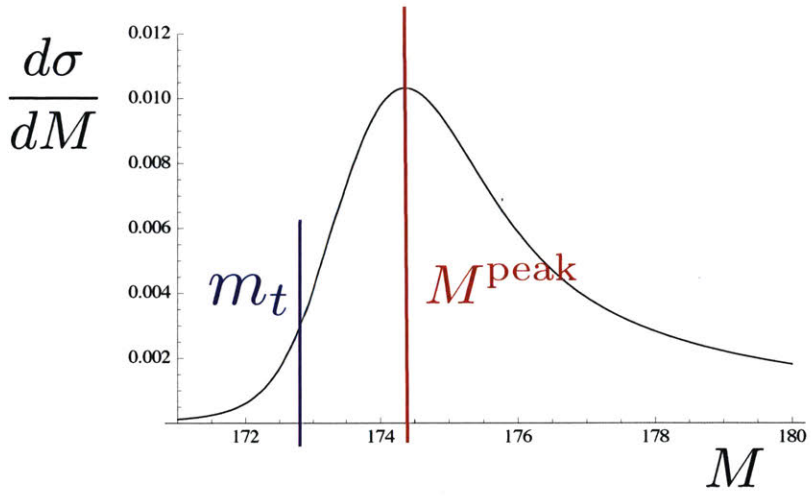

Figure 1-5: The peak position for top mass spectrum is shifted from the actual mass due to radiation, non-perturbative effects, and contamination from the underlying event.

when the rubber band snaps into pieces. Combining both regimes, the end result is a collection of quarks and anti quarks. These particles then further radiate quarks and gluons, collectively referred to as partons, as they propagate, thus creating a shower of particles, called the parton shower. Then they eventually bind together to form composite hadrons. This last process is called hadronization. Thus, parton shower radiation and hadronization change the original BW shape by redistributing the momenta of the top decay products.

There are other complications we run into that have more to do with our experimental limitations. At the LHC we collide protons against protons. The proton is not a fundamental particle but rather a bag of quark and gluons. Often times there are several collisions between incoming quarks and gluons from either of the parent protons which happen at the same time. So the top quark is often produced with several other particles from these other collisions. Since the top quark is heavy, we often have most of the energy of the incoming protons go into creating it, and a small amount in the remaining collisions, but still, these additional collisions produce

particles that get counted with the top decay products further shifting the peak position. These additional collisions are referred to experimentally as the underlying event (UE). Furthermore, the most severe of all experimental complications is called "pile-up": at the LHC we do not circulate individual protons in the beam, but rather bunches of protons. We find that there are collisions between more than one proton-proton pairs from these bunches, that are completely uncorrelated. This problem gets worse at higher energies and luminosities (number of collisions per second). In this thesis we do not consider the effects of pile-up, but we do address the effects of the parton-shower, of hadronization and of the UE.

1.3 Theoretical Challenges

Given such a wide variety of processes contributing to the top mass spectrum we find it helpful to work with Monte Carlo (MC) simulations that incorporate the physics of all these effects. The most precise current measurement of the top mass relies on such simulations. Many of the complications we discussed above also show up in other simpler processes such as in the production of lighter quarks. MCs are constructed and calibrated based on studying such well understood processes. When applied to top quark production studies, the only unknown is then the top mass, which is fed into the MC as a parameter. By comparing the experimental data against simulations one obtains the best fit top mass parameter. One of the most precise measurements of top mass obtained this way by the CMS collaboration at the LHC is $m_t = 172.44 \pm 0.49$ GeV [84], where the uncertainty here (combination of statical and systematic uncertainties) is less than one percent.

However, MC simulations are limited in their ability to reproduce the true theory. In order to gain an understanding of uncertainties from the theory, we first try to understand what a theory calculation in particle physics involves. By theory here we mean the framework of quantum field theories that has developed over the last century. We learned about quantum phenomenon starting in early 1900s by following various clues from atomic spectroscopy. Around the same time the theory of special

relativity was being developed. Quantum mechanics describes physics at the scale of atoms. It is based on a probabilistic interpretation, unlike deterministic classical mechanics. Classical mechanics can be thought of as averaging over the quantum effects to describe gross macroscopic phenomena. Another limit where classical mechanics needs modification is when we consider objects moving at speeds close to speed of light, and in this limit special relativity is the appropriate generalization of classical mechanics. These two theoretical frameworks were studied and tested independently in the first half of twentieth century, but later on with the advent of experiments that probed subatomic particles that moved close to speed of light, a relativistic generalization of quantum mechanics was discovered, which we refer to as quantum field theory (QFT).

QFT is a generic term for a framework of theories. The Standard Model (SM) is a specific QFT with the ingredients that correspond to the particles and the forces that we observe in nature. At the heart of the QFT framework each particle, either a matter or force carrier particle, is associated with a field that takes a value at each point in space at a specified time, or at a point in space-time. As an example, we can describe the temperature of a room by specifying the "temperature field" that is simply the temperature at every point in the room, at a given time. However, in QFTs these values need not be simply real numbers, but could be complex numbers, vectors, matrices or even more abstract mathematical objects. This should not be worrisome since in the experiments we do not probe the actual values of the fields (unlike measuring the temperature) but rather the probabilities of changing of one field configuration into another. For example the number of times we observe a certain particle being created in particle collisions with certain energy from a pair of incoming particles can be related to a calculation of one such probability.

QFTs provide a convenient way to encode the mathematical description of all the physical phenomena. A single equation for the SM QFT encodes within it all the physics from which everything we know and observe in nature follows (except for the phenomena involving gravity, and ignoring potential small deviations from experiments that the SM might fail to explain). Collider experiments measure the

probabilities for various processes that are tested against the theoretical predictions from QFTs. The task at hand is to define an observable for measuring the top mass that is free from contamination coming from uninteresting background processes. We learned that effects of hadronization and UE have an impact on the peak position and the shape of the spectrum. We would like to work with observables that are less sensitive to these effects, and are amenable to theoretical calculations.

The intrinsic non-deterministic quantum nature of these processes makes such calculations quite challenging technically. Here is an example to illustrate the nature of this complexity: let us recall how the calculation of the Coulomb force between two charge particles goes. We learned how to calculate the electrostatic force acting between two objects if we know their charges and the distance between them. This is a simple matter of plugging the values of charges and the distance into the equation and getting a number out. However, we rarely consider questions such as does the presence of a charged particle at a certain distance affect the charge of the other particle? We assume the charges to be constant and not changing as a function of distance. It turns out, this assumption is no longer true at subatomic distances, and this simple classical picture breaks down. At very short distance scales, the electromagnetic charge itself is a function of distance. The charge of one electron that another electron "sees" gets larger and larger as they approach each other.

Quantum Electrodynamics (QED), the first QFT written down to describe electromagnetism, provides the explanation for this phenomenon. It was observed that the Dirac equation in QED that describes the electron field needed, for the sake of theoretical consistency, an anti-electron, or positron field. Furthermore, it allowed for creation and annihilation of electron-positron pairs in vacuum entirely on their own. This changed our understanding, showing that the vacuum is not really empty after all. It has particle anti-particle pairs popping in and out constantly. These particles are called virtual particles, to distinguish them from 'real' electrons which exist indefinitely (unless they encounter a positron on their way and annihilate). In fact, this seemingly bizarre phenomenon has been confirmed experimentally by what is known as the 'Casimir Force'. Two metal plates in vacuum placed nanometers apart can feel

a tiny attraction to each other even if there's no external electromagnetic field. These virtual electron-positron pairs, being oppositely charged, create polarization in the plates which makes them attract each other [89].

The existence of virtual particles also provides an explanation for the varying electron charge as a function of distance. The virtual pairs surrounding an electron orient themselves such that the positively charged particles are closer to the electron and the negatively charged particles away from them. This cloud of virtual particles then screens the charge of electron, thereby diminishing it, but the closer we go into the cloud more charge we see. Hence, the charge of the electron becomes a 'scale' dependent quantity. We use the term scale to refer to either distance or energy scales. Concepts of energy and distance are used quite interchangeably in particle physics. Short distances correspond to high energy and vice versa. This is analogous to Heisenberg Uncertainty principle which constrains simultaneous measurement of energy and time, or momentum and distance, to arbitrary precision. We have already seen an example of this: the decay of the top quark introduces a width of about 1.4 GeV in the BW spectrum due to its finite lifetime.[2] It is often more convenient to describe particle physics in terms of energy scales rather than distance scales.

We find that similar quantum effects change the behavior of the mass too and make it a function of the scale at which the process takes place. The QFT for strong force is called Quantum Chromodynamics. The "chromo" refers to the 'color charge' carried by quarks and gluons, similar to positive and negative electromagnetic charge. QCD predicts how quantum corrections affect the mass. Hence, to make mass measurement of top quark more meaningful we must know something more than just a number. That 'more' has to do with the understanding of how the quantum effects shift the mass as the energy scale at which the mass is being probed is changed. This is referred to as specifying the *definition* of top mass.[3] The MC methods that were described above have a difficult time in accurately accounting for such delicate quantum effects

[2]As a simple example, X-rays carry more energy than infrared light, and they also have shorter wavelength. X-rays when shine on an atom can knock an electron off as opposed to longer wavelength infrared waves.

[3]In technical terms, we must know the renormalization scheme the mass is measured in, or how higher order corrections affect the mass definition.

since their treatment of real and virtual radiation are intrinsically tied together.

We note that the simulations of the kind described above incorporate various approximations and models, and hence are not first principle simulations of QCD. They incorporate approximate theoretical descriptions for the sub-processes such as production of particles, their decays, and parton shower, and models for hadronization and UE effects.[4] These components are then patched together to simulate the full event, but only to a limited accuracy. As a result the MC top mass parameter, which we call $m_t^{\rm MC}$ does not have a precise field theoretic definition that can be described by calculations with the Standard Model lagrangian. It has been estimated that this introduces a theory uncertainty of 0.5-1.0 GeV, which is of the same level as the experimental uncertainty.

1.4 Effective Field Theories

To go beyond sub-percent precision for the top mass measurement we must turn to theoretical predictions that are more precise than the MC simulations, but also equally sophisticated in their ability to account for variety of sub-processes. This is a challenging task because the top mass measurement involves multiple widely separated energy scales. It is also a very exciting problem for the very same reason as this unique feature can be exploited to make use of the well known framework of 'Effective Field Theory' that we explain below. Knowing the energy scales that characterize a physical system can provide a great simplification and also guide us towards the solution.

Consider an example where an engineer is trying to gain understanding of a system that involves flow of a liquid through various components. Let's say the engineer wants to understand how to predict properties such as pressure and the speed of the fluid at various locations of the system. They are essentially seeking an explanation in the language of hydrodynamics where a fluid is imagined to be a field with macro-

[4]There are first principle simulations of QCD called Lattice QCD simulations. These simulate QCD exactly by discretizing the space-time, however, they are intrinsically Euclidean and hence unable to directly compute the outcome of high energy collider experiments.

scopic measurable properties at each point in space, such as the temperature, pressure, density and fluid speed at a given point. At very small distances the fluid, however, looks entirely different in composition - one sees a picture of distinct molecules interacting with each other through electromagnetic forces. Macroscopic quantities such as pressure or temperature are no longer sensibly defined at such short distances.

At the same time, we can be completely unaware of the molecular structure of the fluid, be it water or oil, and still provide a consistent explanation of its macroscopic motion by measuring its bulk properties such as viscosity and specific heat, and make predictions based on hydrodynamics. The key point is that hydrodynamics is a very convenient tool to use for such practical applications, even though it may fail to tell us much about physics at molecular distances. One can make rough statements about the strength of the intermolecular interaction based on how viscous the fluid is, but a more precise explanation demands a short distance description. More broadly, hydrodynamics is referred to as the "effective theory" to distinguish it from the "full theory" based on a description starting at molecular scales. Another well known example of an effective theory is Ohm's law for circuits that can be applied to a variety of materials without having to understand the distribution and flow of individual electrons. At the same time, it is possible to derive the long distance quantities such as resistance based on a short distance model.

Such a distinction between a physics description at short and long distances of the same system has direct analogies in particle physics. Effective theories become a very useful tool for describing processes at particle colliders where multiple sub-processes contribute at different energy scales. The analogy presented above in Sec. 1.2 in terms of slack and stretched rubber band is precisely creating a distinction between short and long distance physics respectively. The physics of formation of the top quark from the incoming beams is a short distance phenomenon whereas its subsequent decay, parton shower radiation and hadronization are longer distance phenomena. We mentioned above that processes such as hadronization are universal in nature in the sense that these effects can be studied in systems involving lighter quarks. This is precisely a consequence of the fact that the slack and the stretched rubber band

scenarios are widely separated in energy scales and thus enable an effective theory treatment.

One would find it extremeley hard to predict macroscopic behavior of water starting from a description based on its molecular composition H_2O. Similarly, processes such as the details of hadronization and underlying event are very challenging to calculate from first principles QCD. To tackle such problems, an Effective Field Theory (EFT) treatment for QCD processes in collider physics has been developed over the last two decades that has made such processes theoretically tractable, which is called Soft Collinear Effective Theory (SCET). EFTs have also been applied to systems that contain heavy quarks where the mass of the heavy quark interacting with lighter particles is much larger than the energies of other particles in the system, called Heavy Quark Effective Theory (HQET). An example is a hadron consisting of a bottom quark with a mass of about 4 GeV, and a lighter up or down quark whose mass is over a thousand times smaller. These two frameworks, SCET and HQET, simplify calculations and enable predictions that are not easy to calculate directly from QCD. The work presented here combines these two bodies of work to describe top mass measurements that involve understanding both the collider environment, and the top-decay and radiation into particles of much smaller masses.

To see why this works we note that in an EFT framework one distinguishes the energy scales relevant to the problem that are widely separated from each other. One then associates different fields to the particles based on their energies. This is in contrast to QCD where a quark is always associated with the same field no matter how fast or slow it is. In other words, EFT plays a role of hydrodynamics providing a description in a language that is quite different from the full QCD theory, and at the same time, much more practical to work with. Analogous to parameters in hydrodynamics, such as viscosity, the EFT also introduces new quantities that can be either calculated from first principles or measured separately, and are more directly related to the specific problem than the parameters of QCD. Hence, EFTs like SCET and HQET are very useful tools for complex problems like top mass measurement.

We have pointed out earlier that MCs are limited in their ability to accurately

account for quantum corrections to the top mass, which limited applying results results of the measurement while retaining a precision beyond 1 GeV. Top mass measurements using EFT methods hold the promise of improving this precision either directly or in combination with MC. EFTs allow for greater precision since they involve calculation of individual objects that involve only a single scale, which are then combined to give a full result. These sub-calculations can be performed with a greater precision than the case where we try to tackle a multi-scale problem at once. The level of sophistication thus obtained from EFT calculations competes with the MC methods described above and also help us measure the mass with a theoretically well defined mass definition by accurately accounting for quantum effects.

1.5 Top Mass Measurement Using Jets

The second challenge lies in being able to construct observables that are as free as possible from contamination from the UE and can be calculated in the EFT framework. At the LHC, experimentalists employ sophisticated algorithmic procedures, known as jet reconstruction algorithms, to identify particles generated in a specific process in particle collisions. Here, "jet" refers to a spray of particles in a narrow cone - a feature that is very commonly observed in high energy collisions at particle colliders. Energetic particles produced in a collision further radiate more and more particles in the direction of their motion resulting in a jet like structure. An example is shown in Fig. 1-2 in the right panel where the top and anti-top quark are produced back to back and their radiation is collimated in a narrow cone, referred to here as jets. Jet algorithms are very useful tools in identifying the right set of particles, for example the decay products of top quarks. The measurement of the top quark mass using jets involves identifying the jets associated with the top quark decay products and combining the momenta of all the particles in these jets to obtain the mass. One then obtains a distribution that looks like the idealized spectrum shown in Fig. 1-5.

As mentioned above, processes like initial state radiation, final state radiation, or particles from the underlying event can contaminate or deplete the jet by introducing

particles in the jet region, so that they are no longer those associated with the top quark. To overcome this problem as much as possible, experimentalists take a second look at the jet and make use of techniques known as "jet grooming" to "groom" away as much contamination as possible. The jet grooming algorithm makes a decision to either keep a particle in the jet or throw it away, such that most of the particles that accidentally ended up in the jet region from outside can be removed. Thus jet grooming is an extremely effective experimental tool that allows us to reduce such contamination.

Only very recently, calculations using EFT methods for jet based measurements with grooming have started to become available. In the literature, the EFT description of groomed jet observables has only been carried out for processes that involve lighter quarks [51]. Such calculations are not only challenging for the reasons mentioned above, but they have an added complexity due to the special nature of jet algorithms and jet grooming. Given such powerful features of grooming it is highly desirable to employ it for the top mass measurement. This thesis presents a calculation for the top mass measurement using jet grooming in an EFT framework. The predictions from theory are compared with MC simulations and very promising results are obtained. Comparing Quantum Field Theory calculations against MC also helps us pin down numerically the nature of the MC top mass parameter, $m_t^{\rm MC}$, encoded in the simulations, that is otherwise very hard to precisely interpret.

1.6 Guide for the Reader

We now present an outline of rest of the thesis: In Chapter 2 we briefly describe theoretical challenges faced in calculating top jet mass cross-section at the LHC, thus clarifying the problem statement that is being addressed in the subsequent chapters. Chapter 3 reviews the basics of SCET and HQET. In Chapter 4 we derive the factorized 2-jettiness cross-section formula for $pp \to t\bar{t}$. We then consider the application of soft drop grooming for top jets in Chapter 5. In the first part of Chapter 5 we perform a mode and power counting analysis to derive the "light grooming" constraints

on soft drop parameters that allow an EFT treatment of the groomed jet mass distribution. We then perform a detailed study with PYTHIA to assess the performance of "light grooming" in improving the robustness of the top mass extraction from a jet mass measurement. The last part of the chapter is where we test predictions of factorized cross section by comparison with PYTHIA, which allows us to calibrate the $m_t^{\rm MC}$ parameter. In Chapter 6 we calculate the missing 2-loop matching coefficient between HQET and SCET that allows us to perform a resummation of the factorized cross-section for $e^+e^- \to t\bar{t}$ at a higher order than currently known [50]. The work described in Chapter 5 has appeared recently in Ref. [71]. Chapter 6 is published in Ref. [72].

Chapter 2

Top Mass Measurement

The top quark mass is one of the most important parameters in the Standard Model. As the heaviest observed fermion, the top quark provides an important probe for the Higgs sector, and gives dominant contributions to many electroweak observables, see eg. [48], thus providing strong benchmark constraints for extensions of the Standard Model. Furthermore, the mass of the top quark and the Higgs boson represent crucial parameters in studies of the stability of the Standard Model vacuum [30, 7, 28, 8, 24, 25].

2.1 Top Mass Measurement Methods

The top mass has been measured in different ways. We can distinguish two classes as kinematic extractions and extractions using more inclusive variables like the total cross-section. Kinematic extractions of the top mass involve a jet-based observable and measurement of a sophisticated differential cross-section. Direct calculations of differential cross-sections in theory are hard to calculate and experimentalists rely on Monte Carlo (MC) based template and matrix element methods [85, 42], which aim to account for essentially all of the kinematic final state information in the top quark events. MC simulations are very useful here because of their ability to simulate different physics sub-processes in a fully differential manner. This method yields the most precise value of top mass as $m_t^{\mathrm{MC}} = 172.44 \pm 0.49$ GeV (CMS) [84], $m_t^{\mathrm{MC}} =$

172.84 ± 0.70 GeV (ATLAS) [1] and $m_t^{\rm MC} = 174.34 \pm 0.64$ GeV (Tevatron) [62]. The MC superscript emphasizes that the renormalization scheme of the mass extracted depends on the details of the MC generator.

However, this approach does not account for the relation of the extracted MC top quark parameter to an unambiguous field theoretic QCD top mass definition [75, 100, 65], which depends on the shower dynamics and its interface with hadronization. Processes like hadronization, and the amount of underlying event activity are to some degree universal and can be calibrated by ensuring that MC agrees with other experiments. The UE is same in the events with or without top quark production. Furthermore, the MC top mass parameter does not have a precise field theoretic definition. Identifying these values with a Lagrangian top-mass scheme m_t induces an additional ambiguity at the 0.5–1.0 GeV level [75, 65]. While it seems unlikely that the template and matrix element analyses can be based on first principle QCD calculations which can be systematically improved to specify the top mass scheme unambiguously, it is quite plausible that other highly sensitive top mass observables can be devised which can clarify the issue by making high precision theoretical calculations feasible. Calibration of $m_t^{\rm MC}$ based on such observables has been studied recently in e^+e^- collisions [27].

The measurement of the total cross-section provides an alternative way of measuring the top mass [41]. In this case one can perform a direct comparison of the $\overline{\rm MS}$ renormalized cross-section of top production with the experiment. This allows one to extract top mass in $\overline{\rm MS}$ scheme. However, this cross-section is not very sensitive to m_t and the uncertainties in the normalization limit the measurement to the accuracy to a few GeV's, and hence cannot compete with a kinematic extraction. This is a general trend for more inclusive measurements, they cannot compete with the experimental sensitivity of kinematic extractions.

2.2 Theoretical Challenges

Precision measurements of the top quark mass are a difficult task due to challenges from both experimental and theoretical sides. Our aim is two-fold:

1. Propose an observable that is sensitive to the top mass and is robust against extraneous effects in a hadron collider.

2. Provide a systematically improvable theoretical description of such an observable that allows one to precisely measure the top mass while accounting for the quantum effects that have remained beyond the scope of MC-based methods.

In the following sections we discuss several aspects of solving this problem that are relevant to top mass measurement at the LHC.

2.2.1 Observable for measuring top mass

We are interested in using observables that are inclusive over the top decay products, are sensitive to the top mass, and have the level of simplicity that they can be described with direct computations from QFT and EFT. Using the momenta of the radiation from the top quark and the decay products, we attempt to reconstruct the top mass. A jet-based measurement on a boosted top sample is a desirable candidate. With sufficient boost the decay products can be contained in a cone or a fat top jet with jet radius $R \sim 1$. Jet reconstruction at LHC involves specification of jet algorithm and jet radius, that can introduce extraneous effects in top mass measurements. The dependence on these jet properties needs to be either eliminated or understood in the theory.

2.2.2 Top Mass Scheme

We have already alluded above to the fact that any measurement of top mass must be related to a precise field theoretic definition. This corresponds to specifying a top mass scheme. A renormalization scheme specifies how the bare top mass paramater in the QCD Lagrangian gets renormalized and then modified by finite quantum corrections.

As mentioned above, MC simulations do not have the needed accuracy to precisely account for these quantum corrections. The gross handling of parton shower and non-perturbative effects such as hadronization creates an inherent ambiguity of $\mathcal{O}(1)$ GeV in the definition of m_t^{MC}.

The most commonly used schemes for mass renormalization are the pole mass and $\overline{\mathrm{MS}}$ scheme. The pole mass scheme is defined by fixing the top mass to the pole of the tree level propagator at all orders in perturbation theory, and absorbing all the higher order corrections in the mass counterterm. However, this definition suffers from the so called "Renormalon" ambiguity that is related to factorial divergence of higher order self energy correction graphs. As a result m_t^{pole} cannot be specified in perturbation theory to an accuracy better than Λ_{QCD}. There have been studies to estimate the ultimate precision with many orders in perturbation theory that one can achieve in defining the pole mass. In Ref. [18] this uncertainty was estimated to be about 70 MeV, however, more careful considerations of heavy quark symmetries yield a more conservative estimate of 250 MeV [70]. In practice often only lower order perturbative predictions are available, and values for the pole mass can shift by $\mathcal{O}(500$ MeV) when determined at different orders. As a result it is not desirable to express the top mass in the pole mass scheme.

The class of schemes free from renormalon ambiguities are referred to as short distance mass schemes. The $\overline{\mathrm{MS}}$ scheme is one such example. Short distance schemes such as the $\overline{\mathrm{MS}}$ scheme impose a natural IR cutoff on the self energy graphs related to the scale of renormalization. This cutoff protects the renormalized mass from the infrared ambiguity.

However, within the class of short distance mass schemes, theoretical calculations require us to use only the schemes that employ a scale for renormalization that is physically sensible in relation to the other energy scales presented in the measurements. As we will see below, this can also be phrased in the Effective Theory language as choosing renormalization scales that do not spoil the power counting of the effective theory.

In the case of kinematic top mass reconstruction, we do a jet-based mass mea-

surement that is inclusive over the decay product. This corresponds to focusing on the region around m_t where the cross-section peaks. Here the Breit Wigner sets the natural scale Γ_t= 1.4 GeV in the problem. For the specific case of the $\overline{\text{MS}}$ scheme the scale for the mass is m_t itself and the first order correction to m_t is $\sim \alpha_s m_t \sim 7$ GeV. This correction, being much bigger than Γ_t, swamps the Breit Wigner, thus making $\overline{\text{MS}}$ scheme unsuitable for kinematic extraction. This happens because the scale associated with the $\overline{MS}$ mass is too large, being $\gg \Gamma_t$.

In Refs. [67, 66] an appropriate scheme for kinematic top mass extraction was proposed. This is known as the MSR scheme. It is based on the coefficients of the $\overline{\text{MS}}$ scheme but the size of the fixed order corrections can be controlled by a parameter R so that the scheme is defined at smaller scales. The relation of the MSR mass $m_t(R,\mu)$ to the pole mass is given by

$$m_t^{\text{pole}} = m_t(R,\mu) + \delta m_t(R,\mu), \tag{2.1}$$

where $\delta m_t(R,\mu)$ has a perturbative expansion

$$\delta m_t(R,\mu) = R\sum_{n=1}^{\infty}\sum_{k=0}^{n} a_{nk}\left[\frac{\alpha_s(\mu)}{4\pi}\right]^n \ln^k\frac{\mu}{R}, \tag{2.2}$$

where the a_{nk} are numerical coefficients that are identical to the case of the $\overline{\text{MS}}$ scheme. For the $\overline{\text{MS}}$ scheme we have $R = \overline{m}$. Instead choosing $R \sim \Gamma_t$ for the MSR mass yields a renormalization scheme that is appropriate for kinematic extractions.

This scheme is not a unique choice with $R \sim \Gamma_t$ but is convenient since it has a simple relation to the $\overline{\text{MS}}$ scheme. This means that the perturbative results are known at 4-loop orders, enabling a precise scheme conversion. For further details, including explicit results for the a_{nk}s, see Ref. [67].

2.2.3 Large Logarithms in Cross Section

Top quark production is a complex process since it involves contribution from physics at multiple energy scales. For boosted tops we require that they be produced with

energy Q such that $m_t \ll Q$. For pp collisions this corresponds to top p_T's above 400-500 GeV. Higher p_T's are not only desirable for inclusive measurement over the decay products, they also enable an effective theory treatment of the jet mass cross-section as we will see below. We are interested in performing measurements in the peak region where the energy scale is set by the top decay width $\Gamma_t = 1.4\,\text{GeV} \ll m_t$. And, then there are non-perturbative effects of hadronization that scale as $\sim \Lambda_{\text{QCD}} \simeq 300$ MeV $< \Gamma_t$.

The presence of these hierarchically separated scales generate large logarithms L of ratios of these scales in the cross-section. The ("cumulative")cross section is schematically

$$\begin{aligned} \mathrm{d}\sigma \sim \sigma_0 \Big(& 1 + \alpha_s L^2 + \alpha_s^2 L^4 + \alpha_s^3 L^6 + \dots \\ & + \alpha_s L^1 + \alpha_s^2 L^3 + \alpha_s^3 L^5 + \dots \\ & + \alpha_s L^0 + \alpha_s^2 L^2 + \alpha_s^3 L^4 + \dots \\ & + \alpha_s L^1 + \alpha_s^2 L^3 + \dots \Big) , \end{aligned} \tag{2.3}$$

where σ_0 is the Born cross-section, and we show the structure of logarithms at each order in α_s. L could refer to $\ln(Q/m_t)$, $\ln(m_t/\Gamma_t)$, etc. For a large separation between the scales, $\alpha_s L \sim 1$ and a strict expansion in α_s is no longer a good expansion.

One must go beyond traditional fixed order perturbation theory to correctly sum these series of logarithms that organize themselves in the pattern in Eq. (2.3). This can be done very systematically in the framework of Effective Field Theories (EFT) by distinguishing fields at different energy scales.

2.2.4 Initial State Radiation, Final State Radiation, and Underlying Event

The initial state radiation (ISR) corresponds to radiation along the beam that is emitted from incoming protons. ISR can affect the measurement if the radiation ends up in $t\bar{t}$ jets. ISR can be studied in the processes with little activity in the beam

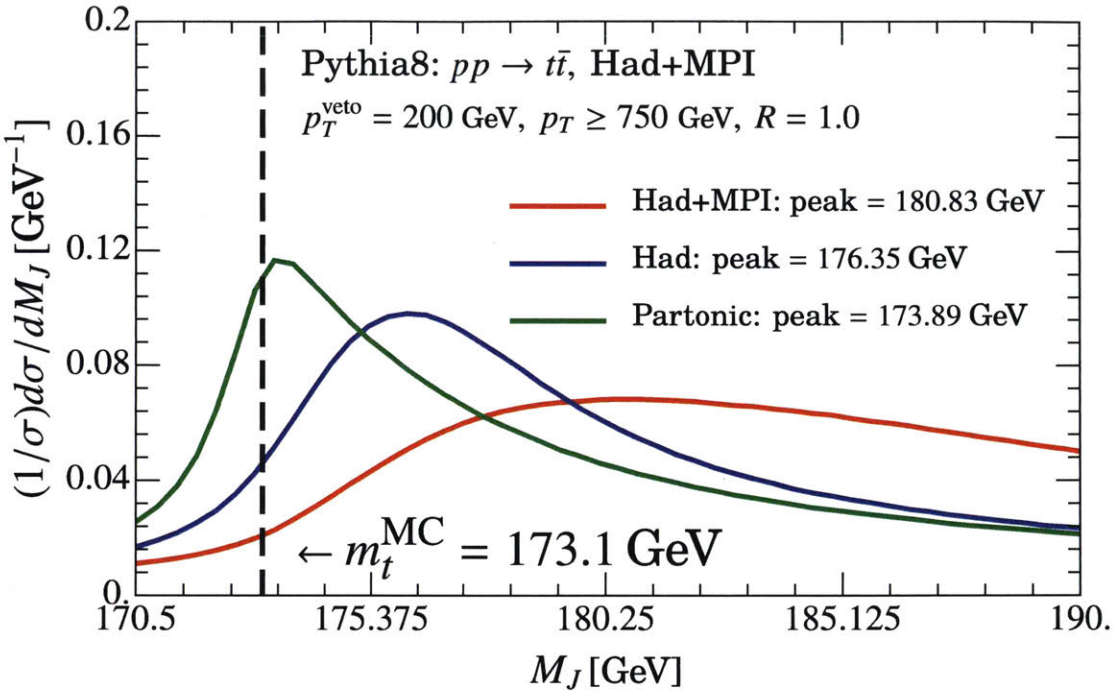

Figure 2-1: Effect of hadronization and underlying event (modeled through MPI in PYTHIA) on the peak position.

region [110]. Unlike jets in the central region, the radiation in the beam often cannot be fully measured. We would like to work with observables where the beam radiation can be decoupled from the $t\bar{t}$ jets as much as possible. An event with strong ISR radiation is likely to contaminate the top jets more. Hence, it is a helpful strategy to limit the activity in the beam region by imposing a veto on the radiation outside the top jets.

The final state radiation here refers to the parton shower and hadronization of top decay products. Hadronization is an inherently non perturbative process, but it can be treated in the framework of factorization. Furthermore, corrections to jet mass spectra (or to equivalent event shapes) from hadronization often can be proven to be universal across several processes. As a result, for example, one could use the corrections from studying jets from massless quarks to describe hadronization effects in top jets. These hadronization corrections are of order 0.5-2.0 GeVs [54]. Underlying event (UE) populate the event with soft particles at a scale larger than hadronization, and can more significantly contaminate the measurement. The UE

activity is measured in the regions away from the phase space of hard jets [33]. There is no theoretically rigorous treatment of UE available and the effect of the radiation needs to be modeled for the measurement, if it cannot be eliminated completely. While the UE remains outside the framework of factorization, a promising method is to extend the treatment of hadronization in order to account for effects of the UE to the peaked jet mass spectrum in $pp \to Z+$ jet [111]. In this study we use the multi parton interaction (MPI) modeling of the UE in PYTHIA.

The top jet mass spectrum is highly sensitive to contamination from initial state radiation (ISR) and the underlying event, that shifts the peak position and affects the overall shape. In Fig. 5-1 we show the top-jet mass spectrum from PYTHIA8 simulations in three different cases: partonic, with hadronization turned on, and with both hadronization and MPI turned on. We see that the peak gets shifted by ~ 5 GeV on turning on MPI, while the shift is ~ 2 GeV from including hadronization. The top mass spectrum is hence sensitive to the MC tuning that fixes the hadronization and underlying event.

2.2.5 Color Channels, Parton Distribution Functions, and Color Reconnection

In an e^+e^- collider the top anti-top pair is produced in a singlet state, whereas in a pp collision we have various color channels for $qq \to t\bar{t}$ and $gg \to t\bar{t}$ processes [82]. Our theory enables us to perform calculations assuming that the initial and final states are partons. This perturbative cross-section is then combined with parton distribution functions PDFs to account for the initial proton states. Since PDFs are universal non-perturbative objects they are are determined by global fits to other collider data. Hence, in line with the treatment of ISR, we would like to decouple the contribution from PDFs from the top jet mass measurement. Furthermore, there can be interference between the gluons emitted from the initial state and final state lines, which can also change the color channel. Our treatment of final state dynamics must also be able to handle measuring the mass of the unstable colored top quark.

2.2.6 Pile-up

Pile-up corresponds to multiple pp collisions in the same event. Radiation from pile-up is truly uncorrelated with the collision that generates $t\bar{t}$ jets. It strongly affects observables like the mass of large-R jets. The contribution of pile up scales as R^3 [2], which could be problematic for fat top jets with $R \sim 1$. In our study we do not consider effects of pile-up and assume that they can be handled experimentally and that implementing a pile up mitigation strategy will not significantly modify the kinematic spectrum. This deserves to be explored in a dedicated study and we will comment more in later sections.

Chapter 3

Theoretical set up

In this chapter we discuss the basics of the Effective Field Theory (EFT) framework that forms the basis of the calculations presented in this thesis. The central feature of these EFTs is that they contain modes, the relevant quark and gluon degrees of freedom, that are distinguished based on their momenta. As mentioned above, boosted top quark production with subsequent decays in the peak region of the invariant mass distributions involves physical effects in a range of widely separated energy scales that necessitates replacing fixed order computations by resummed calculations. The hierarchy between the production energy Q, the top mass m, the decay width Γ_t and the hadronization scale $\Lambda_{\rm QCD}$ is given by $Q \gg m \gg \Gamma_t > \Lambda_{\rm QCD}$. The relevant EFTs for this hierarchy are the Soft Collinear Effective Theory (SCET) and Heavy Quark Effective Theory (HQET) which we introduce in this chapter. A similar set up of effective theories has also played an important role in B-meson physics [21, 94, 12, 13, 23, 93].

3.1 SCET

SCET is the effective theory of QCD suitable for collider physics applications [10, 11, 15, 14]. In this section we first describe the relevant kinematics and then discuss the field theory structure in terms of SCET fields, Lagrangians, and operator building blocks.

3.1.1 Light Cone Kinematics

SCET contains quark and gluon fields that have collinear or soft scaling of momenta defined with respect to specific directions and characterized by a power counting parameter $\lambda \ll 1$. The power counting parameter determines the size of corrections that have been ignored when approximating QCD by SCET. Let us consider a jet (either a quark or a gluon induced jet) in the direction $\hat{n}$. Using $\hat{n}$ we define the two light cone vectors:

$$n^\mu = (1, \hat{n}), \qquad \bar{n}^\mu = (1, -\hat{n}), \tag{3.1}$$

such that

$$n^2 = \bar{n}^2 = 0, \qquad n \cdot \bar{n} = 2. \tag{3.2}$$

These light cone vectors allow us to decompose any four vector p^μ in a basis so that we have

$$p^\mu = p^- \frac{n^\mu}{2} + p^+ \frac{\bar{n}^\mu}{2} + p_\perp, \qquad p^\mu \equiv (p^+, p^-, p_\perp), \tag{3.3}$$

where

$$p^+ = n \cdot p, \qquad p^- = \bar{n} \cdot p, \qquad p_\perp^\mu = p^\mu - \left(p^- \frac{n^\mu}{2} + p^+ \frac{\bar{n}^\mu}{2} \right). \tag{3.4}$$

From Eqs. (3.2) and (3.3) we have

$$p^2 = p^+ p^- - p_\perp^2. \tag{3.5}$$

Next, the power counting parameter λ depends on the energy scales in the problem and the type of measurement being performed. Consider a dijet process in an e^+e^- collider, with jets of mass M produced with energy $E_J = Q/2$, where Q is the center of mass energy. In this case the power counting parameter is given by $\lambda = M/Q \ll 1$.

This allows us to distinguish momenta that have collinear or soft scaling with respect to the direction $\hat{n}$ according to the relative scaling of their $+$, $-$, and $\perp$ momentum components defined in Eq. (3.3):

$$\begin{aligned} n\text{-collinear} &\sim Q\left(\lambda^2, 1, \lambda\right), \\ \bar{n}\text{-collinear} &\sim Q\left(1, \lambda^2, \lambda\right), \\ \text{ultrasoft} &\sim Q(\lambda^2,\, \lambda^2,\, \lambda^2)\,. \end{aligned} \tag{3.6}$$

We first note that these momenta correspond to particles that are allowed to be on-shell. This can be seen from Eq. (3.5). Modes that have the homogeneous scaling in Eq. (3.6) are technically referred to as ultrasoft modes to distinguish them from soft modes that scale as $Q(\lambda, \lambda, \lambda)$. In SCET quarks and gluons with collinear and ultrasoft scalings are associated with different fields. Hence, SCET is not Lorentz invariant like QCD and is specific to the frame of reference.[1] Energetic particles that move along the direction of the $\hat{n}$ jet have n-collinear scaling. We can verify that particles with these scaling contribute to a mass $M \sim Q\lambda$ for the jet:

$$\begin{aligned} M_{\text{jet}}^2 &= p_n^2 \\ &= p^+ p^- - p_\perp^2 \\ &\sim Q(\lambda^2) \times Q - Q^2\lambda^2 \sim Q^2\lambda^2 = M^2\,, \end{aligned} \tag{3.7}$$

Furthermore, adding ultrasoft particles to the the jet also give dominant contributions of $Q\lambda$ to M:

$$\begin{aligned} M_{\text{jet}}^2 &= \left(p_n + p_{us}\right)^2 \\ &\sim \left(p_n + p_{us}\right)^+ \times \left(p_n + p_{us}\right)^- - \left(p_n + p_{us}\right)_\perp^2 \\ &\sim Q(\lambda^2 + \lambda^2) \times Q(1 + \lambda^2) - Q^2(\lambda + \lambda^2)^2 \sim Q^2\lambda^2 = M^2\,, \end{aligned} \tag{3.8}$$

[1]There are, however, residual Lorentz symmetries in the theory known as Reparameterization Invariance (RPI) [95], and factorization based predictions do provide a frame independent description of the dynamics at the order one is working.

where we observe that the ultrasoft fields only contribute through the + component that is of the same order as the collinear + component. This implies that the jet mass spectrum calculated in SCET will have contribution to the mass from both ultrasoft and collinear fields. In the same way, the ultrasoft fields can also contribute to the jet in the opposite direction. This has the consequence that for a simple jet mass observable considered here the masses of the two jets cannot be described independently but are rather coupled through the ultrasoft particles. We will later see that application of grooming overcomes this by removing particles with ultrasoft scaling in Eq. (3.6), in which case, the dominant dynamics of the jets become truly independent of each other.

We can make a further simplification by making sure that our jet axis defined by $\hat{n}$ aligns with the jet three momentum as closely as possible. This makes the $\perp$ component smaller and then the jet mass is simply given by

$$M_{\text{jet}}^2 = p^+ p^- + \mathcal{O}(p_\perp^2) = p^+ Q + \mathcal{O}(p_\perp^2)\,. \tag{3.9}$$

Thus calculating the jet mass cross section in SCET is equivalent to measuring the p^+ component of the jet with a carefully aligned axis. Hence, following Eq. (3.5), even though ultrasoft particles have a smaller virtuality of $p_s^2 \sim Q^2\lambda^4 \ll p_n^2 \sim Q^2\lambda^2$ they contribute equally to the jet mass as collinear modes since their + components are commensurate.

3.1.2 SCET Fields, Lagrangian, and Operator Building Blocks

SCET as an effective theory reproduces the infrared collinear and soft divergences of QCD. This is made possible by assigning a separate fields for the three momentum scalings shown in Eq. (3.6). We display the corresponding fields in Tab. 3.1.

The SCET Lagrangian consisting of these fields is given by

$$\mathcal{L}_{\text{SCET}}^{(0)} = \mathcal{L}_{us}^{(0)} + \sum_{n_i} \mathcal{L}_{n_i}^{(0)}(\xi_{n_i}, A_{n_i}, n_i \cdot A_{us})\,, \tag{3.10}$$

SCET Modes	Scaling	Fields
n-collinear	$Q(\lambda^2, 1, \lambda)$	$(\xi_n,\ A_n^\mu)$
$\bar{n}$-collinear	$Q\,(1, \lambda^2, \lambda)$	$(\xi_{\bar{n}},\ A_{\bar{n}}^\mu)$
ultrasoft	$Q(\lambda^2,\ \lambda^2,\ \lambda^2)$	(ψ_{us}, A_{us}^μ)

Table 3.1: Summary of the EFT modes set up, scaling, and fields in SCET with a power counting parameter λ and large momentum scale Q.

where the superscript (0) indicates that the Lagrangian is expressed in leading order in the λ expansion. Here n_i refers to the collinear directions, which for our case are n and $\bar{n}$. The term $n_i \cdot A_{us}$ indicates that the ultrasoft gluons couple to the collinear fields through their + component. The SCET fields themselves have a specific scaling in λ. Gauge transformations require that gluon fields scale the same way as their momentum. Hence

$$A_n^\mu \sim (\lambda^2, 1, \lambda)\,, \qquad A_{\bar{n}}^\mu \sim (1, \lambda^2, \lambda)\,, \qquad A_{us}^\mu \sim\ (\lambda^2, \lambda^2, \lambda^2)\,, \tag{3.11}$$

while the collinear quark ξ_{n_i} and ultrasoft quark ψ_{us} fields scale as λ and λ^3 respectively. This is very helpful in determining which operators in SCET contribute at leading order and which ones at subleading orders. In this thesis, for example, we do not consider operators involving ultrasoft quark fields since they are subleading in the λ expansion. The collinear quark Lagrangian is given by:

$$\mathcal{L}_{n\xi}^{(0)} = e^{-x\cdot\overline{\mathcal{P}}}\bar{\xi}_n\Big(in\cdot D + i\not{D}_{n\perp}W_n^\dagger\frac{1}{\overline{\mathcal{P}}}W_n i\not{D}_{n\perp}\Big)\frac{\not{\bar{n}}}{2}\xi_n\,, \tag{3.12}$$

where

$$iD_{n\perp}^\mu = \mathcal{P}_\perp^\mu + gA_{n\perp}^\mu\,, \tag{3.13}$$

$$in\cdot D_n = in\cdot\partial + gn\cdot A_n + gn\cdot A_{us}\,, \tag{3.14}$$

and W_n is a collinear Wilson line discussed further below. We first note that given

the scaling in Tab. 3.1 we identify three different energy scales in SCET: Q, $Q\lambda$, and $Q\lambda^2$. We explain the meaning of various terms in Eq. (3.12) by relating them to these three scales:

1. The $Q\lambda^2$ scale: The x dependence encodes fluctuations at the lowest energy scale $Q\lambda^2$ that corresponds to the longest distances, the IR region of our theory. As mentioned above the ultrasoft fields that scale as λ^2 can only contribute through the $+$ component which is of the same order as the collinear $+$ component. Hence, we note their presence in the derivative $n \cdot D_n$ along side the collinear gluon term. All the terms in the parentheses Eq. (3.12) scale as λ^2.

2. The $Q\lambda$ scale: Next we have the $\perp$ projections of derivatives which describe physics at the scale $Q\lambda$. We do not simply have a derivative with respect to x since that gives contributions at $\sim Q\lambda^2$ that are subleading for this energy scale. Neither we see $\perp$ ultrasoft gluons in Eq. (3.13) since they are also power suppressed. The "label" operator $\mathcal{P}_\perp$ picks out the $\mathcal{O}(Q\lambda)$ momentum. We also notice the $\perp$ component of collinear gluons are included since they also scale as $\mathcal{O}(\lambda)$.

3. The Q scale: Lastly we have the label momentum operator $\overline{\mathcal{P}}$ that picks out the $\mathcal{O}(Q)$ momentum corresponding to the shortest length scales. We notice that this operator appears in the denominator making the SCET action non local at this scale. This should not be surprising since we have integrated out all the high energy fluctuations at scale Q from the theory, which are present in QCD that is local at all the energy scales. The action is, however, local at the scales $Q\lambda$ and $Q\lambda^2$.

We note that unlike the other derivative terms we do not see a $g\bar{n} \cdot A_n$ term next to $\overline{\mathcal{P}}$. This term is actually hiding in W_n, the collinear Wilson line, defined as

$$W_n(x) = \left[\sum_{\text{perms}} \exp\left(\frac{-g}{\overline{\mathcal{P}}} \bar{n} \cdot A_n(x) \right) \right], \tag{3.15}$$

where the sum is performed over permutations of terms obtained after expanding the exponential. In fact, the identity

$$\frac{1}{i\bar{n}.D_n} = \frac{1}{\overline{\mathcal{P}} + g\bar{n}\cdot A_n} = W_n^\dagger \frac{1}{\overline{\overline{\mathcal{P}}}} W_n \,, \tag{3.16}$$

can be used to express the derivative at scale Q which has a form similar to that in Eq. (3.13). It is helpful to write it in terms of collinear Wilson lines since it illustrates another important point: given the fact that the $-$ component of the collinear gluons A_n is $\mathcal{O}(1)$ in power counting we are allowed to have arbitrarily many insertions of the $\bar{n}\cdot A_n$ field, represented by the infinite terms collected in Eq. (3.15). Physically this is a result of arbitrary number of emissions of n-collinear gluons from particles that ARE NOT n-collinear, and the formation of these interactions into Wilson lines is dictated by gauge symmetry.

Given that various quarks and gluons are being distinguished based on their momenta the generic gauge transformations of QCD are no longer symmetries of SCET either, since gauge transformations of arbitrary momenta can change the momentum scaling of the SCET fields, thus mixing them into one another. As a result, we restrict ourselves to gauge transformations that are specific to the n-collinear, $\bar{n}$-collinear and ultrasoft fields and in general any observable calculated in SCET must be invariant with respect to gauge transformation in the three sectors. We note that the n-collinear quarks and gluons transform with both n-colliear and ultrasoft gauge transformations, but the ultrasoft field transform only under ultrasoft gauge transformations.

We do not give explicit expressions of the Lagrangian for the collinear gluon and ultrasoft fields here. These expressions can be found in Ref. [14]. We instead summarize some of the key points: The collinear gluon Lagrangian involves similar multipole expansions of the derivative terms as in Eqs. (3.13) and (3.14). The gauge fixing term in this Lagrangian breaks collinear gauge symmetry, as it should, but it is made covariant with respect to ultrasoft gluons, which makes them background fields from the perspective of collinear fields. This is to avoid fixing the gauge for ultrasoft fields in the collinear gluon Lagrangian. Lastly, the Lagrangian for ultrasoft fields is

identical to the QCD Lagrangian.

Having laid out the formalism for dynamical terms for SCET fields in Eq. (3.10) we can now add operators that are specific to the process of interest. These operators have a scaling in λ that is given by the sum of the scaling of all the fields and derivatives appearing in them. To preserve gauge symmetry it is helpful to write down operators in terms of specific combinations of the fields displayed in Tab. 3.1 that are individually gauge invariant, and serve as building blocks for constructing any type of operator.

The gauge invariant building blocks for collinear operators are given by

$$\chi_n = W_n^\dagger \xi_n\,, \qquad \mathcal{B}_{n\perp}^\mu = \frac{1}{g}\big[W_n^\dagger i D_{n\perp}^\mu W_n\big]\,, \qquad \mathcal{P}_{n\perp}^\mu\,, \tag{3.17}$$

where in the second term the derivatives act within the square brackets. To lowest order $\mathcal{B}_{n\perp}^\mu = A_{n\perp}^\mu - (\mathcal{P}_\perp^\mu/\overline{\mathcal{P}})\bar{n}\cdot A_n + \ldots$ These objects scale as λ and are gauge invariant with respect to n-collinear gauge transformations. Every other combination of collinear fields can be expressed in terms of these three building blocks.

The ultrasoft fields are handled in a different manner. It can be shown that by redefining the collinear fields as

$$\xi_n \to Y_n \xi_n \qquad A_n^\mu \to Y_n A_n^\mu Y_n^\dagger\,, \tag{3.18}$$

where the ultrasoft Wilson line is defined by

$$Y_n(x) = \mathrm{P}\left[ig\int_{-\infty}^{0} \mathrm{d}s\, n\cdot A_{us}(x+ns)\right], \tag{3.19}$$

one decouples the redefined fields completely from the ultrasoft fields. Hence, as a result the $gn\cdot A_{us}$ term in Eq. (3.14) drops out. This is referred to as BPS field redefinition and it implements soft-collinear factorization [14].

3.2 HQET

Heavy Quark effective theory describes dynamics of QCD systems with a heavy quark that interacts predominantly through soft interactions [46, 76, 77, 60, 58]. HQET has been very successful in explaining new emergent spin-flavor symmetries in the heavy quark limit with $m_Q \to \infty$. Here the hard scale is set by the mass of the heavy quark. For case of mesons containing bottom or charm quark the low energy scale is $\Lambda_{\rm QCD}$, however, given that top quark decays before it hadronizes the low energy physics is dominated by $\Gamma_t = 1.4$ GeV. We will see later on that there are non-perturbative corrections too from radiation associated with hadronization that can be handled by a simple extension of the formalism we present below.

Analogous to SCET the description of HQET is dependent on the frame. Here the frame is set by the velocity vector v^μ of the heavy quark, where $v^2 = 1$. Using v the momentum of the heavy quark is given by

$$p^\mu = m_Q v^\mu + k^\mu \,, \tag{3.20}$$

where $|k^\mu| \ll m_Q$. Here k^μ represents small shifts to the heavy quark momentum by soft particles. This implies that in the heavy quark limit the velocity v^μ is conserved unless there is a hard scattering, such as a weak decay of the heavy quark. Since we are interested in scales that are much smaller than the heavy quark mass we integrate out the anti-quarks. This is accomplished at tree level by removing fluctuations of order m_Q with a field redefinition

$$\psi(x) = \sum_v e^{-im_Q v\cdot x} h_v(x) \,, \tag{3.21}$$

which results in $\partial^\mu h_v \sim \mu_{\rm low} h_v(x)$ where $\mu_{\rm low}$ is the relevant low energy scale (in our case $\mu_{\rm low} \sim \Gamma_t$. The HQET Lagrangian is then given by

$$\mathcal{L}_{\rm HQET} = \bar{h}_v \, iv\cdot D \, h_v \,, \tag{3.22}$$

where $iD^\mu = i\partial^\mu + gA^\mu$.

3.3 EFTs for Top Jet Mass Measurement

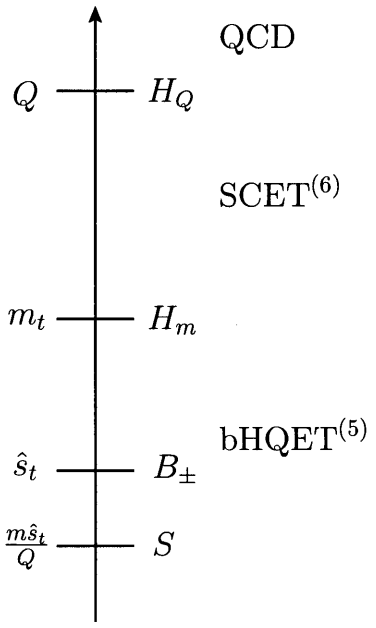

Figure 3-1: EFT setup for boosted top jets in the peak region.

We show in Fig. 3-1 the EFT setup for $e^+e^- \to t\bar{t}$ process [49, 50]. First, the hard modes with fluctuations with virtualities of order $\sim Q$ are integrated out in QCD. The corresponding low-energy theory, SCET, then allows us to resum large logarithms between Q and m. In a second step all fluctuations with virtualities of order $\sim m$ are integrated out, and SCET is thus matched onto bHQET, which allows resummation of logarithms between m and Γ_t. The theory is denoted "bHQET" with an extra b to remind us that here the velocity v^μ is boosted. We indicate the number of dynamic flavors in the theory through superscripts (5) and (6).

We are interested in the region where each of the jet invariant masses, for the top M_t and antitop $M_{\bar{t}}$, is close to the top quark mass, i.e.,

$$\hat{s}_{t,\bar{t}} \equiv \frac{M_{t,\bar{t}}^2 - m^2}{m} \ll m\,. \tag{3.23}$$

The peak region is characterized by $\hat{s}_{t,\bar{t}} \sim \Gamma_t$, and corresponds with the peak of the M_t dependent cross section, while the tail region corresponds to $\hat{s}_{t,\bar{t}} \gg \Gamma_t$ while still satisfying Eq. (3.23).

We first begin by generalizing the collinear quark Lagrangian presented in Eq. (3.12)

to include massive degrees of freedom for the top quark [92]:

$$\mathcal{L}^{(0)}_{n\xi} = e^{-x\cdot\overline{\mathcal{P}}}\bar{\xi}_n\Big(in\cdot D + (i\not{D}_{n\perp} - m)W_n^\dagger\frac{1}{\overline{\mathcal{P}}}W_n(i\not{D}_{n\perp} + m)\Big)\frac{\bar{\not{n}}}{2}\xi_n\,, \tag{3.24}$$

In order to keep power counting consistent in SCET we now demand that the jet mass be of the same scale as m, so that we avoid introducing another hierarchy of scales in the problem. This leads to the scaling shown in Tab. 3.1 but with λ now given by m/Q. While this includes the region represented by Eq. (3.23) it still allows for mass fluctuations in SCET with $M^2_{t,\bar{t}} \sim m^2$ where $\hat{s}_{t,\bar{t}}$ can be even $\mathcal{O}(m)$. Therefore in this context SCET just plays a role of an intermediate EFT in which the observable is not yet obtained at the desired smaller scale.

We also include an additional mode in the SCET theory that scales as (m, m, m), or $Q(\lambda, \lambda, \lambda)$. We refer to this mode as the mass mode. Unlike ultrasoft modes, the mass modes cannot contribute to the final jet mass measurement and first appear at two loop order. This can be seen by repeating the steps leading to Eq. (3.8), demonstrating that final state mass modes spoil the power counting:

$$\begin{aligned} M^2_{\text{jet}} &= \big(p_n + p_m\big)^2 \\ &\sim \big(p_n + p_m\big)^+ \times \big(p_n + p_m\big)^- - \big(p_n + p_m\big)^2_\perp \\ &\sim Q(\lambda^2 + \lambda) \times Q(1 + \lambda) - Q^2(\lambda + \lambda)^2 \sim Q^2\lambda = m\,Q\,, \end{aligned} \tag{3.25}$$

Hence, mass modes cannot contribute to the measurement through real radiation. However, as we will see below, these modes contribute through virtual effects of top bubbles at $\mathcal{O}(\alpha_s^2)$.

Next we turn to the full bHQET theory for unstable top quarks. This bHQET Lagrangian is given by

$$\mathcal{L}_{\text{HQET}} = \bar{h}_{v_t}\big(iv_t\cdot D_{v_t} - \delta m + \frac{i}{2}\Gamma_t\big)h_{v_t}\,, \tag{3.26}$$

where h_{v_t} is the bHQET field for the top quark with velocity v_t^μ. Here we have labeled the covariant derivative D in Eq. (3.22) with subscript v_t to emphasize that the gluons

bHQET Modes	Scaling	Fields
n-ucollinear	$\left(\frac{m\hat{s}_t}{Q}, \frac{Q\hat{s}_t}{m}, \hat{s}_t\right)$	$(h_{v_t}, A^\mu_{v_t})$
$\bar{n}$-ucollinear	$\left(\frac{Q\hat{s}_t}{m}, \frac{m\hat{s}_t}{Q}, \hat{s}_t\right)$	$(h_{v_{\bar{t}}}, A^\mu_{v_{\bar{t}}})$
ultrasoft	$\left(\frac{m\hat{s}_t}{Q}, \frac{m\hat{s}_t}{Q}, \frac{m\hat{s}_t}{Q}\right)$	(ψ_{us}, A^μ_{us})

Table 3.2: Summary of the EFT modes set up, scaling, and fields in bHQET.

A_{v_t} that appear here have ultracollinear scaling. In bHQET the pole mass term is integrated out and we are left with the residual δm term that relates pole mass to a specific mass scheme, such as the MSR scheme defined in Eq. (2.1). The velocity $v^\mu_{t,\bar{t}}$ for the top and anti-top jets produced are given by

$$v_t^\mu = \left(\frac{m}{Q}, \frac{Q}{m}, \mathbf{0}_\perp\right), \qquad v_{\bar{t}}^\mu = \left(\frac{Q}{m}, \frac{m}{Q}, \mathbf{0}_\perp\right), \tag{3.27}$$

where both sets of components are defined with respect to the top jet direction using n^μ and $\bar{n}^\mu$ respectively.

The Γ_t width term in Eq. (3.26) correctly reproduces the Breit Wigner shape for the top quark. We refer to this theory as the boosted Heavy Quark Effective Theory (bHQET). In order to understand the scaling of modes in bHQET we note that the jet mass fluctuations are now restricted to the desired scale for the measurement $\hat{s}_t \gtrsim \Gamma_t$. Hence in the frame of top quark the modes simply get boosted to yield the scaling shown in Tab. 3.2. We refer to these modes as $n, \bar{n}$-ultracollinear (ucollinear or uc) modes to distinguish them from collinear modes in SCET with higher virtuality.

Ultrasoft modes can be added to bHQET in a very similar manner to SCET. From Tab. 3.2 we note that they are now at lower virtuality than in SCET. From the discussion in the previous chapter we learned that the ultrasoft modes couple to the collinear fields only through the + component which can be implemented by a simple replacement:

$$iD_t^\mu \to i\mathcal{D}_t^\mu = i\tilde{\partial}^\mu_{v_t} + gA^\mu_{v_t} + \frac{\bar{n}}{2} g\, n\cdot A_{us}\,, \tag{3.28}$$

which results in the coupling $(Q/m)g\,n\cdot A_{us}$ to the heavy quark field in Eq. (3.26). Here we have performed a multipole expansion for the ∂^μ in Eq. (3.22) term similar to that in SCET to give

$$i\partial^\mu \to i\tilde{\partial}^\mu_{v_t} = \frac{n^\mu}{2}\overline{\mathcal{P}} + \mathcal{P}^\mu_\perp + \frac{\bar{n}^\mu}{2} n\cdot i\partial\,, \tag{3.29}$$

where the label momentum operators $\overline{\mathcal{P}}$ and $\mathcal{P}^\mu_\perp$ pick out the components of size $Q\Gamma_t/m$ and Γ_t respectively, and the $n.i\partial$ corresponds to the residual momentum components of size $m\Gamma_t/Q$.

Furthermore, the ultrasoft modes can be decoupled from the bHQET fields in the same way as we did above for the collinear fields in Eq. (3.18):

$$h_{v_t} \to Y_n h_{v_t}\,, \qquad A^\mu_{v_t} \to Y_n\, A^\mu_{v_t}\, Y_n^\dagger\,. \tag{3.30}$$

Together these ingredients give the theoretical set up that we need for our calculations.

Chapter 4

Top Mass Measurement at the LHC

Boosted top quarks are desirable for a kinematic extraction of the top mass since the decay products can be contained in a single jet and one can perform an inclusive measurement on the top jet. In Ref. [50] a kinematic extraction of the top mass at future e^+e^- colliders was proposed through the measurement of the hemisphere mass distribution. Here we derive a corresponding factorization for a top-mass sensitive observable for the $pp \to t\bar{t}$ process. There are two basic methods that can be used to extract the top mass from data using our results:

i) One can make a direct comparison of the factorization based cross section result with experimental data, fitting the top-mass m_t together with any hadronic parameters.

ii) One can use the factorization result to calibrate the meaning of the top mass parameter in Monte Carlo simulations, by fitting m_t and hadronic parameters to Monte Carlo simulation data. This numerically determines a translation between $m_t^{\rm MC}$ and a top mass in a short distance scheme. The Monte Carlo simulation may then be extrapolated to other regions of the parameters and directly compared to data.

The correspondence between experimental data, Monte Carlo simulations, and factorization is shown in Fig. 4-1.

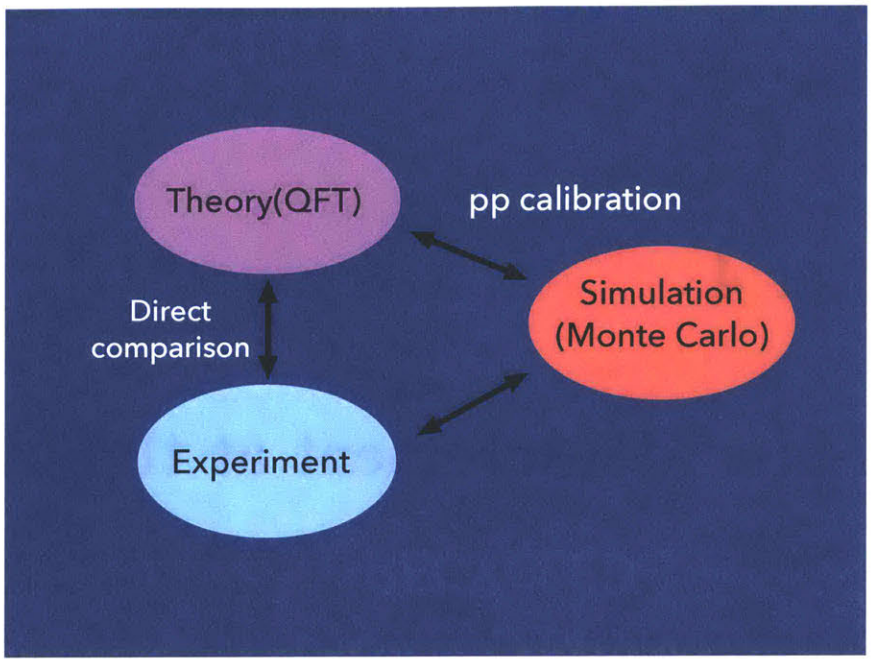

Figure 4-1: The factorized cross section can be either compared directly with the experimental data or can be used to calibrate the MC top mass parameter m_t^{MC}.

To extend the $e^+e^- \to t\bar{t}$ calculation to pp collisions using the 2-jettiness variable we draw upon the work presented in Ref. [80] where the 1-jettiness variable was used to describe the $pp \to$ Higgs + 1 jet process. Various issues such as veto in the beam region, non global logarithms (NGL), and choice of renormalization scales explored there are also relevant to our work. In this chapter we derive the formula for factorized cross section at Next to leading log accuracy (NLL). For a differential cross section $\mathrm{d}\sigma/\mathrm{d}M_J$ we define orders of logarithmic accuracy through the logarithm of cross section in cumulant space. Schematically we have

$$\begin{aligned}\ln\left[\int_0^{M_J^{\mathrm{cut}}} \mathrm{d}M_J \frac{\mathrm{d}\sigma}{dM_J}\right] &\sim \ln\left[\sim 1 + \alpha_s\big(L^2 + L + 1\big) + \alpha_s^2\big(L^4 + L^3 + \dots\big) + \dots\right] \\ &\sim \sum_k (\alpha_s L)^{k+1} + \sum_k (\alpha_s L)^k + \sum_k \alpha_s (\alpha_s L)^k + \dots\,, \end{aligned} \tag{4.1}$$

where truncation up to the first two terms defines NLL accuracy, including the next term brings us to NNLL, and so on. In this chapter we consider measurements without jet grooming, then extend discussion to include jet grooming in Chapter 5.

4.1 Mass Sensitive Observable

We propose using a jet mass measurement that can be calculated with the aid of the 2-jettiness variable in order to measure the top mass from a boosted top sample in pp collisions. We extend the factorization theorem already known for the 2-jettiness measurement for massless jets to the case of top jets. We will be focusing on the case of exclusive top production, and later comment on how one can make a generalization for the inclusive case with the aid of soft drop grooming which also has other advantages.

The 2-jettiness event shape, $\mathcal{T}_2$, divides the event into various sectors: the top and anti-top jet sectors and the beam sector. The jet regions are defined using a specific algorithm and a minimization procedure, and the remaining region is considered as the beam region. The particle momenta are combined linearly in each region which yields a quantity that can be directly related to the invariant masses of the jets. The 2-jettiness for pp collisions is defined as follows

$$\begin{aligned}\mathcal{T}_2 &= \min_{n_t, n_{\bar{t}}} \sum_i \min\{\rho_{\text{jet}}(p_i, n_t), \rho_{\text{jet}}(p_i, n_{\bar{t}}), \rho_{\text{beam}}(p_i)\} \\ &= \mathcal{T}_2^t + \mathcal{T}_2^{\bar{t}} + \mathcal{T}_2^{\text{beam}}\,, \end{aligned} \tag{4.2}$$

where the sum runs over all the particles in the event with momentum p_i, and ρ specifies a distance measure to the jet axes, $n_{t,\bar{t}}$, or to the beam. A given particle will fall in one of these regions depending on the smallest of all three distances given by the ρ's. Anti-kT [32] is the standard jet algorithm currently being employed at the LHC. We use the XCone jet algorithm introduced in Ref. [108] to obtain two exclusive top jets and also specify the distance measure ρ. The XCone algorithm yields circular jets just like jets obtained from Anti-kT algorithm, and since it is based on 2-jettiness it allows us to simply write down an all orders factorization theorem.

For the XCone measure, we have

$$\rho_{\text{jet}}(p_i,\, n_J) \;=\; \frac{2\,\cosh y_J}{R^2}\, n_J \cdot p_i \;=\; \frac{2\, q_J \cdot p_i}{Q_J}\,, \qquad \rho_{\text{beam}}(p_i) \;=\; p_{T_i}\,, \tag{4.3}$$

where y_J is the rapidity, R is the jet radius, and $n_J = \{1, \vec{n}_J\}$ is a normalized light like axis for a jet in direction $\vec{n}_J$. In order to contain the decay products we need $R \gg m/p_T$, where p_T is the transverse momentum of the top jet. Eq. (4.3) specifies a reference momentum q_J and a normalization factor Q_J given by

$$q_J = E_J\, n_J\,, \qquad Q_J = R^2 E_J/\cosh y_J\,, \tag{4.4}$$

where E_J is the jet energy

$$E_J = \sqrt{p_T^2 \cosh^2 \eta_J + m_J^2} = \cosh y_J \sqrt{p_T^2 + m_J^2}\,, \tag{4.5}$$

and η_J is the pseudorapidity of the jet.

For large p_T we can approximate Q_J as $R^2 p_T$. Here Q_J is the large momentum in the jet direction. We can decompose the jet momentum p_J in terms of $(p_J^+, p_J^-, p_{J\perp})$ components defined relative to the jet axis n_J and an auxiliary vector $\bar{n}_J$ obeying $\bar{n}_J^2 = 0$ and $n_J \cdot \bar{n}_J = 2$:

$$p_J^+ = n_J \cdot p_J\,, \qquad p_J^- = \bar{n}_J \cdot p_J\,, \qquad p_{J\perp} = p_J - \frac{n_J}{2}\, p_J^- - \frac{\bar{n}_J}{2}\, p_J^+\,. \tag{4.6}$$

Hence, we have

$$\mathcal{T}_2^J = \frac{2E_J\, n_J \cdot p_J}{Q_J} = \frac{2E_J\, p_J^+}{Q_J}\,, \tag{4.7}$$

and the jet mass can be written as

$$m_J^2 = p_J^+ p_J^- + p_{J\perp}^2 = p_J^+ p_J^- - \vec{p}_J{}^2\,, \tag{4.8}$$

where $\vec{p}_{J\perp}$ is the component perpendicular to the jet axis. The jet axis $n_J^\mu = \left(1, \hat{n}_J\right)$ is a light like vector where $\hat{n}_J$ can be expressed as

$$\hat{n}_J = \left(\frac{\cos\phi_J}{\cosh y_J}, \frac{\sin\phi_J}{\cosh y_J}, \tanh y_J\right). \tag{4.9}$$

The XCone algorithm includes an axes minimization procedure which minimizes the $\vec{p}_{J\perp}$ momentum. As explained in Ref. [108], for jets from massless particles, where $p_J^- = 2E_J\big(1+\mathcal{O}(m_J^2/E_J^2)\big)$, with this axes minimization feature one can relate $\mathcal{T}_2^J$ to the jet mass using Eq. (4.7):

$$m_J^2 = Q_J\,\mathcal{T}_J + \mathcal{O}\big(p_{J\perp}^2\big)\,, \tag{4.10}$$

where we also indicate the error in misalignment between the jet axis $\vec{n}_J$ and the jet momentum $\vec{p}_J$. Choosing the $\hat{n}_J$ vector to be aligned with the jet 3-momentum makes $p_{J\perp}$ vanish exactly.

4.2 Effective Theory Above The Top Mass Scale

Our strategy to derive the top-jet mass cross section in the peak region is to carry out two step matching from QCD to SCET and then to bHQET. We use the massive SCET Lagrangian in Eq. (3.24) to describe jet mass fluctuations $M_J^2 \sim m^2$. We then match the SCET cross section to two copies of boosted Heavy Quark Effective Theory for the top and the anti-top jet. Here the mass fluctuations are restricted in the Breit-Wigner region around the top mass: $M_J^2 - m^2 \sim m\Gamma_t$.

In this section we follow the steps along the lines of derivation presented in Ref. [49] to derive the SCET factorization theorem for top mass measurement in the peak region using the 2-jettiness variable described above. We start by presenting the relevant operators in QCD and SCET, and the details of matching calculation. We then describe the details of renormalization group evolution (RGE) and RG consistency conditions.

The expansion parameter in SCET is $\lambda \sim m/Q_{t,\bar{t}}$. We have a different scaling for the beam region. As we show below, for the NLL analysis that we consider, the beam region factorizes from the jet region and can be treated independently. We split the beam region into two parts defined by the incoming directions $n_{a,b}$.

We summarize the modes in Table 4.1 with the corresponding scaling and the

SCET Modes	Scaling	Fields
n_B-collinear	$\left(\mathcal{T}_B, Q_J, \sqrt{Q_J \mathcal{T}_B}\right)_{a,b}$	$(\xi_{n_a}, A^\mu_{n_a})$, $(\xi_{n_b}, A^\mu_{n_b})$
n_J-collinear	$\left(\frac{m^2}{Q_J}, Q_J, m\right)_{t,\bar{t}}$	$(\xi_{n_t}, A^\mu_{n_t})$, $(\xi_{n_{\bar{t}}}, A^\mu_{n_{\bar{t}}})$
ultrasoft	$\sqrt{Q_J \mathcal{T}_B}(1,1,1)$ $\frac{m^2}{Q_J}(1,1,1)$, $\Lambda_{\rm QCD}(1,1,1)$	$(\psi_{S_B}, A^\mu_{S_B})$ (ψ_{us}, A^μ_{us})
mass	$m(1,1,1)$	(ξ_m, A^μ_m)

Table 4.1: Summary of the EFT modes set up, scaling, and fields in SCET above the top mass scale. Here the subscript i on the momentum components refers to the appropriate axis n_i. We take Q_J to be the appropriate large momentum in the jet direction.

associated fields. We notice that in $pp \to t\bar{t}$ we no longer have back to back top and anti-top jets. Hence we generalize the notation presented in Chapter 3 such that $(+,-,\perp)$ directions then are defined with respect to the jet directions $n_t, n_{\bar{t}}$, or the beam directions n_a, n_b.

4.2.1 SCET Operators

For $pp \to t\bar{t}$ we have the following partonic production channels:

$$q\bar{q} \to t\bar{t}, \qquad gg \to t\bar{t}. \tag{4.11}$$

The operators in SCET are constructed using the collinear building blocks defined in Eq. (3.17). In the $q\bar{q} \to t\bar{t}$ channel, the SCET operators are

$$\begin{aligned}
\mathcal{O}_1^{ij}(\omega_b, \omega_a, \omega_t, \omega_{\bar{t}}) &= (\overline{\chi}_{n_b,\omega_b}\, Y^\dagger_{n_b}\, \Gamma^i \mathbf{T^A}\, Y_{n_a}\, \chi_{n_a,\omega_a})(\overline{\chi}_{n_t,\omega_t}\, Y^\dagger_{n_t}\, S^\dagger_{n_t}\, \Gamma^j \mathbf{T^A}\, S_{n_{\bar{t}}}\, Y_{n_{\bar{t}}}\, \chi_{n_{\bar{t}},\omega_{\bar{t}}})\,, \\
\mathcal{O}_2^{ij}(\omega_b, \omega_a, \omega_t, \omega_{\bar{t}}) &= (\overline{\chi}_{n_b,\omega_b}\, Y^\dagger_{n_b}\, \Gamma^i \mathbf{1}\, Y_{n_a}\, \chi_{n_a,\omega_a})(\overline{\chi}_{n_t,\omega_t}\, Y^\dagger_{n_t}\, S^\dagger_{n_t}\, \Gamma^j \mathbf{1}\, S_{n_{\bar{t}}}\, Y_{n_{\bar{t}}}\, \chi_{n_{\bar{t}},\omega_{\bar{t}}})\,,
\end{aligned} \tag{4.12}$$

where $T_I = \mathbf{1}, \mathbf{T^A}$. Γ^i, Γ^j denote the Dirac or spin structures. The ω_i's corresponds to the large label momentum

$$\omega_{t,\bar{t}} = 2E_{t,\bar{t}}\,, \qquad \omega_{a,b} = x_{a,b}E_{\rm cm}\,, \tag{4.13}$$

where $x_{a,b}$ are the momentum fractions of incoming partons. The SCET quark fields with label $\omega_{t,\bar{t}}$ are defined as

$$\chi_{n_t,\omega_t} = \delta(\bar{n}_t\cdot\mathcal{P}-\omega_t)W^\dagger_{n_t}\xi_{n_t}\,. \tag{4.14}$$

The quark fields are written after applying the field redefinition to decouple usoft gluons. We notice in Eq. (4.12) presence of additional Wilson lines $S_{n_{t,\bar{t}}}$ for the top and anti-top jets. These Wilson lines are defined in the same way as the ultra-soft Wilson lines in Eq. (3.19) but made out of soft mass mode gluons shown in Tab. 4.1.

Similarly, in the $gg \to t\bar{t}$ channel there are three color structures:

$$\begin{aligned}
\Theta_1^j(\omega_t,\omega_a,\omega_b,\omega_{\bar{t}}) &= \overline{\chi}_{n_t,\omega_t}\,Y^\dagger_{n_t}\,S^\dagger_{n_t}\,\Gamma^{\mu\nu}_j\mathbf{T^C}\mathbf{T^D}\,S^\dagger_{n_t}\,Y_{n_{\bar{t}}}\,\chi_{n_{\bar{t}},\omega_{\bar{t}}}\,\mathcal{Y}^{EC}_{n_a}\,(\mathcal{B}^E_{n_a\perp\mu})_{\omega_a}\,\mathcal{Y}^{FD}_{n_b}\,(\mathcal{B}^F_{n_b\perp\nu})_{\omega_b}\,,\\
\Theta_2^j(\omega_t,\omega_a,\omega_b,\omega_{\bar{t}}) &= \overline{\chi}_{n_t,\omega_t}\,Y^\dagger_{n_t}\,S^\dagger_{n_t}\,\Gamma^{\mu\nu}_j\mathbf{T^D}\mathbf{T^C}\,S^\dagger_{n_t}\,Y_{n_{\bar{t}}}\,\chi_{n_{\bar{t}},\omega_{\bar{t}}}\,\mathcal{Y}^{EC}_{n_a}\,(\mathcal{B}^E_{n_a\perp\mu})_{\omega_a}\,\mathcal{Y}^{FD}_{n_b}\,(\mathcal{B}^F_{n_b\perp\nu})_{\omega_b}\,,\\
\Theta_3^j(\omega_t,\omega_a,\omega_b,\omega_{\bar{t}}) &= \overline{\chi}_{n_t,\omega_t}\,Y^\dagger_{n_t}\,S^\dagger_{n_t}\,\Gamma^{\mu\nu}_j\delta^{\mathbf{CD}}\,S^\dagger_{n_t}\,Y_{n_{\bar{t}}}\,\chi_{n_{\bar{t}},\omega_{\bar{t}}}\,\mathcal{Y}^{EC}_{n_a}\,(\mathcal{B}^E_{n_a\perp\mu})_{\omega_a}\,\mathcal{Y}^{FD}_{n_b}\,(\mathcal{B}^F_{n_b\perp\nu})_{\omega_b}\,,
\end{aligned} \tag{4.15}$$

where the three color channels are given by $T_{CD} = \mathbf{T^C}\mathbf{T^D}, \mathbf{T^D}\mathbf{T^C}$, and $\delta^{\mathbf{CD}}$. Here the ultrasoft Wilson lines in adjoint representation can be defined by the relation

$$\mathbf{T^C}\,\mathcal{Y}^{CD}_n(x) = Y_n(x)\,\mathbf{T^D}\,Y^\dagger_n(x)\,. \tag{4.16}$$

4.2.2 SCET Factorized cross section

Here we present the derivation of the SCET cross section for the quark channel. Results for gluon channels can be analogously generalized and we treat the color mixing between these channels in Sec. 4.2.3. The total cross section of $pp \to X$ in QCD is given by

$$\sigma = \sum_X^{\text{res.}} (2\pi)^4 \delta^4(P_a + P_b - p_X) \sum_{\Gamma,I,J} \langle pp|X\rangle\langle X|pp\rangle \,, \tag{4.17}$$

where X refers to all the final state particles in the top, anti-top jets and the beam region, and $P_{a,b}$ are the momenta of incoming protons. The transition here is mediated by the QCD Lagrangian. The corresponding formula in SCET is given by

$$\begin{aligned}\sigma = &\sum_{n_t,n_{\bar t}} \sum_{\Gamma,I,J} \sum_{X_i}^{\text{res.}} (2\pi)^4 \delta^4(P_a + P_b - p_{X_{n_a}} - p_{X_{n_b}} - p_{X_{n_t}} - p_{X_{n_{\bar t}}} - p_{X_s})\, \mathcal{M} \\ &\int \mathrm{d}\omega_a\, \mathrm{d}\omega_b\, \mathrm{d}\omega_t\, \mathrm{d}\omega_{\bar t}\, \mathrm{d}\omega'_a\, \mathrm{d}\omega'_b\, \mathrm{d}\omega'_t\, \mathrm{d}\omega'_{\bar t}\, C^{\Gamma}_{Q,I}(\omega_{n_a},\omega_{n_b},\omega_t,\omega_{\bar t}) \big(C^{\Gamma}_{Q,J}(\omega'_{n_a},\omega'_{n_b},\omega'_t,\omega'_{\bar t})\big)^\star \\ &\langle pp|(\mathcal{O}^{\Gamma}_J)^\dagger|X_{n_a}\, X_{n_b}\, X_{n_t}\, X_{n_{\bar t}}\, X_s\rangle\langle X_{n_a}\, X_{n_b}\, X_{n_t}\, X_{n_{\bar t}}\, X_s|\mathcal{O}^{\Gamma}_I|pp\rangle \,,\end{aligned} \tag{4.18}$$

where C_Q is defined as the matching coefficient between the QCD and SCET operators. Here $C_Q = C^{\kappa\Gamma}_{Q,I}(\{s_{ij}\})$ with s_{ij} being the hard scales in the problem. We have also factored out the contribution of mass mode Wilson lines $\mathcal{M}$ that only show up at 2-loops. These effects are explored in Chapter 6. The 'res.' in Eq. (4.18) denotes restriction on final state momenta. For now we have kept a sum over the n_t and $n_{\bar t}$ directions which will be removed when we consider the differential cross section below. We have factorized the final state into collinear particles in the four directions and ultrasoft particles. This allows us to separate matrix elements involving operators containing only mode:

$$\begin{aligned}&\langle pp|(\mathcal{O}^{ij}_J)^\dagger|X_{n_a}\, X_{n_b}\, X_{n_t}\, X_{n_{\bar t}}\, X_s\rangle\langle X_{n_a}\, X_{n_b}\, X_{n_t}\, X_{n_{\bar t}}\, X_s|\mathcal{O}^{ij}_I|pp\rangle \\ &= \langle pp|\overline{T}\{(\overline{\chi}_{n_a,\omega'_a}\, Y^\dagger_{n_a}\, \overline{\Gamma}^i \overline{T}_J\, Y_{n_b}\, \chi_{n_b,\omega'_b})(\overline{\chi}_{n_{\bar t},\omega'_{\bar t}}\, Y^\dagger_{n_{\bar t}}\, \overline{\Gamma}^j \overline{T}_J\, Y_{n_t}\, \chi_{n_t,\omega'_t})\}|X_{n_a}\, X_{n_b}\, X_{n_t}\, X_{n_{\bar t}}\, X_s\rangle \\ &\times \langle X_{n_a}\, X_{n_b}\, X_{n_t}\, X_{n_{\bar t}}\, X_s|T\{(\overline{\chi}_{n_b,\omega_b}\, Y^\dagger_{n_b}\, \Gamma^i T_I\, Y_{n_a}\, \chi_{n_a,\omega_a})(\overline{\chi}_{n_t,\omega_t}\, Y^\dagger_{n_t}\, \Gamma^j T_I\, Y_{n_{\bar t}}\, \chi_{n_{\bar t},\omega_{\bar t}})\}|pp\rangle\end{aligned}$$

$$
\begin{aligned}
&= \mathrm{Tr}\left[\frac{\not{n}_a}{4N_C}\Gamma^i\frac{\not{n}_b}{4N_C}\overline{\Gamma}^i\right]\mathrm{Tr}\left[\frac{\not{n}_{\bar{t}}}{2}\Gamma^j\frac{\not{n}_t}{2}\overline{\Gamma}^j\right] \\
&\times\left[\langle p(P_a)|\overline{\chi}_{n_a,\omega_a'}|X_{n_a}\rangle\langle X_{n_a}|\frac{\bar{\not{n}}_a}{2}\chi_{n_a,\omega_a}|p(P_a)\rangle\right]\left[\langle p(P_b)|\frac{\bar{\not{n}}_b}{2}\chi_{n_b,\omega_b'}|X_{n_b}\rangle\langle X_{n_b}|\overline{\chi}_{n_b,\omega_b}|p(P_b)\rangle\right] \\
&\times\left[\langle 0|\overline{\chi}_{n_{\bar{t}},\omega_{\bar{t}}'}|X_{n_{\bar{t}}}\rangle\langle X_{n_{\bar{t}}}|\frac{\bar{\not{n}}_{\bar{t}}}{4N_C}\chi_{n_{\bar{t}},\omega_{\bar{t}}}|0\rangle\right]\left[\langle 0|\frac{\bar{\not{n}}_t}{4N_C}\chi_{n_t,\omega_t'}|X_{n_t}\rangle\langle X_{n_t}|\overline{\chi}_{n_t,\omega_t}|0\rangle\right] \\
&\times\left[\langle 0|(\overline{Y}_{n_a})^{ca}(\overline{T}_J Y_{n_b})^{cb}(\overline{Y}_{n_{\bar{t}}})^{rp}(\overline{T}_J Y_{n_t})^{rq}|X_s\rangle\langle X_s|(Y_{n_b}^\dagger T_I)^{bc}(Y_{n_a})^{ac}(Y_{n_t}^\dagger T_I)^{qr}(Y_{n_{\bar{t}}})^{pr}|0\rangle\right].
\end{aligned}
\tag{4.19}
$$

The T ($\overline{T}$) in the first equality keeps track of time (anti-time) ordering. In the second equality we have rewritten expressions such that every term is spin and color singlet. We also note that contraction with states in collinear matrix elements sets $\omega_i' = \omega_i$.

To impose the 2-jettiness measurement constraints we insert the identity operator:

$$
1 = \int \mathrm{d}^4 p_s \delta^4(p_s - P_{X_s}) \prod_{i=a,b,t,\bar{t}} \mathrm{d}^4 p_{n_i} \delta^4(p_{n_i} - P_{X_{n_i}}) \,. \tag{4.20}
$$

We now separate the label and residual parts of the momenta as follows:

$$
\begin{aligned}
p_{n_i} &= \tilde{p}_{n_i} + k_{n_i}\,, & p_s^\mu &= k_s^\mu\,, & P_{X_s}^\mu &= K_{X_s}^\mu\,, \\
P_{X_{n_i}}^- &= \tilde{P}_{X_{n_i}}^- + K_{X_{n_i}}^-\,, & P_{X_{n_i}}^\perp &= \tilde{P}_{X_{n_i}}^\perp + K_{X_{n_i}}^\perp\,, & P_{X_{n_i}}^+ &= K_{X_{n_i}}^+\,,
\end{aligned}
\tag{4.21}
$$

such that

$$
\int \mathrm{d}^4 p_{n_i} = \frac{1}{2}\sum_{\tilde{p}_{n_i}} \int \mathrm{d}\, k_{n_i}^+ \int \mathrm{d}\, k_{n_i}^- \int \mathrm{d}\, k_{n_i}^\perp \,. \tag{4.22}
$$

We write the δ functions for collinear sectors in Eq. (4.20) as

$$
\begin{aligned}
\delta^4(p_{n_i} - P_{X_{n_i}}) &= \delta_{\tilde{p}_{n_i},\tilde{P}_{X_{n_i}}}\,\delta^4(k_{n_i} - K_{X_{n_i}}) \\
&= \delta_{\tilde{p}_{n_i}^-,\omega_i}\,\delta_{\tilde{p}_{n_i}^\perp,\tilde{P}_{X_{n_i}}^\perp}\int \frac{\mathrm{d}^4 x_i}{(2\pi)^4} e^{i\left(k_{n_i} - K_{X_{n_i}}\right)\cdot x_i}\,,
\end{aligned}
\tag{4.23}
$$

$$
\delta^4(p_s - P_{X_s}) = \int \frac{\mathrm{d}^4 y}{(2\pi)^4} e^{i\left(k_s - K_{X_s}\right)\cdot y}\,. \tag{4.24}
$$

As a next step we impose the 2-jettiness measurement for the XCone measure in Eq. (4.3) to remove the restriction on states in Eq. (4.18):

$$
\begin{aligned}
1 &= \int \mathrm{d}\mathcal{T}^t \delta\Big(\mathcal{T}^t - \frac{\omega_t\,(K^+_{n_t} + K^{t+}_s)}{Q_t}\Big) \int \mathrm{d}\mathcal{T}^{\bar{t}} \delta\Big(\mathcal{T}^{\bar{t}} - \frac{\omega_{\bar{t}}\,(K^+_{n_{\bar{t}}} + K^{\bar{t}+}_s)}{Q_{\bar{t}}}\Big) \\
&\quad \times \int \mathrm{d}\mathcal{T}^a \delta(\mathcal{T}^a - K^\perp_{n_a} - K^{\perp a}_s) \int \mathrm{d}\mathcal{T}^b \delta(\mathcal{T}^b - K^\perp_{n_b} - K^{\perp b}_s) \\
&= \int \mathrm{d}\mathcal{T}^t \delta\Big(\mathcal{T}^t - \frac{\omega_t\,(k^+_{n_t} + k^{t+}_s)}{Q_t}\Big) \int \mathrm{d}\mathcal{T}^{\bar{t}} \delta\Big(\mathcal{T}^{\bar{t}} - \frac{\omega_{\bar{t}}\,(k^+_{n_{\bar{t}}} + k^{\bar{t}+}_s)}{Q_{\bar{t}}}\Big) \\
&\quad \times \int \mathrm{d}\mathcal{T}^a_B \delta(\mathcal{T}^a - k^\perp_{n_a} - k^{\perp a}_s) \int \mathrm{d}\mathcal{T}^b_B \delta(\mathcal{T}^b - k^\perp_{n_b} - k^{\perp b}_s)
\end{aligned}
\tag{4.25}
$$

where in the first step we have split the soft contribution to each sector and in the second step we have used the δ functions in Eq. (4.20). As shown in App. A measuring rapidity and p_T of both top and anti-top jets fixes all the hard scale ω_i's. Measuring the azimuthal angle of the jets further fixes the label $\perp$ components of the beam momenta. We use the exponential factors $e^{-iK_{X_{n_i}}\cdot x_i}$ and $e^{-iK_{X_{n_s}}\cdot y}$ to translate the collinear and soft fields in Eq. (4.19) to positions x_i and y respectively, bringing Eq. (4.18) to the following form of the SCET factorized cross section:

$$
\begin{aligned}
\frac{\mathrm{d}\sigma(\Phi_{t\bar{t}})}{\mathrm{d}\mathcal{T}_t \mathrm{d}\mathcal{T}_{\bar{t}} \mathrm{d}\mathcal{T}^a_B \mathrm{d}\mathcal{T}^a_B} &= \sigma_0\, \mathcal{M}(m,\mu) \int \mathrm{d}k^+_{n_t}\, \mathrm{d}k^+_{n_{\bar{t}}}\, \mathrm{d}k_{\perp a}\, \mathrm{d}k_{\perp b} \\
&\quad \mathrm{tr}\Big[\hat{H}^\kappa_Q(\Phi_{t\bar{t}},\mu)\, \hat{S}^\kappa_2\Big(\mathcal{T}^{t,\bar{t}} - \frac{\omega_{t,\bar{t}}\, k^+_{n_{t,\bar{t}}}}{Q_{t,\bar{t}}}, \mathcal{T}^{a,b}_B - k_{\perp a,b}, \mu, \frac{\nu}{\mu}\Big)\Big] \\
&\quad \times\ \omega_t J_{n_t}(\omega_t\, k^+_{n_t} - m^2, m, \mu)\, \omega_{\bar{t}} J_{n_{\bar{t}}}(\omega_{\bar{t}}\, k^+_{n_{\bar{t}}} - m^2, m, \mu) \\
&\quad \times B_{\kappa_a}\Big(k_{\perp a}, x_a, \mu, \frac{\nu}{\omega_b}\Big)\, B_{\kappa_b}\Big(k_{\perp b}, x_b, \mu, \frac{\nu}{\omega_b}\Big)\,.
\end{aligned}
\tag{4.26}
$$

Here σ_0 is the Born cross section, $\Phi_{t,\bar{t}}$ is the top and anti-top jet phase space. There is an implicit sum on the label κ in Eq. (4.26) that refers to the partonic channels $q\bar{q} \to t\bar{t}$ or $gg \to t\bar{t}$. The various functions appearing in Eq. (4.26) are given by:

$$
\hat{H}^\kappa_Q(\Phi_{t\bar{t}},\mu)_{IJ} = \sum_\Gamma C^{\kappa\Gamma}_{Q,I}(\{\omega_i\}) C^{\kappa\Gamma\star}_{Q,J}(\{\omega_i\})\,,
\tag{4.27}
$$

$$
J_{n_t}(\omega_t\, k^+_{n_t} - m^2, m, \mu)
$$

$$
\begin{aligned}
&= \frac{(2\pi)^2}{N_C} \int \frac{\mathrm{d}x^-}{2\omega_t}\, e^{ik^+_{n_t} x^-/2}\, \mathrm{tr}\langle 0| \left[\frac{\bar{n}\!\!\!/_t}{2} \chi_{n_t}\Big(x^- \frac{n_t}{2}\Big) \big[\delta(\omega_t + \overline{\mathcal{P}}_{n_t}) \delta^2(\mathcal{P}_{n_t \perp}) \overline{\chi}_{n_t}(0)\big] \right] |0\rangle \,, \\
& J_{n_{\bar{t}}}(\omega_{\bar{t}}\, k^+_{n_{\bar{t}}} - m^2, m, \mu) \\
&= \frac{(2\pi)^2}{N_C} \int \frac{\mathrm{d}x^-}{2\omega_{\bar{t}}}\, e^{ik^+_{n_{\bar{t}}} x^-/2} \langle 0| \left[\overline{\chi}_{n_{\bar{t}}}\Big(x^- \frac{n_{\bar{t}}}{2}\Big) \frac{\bar{n}\!\!\!/_{\bar{t}}}{2} \big[\delta(\omega_{\bar{t}} + \overline{\mathcal{P}}_{n_{\bar{t}}}) \delta^2(\mathcal{P}_{n_{\bar{t}} \perp}) \chi_{n_{\bar{t}}}(0)\big] \right] |0\rangle \,, \\
& B_{q_a}\left(k_{\perp a}, x_a, \mu, \frac{\nu}{\omega_a}\right) \\
&= \frac{1}{\omega_a} \theta(\omega_a) \langle p(P_a)| \overline{\chi}_{n_a}(0) \frac{\bar{n}\!\!\!/_a}{2} \big[\delta(\omega_a - \overline{\mathcal{P}}_{n_a}) \frac{1}{2\pi} \delta(k_{\perp a} - |\vec{\mathcal{P}}_{n_a \perp}|) \chi_{n_a}(0)\big] |p(P_a)\rangle \,, \\
& B_{q_b}\left(k_{\perp b}, x_b, \mu, \frac{\nu}{\omega_b}\right) \\
&= \frac{1}{\omega_b} \theta(\omega_b)\, \mathrm{tr} \langle p(P_b)| \frac{\bar{n}\!\!\!/_b}{2} \chi_{n_b}(0) \big[\delta(\omega_b - \overline{\mathcal{P}}_{n_b}) \frac{1}{2\pi} \delta(k_{\perp b} - |\vec{\mathcal{P}}_{n_a \perp}|) \overline{\chi}_{n_b}(0)\big] |p(P_b)\rangle \,, \\
& \hat{S}^{\kappa}_2\Big(\{k_m\}, \{n_l\}, \{d_m\}, \mu, \frac{\nu}{\mu}\Big) \\
&= \langle 0| (\overline{Y}^T_{n_a} \overline{T}_J Y_{n_b})^{ab} (\overline{Y}^T_{n_{\bar{t}}} \overline{T}_J Y_{n_t})^{cd} \prod_m \delta\big(k_m - \hat{\mathcal{T}}^{(m)}\big) (Y^\dagger_{n_b} T_I Y^T_{n_a})^{ba} (Y^\dagger_{n_t} T_I Y^T_{n_{\bar{t}}})^{dc} |0\rangle \,.
\end{aligned}
$$

where we have represented the soft function in a compact notation, and the analogous results for the gluon beam functions B_g can be found in Ref. [55]. Here $\{k_m\}$ are the arguments of the jet and beam functions. The $\hat{\mathcal{T}}^{(m)}$ operator replaces $\mathcal{T}^{(m)}$ in Eq. (4.25) and is applied on all particles in region m defined by direction n_m and distance measure d_m. Eq. (4.26) is valid for both channels and incorporates the fact that the steps above can be generalized for the gg channel. The operators have been renormalized which introduces dependence on μ.

The beam functions contain PDFs in them as can be shown by their operator product expansion:

$$
B_i(x, k_\perp, \mu) = \sum_j \int_x^1 \frac{\mathrm{d}z}{z} \mathcal{I}_{ij}\Big(\frac{x}{z}, k_\perp, \mu\Big) f_j(z, \mu) \left[1 + \mathcal{O}\Big(\frac{\Lambda^2_{\mathrm{QCD}}}{k^2_\perp}\Big)\right] , \tag{4.28}
$$

where $\mathcal{I}_{ij}$ are perturbatively calculable matching coefficients. The ν scale in the beam and the soft function indicates that they are $\mathrm{SCET_{II}}$ type and contain rapidity divergences [37].

We now make the following change of variables using Eq. (4.10):

$$\mathcal{T}^{t,\bar{t}} = \frac{M_t^2}{Q_{t,\bar{t}}}\,, \qquad \omega_{t,\bar{t}}\, k^+_{n_{t,\bar{t}}} = s_{t,\bar{t}} + m^2\,, \tag{4.29}$$

which gives

$$\begin{aligned}\frac{\mathrm{d}\sigma(\Phi_{t\bar{t}})}{\mathrm{d}M_t^2 \mathrm{d}M_{\bar{t}}^2 \mathrm{d}\mathcal{T}_B^a \mathrm{d}\mathcal{T}_B^a} = \frac{\sigma_0\, \mathcal{M}(m,\mu)}{Q_t Q_{\bar{t}}} \int \mathrm{d}s_t\, \mathrm{d}s_{\bar{t}}\, \mathrm{d}k_{\perp a}\, \mathrm{d}k_{\perp b} \\ \mathrm{tr}\Big[\hat{H}_Q^\kappa(\Phi_{t\bar{t}},\mu)\, \hat{S}_2^\kappa\Big(\frac{M_{t,\bar{t}}^2 - m^2 - s_{t,\bar{t}}}{Q_{t,\bar{t}}}, \mathcal{T}_B^{a,b} - k_{\perp a,b}, \mu, \frac{\nu}{\mu}\Big)\Big] \\ \times B_a\Big(k_{\perp a}, x_a, \mu, \frac{\nu}{\omega_b}\Big) B_b\Big(k_{\perp b}, x_b, \mu, \frac{\nu}{\omega_b}\Big)\, J_{n_t}(s_t, m, \mu)\, J_{n_{\bar{t}}}(s_{\bar{t}}, m, \mu)\,.\end{aligned} \tag{4.30}$$

We now explore the properties of this result and discuss the ingredients needed for the NLL implementation. Most of the parts of Eq. (4.30) have already been calculated. The fully differential beam functions have been calculated at 2 loops in Ref. [57]. The results for the soft function for generic N-jettiness measures at 1-loop, such as the XCone measure we employ, appeared recently in Ref. [20]. For the case of top quarks we will further match the massive SCET jet functions $J_{t,\bar{t}}$ to bHQET jet functions that have been known up to 2-loops [78]. Hard function at NNLL order for $pp \to q\bar{q}$ as been presented in Refs. [102, 82]. The remaining ingredient is the hard function for matching between SCET and bHQET theory for $pp \to t\bar{t}$ that we derive below.

4.2.3 SCET Hard Function Running

Various ingredients in Eq. (4.30) are specified at a common μ scale. We adopt a convention to set the $\mu = \mu_S$, the soft scale, and run down the hard, jet and the beam functions down to μ_S through RG evolution. Below we provide the expressions for the RGE for these functions to arrive at a final NLL factorization formula. We first consider the running of the SCET hard function in Eq. (4.27) and derive results needed for the discussion of bHQET matching coefficient below in Sec. 4.3. At tree

level we have

$$\hat{H}_Q^{qq} = 8g^4 \frac{\hat{t}^2+\hat{u}^2}{\hat{s}^2} \begin{pmatrix} 1 & 0 \\ 0 & 0 \end{pmatrix}, \qquad \hat{H}_Q^{gg} = 8g^4 \frac{\hat{t}^2+\hat{u}^2}{\hat{s}^2} \begin{pmatrix} \hat{u}/\hat{t} & 1 & 0 \\ 1 & \hat{t}/\hat{u} & 0 \\ 0 & 0 & 0 \end{pmatrix}. \quad (4.31)$$

Ignoring the top mass for highly boosted jets in SCET the partonic Mandelstam variables are given by

$$\hat{s} = x_a x_b Q_{\rm cm}^2, \qquad \hat{t} = -x_a Q_{\rm cm} p_t^T e^{-\eta_t}, \qquad \hat{u} = -x_b Q_{\rm cm} p_t^T e^{\eta_t}. \quad (4.32)$$

We make use of the formulas presented in Ref. [82] for deriving resummed expression of H_Q^κ. The running of the Wilson coefficient is given by[1]

$$\mu \frac{d}{d\mu} C_{Q,J}^{\kappa\Gamma}(\{s_{ij}\},\mu) = (\Gamma_Q^\kappa)_{IJ}\, C_{Q,I}^{\kappa\Gamma}(\{s_{ij}\},\mu), \quad (4.33)$$

where

$$(\Gamma_Q^\kappa)_{IJ} = \sum_{(i,j)} \frac{(\mathbf{T}_i\cdot\mathbf{T}_j)_{IJ}}{2} \gamma_{\rm cusp}(\alpha_s) \ln\frac{\mu^2}{-s_{ij}} + \delta_{IJ}\sum_i \gamma_i(\alpha_s). \quad (4.34)$$

Here $s_{ij} = 2\sigma_{ij} p_i\cdot p_j + i0$, and $\sigma_{ij} = +1$ if p_i and p_j are both incoming or outgoing and $\sigma_{ij} = -1$ otherwise. $\gamma_{\rm cusp}$ is related to the cusp anomalous dimension as $\gamma_{\rm cusp} = \Gamma_i^{\rm cusp}/c_i$, for $i = q, g$, which up to NLL order for a quark is given by

$$\Gamma^{\rm cusp} = 4C_F\Big(\frac{\alpha_s}{4\pi}\Big) + 4C_F\Big[\Big(\frac{67}{9}-\frac{\pi^2}{3}\Big)C_A - \frac{20}{9}T_F n_f\Big]\Big(\frac{\alpha_s}{4\pi}\Big)^2, \quad (4.35)$$

and $\gamma_q = \big(\frac{\alpha_s}{4\pi}\big)(-3C_F)$ and $\gamma_g = \big(\frac{\alpha_s}{4\pi}\big)(-\beta_0)$. We rearrange the expression as follows:

$$(\Gamma_Q^\kappa)_{IJ} = \sum_i \sum_{(j\neq i)} \frac{(\mathbf{T}_i\cdot\mathbf{T}_j)_{IJ}}{2} \gamma_{\rm cusp}(\alpha_s) \ln\frac{\mu^2}{-s_{ij}} + \delta_{IJ}\sum_i \gamma_i(\alpha_s),$$

[1]Our notation here differs from Ref. [82] in that we have a transpose of Γ_Q^κ related to difference between evolution of the operator vs. Wilson coefficient.

$$
\begin{aligned}
&= \sum_i \sum_{(j\neq i)} \frac{(\mathbf{T}_i\cdot\mathbf{T}_j)_{IJ}}{2}\,\gamma_{\rm cusp}(\alpha_s)\Big[\ln\frac{\mu_\kappa^2}{-s_{ij}}+\ln\frac{\mu^2}{\mu_\kappa^2}\Big]+\delta_{IJ}\sum_i\gamma_i(\alpha_s),\\
&= \sum_i \sum_{(j\neq i)} \frac{(\mathbf{T}_i\cdot\mathbf{T}_j)}{2}\,\gamma_{\rm cusp}(\alpha_s)\ln\frac{\mu_\kappa^2}{-s_{ij}}+\delta_{IJ}\sum_i\frac{c_i}{2}\,\gamma_{\rm cusp}(\alpha_s)\ln\frac{\mu_\kappa^2}{\mu^2}+\delta_{IJ}\sum_i\gamma_i(\alpha_s),\\
&= \gamma_{\rm cusp}(\alpha_s)\mathbf{M}^\kappa_{IJ}+\Big[\gamma_{\rm cusp}(\alpha_s)\frac{c_Q^\kappa}{2}\ln\frac{\mu_\kappa^2}{\mu^2}+\gamma_Q^\kappa\Big]\delta_{IJ}\,, \qquad (4.36)
\end{aligned}
$$

where the non-diagonal matrix $\mathbf{M}^\kappa$ is given by

$$
\mathbf{M}^\kappa_{IJ} = \sum_i\sum_{(j\neq i)}\frac{(\mathbf{T}_i\cdot\mathbf{T}_j)_{IJ}}{2}\ln\frac{\mu_\kappa^2}{-s_{ij}}\,, \qquad (4.37)
$$

and

$$
\begin{aligned}
c_Q^\kappa &= \sum_i c_i = (n_q+n_{\bar q})\,C_F+n_gC_A\,,\\
\gamma_Q^\kappa(\alpha_s) &= \sum_i\gamma_i(\alpha_s) = (n_q+n_{\bar q})\,\gamma_q(\alpha_s)+n_g\gamma_g(\alpha_s)\,. \qquad (4.38)
\end{aligned}
$$

Here we have introduced an auxiliary scale μ_κ that is chosen to simplify the form of $\mathbf{M}^\kappa$ for the partonic channel κ. $n_{q,\bar q,g}$ are the number of quarks and gluons involved in the $2\to 2$ process. We have

$$
\begin{aligned}
\mathbf{M}^{qq}(\mu_{qq}^2=-s) &= \begin{pmatrix} \frac{1}{2}\big(-(C_A+C_d)\ln(\frac{s}{t})+(-C_A+C_d)\ln(\frac{s}{u}) & -2\ln(\frac{s}{t})+2\ln(\frac{s}{u}) \\ 2C_1\big(\ln(\frac{s}{t}+\frac{s}{u}) & 0 \end{pmatrix},\\
\mathbf{M}^{gg}(\mu_{gg}^2=-t) &= \begin{pmatrix} -C_F\ln\left(\frac{t}{s}\right) & 0 & 2\ln\left(\frac{t}{u}\right) \\ 0 & -C_F\ln\left(\frac{t}{s}\right)-C_A\ln\left(\frac{t}{u}\right) & -2\ln\left(\frac{t}{u}\right) \\ \frac{1}{2}C_A\ln\left(\frac{s}{u}\right) & \frac{1}{2}C_A\ln\left(\frac{s}{t}\right) & -(C_F+C_A)\ln\left(\frac{t}{s}\right) \end{pmatrix}. \qquad (4.39)
\end{aligned}
$$

We solve Eq. (4.33) for H_Q^κ by diagonalizing the color space matrix $\mathbf{M}^\kappa$. We perform a rotation in color space

$$
\hat{\mathcal{H}}^\kappa_{Q,KK'} = F^\kappa_{KI}F^*_{K'J}\hat{H}^\kappa_{Q,IJ} = (F^\kappa\cdot\hat{H}^\kappa_Q\cdot F^{\kappa\dagger})_{KK'}\,,
$$

$$\mathrm{tr}[\hat{H}_Q^\kappa \hat{S}_2^\kappa] = \mathrm{tr}\Big[\hat{\mathcal{H}}_Q^\kappa \left((F^{\kappa\dagger})^{-1} \cdot \hat{S}_2^\kappa \cdot (F^\kappa)^{-1}\right)\Big], \tag{4.40}$$

such that the matrix F^κ diagonalizes $\mathbf{M}^\kappa$. This allows to evolve $\hat{\mathcal{H}}_Q^\kappa$ multiplicatively:

$$\begin{aligned}\hat{\mathcal{H}}^\kappa_{Q,KK'}(\{s_{ij}\},\mu;\mu_Q) = \hat{\mathcal{H}}^\kappa_{Q,KK'}(\{s_{ij}\},\mu_Q)\exp\Bigg[&2c_Q^\kappa S(\mu,\mu_h) \\ &- 2A_Q^\kappa(\mu,\mu_Q) - A_\Gamma(\mu,\mu_Q)\bigg(\lambda_K^\kappa + \lambda_{K'}^{\kappa\star} + c_Q^\kappa \ln\Big|\frac{\mu_\kappa^2}{\mu_Q^2}\Big|\bigg)\Bigg],\end{aligned} \tag{4.41}$$

where the functions S, A_H, and A_Γ are given by

$$\begin{aligned} S(\mu,\mu_Q) &= -\int_{\alpha_s(\mu_Q)}^{\alpha_s(\mu)} d\alpha\, \frac{\gamma_{\mathrm{cusp}}(\alpha)}{\beta(\alpha)} \int_{\alpha_s(\mu_Q)}^{\alpha} \frac{d\alpha'}{\beta(\alpha')}, \\ A_\Gamma(\mu,\mu_Q) &= -\int_{\alpha_s(\mu_Q)}^{\alpha_s(\mu)} d\alpha\, \frac{\gamma_{\mathrm{cusp}}(\alpha)}{\beta(\alpha)}, \\ A_Q^\kappa(\mu,\mu_Q) &= -\int_{\alpha_s(\mu_Q)}^{\alpha_s(\mu)} d\alpha\, \frac{\gamma_Q^\kappa(\alpha)}{\beta(\alpha)}. \end{aligned} \tag{4.42}$$

We observe from Eq. (4.30) that the soft function consists of multiple scales and couples the jet and the beam directions. It was pointed out in Ref. [80] that up to two loops non-global terms in the soft function can be refactorized for different collinear regions. As an important consequence this allows us to separate the treatment of the beam and the jet regions by choosing a different soft scale μ_{S_i} for each sector. We ignore rapidity scale dependence for this discussion. With tree level matching and NLL evolution we have

$$\begin{aligned}\hat{S}_2^\kappa\big(k^+_{n_{t,\bar{t}}}, \mathcal{T}_B^{a,b}, \mu\big) = \hat{\mathcal{S}}^\kappa \prod_{i=t,\bar{t}} \int \mathrm{d}k_i'\, U_{S_i}\big(k^+_{n_i} - k_i', \mu, \mu_{S_i}\big)\delta(k_i') \\ \prod_{j=a,b} \int \mathrm{d}k'_{j\perp}\, U_{S_j}\big(\mathcal{T}_B^j - k'_{j\perp}, \mu, \mu_{S_j}\big),\end{aligned} \tag{4.43}$$

where

$$\hat{\mathcal{S}}^{qq} = \begin{pmatrix} \frac{1}{2}C_A C_F & 0 \\ 0 & C_A^2 \end{pmatrix}, \qquad \hat{\mathcal{S}}^{gg} = \begin{pmatrix} C_A C_F^2 & -\frac{1}{2}C_F & C_A C_F \\ -\frac{1}{2}C_F & C_A C_F^2 & C_A C_F \\ C_A C_F & C_A C_F & 2C_F C_A^2 \end{pmatrix}. \tag{4.44}$$

Similarly in a top down RG evolution picture we can generalize Eq. (4.41) to evolve the hard function to multiple soft scales as follows:

$$\begin{aligned} \hat{\mathcal{H}}^{\kappa}_{Q,KK'}(\{s_{ij}\},\{\mu_{S_i}\};\mu_Q) &= \hat{\mathcal{H}}^{\kappa}_{Q,KK'}(\{s_{ij}\},\mu_Q) \\ &\times \exp\Big[2\sum_i c_i S(\mu_{S_i},\mu_Q) - 2\sum_i A^i_Q(\mu_{S_m},\mu_Q) - \ln\Big|\frac{\mu^2_\kappa}{\mu^2_Q}\Big|\sum_i c_i A_\Gamma(\mu_{S_i},\mu_Q)\Big] \\ &\times \exp\Big[-\frac{(\lambda^\kappa_K + \lambda^{\kappa\star}_{K'})}{4}\sum_i A_\Gamma(\mu_{S_i},\mu_Q)\Big]. \end{aligned} \tag{4.45}$$

An important consequence of Eq. (4.43) is that we can independently treat the beam region at NLL order. By integrating over $\mathcal{T}_B$ up to a value $\mathcal{T}_B^{\rm cut}$ which implements a veto in the beam region. This plays an important role in limiting the contribution from the underlying event. Beam vetoes have been studied for different beam measures in Refs. [53, 113]. Our analysis of M_J is then essentially insensitive to the precise implementation of the beam veto once we normalize the spectrum. In Chapter 5 we implement a veto in our PYTHIA studies by imposing a p_T-veto cut on additional jets in the event.

4.3 Effective Theory Below The Top Mass Scale

Here we discuss the EFT for top jets in the peak region defined by Eq. (3.23). In Table 4.2 we present the modes in the bHQET theory. We note that the soft fields and the collinear modes in the beam direction remain the same. The soft modes for the top and anti-top jet continue to be described by the same fields as above but are now at a lower virtuality of $m\Gamma_t/Q_{t,\bar{t}}$. The heavy quark fields $h_{v_{t,\bar{t}}}$ are defined with

bHQET Modes	Scaling	Fields
n_B-collinear	$\left(\mathcal{T}_B, Q_J, \sqrt{Q_J \mathcal{T}_B}\right)_B$	$(\xi_{n_a}, A^\mu_{n_a})$, $(\xi_{n_b}, A^\mu_{n_b})$
$n_{t,\bar{t}}$-ultra collinear	$\left(\frac{m}{Q_J}\Gamma_t, \frac{Q_J}{m}\Gamma_t, \Gamma_t\right)_{t,\bar{t}}$	(h_{v_t}, A_{v_t}), $(h_{v_{\bar{t}}}, A_{v_{\bar{t}}})$
ultra soft	$\mathcal{T}_B(1,1,1)$	$(\psi_{S_B}, A^\mu_{S_B})$
	$\frac{m\Gamma_t}{Q_J}(1,1,1)$, $\Lambda_{\rm QCD}(1,1,1)$	(ψ_{us}, A^μ_{us})

Table 4.2: Summary of the EFT modes set up, scaling, and fields in bHQET below the top mass scale.

four-velocities

$$v_t^\mu = \frac{n_t^\mu}{2}\frac{Q_t}{m} + \frac{\bar{n}_t^\mu}{2}\frac{m}{Q_t}\,, \qquad v_{\bar{t}}^\mu = \frac{n_{\bar{t}}^\mu}{2}\frac{Q_{\bar{t}}}{m} + \frac{\bar{n}_{\bar{t}}^\mu}{2}\frac{m}{Q_{\bar{t}}}\,, \tag{4.46}$$

which are time-like, $v_t^2 = v_{\bar{t}}^2 = 1$. This results in the same soft function and beam functions in the low energy theory evaluated with 5 light flavors below the top mass scale.

From the perspective of matching the effective theories we can write

$$C^{\kappa\Gamma}_{Q_{t,\bar{t}},I}(\{\omega_i\},\mu)\,\mathcal{O}^{\kappa\Gamma}_{\rm SCET,\,I}(\mu) = C^{\kappa\Gamma}_{b,I}\left(\{\omega_i\}, m, \frac{Q_{t,\bar{t}}}{m}, \mu\right)\mathcal{O}^{\kappa\Gamma}_{\rm bHQET,\,I}(\mu)\,, \tag{4.47}$$

Where we have included dependence on the boost factor Q/m. Matching between SCET and bHQET only involves top and anti-top sector, and is independent of the color, spin structure, and the partonic channel:

$$\mathcal{O}^{\kappa\Gamma}_{\rm SCET,\,I}(\mu_t) = C_m\left(m, \frac{Q_{t,\bar{t}}}{m}, \mu_t\right)\mathcal{O}^{\kappa\Gamma}_{\rm bHQET,\,I}(\mu_t)\,, \tag{4.48}$$

where the matching is performed at scale $\mu_t \sim m$. The coefficient C_m is the same as the result derived in Refs. [50] for the $e^+e^- \to t\bar{t}$ process. In Chapter 6 we will present the two-loop result for C_m. From Eqs. (4.47) and (4.48) we can identify the bHQET Wilson coefficient C_b as

$$C^{\kappa\Gamma}_{b,I}\left(\{\omega_i\}, m, \frac{Q_{t,\bar{t}}}{m}, \mu_t\right) = C_m\left(m, \frac{Q_{t,\bar{t}}}{m}, \mu_t\right) C^{\kappa\Gamma}_{Q_{t,\bar{t}},I}(\{\omega_i\},\mu_t)\,. \tag{4.49}$$

The bHQET hard function can now be written as

$$\hat{H}^{\kappa}_{b,\,IJ}\left(\{\omega_i\}, m, \frac{Q_{t,\bar{t}}}{m}, \mu_t\right) = \sum_{\Gamma} C^{\kappa\Gamma}_{b,\,I}\left(C^{\kappa\Gamma}_{b,\,J}\right)^{\star}$$
$$= \underbrace{\left|C_m\left(m, \frac{Q_{t,\bar{t}}}{m}, \mu_t\right)\right|^2}_{H_m} \hat{H}^{\kappa}_{Q_{t,\bar{t}},\,IJ}(\{\omega_i\}, \mu_t)\,. \tag{4.50}$$

We are now in a position to state the bHQET factorization theorem:

$$\frac{\mathrm{d}\sigma^{\kappa}(\Phi_{t\bar{t}})}{\mathrm{d}M_t^2 \mathrm{d}M_{\bar{t}}^2 \mathrm{d}\mathcal{T}_B^a \mathrm{d}\mathcal{T}_B^a} = \sigma_0 \frac{m^2}{Q_t Q_{\bar{t}}} \int \mathrm{d}\hat{s}_t' \,\mathrm{d}\hat{s}_{\bar{t}}' \,\mathrm{d}k_{\perp a} \,\mathrm{d}k_{\perp b} \tag{4.51}$$
$$\mathrm{tr}\left[\hat{H}_b^{\kappa}(\Phi_{t\bar{t}}, \mu)\, \hat{S}_2^{\kappa}\left(\frac{m}{Q_{t,\bar{t}}}(\hat{s}_{t,\bar{t}} - \hat{s}'_{t,\bar{t}}), \mathcal{T}_B^{a,b} - k_{\perp a,b}, \mu, \frac{\nu}{\mu}\right)\right]$$
$$\times\, B_a\left(k_{\perp a}, x_a, \mu, \frac{\nu}{\omega_b}\right) B_b\left(k_{\perp b}, x_b, \mu, \frac{\nu}{\omega_b}\right)$$
$$\times\; J_B^t(\hat{s}_t, \Gamma_t, \delta m, \mu)\, J_B^{\bar{t}}(\hat{s}_{\bar{t}}, \Gamma_t, \delta m, \mu)\,,$$

where $\hat{s}_t$ is defined in Eq. (3.23) and $\Phi_{t,\bar{t}}$ is a shorthand for the variables $\{\omega_i, m, Q_{t,\bar{t}}/m\}$.

We also notice that the contribution from mass modes $\mathcal{M}(m,\mu)$ has been absorbed in H_m defined in Eq. (4.50). The matching results in bHQET jet functions that depend on the scale Γ_t and are defined by [78]:

$$J_B^t(\hat{s}_t = 2v_t.r, \Gamma_t, \delta m, \mu) \tag{4.52}$$
$$= \left(\frac{-1}{4\pi N_C m}\right) \mathrm{Im}\left[i \int \mathrm{d}^4x\, e^{ir.x} \langle 0|\mathrm{T}\{\bar{h}_{v_t}(0) W_{n_t}(0) W_{n_t}^{\dagger}(x) h_{v_t}(x)\}|0\rangle\right],$$

It is through the residual mass term δm appearing in the bHQET jet functions J_B that the top quark mass scheme is specified unambiguously beyond tree-level. As discussed above, valid options include the jet mass scheme [49, 50, 78] or the MSR mass scheme [75, 78] which matches continuously onto $\overline{\mathrm{MS}}$. These two mass schemes have an adjustable cutoff parameter R which controls the scaling of higher order corrections. We will use the MSR scheme here. The anomalous dimension equation

for the MSR mass is given by so-called R-evolution where

$$R\frac{d}{dR}m(R) = -R\,\gamma_R[\alpha_s(R)]\,,$$
$$\gamma_R[\alpha_s(R)] = \sum_{n=0}^{\infty}\gamma_n^R\left[\frac{\alpha_s(R)}{4\pi}\right]^{n+1}. \tag{4.53}$$

Defining $t_i \equiv -2\pi/(\beta_0\alpha_s(R_i))$ the LL solution of the R-evolution equation for the MSR mass is

$$m(R_1) - m(R_0) = \frac{\Lambda_{\rm QCD}\,\gamma_0^R}{2\beta_0}\int_{t_1}^{t_0} dt\,\frac{e^{-t}}{t}\,, \tag{4.54}$$

where the LL anomalous dimension coefficient $\gamma_0^R = 4C_F$. Since $t_1 < t_0 < 0$ this integral is convergent.

4.3.1 bHQET Hard Function Running

Here we discuss the evolution of $\hat{H}_b$ to the new ultra-soft scales in bHQET shown in Tab. 4.2, which we continue to refer to as μ_{S_i}. From Eq. (4.50) it follows that the part of the RG evolution of the bHQET hard function that involves running the from the SCET matching scale $\mu_Q \sim Q$ to the bHQET matching scale $\mu_t \sim m$ is given by Eq. (4.45). In this section we derive the expression for running below μ_m. We have

$$\begin{aligned}
\vec{C}_b(\mu) &= \hat{U}_{C_b}(\mu,\mu_t)\,\vec{C}_b(\mu_t),\\
&= \hat{U}_{C_b}(\mu,\mu_t)\,C_m(\mu_t)\,\vec{C}_Q(\mu_t)\\
&= \hat{U}_{C_b}(\mu,\mu_t)\,C_m(\mu_t)\,\hat{U}_C(\mu_t,\mu_Q)\,\vec{C}_Q(\mu_Q)\,,
\end{aligned} \tag{4.55}$$

where we have suppressed the Γ and κ indices for simplicity and represented the Wilson coefficients as vectors in color space. Following Ref. [50] the RG evolution and UV divergences of soft function are independent of the choice of the 2-jettiness measure. This allows us to calculate the anomalous dimension of $\vec{C}_b(\mu_t)$ using the known 5-flavor anomalous dimension of the SCET matching coefficient for jets from massless quarks stated in Ref. [79]. The μ independence of the 2-jettiness cross-section

for jets from massless quarks, analogous to Eq. (4.26), is given by

$$0 = \mu\frac{d}{d\mu}\int\Big[\prod_{i=a,b,1,2} ds_i\, \mathcal{J}_i(s_i,\mu)\Big]\,\vec{C}_Q^{\dagger}(\mu)\,\hat{S}_2(\{\tau^i - \frac{s_i}{Q_i}\},\mu)\,\vec{C}_Q(\mu)\,, \tag{4.56}$$

where $\mathcal{J}_i$ are the SCET jet functions for massless quarks. We note that Eq. (4.57) is expressed in 5 flavor scheme. This yields

$$\hat{\Gamma}^{5f}_{C_Q}(\mu)\prod_i \delta(k_i) = -\frac{1}{2}\mathbf{1}\sum_i\Big[Q_i\Gamma_{\mathcal{J}_i}(Q_i k_i,\mu)\prod_{j\neq i}Q_j\delta(Q_j k_j)\Big] - \hat{\Gamma}^{\dagger}_S(\{k_i\},\mu) \tag{4.57}$$

Similarly, the consistency condition in bHQET gives

$$\hat{\Gamma}^{5f}_{C_b}(\mu)\prod_i \delta(k_i) = -\frac{1}{2}\mathbf{1}\sum_i\Big[Q_i^b\Gamma_{\mathcal{J}_i}(Q_i^b k_i,\mu)\prod_{j\neq i}Q_j^b\,\delta(Q_j^b k_j)\Big] - \hat{\Gamma}^{\dagger}_S(\{k_i\},\mu)\,, \tag{4.58}$$

where $Q_j^b = Q_j$ for $j = a, b$ and $Q_j^b = Q_j/m$ for $j = t, \bar{t}$. The anomalous dimension of the SCET jet function is given by

$$\Gamma_{\mathcal{J}_i}(s,\mu) \;=\; -2\,c_i\,\gamma_{\rm cusp}[\alpha_s(\mu)]\frac{1}{\mu^2}\left[\frac{\mu^2\,\theta(s)}{s}\right]_+ + \gamma_{\mathcal{J}_i}[\alpha_s(\mu)]\,\delta(s)\,. \tag{4.59}$$

Subtracting Eq. (4.58) from Eq. (4.57) and using Eq. (4.59) we have

$$\frac{Q_i}{m}\Gamma_{\mathcal{J}_i^b}\Big(\frac{Q_i}{m}k_i\Big) - Q_i\Gamma_{\mathcal{J}_i}(Q_i k_i) = \delta(k_i)\Big[2c_i\gamma_{\rm cusp}[\alpha_s(\mu)]\ln\frac{m}{\mu} + \gamma^i_{\mathcal{J}^b}[\alpha_s(\mu)] - \gamma^i_{\mathcal{J}}[\alpha_s(\mu)]\Big]\,, \tag{4.60}$$

which gives

$$\begin{aligned}\hat{\Gamma}^{\kappa\,5f}_{C_b}(\mu) = \gamma_{\rm cusp}[\alpha_s(\mu)]\,\mathbf{M}^{\kappa}_{IJ} + \delta_{IJ}\Bigg\{&\sum_{i=a,b}\ln\frac{\mu_\kappa^2}{\mu^2}\frac{c_i}{2}\,\gamma_{\rm cusp}[\alpha_s(\mu)] + \sum_{i=a,b,t,\bar{t}}\gamma_i(\alpha_s)\\ &- \frac{1}{2}\sum_{i=t,\bar{t}}\Big[\ln\frac{m_t^2}{\mu_\kappa^2}c_i\gamma_{\rm cusp}[\alpha_s(\mu)] + \gamma^i_{J_b}[\alpha_s(\mu)] - \gamma^i_J[\alpha_s(\mu)]\Big]\Bigg\},\end{aligned} \tag{4.61}$$

Thus, we can now write the evolution of the hard function from μ_t to $\{\mu_{S_i}\}$ as

$$\hat{\mathcal{H}}^{\kappa}_{b,KK'}(\{\mu_{S_i}\},\mu_t,\mu_Q) = \hat{\mathcal{H}}^{\kappa}_{b,KK'}(\{s_{ij}\},\mu_t,\mu_Q)$$
$$\exp\Big[2\sum_{i=a,b} c_i\, S(\mu_{S_i},\mu_t) - 2\sum_{i=a,b,t,\bar{t}} A^i_Q(\mu_{S_i},\mu_t) - \sum_{i=t,\bar{t}}[A^i_J(\mu_{S_i},\mu_t) - A^i_{J_b}(\mu_{S_i},\mu_t)]\Big]$$
$$\exp\Bigg[-\frac{(\lambda^{\kappa}_K+\lambda^{\kappa *}_{K'})}{4}\sum_{i=a,b,t,\bar{t}} A_\Gamma(\mu_{S_i},\mu_t) - \sum_{i=a,b} c_i\, A_\Gamma(\mu_{S_i},\mu_H)\ln\Big|\frac{\mu^2_\kappa}{\mu^2_t}\Big|$$
$$-\sum_{i=t,\bar{t}} c_i\, A_\Gamma(\mu_{S_i},\mu_t)\ln\Big|\frac{\mu^2_\kappa}{m^2_t}\Big|\Bigg], \tag{4.62}$$

where the functions $A^i_{H,J}$ and A^i_{H,J_b} are given by

$$A^i_J(\mu,\mu_H) = -\int_{\alpha_s(\mu_H)}^{\alpha_s(\mu)} d\alpha\,\frac{\gamma^i_J(\alpha)}{\beta(\alpha)}, \qquad A^i_{J_b}(\mu,\mu_H) = -\int_{\alpha_s(\mu_H)}^{\alpha_s(\mu)} d\alpha\,\frac{\gamma^i_{J_b}(\alpha)}{\beta(\alpha)} \tag{4.63}$$

The evolution of the hard function $H_{b,KK'}(\{s_{ij}\},\mu_t,\mu_H)$ in Eq. (4.62) between μ_H and μ_t is given by

$$\hat{\mathcal{H}}^{\kappa}_{b,KK'}(\{s_{ij}\},\mu_t,\mu_Q) = H_m(m_t,\mu_t)\hat{\mathcal{H}}^{\kappa}_{Q,KK'}(\{s_{ij}\},\mu_Q)$$
$$\exp\Big[2\sum_i c_i\, S(\mu_t,\mu_Q) - 2\sum_i A^i_Q(\mu_t,\mu_Q) - \ln\Big|\frac{\mu^2_\kappa}{\mu^2_Q}\Big|\sum_i c^i_Q A_\Gamma(\mu_t,\mu_Q)\Big]$$
$$\exp\Big[-\frac{(\lambda^{\kappa}_K+\lambda^{\kappa\star}_{K'})}{4}\sum_i A_\Gamma(\mu_t,\mu_Q)\Big], \tag{4.64}$$

where $\hat{\mathcal{H}}^{\kappa}_{Q,KK'}(\{s_{ij}\},\mu_Q)$ is the SCET hard function at the hard scale μ_Q.

4.3.2 bHQET Jet Function Running

The RG evolution for the bHQET jet takes the form

$$J^t_B(\hat{s}_t,\mu_{S_t}) = \int d\hat{s}'_t\; U^t_{J_B}(\hat{s}_t-\hat{s}'_t,\mu_{S_t};\mu_\Gamma) J^t_B(\hat{s}'_t,\mu_\Gamma)\,. \tag{4.65}$$

The evolution factors are well-known and have the generic form

$$U^t_{J_B}(\hat{s}_t - \hat{s}'_t, \mu; \mu_0) = \frac{e^K \left(e^{\gamma_E}\right)^\omega}{\Gamma[-\omega]\mu_0} \left[\frac{(\mu_0)^{1+\omega}\theta(\hat{s}_t - \hat{s}'_t)}{(\hat{s}_t - \hat{s}'_t)^{1+\omega}}\right]_+ . \tag{4.66}$$

The functions $K = K(\mu, \mu_0)$ and $\omega = \omega(\mu, \mu_0)$ at NLL order are given by

$$\omega(\mu, \mu_0) = -\frac{\Gamma_0}{j\beta_0}\left[\ln r + \left(\frac{\Gamma_1}{\Gamma_0} - \frac{\beta_1}{\beta_0}\right)\frac{\alpha_s(\mu_0)}{4\pi}(r-1)\right], \tag{4.67}$$

$$K(\mu, \mu_0) = \frac{-2\pi\Gamma_0}{\beta_0^2}\left\{\frac{r - 1 - r\ln r}{\alpha_s(\mu)} + \frac{\gamma_0\beta_0}{4\pi\Gamma_0}\ln r + \left(\frac{\Gamma_1}{\Gamma_0} - \frac{\beta_1}{\beta_0}\right)\frac{1 - r + \ln r}{4\pi} + \frac{\beta_1}{8\pi\beta_0}\ln^2 r\right\}$$

where $r = \frac{\alpha_s(\mu)}{\alpha_s(\mu_0)}$. Here γ_i are the coefficients of the non cusp anomalous dimension [78].

4.3.3 Factorization Formulas

We now combine the results from above sections to derive the final form of the cross section at NLL accuracy. Prior to carrying out the resummation of large logarithms and adding the non-perturbative hadronization function we just have the tree level cross-section given by

$$\frac{\mathrm{d}\sigma}{\mathrm{d}M_t^2\,\mathrm{d}M_{\bar{t}}^2\,\mathrm{d}\eta_t\,\mathrm{d}\eta_{\bar{t}}\,\mathrm{d}p_T} = \frac{p_T\,\sigma_0}{4\pi Q^4 N^k_{init.}}\frac{1}{x_a^* x_b^*} f_a(x_a^*, \mu_{n_a}) f_b(x_b^*, \mu_{n_b}) \mathrm{Tr}\left[\hat{H}_Q^\kappa(\hat{s}, \hat{t}, \hat{u}) \cdot \hat{S}_2^\kappa\right] \times \frac{\Gamma_t^2 m^2}{\pi^2}\frac{1}{\left[(M_t^2 - m^2)^2 + m^2\Gamma_t^2\right]\left[(M_{\bar{t}}^2 - m^2)^2 + m^2\Gamma_t^2\right]} . \tag{4.68}$$

Here $N^\kappa_{init.}$ is the number of initial states for the partonic channel $\kappa = \{q\bar{q}, gg\}$ and the partonic Mandelstam variables are understood to be evaluated with $x^*_{a,b}$ given by

$$x_a^* \equiv \frac{p_t^T}{Q}(e^{\eta_t} + e^{\eta_{\bar{t}}}), \qquad x_b^* \equiv \frac{p_t^T}{Q}(e^{-\eta_t} + e^{-\eta_{\bar{t}}}), \tag{4.69}$$

and the PDFs $f_{a,b}$ are evaluated at the scale μ_{n_a,n_b}. We discuss some of the steps leading to Eq. (4.68) in App. A.

Combining the various resummed functions from the previous sections and adding

the non-perturbative function discussed in detail in the next section, the full NLL cross section is

$$\frac{d\sigma}{dM_{J_t}^2 dM_{J_{\bar{t}}}^2 d\eta_t d\eta_{\bar{t}} dp_T} = \frac{p_T\,\sigma_0}{4\pi Q^4 N_{init.}^k} \mathrm{Tr}\Big[\hat{\mathcal{H}}_b^\kappa(\hat{s},\hat{t},\hat{u},\{\mu_{S_i}\};\mu_t;\mu_Q)\cdot\hat{S}_2^\kappa\Big] \tag{4.70}$$
$$\frac{1}{x_a^* x_b^*} f_a(x_a^*,\mu_{n_a}) f_b(x_b^*,\mu_{n_b})\,\mathcal{K}(M_{\rm cut},\mu_{S_a},\mu_{n_a})\mathcal{K}(M_{\rm cut},\mu_{S_b},\mu_{n_b})$$
$$\int_0^\infty d\ell^+ \int_0^\infty d\ell^-\; F(\ell^+,\ell^-) P\Big(\frac{M_{J_t}^2-m_t^2}{m_t} - \frac{Q_t}{m_t}\ell^+\Big) P\Big(\frac{M_{J_{\bar{t}}}^2-m_t^2}{m_t} - \frac{Q_{\bar{t}}}{m_t}\ell^-\Big)\,.$$

Here P is given by the RG evolved expression of the bHQET jet function:

$$\begin{aligned} P(\hat{s}_t) &= \int_{-\infty}^{\infty} d\hat{s}_t'\, U_{J_B}^t(\hat{s}_t-\hat{s}_t',\mu_{S_t};\mu_{\Gamma_t}) J_B^t(\hat{s}_t',\Gamma,\mu_{\Gamma_t}) \\ &= \frac{1}{\pi m_t}\mathrm{Im}\Big[\frac{e^K(\mu_{\Gamma_t}e^{\gamma_E})^\omega \Gamma(1+\omega)}{(-\hat{s}_t-i\Gamma_t)^{1+\omega}}\Big]\,. \end{aligned} \tag{4.71}$$

We also note that the hard and soft function matrices in Eq. (4.70) have been defined after performing the rotation in color space as shown in Eq. (4.40). In the second line of Eq. (4.70) we have defined $\mathcal{K}(M_{\rm cut})$ as the contribution of beam functions integrated up to $\mathcal{T}_B = M_{\rm cut}$. We see that it only affects the normalization.

4.4 Nonperturbative Hadronization Function

We now consider the non-perturbative corrections to the factorized cross section for ungroomed top jets. Here, the differential cross section gets significant corrections in the peak region for $\hat{s}_t \sim Q/m\Lambda_{\rm QCD}+\Gamma_t$, and in the tail region where $\hat{s}_t \gg Q/m\Lambda_{\rm QCD}+\Gamma_t$ the perturbative corrections are dominant. In Ref. [74] the strategy suggested for $e^+e^- \to$dijets in order to incorporate non-perturbative corrections correctly in the $\overline{\rm MS}$ scheme, and smoothly turn off the non-perturbative corrections in the tail region, was to include a non-perturbative function through a convolution in the l^+, l^- variable in the hemisphere soft function for $t\bar{t}$ dijets in e^+e^- collisions. The fact that the convolution is in these variables follows from the power counting for the non-perturbative mode and the form of the measurement. (Similar results were also

derived for the soft (shape) function in $b \to s\gamma$ decays in Ref. [93].) The moments of this non-perturbative function are defined by field theory matrix elements of specific operators involving Wilson lines. In this case with ultrasoft modes, one extends the measurement function to include the non-perturbative mode as follows:

$$\begin{aligned} 1 &= \int \mathrm{d}l^+ \, \delta\big(l^+ - n\cdot(\hat{p}_{us} + \hat{p}_\Lambda)\big) \\ &= \int \mathrm{d}l^+ \mathrm{d}k \, \delta(l^+ - k - n\cdot\hat{p}_{us}) \, \delta(k - n\cdot\hat{p}_\Lambda) \,, \end{aligned} \tag{4.72}$$

which allows one to employ the following form for the soft function

$$S_{\mathrm{hemi}}(l^+, l^-, \mu) = \int \mathrm{d}l^+ \mathrm{d}l^- \, S^{\mathrm{part}}_{\mathrm{hemi}}(l^+ - k^+, l^- - k^-, \mu) \, F(k^+, k^-) \,. \tag{4.73}$$

Here the two arguments refer to the top and anti top jets that are coupled in the ungroomed jet mass measurement. The $F(k^\pm)$ is the non-perturbative function that peaks around $k^\pm \sim \Lambda_{\mathrm{QCD}}$ and falls off for $k^\pm \gg \Lambda_{\mathrm{QCD}}$. It is identical to that of a jet initiated by a massless quark.

In our case with additional contributions from the beam region the soft function depends on four variables rather than two. However for our purposes it suffices to neglect non-perturbative corrections to the jet-veto distribution since we will mostly fix this variable, and then cancel out the majority of jet-veto effects by looking at normalized M_J spectra. Therefore even for the four variable case we only consider a two-variable non-perturbative function F,

$$\hat{S}(l_t, l_{\bar{t}}, l_a, l_b \mu) = \int \mathrm{d}l^+ \mathrm{d}l^- \, \hat{S}^{\mathrm{part}}(l_t - k, l_{\bar{t}} - k', l_a, l_b, \mu) \, F(k, k') \,. \tag{4.74}$$

As a further simplification, although $\hat{S}$ and $\hat{S}^{\mathrm{part}}$ are color matrices, we consider F to be a scalar rather, so that all entries of the perturbative soft function in color space are modified by hadronization in the same manner. Considering more general matrix valued non-perturbative functions F would allow one to explore for color correlations in the hadronization between the jet and beam regions, but the addition of more

parameters would also make such an analysis quite involved, and it is beyond the scope of our work. Obviously the function F in Eq. (4.74) need not be the same as for e^+e^- in Eq. (4.73) (despite our abuse of notation by giving them the same names).

The exact form of F for our implementation for ungroomed top jets is stated in Sec. 5.5.1 below. This function is normalized

$$1 = \int \mathrm{d}k \, \mathrm{d}k' \, F(k, k') \,, \tag{4.75}$$

and it can be determined by fitting its first few moments defined by

$$\Omega_{n,m} = \int \mathrm{d}k \, \mathrm{d}k' \, k^n \, k'^m \, F(k, k') \,. \tag{4.76}$$

The first moment of F, $\Omega_1 \equiv \Omega_{1,0} = \Omega_{0,1}$ has a special significance since it sets the dominant momentum scale for this non-perturbative function, and allows us to parameterize the size of the non-perturbative corrections. For example, we parameterize the second moment $\Omega_2 \equiv \Omega_{2,0}$ as

$$x_2 = \frac{\Omega_2^c}{\Omega_1^2} = \frac{\Omega_2 - \Omega_1^2}{\Omega_1^2} \,, \tag{4.77}$$

where Ω_2^c is the 2nd cumulant moment of F. From carrying out a dedicated study we find that the dependence of the peak position on the higher moments is most often sub-leading when they are parameterized in terms of dimensionless parameters like x_2. This involves considering Ω_1 and x_2 as independent parameters, and the same conclusion is not reached if we instead take the parameters as Ω_1 and Ω_2 since these are both dimensionful and more highly correlated. Using dimensionless parameters for higher moments allows us to specify the scale of the non-perturbative corrections solely by referring to the first moment. For the ungroomed jet mass there is also a third moment parameter, $\Omega_{1,1}/\Omega_1^2$ that encodes information about cross correlations between the k and k' variables. Since our focus is on one-dimensional jet mass spectra, where the other jet-mass variables is integrated over, this parameter becomes redundant, and hence is not considered here. We explore the dependence of the cross

section on Ω_1 and x_2 in detail in Sec. 5.5.2.

Note that for pp collisions with and without jet grooming we always use moment parameters defined in the $\overline{\text{MS}}$ scheme since we have not yet fully derived the necessary framework to implement the short distance gap scheme for moments that has been discussed for $e^+e^- \to t\bar{t}$, cf. [74].

4.5 Underlying Event Model

For the jet mass measurement inside conical jet of radius R, the main impact of the underlying event is to populate the jet with additional soft radiation that is at somewhat higher energy than the radiation associated with hadronization. This radiation is expected to be predominantly uncorrelated with the jet direction and hence uniform across the jet cone. The contribution of these UE effects lies outside the scope of our factorization theorem, and it has been proposed that this is related to the neglect of so-called non-factorisable contributions from Glauber exchange when deriving the factorization theorem [56]. While it is known from Ref. [106] how to incorporate such Glauber exchanges into SCET, the connection of these effects to underlying event is beyond the scope of this work.

Therefore to account for the contributions of UE we adopt a reasonable physical model proposed in Ref. [111] that appears to accurately account for the impact of this type of radiation on jet mass measurements. In particular, it was shown that MPI in PYTHIA for the ungroomed jet mass spectrum can be well modeled by simply changing the hadronic parameters in the soft non-perturbative function F [111]. This model is reasonable because in both cases we are describing soft radiation effects, just at a larger scale in the case of MPI. Adopting this approach simply changes the meaning of the moment parameters Ω_n determining F. We will add an extra superscript MPI to indicate when this assumption is being used:

$$\Omega_n \to \Omega_n^{\text{MPI}}\,. \tag{4.78}$$

In Ref. [111] it was even noticed there that for jet-mass measurements in $pp \to Z$+jet and $pp \to H$+jet that the change in the spectrum obtained when adding MPI to a hadronic PYTHIA cross section is accurately captured by shifting a single first moment parameter Ω_1 with an exponential functional form for $F(k)$ which only has this one parameter. Since it is not clear if this will remain true in general we will here allow all moment parameters Ω_n to be modified in the presence of UE as in Eq. (4.78).

Chapter 5

Top Mass Determination with Jet Grooming

The top jet mass spectrum is highly sensitive to contamination from initial state radiation (ISR), underlying event, and pile-up, that shifts the peak position and affects the overall shape. Radiation from pile-up is truly uncorrelated with the event while that from ISR and the Underlying Event (UE) are only weakly correlated with the dynamics of the boosted top jet. UE effects are often modeled in Monte Carlo simulations by Multi Parton Interactions(MPI), and we therefore use both terms. In our study we do not consider effects of pile-up and assume that they can be handled experimentally without significant modifications to the spectrum. In Fig. 5-1 we show the top-jet mass spectrum from PYTHIA8 simulations in three different cases: partonic, with hadronization turned on, and with both hadronization and MPI turned on. We see that the peak gets shifted by ~ 5 GeV on turning on MPI, whereas the shift is ~ 2 GeV after including hadronization.

As mentioned in the previous section, contamination from the MPI can be modeled quite well by modifying the shape function which describes hadronization. However, it is not ideal to have such a large shift that needs to be modeled. We therefore seek top mass sensitive kinematic observables that are largely insensitive to contamination, thus reducing an important systematic uncertainty.

Contamination in the boosted top jet that is uncorrelated or only weakly correlated

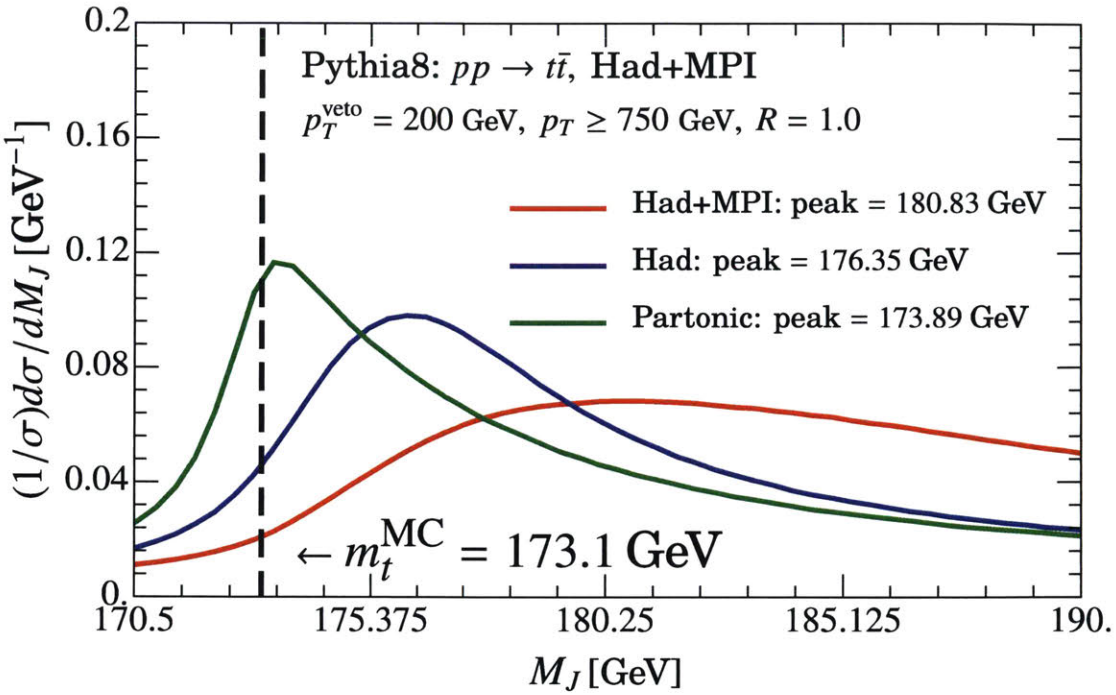

Figure 5-1: Partonic, Had, Had+MPI for no SD case.

tends to be either soft and/or at wide angles from the jet axis. Jet grooming can help reduce these effects by grooming away soft wide angle radiation that also includes radiation from MPI interactions. Several grooming algorithms have been proposed in the literature, including mass drop [29], pruning [47], and trimming [88]. These algorithms yield new observables, which then require modified theoretical calculations, and some of them are more theoretically tractable than others [116, 44, 43]. For our application to top quark jets we consider the modern version of minimal mass drop, called the soft drop grooming algorithm [90]. Factorization theorem based higher order calculations have been carried out for observables like the jet mass and jet angularities when soft drop is applied to massless quark jets [52, 51], making it a promising procedure for our case.

Soft drop declusters the jet using the Cambridge-Aachen algorithm [45, 117] and sequentially goes through the branching history of the jet analyzing the pair of particles (or sub-jets) at each branch. If the energy fractions of the pair fail to meet a certain criteria then the softer branch is discarded. This procedure is continued until a pair is found that satisfies the criteria, and the combination of this pair then

determines the particles that belong to the final groomed jet. The soft drop criteria for e^+e^- colliders is

$$\frac{\min[E_i, E_j]}{E_i + E_j} > z_{\rm cut} \left(\sqrt{2} \frac{\sin(\theta_{ij}/2)}{\sin(R_0/2)} \right)^\beta \xrightarrow{\theta_{ij} \ll 1} z_{\rm cut} \left(\frac{\theta_{ij}}{R_0'} \right)^\beta , \tag{5.1}$$

with $R_0' = \sqrt{2}\sin(R_0/2)$, while for pp collisions the criteria is

$$\frac{\min[p_{Ti}, p_{Tj}]}{p_{Ti} + p_{Tj}} > z_{\rm cut} \left(\frac{R_{ij}}{R_0} \right)^\beta , \tag{5.2}$$

where the angular distance $R_{ij} = \sqrt{2}\left[\cosh(\eta_i - \eta_j) - \cos(\phi_i - \phi_j)\right]^{1/2}$ in terms of the rapidity η_i and azimuthal angle θ_i of the branch i. Here $z_{\rm cut}$ and β are the soft drop parameters which determine the relative strength of the groomer. We always take $R_0 = 1$ since this parameter is not independent from the choice for $z_{\rm cut}$ and β. If the pair fails this criteria then the softer branch is removed, and the groomer proceeds along the more energetic branch. The procedure stops the first time the soft drop condition is satisfied, and the resulting jet is referred to as the *groomed jet.*

The soft drop procedure also determines a groomed jet radius R_g that corresponds to the largest angle between two branches which pass the soft drop criteria in Eq. (5.2) for the first time. This effectively limits the area of the jet contaminated by soft particles to πR_g^2, which is significantly smaller than the original jet area.

Soft drop grooming has been widely employed in the context of jets from massless particles. As we will see below, soft drop grooming for top quark jets is more subtle due to the nature of the mass measurement for massive particles and the unique decay topology. We will develop an effective theory framework to predict the groomed top jet mass spectrum in the peak region, and derive explicit factorization theorems to predict the associated cross section. Predictions from soft drop and the factorization theorem will also be explored with simulation studies using PYTHIA8. In particular we will find, as expected, that the groomed-jet mass spectrum is much less sensitive to

effects of hadronization and MPI, and thus provides the robustness needed for direct comparison of data with our theory predictions. This work has recently appeared in Ref. [71].

The strength of soft drop groomers is determined by the parameters z_{cut} and β. Higher z_{cut} and smaller β values correspond to more aggressive grooming. We limit ourselves to considering only $\beta \geq 0$ values. Commonly values employed by theorists and experimentalist for other jet grooming studies are $z_{\text{cut}} \simeq 0.1$ and $\beta = 0, 1$, but these choices must be reconsidered for our application. We require the implementation of soft drop grooming on the top jet to achieve three main objectives:

1. remove the dominant soft contamination that would otherwise couple the top jet to the dynamics going on in the rest of the event,

2. keep the top quark decay products,

3. retain the ultra-collinear radiation that specifies the information related to the top-mass scheme, and avoid having soft-collinear radiation depend on the angular distribution of the top decay.

The first objective is the main motivation for using soft drop grooming, while the second and third items are constraints that are imposed by what we desire from our measurement and our ability to theoretically compute the corresponding cross section at the desired level of precision. In particular the top mass measurement using jets requires us to be inclusive over the top-decay products, and hence we must not have the grooming be so aggressive as to remove one of the decay products that we want to measure.

To understand the third point, we recall from our discussion in Sec. 4.3 above that for ungroomed top jets the top mass scheme is specified in the HQET Lagrangian, and this information then enters the cross section through the bHQET jet functions. The jet function is described by the ultra-collinear modes in bHQET that have offshellness $p^2 \sim \Gamma_t^2$ and energies $E_{uc}^2 \sim \Gamma_t^2 Q^2/m^2$, which are smaller than the typical energies $E_i^2 \sim m^2$ of the top decay products. Limiting the strength of grooming so as to not to

modify the ultracollinear modes is therefore a constraint stronger than that needed to just retain the decay products. A more subtle requirement that we make when deriving the factorization theorem, is that the top decay products should not directly influence the dominant perturbative soft radiation that remains inside the groomed jet radius R_g. Together these constraints allow for the full evolution and decay of top jets in the peak region to be described by the same universal bHQET top jet functions J_B as in Sec. 4.3. This J_B remains independent of the soft drop parameters, and the corresponding analysis of appropriate top mass schemes then remains in the same class of "top resonance schemes" discussed for ungroomed top jets. These schemes allow for $R \sim \Gamma_t$ in Eq. (2.2), and include the MSR top mass scheme, discussed in Chapter 2. We will demonstrate in the next few sections that together these three constraints require us to choose soft drop parameters in a restricted range corresponding to what we refer to as a *light soft drop* region.

Below in Sec. 5.1 we consider the effects of soft drop grooming on the ultra collinear and ultra soft modes that were relevant for the peak region prior to grooming. We derive the constraints on the grooming parameters, and determine the relevant modes that are required to describe groomed top jets in the peak region, including collinear-soft and non-perturbative modes. In Sec. 5.2 we analyze these constraints to determine the region where one should carry out measurements that can be compared to our computation of groomed jet masses. Sec. 5.3 is devoted to a derivation of the factorization formulae for soft drop groomed top jets. This includes the important treatment of the dominant residual effects of hadronization which appear in the soft drop factorization theorems through a function F_C defined in the quantum field theory calculation. This is discussed in Sec. 5.3.4. For the modeling of UE effects with soft drop we will adopt the same approach discussed in Sec. 4.5.

The final result of this chapter are factorization theorems for the soft drop top jet-mass cross section. We leave the discussion of the numerical implementation of the factorization theorems to Sec. 5.5.1.

5.1 Modes and Power Counting Analysis

We can get a better understanding of the constraints mentioned above by studying the result of applying of soft drop on the quantum field theory modes which are relevant to describing the cross section in the peak region. Which modes are kept and which ones are groomed away is the key question. In this section we derive some key formulae, which are then analyzed further numerically and summarized in Sec. 5.2.

5.1.1 Perturbative Modes

We consider an emission (or a decay product) of energy E and at an angle θ off the top quark and note that for this emission to contribute to the invariant mass measurement in the peak region it needs to satisfy

$$\hat{s} = 2\, v_t \cdot k \sim \Gamma\,, \tag{5.3}$$

where $\Gamma \geq \Gamma_t$ is the physical width of the distribution in the peak region.[1] Here v_t was defined in Eq. (4.46), k is the four momentum of the emission(s), and z is the energy fraction from k relative to the jet energy. Decomposed along the jet direction we have

$$k_j^\mu = \big(n_j \cdot k, \bar{n}_j \cdot k, k_\perp\big) = \big(E(1-\cos\theta), E(1+\cos\theta), k_\perp\big)\,, \tag{5.4}$$

with the energy fraction, $z = 2E/Q = k^-/Q$. Here Q corresponds the large momentum along the boost direction. For an e^+e^- collider this corresponds to the center of mass energy, and for pp collisions $Q = 2p_T \cosh(\eta_J)$ with p_T and η being jet's transverse momentum and pseudorapidity, respectively. The peak region constraint

[1] In the constraint equations derived in this section we can also replace Γ by the measurement variable $\hat{s} = (M_J^2 - m^2)/m$ as long as we do not consider values $\hat{s} < \Gamma_t$ since the width effectively provides an infrared cutoff which shields this low momentum region.

written in these variables reads

$$z\left[(1-\cos\theta)+\frac{m^2}{Q^2}(1+\cos\theta)\right]\sim\frac{4m\Gamma}{Q^2}\,. \tag{5.5}$$

Eq. (5.3) states that the scale of fluctuations of momenta in bHQET theory is $\mathcal{O}(\Gamma_t)$. Both ultra-collinear (UC) or ultra-soft modes in bHQET by definition satisfy this constraint. For the ultra-collinear modes that are boosted along the $\hat{n}_t$ direction with small angles θ we have $\theta\sim 2k_\perp/k^-$.

For the emission to pass the soft drop criteria in Eqs. (5.1) and (5.2) we need

$$z\gtrsim z_{\rm cut}\theta^\beta\,. \tag{5.6}$$

Our analysis of this constraint is similar to the case of massless quark jets treated in Ref. [51], just with modifications to account for the massive unstable top quark. When writing this constraint we note that one of the remaining branches i or j will always contain one, two, or all three of the top decay products, so that $\min[E_i,E_j]/(E_i+E_j)\simeq z$ on the LHS. For the pp soft drop constraint we also have $\min[p_{Ti},p_{Tj}]/(p_{Ti}+p_{Tj})\simeq z$ because the difference between p_{Ti} and energy E_i is a factor of $\cosh(\eta_i)$ and at the level of deriving scaling relations the approximation that these $\cosh(\eta_i)$ factors cancel out suffices for this comparison of branches that have momentum within the jet of radius R. On the RHS we adopt a small angle approximation that has correct scaling for $\theta\ll 1$ up to an $\mathcal{O}(1)$ prefactor (which is $R_0'^{-\beta}$ for the e^+e^- case and $[\cosh(\eta_J)/2]^\beta$ for the pp case). For $\theta\sim 1$ the form of the constraint in Eq. (5.6) also retains the same scaling as the unexpanded form.

In the ungroomed factorization theorem it was the ultra-soft modes that introduced couplings between the top quark jet, and other elements in the event, such as the $\bar{t}$ jet and beam radiation. Demanding that ultra-soft modes with $\theta\sim 1$ and $z\sim 2m\Gamma/Q^2$ will always be groomed away implies a lower bound on $z_{\rm cut}$,

$$z_{\rm cut}\gg\frac{2m\Gamma}{Q^2}\,. \tag{5.7}$$

On the other hand, to always keep the ultra-collinear modes which have $\theta_{\text{uc}} \sim 2m/Q$ and $z \sim \Gamma/m$ we require

$$z_{\text{cut}} \left(\frac{2m}{Q}\right)^{\beta} \ll \frac{\Gamma}{m} \quad \Longrightarrow \quad \frac{\Gamma}{m}\left(\frac{Q}{2m}\right)^{\beta} \gg z_{\text{cut}} \,. \tag{5.8}$$

This constraint puts an upper limit on the soft drop parameter z_{cut}. Due to the fact that the small $\Gamma/m \simeq 0.01$ factor is not overcome by the boost factor $(Q/2m)^{\beta}$ this forces us into a light soft drop region.

The decay products have same boost as the ultra-collinear particles, or $\theta_{\text{decay}} \sim \theta_{\text{uc}}$, but with much higher energy $z_{\text{decay}} \sim 1$. A typical value is $z_{\text{decay}} \sim 1/3$. Hence, the condition in Eq. (5.8) is strong enough to ensure that the top decays products are kept. From the constraints considered so far for the modes that existed in the ungroomed factorization theorem we find:

$$z_{\text{decay}} \left(\frac{Q}{2m}\right)^{\beta} \underset{\substack{\text{decay}\\ \text{products}\\ \text{kept}}}{\gg} \frac{\Gamma}{m}\left(\frac{Q}{2m}\right)^{\beta} \underset{\substack{\text{ucollinear}\\ \text{kept}}}{\gg} z_{\text{cut}} \underset{\substack{\text{usoft}\\ \text{vetoed}}}{\gg} \frac{\Gamma}{m}\frac{2m^2}{Q^2} \,. \tag{5.9}$$

For boosted top quarks $Q \gg m$ and there is always a parametric window where these constraints are satisfied. We will see below that both constraints on z_{cut} in Eq. (5.9) will become a bit stronger once the full set of expansions needed for the factorization theorem have been considered.

While the wide angle $\theta \sim 1$ ultra-soft modes are vetoed away, the introduction of the soft drop constraint allows new modes to become active. We now have collinear-soft (CS) modes with momenta p_{cs}^{μ} defined as the modes having the minimum energy and largest angle that passes the soft drop criteria in Eq. (5.6), and still satisfies Eq. (5.5) so that particles of this type contribute to the jet mass measurement. These modes were introduced for describing soft drop factorization in Ref. [51] and also appear in other physical applications of jet physics, being part of the generic SCET$_+$ framework which contains additional modes that are simultaneously collinear and

soft, discussed in Refs. [16, 105, 91, 104]. Parameterizing

$$p_{\rm cs}^{\mu} \sim Q\, z_{\rm min}\left(\frac{\theta_{\rm max}^2}{4},\, 1,\, \frac{\theta_{\rm max}}{2}\right), \tag{5.10}$$

this definition of the collinear-soft modes gives

$$z_{\rm min} = \frac{\Gamma_t}{m}\left(\frac{4m^2}{Q^2}\right)^{\frac{\beta}{\beta+2}}\left(z_{\rm cut}\frac{m}{\Gamma}\right)^{\frac{2}{\beta+2}}, \quad \theta_{\rm max} = \left(\frac{4}{z_{\rm cut}}\frac{m^2}{Q^2}\frac{\Gamma}{m}\right)^{\frac{1}{2+\beta}}. \tag{5.11}$$

Hence, after the application of soft drop we are left with the following perturbative modes:

$$p_{\rm cs}^{\mu} \sim \Gamma_t\frac{Q}{m}(\lambda^2,\, \eta^2,\, \lambda\,\eta)\,, \qquad p_{\rm uc}^{\mu} \sim \Gamma_t\frac{Q}{m}(\lambda^2\,,1,\, \lambda)\,, \tag{5.12}$$

where we have defined expansion parameters

$$\lambda = \frac{m}{Q}\,, \qquad \eta \equiv \left[\left(\frac{2m}{Q}\right)^{\beta} z_{\rm cut}\frac{m}{\Gamma_t}\right]^{\frac{1}{\beta+2}}. \tag{5.13}$$

To be able to factorize the contributions to the cross section between collinear-soft modes and ultracollinear modes we demand the hierarchy

$$1 \gg \eta \gg \lambda\,. \tag{5.14}$$

This results gives us the condition

$$z_{\rm cut}^{\frac{1}{2+\beta}} \gg \frac{1}{2}\left(\frac{\Gamma_t}{m}\frac{4m^2}{Q^2}\right)^{\frac{1}{2+\beta}}, \tag{5.15}$$

which is a stronger constraint on the lower bound of $z_{\rm cut}$ than that in Eq. (5.9) from grooming the ultra-soft radiation. (A numerical study of this constraint is given below in Sec. 5.2.) As another consequence of Eq. (5.14) we note that the collinear-soft mode

is more perturbative than the ultra-soft mode:

$$p_{\rm cs}^2 = \Gamma_t^2 \left[\left(\frac{2m}{Q} \right)^{\beta} z_{\rm cut} \frac{m}{\Gamma_t} \right]^{\frac{2}{\beta+2}} = \eta^2 \Gamma_t^2 \gg p_{\rm us}^2 = \Gamma_t^2 \lambda^2 \,. \tag{5.16}$$

In addition to vetoing the ultra-soft modes, soft drop will groom away all wide angle modes with energy fraction up to $z \sim z_{\rm cut}$. These modes do not contribute to the measurement but they affect the overall normalization of the cross section. Again such modes also appear for massless quark jets in Ref. [51] and we refer to them as either "Global Soft" or just "Soft" with the momentum scaling as

$$p_{S_G} \sim \frac{z_{\rm cut} Q}{2} (1,\, 1,\, 1) \,. \tag{5.17}$$

We will see later on that they are also needed to ensure the consistency of the functions appearing in the factorized cross section under renormalization group evolution.

In Fig. 5-2 we represent the modes discussed above, on the standard p^+-p^- plane, including collinear-soft (CS), ultra-collinear (UC), and Soft. We also display the non-perturbative modes (Λ) that will be discussed in a later section. In this plane modes with fixed invariant mass lie on one of the indicated hyperbole, with smaller invariant masses lying on hyperbole that come closer to the origin. This gives us a sense of relative offshellness of the modes we considered above. As shown in the figure, and following Eq. (5.12), the p^+ components of both the CS and UC modes have the same scaling and the other two components of collinear-soft modes are parametrically smaller, a feature similar to that of ultra-soft modes before grooming. Hence the two modes in Eq. (5.12) will couple in the jet mass factorization theorem through their p^+ momenta. This agrees with our EFT picture where the minus component is fixed to be the hard scale and the jet mass is determined by the plus component in the peak region, as shown in Eqs. (4.7) and (4.10). We notice from Fig. 5-2 that soft modes have higher invariant mass than the collinear-soft modes. To see this we rewrite the

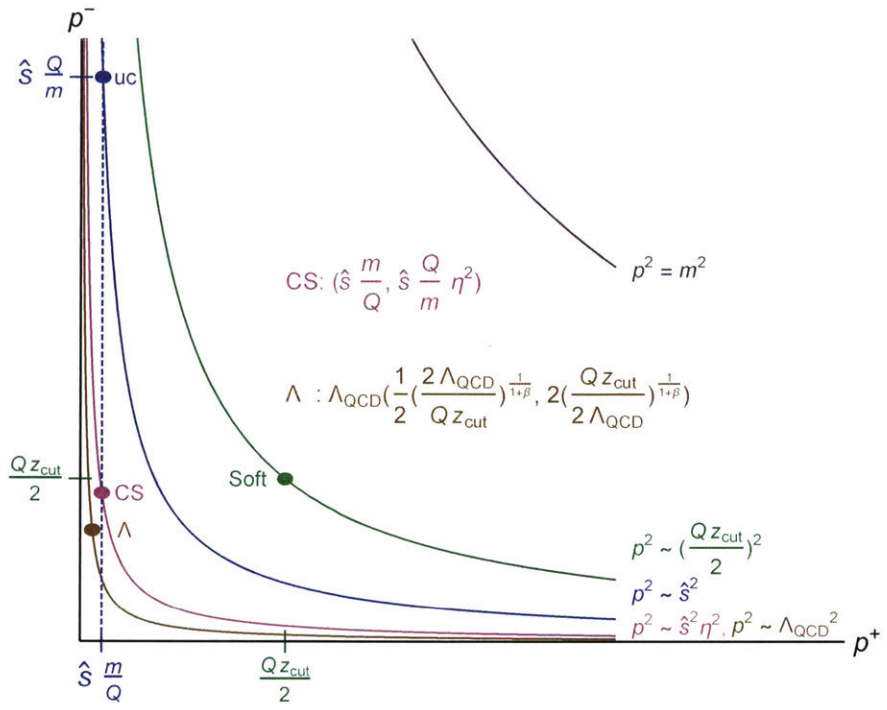

Figure 5-2: Modes on p^+-p^- plane.

constraints in Eq. (5.9) as

$$\epsilon = z_{\rm cut}\left(\frac{2m}{Q}\right)^{\beta}\left(\frac{m}{\Gamma_t}\right) \ll 1\,, \quad \delta = \frac{4}{z_{\rm cut}}\frac{m^2}{Q^2}\frac{\Gamma_t}{m} \ll 1\,, \tag{5.18}$$

where we recall that $z_{\rm cut}$ has been chosen so that these constraints are satisfied. Hence we have

$$p_s^2 \sim z_{\rm cut}^2\frac{Q^2}{4} = \Gamma_t^2\left(\frac{\epsilon}{\delta^{1+\beta}}\right)^{\frac{2}{2+\beta}} \gg \Gamma_t^2\epsilon^{\frac{2}{2+\beta}} = \Gamma_t^2\,\eta^2 \sim p_{\rm cs}^2\,. \tag{5.19}$$

However, the comparison between soft and ultra-collinear modes depends on specific values of ϵ and δ. We can further check that the soft modes lie below the top mass hyperbola, or $Q\,z_{\rm cut} \ll m$ for the experimentally accessible values of Q that we consider here. From Eq. (5.9) we have

$$z_{\rm cut} \ll \frac{\Gamma_t}{m}\left(\frac{Q}{2m}\right)^{\beta} < \frac{2m}{Q}\,, \tag{5.20}$$

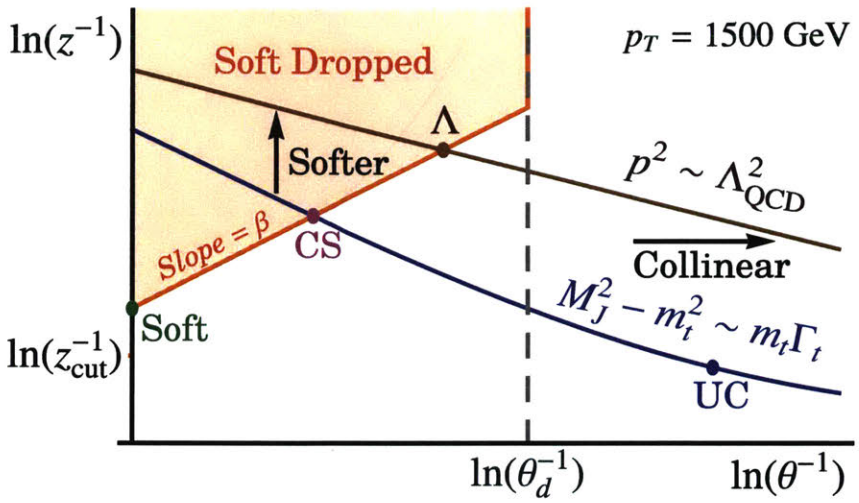

Figure 5-3: Modes on z-θ plane for the "high-p_T" case.

since $\Gamma_t/m < (2m/Q)^{1+\beta}$ for the Qs we consider here, and $\beta = 0, 1, 2$.

5.1.2 Non-Perturbative Modes

Next we turn to the discussion of the non-perturbative mode present after grooming. To facilitate our discussion, we now consider another illustration of the modes and constraints by representing them on the $\ln(1/z)$-$\ln(1/\theta)$ plane in Fig. 5-3. To start out we set $p_T = 1500$ GeV, $\eta_J = 0$, and $\Lambda_{\rm QCD} \sim 300$ MeV. Here the orange line corresponds to the soft drop constraint in Eq. (5.6), and the blue curve represents the peak region constraint in Eq. (5.5). The orange shaded region indicates the particles groomed away by soft drop. The brown line corresponds to the onset of the non-perturbative region, and particles above this line are confined in hadrons.

The location of the modes discussed earlier is also indicated in Fig. 5-3, with modes to the right being more collinear, and modes higher up being softer. The collinear soft mode satisfies the peak region constraint in Eq. (5.5) and lives on the boundary of soft drop region, and hence sits at the intersection of the blue and orange curves. The ultra collinear mode, being higher in virtuality is located to the right on the blue curve. The previous ultrasoft modes that were present at the intersection of blue curve and y-axis are groomed away and we are left with the (global) soft wide

angle modes at the boundary of the soft dropped region (green dot).

The dashed line indicates the point when soft drop stops, which we previously discussed in terms of the groomed jet radius $R_g < R$. Due to the special top decay topology, and for $z_{\rm cut}$ in the range given by Eq. (5.9), the soft drop criterion in Eq. (5.2) is first satisfied when the algorithm reaches the branch that corresponds to a pair of sub-jets of top-decay products of commensurate energy, after having vetoed away the ultra-soft particles at larger angles. If among the decay products labeled by indices d_1, d_2, and d_3, the subjet corresponding to the pair $\{d_1 d_2\}$ stops the groomer, then we define θ_d as

$$\theta_d = \max(\theta_{d_1}, \theta_{d_2})\,, \tag{5.21}$$

where the angles θ_{d_i} are defined with respect to the boosted top jet's jet axis. Thus, the groomed jet radius, R_g, effectively corresponds to $R_g \sim \theta_{\rm d}$ and the soft drop algorithm stops removing particles when it reaches this angle, shown by the dashed line in Fig. 5-3. The boost of the top quark causes the angles $\theta_{d_i} \sim 2m/Q$, so as we increase p_T the dashed line moves to the right along with the UC modes. Although this dashed line turns out to not play a role for our discussion in this subsection, it does have important theoretical and phenomenological consequences that are explored below in the next subsection.

Modes that are collinear and non-perturbative satisfy $p_\Lambda^2 \sim \Lambda_{\rm QCD}^2$ and can be parametrized by their angle θ relative to the jet axis as

$$p_\Lambda^\mu \sim \frac{2\Lambda_{\rm QCD}}{\theta}\left(\frac{\theta^2}{4}, 1, \frac{\theta}{2}\right), \quad z_\Lambda(\theta) \sim \frac{2\Lambda_{\rm QCD}}{Q\,\theta}\,, \tag{5.22}$$

and are represented by the brown line in Fig. 5-3.

To calculate the location of the dominant non-perturbative modes on this line we first can extend the results in Eq. (5.12) to describe the tail region, as well as the non-perturbative region, by making the substitution $\Gamma \to \hat{s}$. Since the collinear-soft modes have the lowest invariant mass of all the three modes considered above, we can ask for what values of the measurement $\hat{s}$ we fall into the non-perturbative region

such that

$$p_{\rm cs}^2 \sim \Lambda_{\rm QCD}^2 \,.$$

This would correspond to the blue curve in Fig. 5-3 moving up as $\hat{s}$ is reduced, and eventually the pink dot meeting the brown line at the point Λ. (In practice we never have to consider $\hat{s} < \Gamma_t$ since Γ_t screens the infrared $\hat{s} \to 0$ region, much like in the function $\hat{s}^2 + \Gamma_t^2$. However this argument still suffices to derive the scaling of the dominant nonperturbative modes.) This leads to

$$\hat{s} \sim \frac{\Lambda_{\rm QCD} Q}{2m} \left(\frac{2\Lambda_{\rm QCD}}{Q z_{\rm cut}} \right)^{\frac{1}{1+\beta}} . \tag{5.23}$$

This mode also corresponds to the maximum angle θ that passes the soft drop criteria:

$$z_{\rm NP}(\theta) \gtrsim z_{\rm cut}\, \theta^\beta \;\Rightarrow\; \theta \lesssim \left(\frac{2\Lambda_{\rm QCD}}{Q\, z_{\rm cut}} \right)^{\frac{1}{1+\beta}} . \tag{5.24}$$

Combining these results gives the scaling for the dominant nonperturbative mode

$$p_\Lambda^2 \sim \Lambda_{\rm QCD}^2 \,, \quad p_\Lambda^+ \sim \frac{\Lambda_{\rm QCD}}{2} \left(\frac{2\Lambda_{\rm QCD}}{Q\, z_{\rm cut}} \right)^{\frac{1}{1+\beta}} , \quad p_\Lambda^- \sim 2\,\Lambda_{\rm QCD} \left(\frac{Q\, z_{\rm cut}}{2\Lambda_{\rm QCD}} \right)^{\frac{1}{1+\beta}} , \tag{5.25}$$

which is shown appearing at the intersection of the brown and orange lines in Fig. 5-3.

5.1.3 Effects of Top-Decay Products

In the previous section we analyzed a case with $p_T = 1500\,\text{GeV}$. For high-p_T top jets the decay products are more collimated and hence in this case the location of the non-perturbative mode is analogous to the case of jets from massless quarks. In particular for high-p_T the dashed line in Fig. 5-3 is always on the right hand side of the Λ modes.

However, for an intermediate p_T range of experimental interest the dashed line moves further to the left, and we find that the dominant non-perturbative modes are

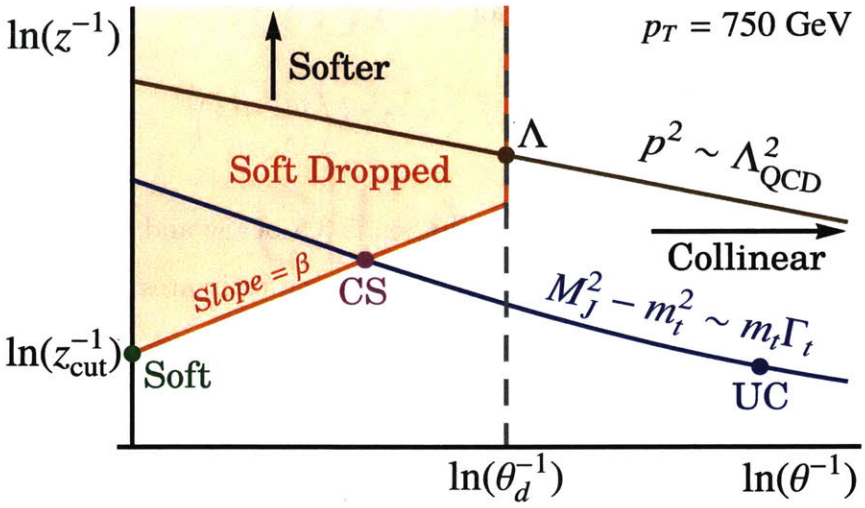

Figure 5-4: Modes on z-θ plane for the "decay" case.

located on the dashed line. This occurs because the brown line now hits the dashed line instead of the orange line. This is shown in Fig. 5-4 for $p_T = 750$ GeV.

In such cases the the nonperturbative modes have the angle set by the decay product that is furthest away from the top jet axis and stops the groomer:

$$\theta_\Lambda \sim \theta_d \,. \tag{5.26}$$

We refer to the two cases in Figs. 5-3 and 5-4 as "high-p_T" and "decay" cases respectively. We can ask at what Q we transition between the two pictures by comparing the p^+ components of the Λ modes, since the contribution of a mode to the measurement is proportional to the plus component contribution as shown in Eq. (4.7). We first parameterize the plus component of the Λ mode in Fig. 5-4 as follows

$$p_\Lambda^+ = \Lambda_{\rm QCD}\,\frac{m}{Q} h(\theta_d)\,, \tag{5.27}$$

where we have factored out the leading dependence on the boost Q/m and parameterized the subleading dependence in an $\mathcal{O}(1)$ number, $h(\theta_d)$, that is related to the fraction of the top quark energy carried by the decay product at angle θ_d. Comparing the p^+ components for the "decay" and "high-p_T" cases in Eqs. (5.27) and (5.25) we

find that the "decay" case is relevant for

$$p_\Lambda^{\text{decay}+} \gtrsim p_\Lambda^{\text{high}\,p_T\,+} \;\Rightarrow\; Q \lesssim 2mh\left(\frac{mhz_{\text{cut}}}{\Lambda_{\text{QCD}}}\right)^{\frac{1}{\beta}}. \tag{5.28}$$

We discuss in detail the calculation of h in Sec. 5.3.5 below and comment further on the range of validity of Eq. (5.28) there. For making estimates one can take $h \simeq 2$ which turns this condition into

$$Q \lesssim 4m\,(\frac{2mz_{\text{cut}}}{\Lambda_{\text{QCD}}})^{1/\beta}. \tag{5.29}$$

Using Eq. (5.22) and Eq. (5.27) we have

$$p_\Lambda^{\text{decay}} \sim \Lambda_{\text{QCD}}\left(\frac{mh}{Q}, \frac{Q}{mh}, 1\right), \tag{5.30}$$

which on comparison with Eq. (5.4) gives

$$h(\theta_d) = \frac{Q}{m}\sqrt{\frac{1-\cos\theta_d}{1+\cos\theta_d}} = \frac{Q}{m}\tan\frac{\theta_d}{2}. \tag{5.31}$$

Another interesting consideration in this intermediate p_T regime for the decay dominated version of the factorization is when we consider larger z_{cut} values. Eq. (5.9) specifies the values of z_{cut} for which the ultra-collinear modes get groomed away. In absence of top decay products this would correspond to the orange line moving down on increasing z_{cut} and eventually meeting the ultra-collinear mode for

$$z_{\text{cut}}^{\text{uc}} \sim \frac{\Gamma_t}{m}\left(\frac{Q}{2m}\right)^{\beta} \tag{5.32}$$

However, the decay products shield the ultra-collinear mode from soft drop grooming ever reaching them, as long as the first inequality in Eq. (5.9) is satisfied. This has important consequences. Since the csoft mode lives on the boundary of soft drop, we note that on increasing z_{cut} the csoft mode will hit the vertical dashed line in Fig. 5-4 already at $z_{\text{cut}} = z_{\text{cut}}^{\text{decay}}$ before soft drop gets close to touching the ultra-collinear

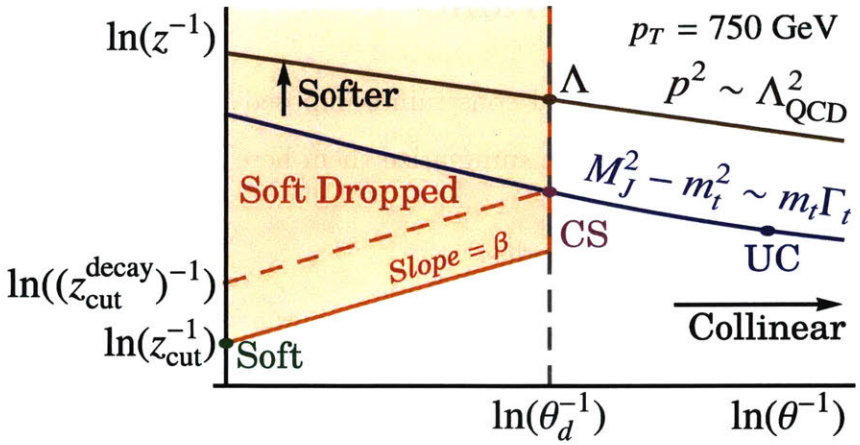

Figure 5-5: Modes on z-θ plane.

modes. This intersection is shown in Fig. 5-5 by the dashed orange line.

$z_{\rm cut}^{\rm decay}$ can be calculated by demanding that both the peak region constraint in Eq. (5.5) and the soft drop criteria in Eq. (5.6) be saturated at $\theta = \theta_d$ given by Eq. (5.31). This gives

$$z_{\rm cut}^{\rm decay} = \frac{\Gamma_t}{mh^2}\left(\frac{Q}{2mh}\right)^{\beta} \simeq \frac{\Gamma_t}{4m}\left(\frac{Q}{4m}\right)^{\beta}, \tag{5.33}$$

which turns out to give a stronger constraint than Eq. (5.32) since $h > 1$.

Further increasing $z_{\rm cut}$ beyond $z_{\rm cut}^{\rm decay}$ will keep the location of csoft mode unchanged. However, the collinear soft mode on the dashed line for these values of $z_{\rm cut}$ is no longer described by Eqs. (5.10) and (5.11), and now instead depends on the decay product phase space which determines θ_d. Thus in this regime the top decay products would also be influencing the perturbative collinear-soft function and not be solely isolated to influencing the perturbative ultra-collinear modes. This regime therefore results in a different theoretical analysis even for the perturbative modes, and consideration of factorization for this regime is beyond the scope of this work. We therefore limit ourselves to values of $z_{\rm cut} \lesssim z_{\rm cut}^{\rm decay}$.

5.2 Kinematic Constraints

We have by now considered several constraints imposed by power counting and validity of factorization theorem. We summarize them here again for convenience:

1. soft drop vetoes ultra-soft modes:

$$z_{\rm cut} \gg \frac{2m\Gamma_t}{Q^2}\,, \tag{5.34}$$

2. soft drop does not touch ultra-collinear modes:

$$z_{\rm cut} \ll \frac{\Gamma_t}{m}\left(\frac{Q}{2m}\right)^{\beta}\,, \tag{5.35}$$

3. collinear-soft modes and ultra-collinear modes factorize:

$$z_{\rm cut}^{\frac{1}{2+\beta}} \gg \frac{1}{2}\left(\frac{\Gamma_t}{m}\frac{4m^2}{Q^2}\right)^{\frac{1}{2+\beta}}\,, \tag{5.36}$$

4. top decay products do not influence the collinear-soft function, $\theta_{CS} \lesssim \theta_d$:

$$z_{\rm cut} \lesssim \frac{\Gamma_t}{4m}\left(\frac{Q}{4m}\right)^{\beta}\,. \tag{5.37}$$

To compare the relative strength of these constraint we plot all four of them for $z_{\rm cut}$ as a function of p_T in Fig. 5-6. Here the dashed curves represent inequalities ($\lesssim$, $\gtrsim$, $\gg$ or $\ll$) in the constraints above replaced with equalities, and the solid lines satisfy the strong inequalities ($\gg$ or $\ll$) by a factor of 3. We find that Eqs. (5.37) and (5.36) provide stronger constraints than Eqs. (5.35) and (5.34). The shaded regions represent the area of parameter space that is ruled out by these restrictions, and is beyond the scope of the factorization theorems we will derive. The combination of above the constraints has a striking consequence of limiting the allowed values of grooming parameters to the region of "light grooming" with $z_{\rm cut} \sim .01$. It also induces a minimum bound $p_T \gtrsim 500$ GeV, and hence requires the top-quark to be

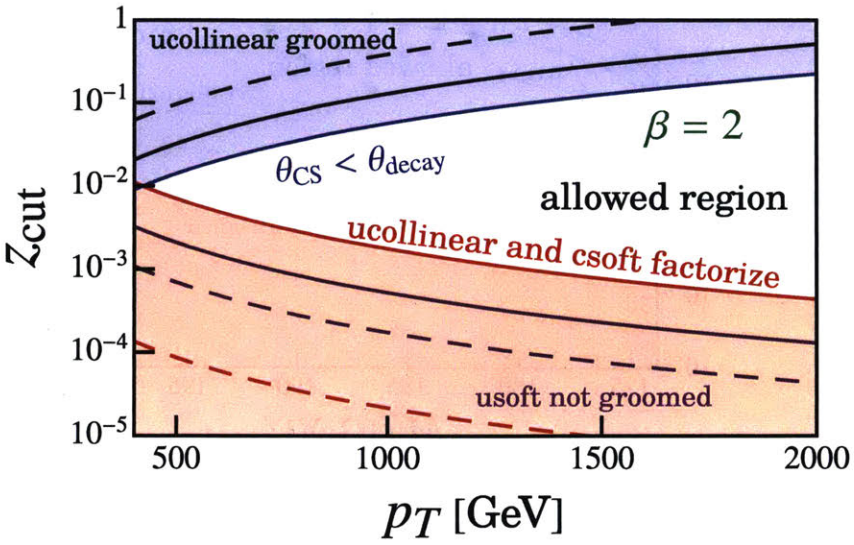

Figure 5-6: Comparing all the constraints as a function of p_T.

more boosted than the expansions needed for deriving our ungroomed factorization theorem.

We also extend the constraints in the peak region to cover tail region by making substitution $\Gamma_t \to \hat{s}_t$, and plot the constraints as a function of M_J in the tail region for $M_J \gtrsim m_t + \Gamma_t$. In the peak region $\hat{s}$ saturates to Γ_t. We see that the constraints in the peak region are modified in the tail such that the expansion parameter for the ultra-collinear and collinear-soft factorization becomes larger the further out on the tail we go.

Below in Fig. 5-8 we also show the constraints for $\beta = 0$ and 1, which correspond to applying more aggressive soft drop. We notice that the restrictions that enable us to derive our factorization theorems are stronger for smaller values of β.

We will later check through PYTHIA8 studies that even with such seemingly strong restrictions on z_{cut} and β, that the light grooming required by theoretical considerations still removes the ultra-soft particles that couple the top-jet to the dynamicss of the rest of the event, as predicted.

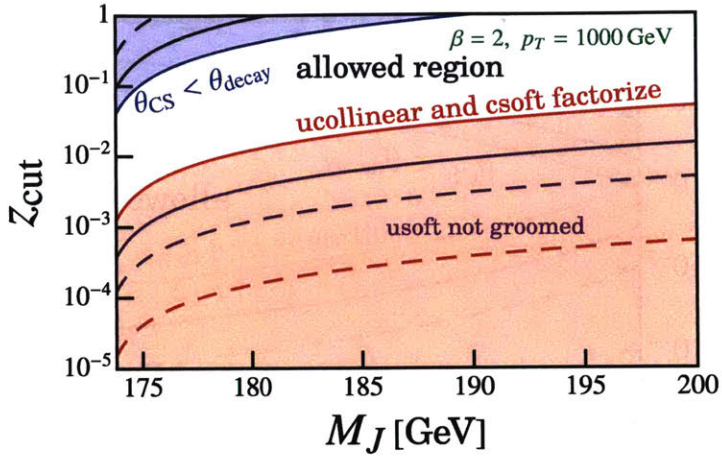

Figure 5-7: Comparing all the constraints as a function of M_J.

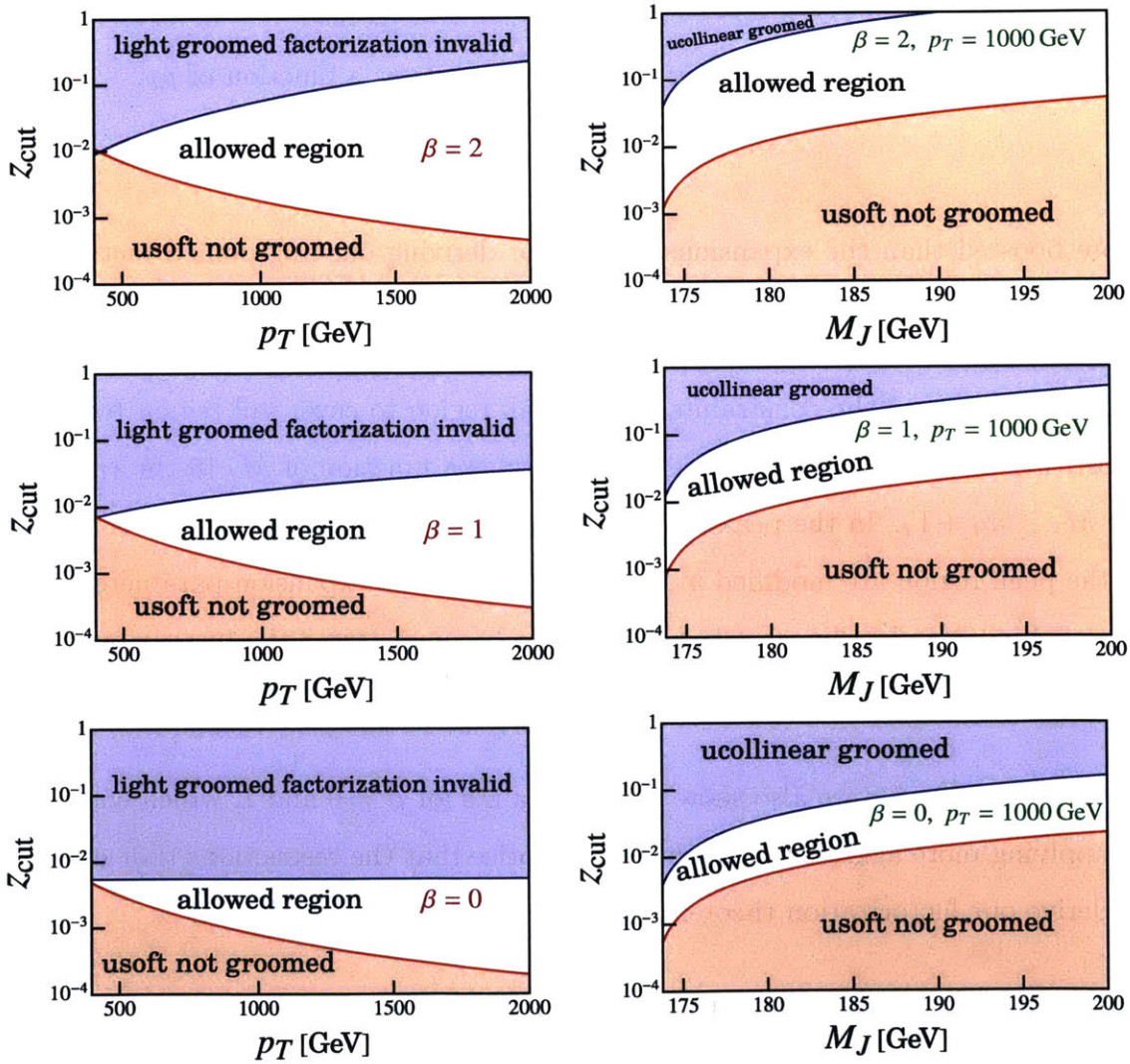

Figure 5-8: Constraints on z_{cut} as function of p_T and M_J for various β.

5.3 Factorization for Soft Drop Groomed Top Jets

Having determined the relevant modes we now describe in detail the EFT for soft drop groomed top jets. For the scales above the top mass we have the same massive SCET as described in Sec. 4.2. However, the low energy theory for the peak region gets modified. We show a schematic of the comparison of the EFTs for top jets before and after grooming in Fig. 5-9. We refer to the low energy theory in the frame of top quark as bHQET$_+$ and it has the ultracollinear and collinear soft modes, summarized in Table 5.1. As an important consequence of jet grooming we now no longer have cross talk between the top and anti-top jet. This is because the ultra-soft particles that coupled to both top and anti-top jets, and the beam region, have been groomed away. This allows for the use of both fully hadronic top decays as well as the use of semi-leptonic top decays, where the jet mass from the hadronically decaying top is measured, and the leptonically decaying top can be used for tagging. In the case where both t and $\bar{t}$ decay hadronically we can consider the two decays as providing independent samples that can be combined, with the jet mass measurement and soft drop grooming done on one or the other of the two jets. Our analysis also applies equally well whether the top-mass is measured from the t jet or the $\bar{t}$ jet, but for simplicity of language we will always refer to the t jet as the one which has jet grooming applied.

5.3.1 Operators in bHQET$_+$

In this subsection we derive the expressions of Wilson lines generated by integrating out off-shell collinear-soft modes, and by doing field redefinition we decouple the the ultracollinear modes from collinear-soft modes. This lays foundation for factorizing the cross section. We then make use of the results in the literature to write down the collinear-soft function for the factorization theorem, and check the consistency of RG running.

For $p^2 \gtrsim m^2$ we have the same collinear modes as in our ungroomed factorization analysis and the relevant operators are described in Sec. 4.2.1. However, the soft

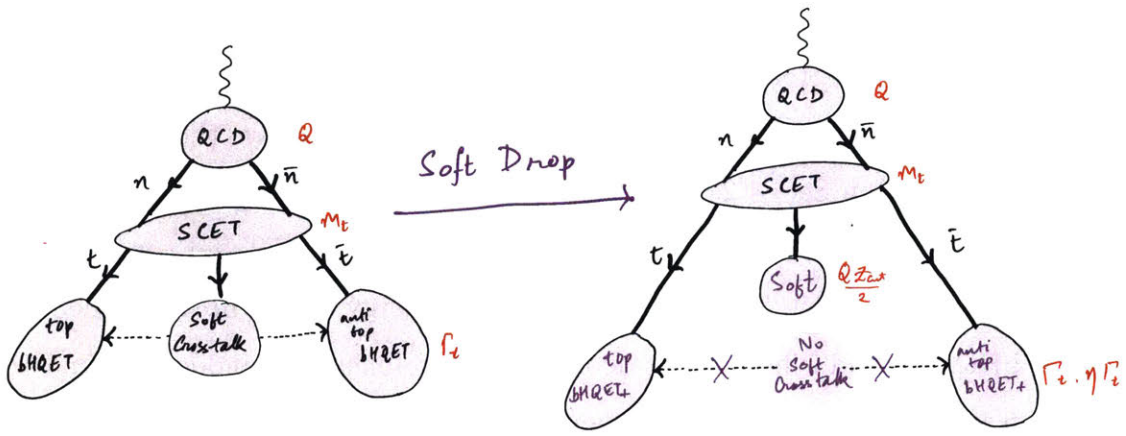

Figure 5-9: Sequence of effective field theories for top invariant mass distribution before and after soft drop grooming.

modes in the Wilson lines now have the scaling given by Eq. (5.17). Due to the factorization of the top-jet from the rest of the event, we can simply denote the beam region our factorization analysis here by an operator Φ^I which does not have to be treated in detail, unlike the ungroomed case. For the top sector and anti-top sectors above the scale m^2 we have

$$\mathcal{O}^I_{\rm SCET} = \overline{\chi}^{(0)}_{n_t} \left(Y^\dagger_{n_t} \, \Gamma^I T^I \, Y_{n_{\bar{t}}} \right) \chi^{(0)}_{n_{\bar{t}}} \, \Phi^I \,, \tag{5.38}$$

where T^I are color matrices and Γ^I denotes the Dirac structure in the channel I. The (0) superscript indicates that the fields have been defined after BPS field-redefinition to decouple soft gluons. In all the expressions below we will drop the (0) superscript. Note that if we consider the case where the rest of the event is exclusive with a veto of all jets beyond the t and $\bar{t}$ which have transverse jet momenta $p_T > p_T^{\rm veto}$, then the Φ^I field will also in general contain Wilson lines Y_{n_a} and Y_{n_b} for the beam region, and hence does not factorize from the global soft contributions. (This is clearest if the veto scale is commensurate with the soft scale $p_T^{\rm veto} \sim Q z_{\rm cut}$.) This occurs because only the contributions contributing to the jet mass spectrum fully factorize, not the contributions needed to compute the overall normalization.

bHQET$_+$ Modes	Scaling	Fields
$n_{t,\bar{t}}$-ultra collinear	$\left(\frac{m}{Q_J}\Gamma_t,\ \frac{Q_J}{m}\Gamma_t,\ \Gamma_t\right)_{t,\bar{t}}$	$(h_{v_t},\ A_{v_t}),\ (h_{v_{\bar{t}}},\ A_{v_{\bar{t}}})$
$n_{t,\bar{t}}$-csoft	$\left(\frac{m}{Q_J}\Gamma_t,\ \frac{Q_J}{m}\Gamma_t\,\eta^2,\ \Gamma_t\,\eta\right)_{t,\bar{t}}$	$(\xi^{cs}_{n_t},\ A^{cs}_{n_t}),\ (\xi^{cs}_{n_{\bar{t}}},\ A^{cs}_{n_{\bar{t}}})$
global soft	$\frac{Qz_{\rm cut}}{2}(1,1,1)$	$(\psi_{S_G}, A^{\mu}_{S_G})$

Table 5.1: Summary of the EFT modes set up, scaling, and fields in bHQET$_+$ theory for groomed top jets. η is defined in Eq. (5.13). We have displayed here only perturbative modes.

The bHQET$_+$ Lagrangian is given by

$$\mathcal{L}^t_{\rm bHQET_+} = \bar{h}_{v_t}\left[iv_t.\mathcal{D}_{v_t} - \delta m + \frac{i}{2}\Gamma_t\right]h_{v_t}\,, \tag{5.39}$$

where Γ_t is the total width of the unstable top-quark and

$$i\mathcal{D}^{\mu}_{v_t} = i\tilde{\partial}^{\mu}_{v_t} + gA^{\mu}_{v_t} + \frac{\bar{n}_t}{2}g\,n_t.A^{cs}_{n_t}\,. \tag{5.40}$$

We have a similar expression for the anti-top case. We note that the csoft gluons couple to the heavy quark field through the $n_t \cdot A^{cs}_{n_t}$ component, similar to the ultrasoft gluon coupling in the ungroomed case. Hence we can perform field redefinition within bHQET$_+$ to decouple the csoft mode:

$$h_{v_t} = X_{n_t}\left[n_t.A^{cs}_{n_t}\right]h^{(0)}_{v_t}\,. \tag{5.41}$$

The analogous decoupling when grooming is done on the anti-top side is

$$h_{v_{\bar{t}}} = X_{n_{\bar{t}}}\left[n_{\bar{t}}.A^{cs}_{n_{\bar{t}}}\right]h^{(0)}_{v_{\bar{t}}}\,. \tag{5.42}$$

Here the superscript (0) indicates that collinear fields are decoupled from the csoft fields. It should not be confused with decoupling from usoft gluons since they are absent in bHQET$_+$ theory after application of grooming.

Now we consider the collinear-soft sector. We note that analogous to the ultra-

collinear Wilson line W_{n_t} we get Wilson lines of csoft modes given by

$$V_{n_t}[\bar{n}_t.A_{n_t}] = \left[\sum_{\text{perms}} \exp\left(\frac{-g}{\bar{n}_t.\mathcal{P}_{n_t}}\bar{n}_t.A^{cs}_{n_t}(x)\right)\right], \tag{5.43}$$

which generated by integrating out offshell fluctiations from attachment to collinear modes in other directions. These Wilson lines are required for the csoft gauge invariance. Hence the matching from SCET to bHQET$_+$ for the top-quark reads

$$\overline{\chi}^{(0)}_{n_t} \to \left(\bar{h}_{v_t} W_{n_t}\right) V_{n_t}\,, \tag{5.44}$$

while if we apply soft drop for the anti-top then we have the analogous result there,

$$\chi^{(0)}_{n_{\bar{t}}} \to V^\dagger_{n_{\bar{t}}} \left(W^\dagger_{n_{\bar{t}}} h_{v_{\bar{t}}}\right). \tag{5.45}$$

Hence, we have in bHQET$_+$ with soft drop grooming on both the t and $\bar{t}$ jets

$$\mathcal{O}^{t\bar{t},I}_{\text{bHQET}_+} = \left(\bar{h}_{v_t} W_{n_t}\right)\left(X^\dagger_{n_t} V_{n_t}\right)\left(Y^\dagger_{n_t}\, T^I \Gamma\, Y_{n_{\bar{t}}} \Phi^I\right)\left(V^\dagger_{n_{\bar{t}}} X_{n_{\bar{t}}}\right)\left(W^\dagger_{n_{\bar{t}}} h_{v_{\bar{t}}}\right). \tag{5.46}$$

All the terms in parentheses will factorize from each other. In the squared matrix element the $\left(\bar{h}_{v_t} W_{n_t}\right)$ will appear in the ultra-collinear jet function J_B, the $\left(X^\dagger_{n_t} V_{n_t}\right)$ in the collinear-soft function for the top-jet S_C. Similarly $\left(W^\dagger_{n_{\bar{t}}} h_{v_{\bar{t}}}\right)$ will appear in the ultra-collinear jet function for the anti-top jet, and $\left(V^\dagger_{n_{\bar{t}}} X_{n_{\bar{t}}}\right)$ for the soft-collinear function for the anti-top jet. Finally the $\left(Y^\dagger_{n_t}\, T^I \Gamma\, Y_{n_{\bar{t}}} \Phi^I\right)$ term will give rise to the global soft function and contributions only affecting the normalization like PDFs and initial state radiation. If instead of grooming both the t and $\bar{t}$ jets, we only groom the t jet then we can write the relevant operator as

$$\mathcal{O}^{t\bar{t},I}_{\text{bHQET}_+} = \left(\bar{h}_{v_t} W_{n_t}\right)\left(X^\dagger_{n_t} V_{n_t}\right)\left(Y^\dagger_{n_t} \Phi'\right), \tag{5.47}$$

where now Φ' includes also terms associated with the $\bar{t}$ jet. Again the same ultra-collinear jet function and collinear-soft function will arise in this case. We discuss

these in more detail in the next section.

5.3.2 Perturbative Cross Section

In this section we derive the factorization theorem for groomed top-jet mass. The SCET factorization for the top sector remains the same as considered in Ref. [49], but we now match to bHQET$_+$. For simplicity we focus on the single top sector in Eq. (5.46) or Eq. (5.47). We start by considering the definition of the bHQET jet function:

$$\begin{aligned} J_B(\hat{s}_t, \Gamma_t, \mu) &= \left(\frac{-1}{4\pi N_C m}\right) \mathrm{Im}\left[i \int \mathrm{d}^4x \, e^{ir.x} \langle 0|\mathrm{T}\{\overline{h}_{v_t}(0) W_{n_t}(0) W_{n_t}^\dagger(x) h_{v_t}(x)\}|0\rangle \right] \\ &= \left(\frac{-1}{N_C m}\right) \mathrm{Im}\left[i \langle 0|\mathrm{T}\{\overline{h}_{v_t}(0) W_{n_t}(0)\, \delta(\hat{s}_t - 2v_t.\hat{p})\, (2\pi)^3 \delta^3(\hat{p}_\perp)\, W_{n_t}^\dagger(0) h_{v_t}(0)\}|0\rangle \right], \end{aligned} \tag{5.48}$$

where $\hat{s}_t = -2v_t.r$. We refer to the projections of the momentum operator $\hat{p}$ transverse to v_t as $\hat{p}_\perp$.

Analogous to the expression of Eq. (5.48) we can now write down the operator definition of the collinear soft function:

$$S_C(l^+, Q, z_{\mathrm{cut}}, \beta) \equiv \frac{1}{N_C} \mathrm{tr} \langle 0|\mathrm{T}\{X_{n_t}^\dagger V_{n_t}\} \delta\big(l^+ - (1 - \hat{\Theta}_{\mathrm{SD}}^{cs})\, n.\hat{p}^{cs}\big) \overline{\mathrm{T}}\{V_{n_t}^\dagger X_{n_t}\}|0\rangle \,. \tag{5.49}$$

Here $\hat{\Theta}_{\mathrm{SD}}^{cs}$ denotes the soft drop grooming operator, which only acts on collinear-soft particles to apply the grooming algorithm. The factorization theorem for the soft drop jet mass for light quark jets was discussed in Ref. [51] and also involves the same function S_C, and further details can be found there, including and a perturbative calculation for this function. There it was demonstrated that the collinear-soft function depends only on single dimensionfull scale in a non-trivial manner. As a result z_{cut} entered the functional dependence of S_C only through a specific combination.

From Eq. (5.12) and Eq. (5.13) we have

$$p_{cs}^2 \sim \Gamma_t^2 \eta^2 = \left(\frac{m\Gamma_t}{Q}\right)^{\frac{2(1+\beta)}{2+\beta}} \left(2^\beta Q z_{\text{cut}}\right)^{\frac{2}{2+\beta}} . \tag{5.50}$$

From Eq. (5.58) we note that the soft function variable $l^+ \sim m\Gamma_t/Q$ which gives

$$p_{cs}^2 \sim \left(l^+\right)^{\frac{2(1+\beta)}{2+\beta}} \left(2^\beta Q z_{\text{cut}}\right)^{\frac{2}{2+\beta}} . \tag{5.51}$$

This is the single scale that appears in S_C and it involves the combination

$$Q_{\text{cut}} \equiv 2^\beta Q z_{\text{cut}} . \tag{5.52}$$

This implies that the arguments of S_C can be reduced from five down to three

$$S_C(l^+, Q, z_{\text{cut}}, \beta, \mu) = S_C\left(l^+, \frac{p_{cs}}{\mu}, \beta\right) = S_C\left(l^+, \frac{\left(l^+\right)^{\frac{1+\beta}{2+\beta}} Q_{\text{cut}}^{\frac{1}{2+\beta}}}{\mu}, \beta\right) \tag{5.53}$$

$$\equiv S_C(l^+, Q_{\text{cut}}, \beta, \mu) . \tag{5.54}$$

In the last line we define a four argument version of S_C for ease of presentation, since the three argument version involves powers of ℓ^+ and Q_{cut} that otherwise make the equations more messy. Our definition of S_C is equivalent to the definition of S_C in Ref. [51] for angularity $e_2^{(2)}$ by a change of variable given by

$$S_C(l^+, Q_{\text{cut}}, \beta, \mu) = \frac{4}{Q} S_C^{\text{Ref.[51]}}\left(e_2^{(2)} = \frac{4l^+}{Q}, Q_{\text{cut}}, \beta, \mu\right) . \tag{5.55}$$

In the case where a jet veto is applied so we have an exclusive top and anti-top jet cross section, then the global soft function S_G for $pp \to t\bar{t}$ can be factorized from the collinear modes in the beam region in a manner analogous to our analysis in the

ungroomed case. This gives

$$(S_G)_{IJ} = \sum_{X_s} \langle 0|(\overline{Y}^T_{n_a} \overline{T}_J Y_{n_b})^{ab} \, (\overline{Y}^T_{n_{\bar{t}}} \overline{T}_J Y_{n_t})^{cd} \, \hat{\delta}_{\rm G} |X_s\rangle \langle X_s| (Y^\dagger_{n_b} T_I Y^\star_{n_a})^{ba} \, (Y^\dagger_{n_t} T_I Y^\star_{n_{\bar{t}}})^{dc} |0\rangle \,, \tag{5.56}$$

where $\hat{\delta}_G$ is the measurement operator on the global soft function, which includes the soft-drop constraint on the top-jet, variables associated with the jet-veto, but importantly, does not depend on the jet mass M_J. The remaining fields inside Φ^I in this case would lead to beam functions and PDFs, much like our analysis of the ungroomed case.

To derive the factorization theorem, we first consider the momentum operator in bHQET$_+$ given by

$$\hat{p} = \hat{p}^{uc} + (1 - \hat{\Theta}^{cs}_{\rm SD}) \, \hat{p}^{cs} \,. \tag{5.57}$$

Hence for groomed jet mass we include the following measurement function in our cross section:

$$\begin{aligned} 1 &= \int \mathrm{d}\hat{s}_t \delta\Big(2v_t.\hat{p}^{uc} + (1 - \hat{\Theta}^{cs}_{\rm SD}) \, 2v_t.\hat{p}^{cs} - \hat{s}_t \Big) \\ &= \int \mathrm{d}\hat{s}_t \delta\Big(2v_t.\hat{p}^{uc} + \frac{Q}{m}(1 - \hat{\Theta}^{cs}_{\rm SD}) \, n.\hat{p}^{cs} - \hat{s}_t \Big) \\ &= \int \mathrm{d}\hat{s}_t \, \mathrm{d}l^+ \delta\Big(2v_t.\hat{p}^{uc} + \frac{Q}{m} l^+ - \hat{s}_t \Big) \, \delta\Big(l^+ - (1 - \hat{\Theta}^{cs}_{\rm SD}) \, n.\hat{p}^{cs} \Big) \,. \end{aligned} \tag{5.58}$$

In the last line the measurement operator has been factorized into terms that only act within the ultra-collinear and collinear-soft sectors. This allows us to obtain the factorization formula for top-jets at the stage where collinear-soft and ultra-collinear modes have been factorized,

$$\frac{\mathrm{d}\sigma}{\mathrm{d}M_t} = N(Q, m, z_{\rm cut}, \Phi_J) \int \mathrm{d}l^+ J_B\Big(\hat{s}_t - \frac{Q}{m} l^+, \, \Gamma_t, \, \delta m, \mu \Big) \, S_C(l^+, Q_{\rm cut}, \beta, \mu) \,, \tag{5.59}$$

where M_t is the mass of the top-jet after soft drop grooming, $\hat{s}_t = (M_t^2 - m^2)/m$, and

we have used a shorthand $\Phi_J = \{p_T, \eta\}$ for the top-jet kinematic variables. In this expression N is a normalization factor that includes the global soft function, PDFs, initial state radiation, as well as the dynamics of the $\bar{t}$ jet. It can be factorized further to calculate these contributions, following for example our analysis for ungroomed jets. For our numerical predictions we compute N using N-Jettiness with XCone or anti-k_T jets [109, 114, 108, 115, 32] and a loose jet-veto following Ref. [80]. We do not dwell on the details of this method since beyond capturing the Born p_T and η dependence of the top-jet our analysis our analysis of soft drop groomed jet mass spectra are quite insensitive to the choices made for this calculation of N.

This result in Eq. (5.59) does not yet contain the additional contribution from factorizing the non-perturbative modes. Although somewhat subtle, we will prove in Sec. 5.3.4 below that in both the high-p_T and decay situations discussed in Sec. 5.1.3 that considering these additional modes only adds to the result in Eq. (5.59) an extra convolution with a non-perturbative function F_C.

5.3.3 Summing Logarithms and Consistency

In this section we demonstrate independence of the cross section on various renormalization scales by deriving consistency relations for the SCET and bHQET$_+$ theory. We first start with rewriting Eq. (5.59) in position space.

$$\frac{\mathrm{d}\sigma}{\mathrm{d}\hat{s}_t} = N(\mu) \int \frac{\mathrm{d}y}{2\pi}\, e^{iy\hat{s}_t}\, \tilde{J}_B(y, \Gamma_t, \delta m, \mu)\, \tilde{S}_C\left(\frac{Q}{m}y, Q_{\mathrm{cut}}, \beta, \mu\right), \tag{5.60}$$

where we have used the Fourier transform

$$\tilde{f}(y,\mu) = \int \mathrm{d}k\, e^{-iky} f(k,\mu)\,. \tag{5.61}$$

We define the anomalous dimensions for each of the position space functions by

$$\mu\frac{\partial}{\partial\mu}\tilde{f}(y,\mu) = \tilde{\gamma}_f\, \tilde{f}(y,\mu)\,, \tag{5.62}$$

noting that in position space the RG equation is multiplicative. Taking derivative with respect to μ on both sides of Eq. (5.60), and using the fact that the cross section is μ independent, we have

$$\gamma_N\left(\frac{Q}{m}, z_{\rm cut}, \beta\right) + \tilde{\gamma}_B(y) + \tilde{\gamma}_{S_C}\left(\frac{Q}{m}y, Q_{\rm cut}\right) = 0\,. \tag{5.63}$$

Here $\tilde{\gamma}_i$ are the anomalous dimensions in position space. We notice that the three terms have different dependence on the variables y, $z_{\rm cut}$, β, and Q/m. Here γ_N is given by

$$\gamma_N = \frac{1}{2}\gamma_{H_m} + \frac{1}{2}\gamma_{S_G} \tag{5.64}$$

where γ_{H_m} is given by anomalous dimension of the matching coefficient H_m defined in Eq. (4.50). γ_{S_G} corresponds to anomalous dimension of global soft function defined in Eq. (5.56). The factor of $1/2$ takes into account the contribution to the top jet only, and not the anti-top. We demand that

1. the y dependence cancels between $\tilde{\gamma}_B$ and $\tilde{\gamma}_{S_C}$,

2. the $z_{\rm cut}$ and β dependence cancels between γ_N and $\tilde{\gamma}_{S_C}$, and

3. the Q/m dependence cancels between γ_N and $\tilde{\gamma}_{S_C}$.

Furthermore, there is at most a single logarithm in the anomalous dimensions with a universal coefficient proportional to the cusp anomalous dimension $\Gamma^{\rm cusp} = \Gamma^{\rm cusp}(\alpha_s)$, which up to NLL order for a quark is given by

$$\Gamma^{\rm cusp} = 4C_F\left(\frac{\alpha_s}{4\pi}\right) + 4C_F\left[\left(\frac{67}{9} - \frac{\pi^2}{3}C_A - \frac{20}{9}T_F n_f\right]\left(\frac{\alpha_s}{4\pi}\right)^2. \tag{5.65}$$

The full anomalous dimensions needed for the resummation of large logarithms at NLL order are as follows:

$$\gamma_{H_m} = -2\,\Gamma^{\rm cusp}\ln\left(\frac{m^2}{Q^2}\right) + (-8C_F)\left(\frac{\alpha_s}{4\pi}\right), \tag{5.66}$$

$$\gamma_{S_G} = \frac{2\,\Gamma^{\rm cusp}}{1+\beta}\ln\left(\frac{\mu^2}{Q_{\rm cut}^2}\right),$$
$$\tilde{\gamma}_B(y) = \Gamma^{\rm cusp}\ln\left((ie^{\gamma_E}y)^2\mu^2\right) + (4C_F)\left(\frac{\alpha_s}{4\pi}\right),$$
$$\tilde{\gamma}_{S_C} = -\Gamma^{\rm cusp}\frac{2+\beta}{1+\beta}\ln\left(\left(iye^{\gamma_E}\right)^{\frac{2(1+\beta)}{2+\beta}}\frac{\mu^2}{Q_{\rm cut}^{\frac{2}{2+\beta}}}\right).$$

Adding $\tilde{\gamma}_B$ and $\tilde{\gamma}_{S_C}$ we have

$$\begin{aligned}\tilde{\gamma}_B(y) + \tilde{\gamma}_{S_C}(y) &= (4C_F)\left(\frac{\alpha_s}{4\pi}\right) - \Gamma^{\rm cusp}\left[\ln\left(\frac{Q^2}{m^2}\right) + \frac{1}{1+\beta}\ln\left(\frac{\mu^2}{Q_{\rm cut}^2}\right)\right] \\ &= -\frac{1}{2}\gamma_{H_m} - \gamma_{S_G}\,.\end{aligned} \tag{5.67}$$

These consistency equations tie together the logarithms obtained by considering the renormalization group evolution of the various functions. We employ standard techniques to solve the RGE equations in momentum space when carrying out the resummation to NLL in order to make predictions using our soft drop factorization theorems.

5.3.4 Factorized Contributions from Non Perturbative Modes

We now consider the non-perturbative corrections to the factorized cross section. Once again the effect of these contributions can be derived by considering the interactions between the dominant non-perturbative modes identified in Secs. 5.1.2 and 5.1.3 and the other modes in the analysis. For the jet mass measurement, the smallest ratio of scales occurs between the non-perturbative modes and the mode of next smallest invariant mass, which are the soft-collinear modes. Therefore we expect to find a convolution between a non-perturbative function and the collinear-soft function, much like the convolution with the ultras=soft function in the ungroomed case. The treatment is, however, more complex here than above. We notice that the soft modes, as well as the non perturbative modes, do not have a simple homogeneous scaling, rather collinear scaling as shown in Eq. (5.22). This complicates the form of the convolution of the perturbative and the non perturbative parts. We also ob-

served in Sec. 5.1.2 that we have two possibilities of non-perturbative modes given by Figs. 5-3 and 5-4; we referred to these two cases as the "high-p_T" and "decay" case. These two cases must be considered separately.

We first consider the "high-p_T" case. In this case the non-perturbative modes can be considered as part of the collinear-soft modes, which must simply be refactorized in order to separate perturbative and non-perturbative components. From Eq. (5.25) we observe that the dominant non-perturbative momenta have

$$n_t \cdot p_\Lambda = Q_{\text{cut}}^{\frac{-1}{1+\beta}} \, k^{\frac{2+\beta}{1+\beta}} \,, \tag{5.68}$$

with $k \sim \Lambda_{\text{QCD}}$. After employing rescaling identities we can remove all dependence on Q_{cut} from the soft-drop groomed non-perturbative function F_C, so that it is only a function $F_C = F_C(k, \beta)$ with mass dimension -1. This allows us to factorize the collinear-soft function as

$$S_C(l^+, Q_{\text{cut}}, \beta, \mu) = \int \mathrm{d}k \; S_C^{\text{part}}\left(l^+ - k\left(\frac{k}{Q_{\text{cut}}}\right)^{\frac{1}{1+\beta}}, Q_{\text{cut}}, \beta, \mu\right) F_C(k, \beta) \,, \tag{5.69}$$

where we have used the notation defined in Eq. (5.53). Here F_C has similar properties as the model function considered for ungroomed top jets with $k \sim \Lambda_{\text{QCD}}$. In particular its dominant support is in the non-perturbative region, all of its moments are given by well defined field theory matrix elements, and it has a tail at large k that falls off faster than any power. However, we observe through the form of the convolution in Eq. (5.69) that the non-perturbative corrections are suppressed by an additional factor of $(\frac{k}{Q_{\text{cut}}})^{\frac{1}{1+\beta}}$. The β dependence in F_C reminds us that contribution of non-perturbative radiation to the groomed jet is dependent on the aggressiveness of soft drop groomer. Furthermore, there is no z_{cut} dependence we have factored out z_{cut} through Q_{cut} in Eq. (5.68). We can thus write down the final "high-p_T" factorization theorem for soft drop groomed tops by incorporating Eq. (5.69) into Eq. (5.59):

$$\frac{\mathrm{d}\sigma^{\text{high}\, p_T}}{\mathrm{d}\hat{s}_t} = N(Q, m, z_{\text{cut}}, \Phi_J) \int \mathrm{d}l^+ J_B\left(\hat{s}_t - \frac{Q}{m} l^+, \, \Gamma_t, \, \delta m, \, \mu\right)$$

$$\times \int \mathrm{d}k\, S_C^{\mathrm{part}}\left(l^+ - k\left(\frac{k}{Q_{\mathrm{cut}}}\right)^{\frac{1}{1+\beta}}, Q_{\mathrm{cut}}, \beta, \mu\right) F_C(k,\beta)\,. \tag{5.70}$$

Note that the moments of this non-perturbative functions are β dependent:

$$\Omega_1^{(\beta)} = \int \mathrm{d}k\, F_C(k,\beta)\,, \qquad x_2^{(\beta)} = \frac{\Omega_2^{(\beta)} - \left(\Omega_1^{(\beta)}\right)^2}{\left(\Omega_1^{(\beta)}\right)^2}\,. \tag{5.71}$$

To see this consider the action of the soft drop grooming operator Θ_{SD} on an emission i with scaling of the "high-p_T" non-perturbative mode given in Eq. (5.25):

$$\Theta_{\mathrm{SD}}^{\Lambda\,\mathrm{high}\,p_T} = \theta(z - z_{\mathrm{cut}}\theta_i^\beta) = \theta\left(\frac{p_i^-}{Q} - z_{\mathrm{cut}}\left(\frac{2\,p_{i\perp}}{p_i^-}\right)^\beta\right) \tag{5.72}$$

$$= \theta\Big((p_i^-)^{1+\beta} - Q_{\mathrm{cut}}\, p_{i\perp}^\beta\Big)\,. \tag{5.73}$$

We now rescale the components of p_i^μ as

$$p_i^+ = Q_{\mathrm{cut}}^{\frac{-1}{2+\beta}}\,(k^+)^{\frac{2+\beta}{1+\beta}}\,, \qquad p_i^- = Q_{\mathrm{cut}}^{\frac{1}{2+\beta}}\,k^{\frac{\beta}{1+\beta}}\,, \qquad p_{i\perp} = k_\perp\,. \tag{5.74}$$

From Eq. (5.25) it follows that k scales as ultrasoft mode: $k^\mu \sim \Lambda_{\mathrm{QCD}}(1,1,1)$, as required by the argument of F_C. This gives

$$\Theta_{\mathrm{SD}}^{\Lambda\,\mathrm{high}\,p_T} = \theta\Big(Q_{\mathrm{cut}}\,(k^-)^\beta - Q_{\mathrm{cut}}\,k_\perp^\beta\Big) = \theta\left(1 - \left(\frac{k_\perp}{k^-}\right)^\beta\right)\,. \tag{5.75}$$

Next we turn to the non-perturbative modes for the decay case. From Eq. (5.27) we can write analog of Eq. (5.68) for the decay case as

$$n_t\,.\,p_\Lambda = \frac{m}{Q}\,h\left(\Phi_d, \frac{m}{Q}\right)k\,, \qquad k \sim \Lambda_{\mathrm{QCD}}\,. \tag{5.76}$$

Here we have made the functional dependence of h on Φ_d, the phase space distribution of the top-decay products, and the top quark boost, explicit. This leads to the

following form for the soft model convolution:

$$S_C(l^+, Q_{\rm cut}, \beta, \mu) = \int \mathrm{d}k\, S_C^{\rm part}\left(l^+ - \frac{mk}{Q} h\left(\Phi_d, \frac{m}{Q}\right), Q_{\rm cut}, \beta, \mu\right) F_C(k, 1)\,. \quad (5.77)$$

Here the model function for the "decay" case is independent of β and the same as that of the "high-p_T", for $\beta = 1$. In the "decay" case, the groomer stops at the angle θ_d defined in Eq. (5.21), as a result of which all the particles with angles less than θ_d are kept. Hence $\Theta_{\rm SD}$ is simply given by

$$\Theta_{\rm SD}^{\Lambda\,\rm decay} = \theta(\theta_d - \theta_i) = \theta\left(\frac{2mh}{Q} - \frac{2\,p_{i\perp}}{p_i^-}\right). \quad (5.78)$$

Here we use Eq. (5.30) to rescale the components as follows

$$p_i^+ = \frac{Q}{mh}\, k^+\,, \qquad p_i^- = \frac{mh}{Q}\, k^-\,, \qquad p_{i\perp} = k_\perp\,, \quad (5.79)$$

which gives

$$\Theta_{\rm SD}^{\Lambda\,\rm decay} = \theta\left(\frac{2mh}{Q} - \frac{2mh}{Q}\,\frac{k_\perp}{k^-}\right) = \theta\left(1 - \frac{k_\perp}{k^-}\right) = \Theta_{\rm SD}^{\Lambda\,\rm high\,p_T}(\beta = 1)\,. \quad (5.80)$$

This shows that the action of the soft drop groomer on non-perturbative modes for the decay case is the same as that of high-p_T case with $\beta = 1$, hence they keep the same set of particles and are described by the same non-perturbative function. We also see that in the decay case there is no β dependence in the non-perturbative function, so the β dependence of the cross section is perturbatively calculable.

Since our jet mass measurement is inclusive over the decay products we must now explicitly integrate over Φ_d. This means that we need to resolve the Breit Wigner inside the ultra-collinear function to include the angluar cross-section of the top decay products. This subtlety was ignored when we originally arrived at Eq. (5.59). We start by considering the fact that the unstable top jet function $J_B(\hat{s}_t, \Gamma_t, \delta m, \mu)$ and

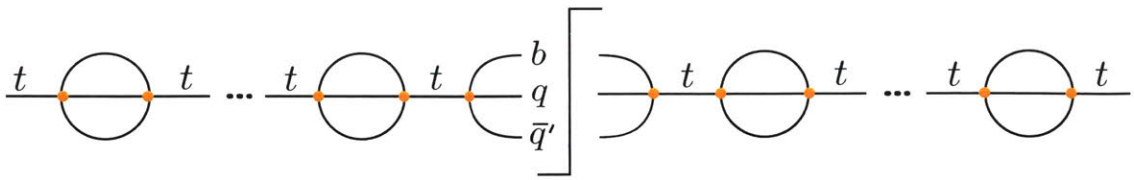

Figure 5-10: Bubble chain for an unstable top quark leading to a Breit-Wigner together with a differential distribution for the top decay products. From the closed two-loop bubble calculation involving $bq\bar{q}'$ only the imaginary top width term is kept.

stable top jet function $J_{B_t}^{\Gamma_t=0}(\hat{s}_t, \delta m, \mu)$ by [50]

$$J_{B_t}(\hat{s}_t, \Gamma_t, \delta m, \mu) = \int_{-\infty}^{\hat{s}_t} \mathrm{d}\hat{s}'_t \; J_{B_t}^{\Gamma_t=0}(\hat{s}_t, \delta m, \mu) \frac{\Gamma_t}{\pi\big(\hat{s}_t'^2 + \Gamma_t^2\big)} \,. \tag{5.81}$$

To include the angluar distribution of the top decay products we define a top-decay resolved jet function:

$$J_{D_t}\left(\hat{s}_t, \Phi_d, \frac{m}{Q}, \delta m, \mu\right) = \int_{-\infty}^{\hat{s}_t} \mathrm{d}\hat{s}'_t \; J_{B_t}^{\Gamma_t=0}(\hat{s}_t - \hat{s}'_t, \delta m, \mu) D_t\left(\hat{s}'_t, \Phi_d, \frac{m}{Q}\right) . \tag{5.82}$$

Here $D_t(\hat{s}', \Phi_d, m_t/Q)$ encodes the angular cross-section of the top-decay products, which can be considered to be a perturbative calculation carried out at a scale $\sim m$, and thus in the hard region. The presence of these boosted colored decay products does not change the nature of the decoupling of the collinear-soft or global soft modes from this jet function, they are still eikonal Wilson lines in the same directions since they only see the total color channel of the decay products, and are independent of the normalization of the light-like vectors on which they depend. By consistency the μ dependence of J_{D_t} is the same as that for J_{B_t} and hence is described by the stable top quark jet function.

The calculation of D_t at lowest order requires a geometric sum of decay product bubbles, where one hadronically decaying bubble is cut, shown in Fig. 5-10. In the non-cut bubbles we just keep Γ_t yielding the resonant contribution

$$D_t\Big(\hat{s}'_t, \Phi_d, \frac{m_t}{Q}\Big) = \frac{\Gamma_t}{\pi(\hat{s}_t'^2 + \Gamma_t^2)} \; d_t\Big(\Phi_d, \frac{m_t}{Q}\Big) \; \Big[1 + \mathcal{O}\Big(\frac{\hat{s}'_t}{m_t}\Big)\Big] \,, \tag{5.83}$$

where $d_t(\Phi_d, m_t/Q)$ is the angular dependence of the top-decay with $\int \Phi_d \, d_t(\Phi_d, m_t/Q) = 1$. For the calculation of d_t we can set $\hat{s}'_t = 0$, leading to the factorized structure in Eq. (5.83). We calculate d_t exactly below in Sec. 5.3.5. Integrating over the decay products phase space Φ_d gives back the unstable top jet function:

$$J_{B_t}(\hat{s}_t, \Gamma_t, \delta m, \mu) = \int \mathrm{d}\Phi_d \, J_{D_t}\left(\hat{s}_t, \Phi_d, \frac{m}{Q}, \delta m, \mu\right). \tag{5.84}$$

We do remark that there may be non-trivial finite perturbative $\mathcal{O}(\alpha_s)$ corrections from gluons that are exchanged between the top-quark and its decay products, but these can still be computed with $\hat{s}'_t = 0$, so Eq. (5.83) remains valid. These corrections are therefore only expected to modify d_t in a calculable way and hence not change the structure of the factorization theorem.

We are now in a position to write down the factorization theorem for the "decay" case:

$$\begin{aligned}
\frac{\mathrm{d}\sigma^{\text{decay}}}{\mathrm{d}\hat{s}_t} &= N(Q, m, z_{\text{cut}}, \Phi_J) \int \mathrm{d}l^+ \int \mathrm{d}\Phi_d \int \mathrm{d}\hat{s}'_t \, D_t\Big(\hat{s}'_t, \Phi_d, \frac{m}{Q}\Big) \, J_{B_t}^{\Gamma_t=0}\Big(\hat{s}_t - \hat{s}'_t - \frac{Q}{m} l^+, \, \mu\Big) \\
&\quad \times \int \mathrm{d}k \, S_C^{\text{part}}\left(l^+ - \frac{mk}{Q} h\Big(\Phi_d, \frac{m}{Q}\Big), Q_{\text{cut}}, \beta, \mu\right) F_C(k, 1) \\
&= N(Q, m, z_{\text{cut}}, \Phi_J) \int \mathrm{d}l^+ \int \mathrm{d}\Phi_d \, d_t\Big(\Phi_d, \frac{m}{Q}\Big) \, J_{B_t}\Big(\hat{s}_t - \frac{Q}{m} l^+, \, \Gamma_t, \, \mu\Big) \\
&\quad \times \int \mathrm{d}k \, S_C^{\text{part}}\left(l^+ - \frac{mk}{Q} h\Big(\Phi_d, \frac{m}{Q}\Big), Q_{\text{cut}}, \beta, \mu\right) F_C(k, 1) \,,
\end{aligned} \tag{5.85}$$

where we have used Eqs. (5.81) and (5.83) to recover the stable top jet function. We can further simplify Eq. (5.85) by rescaling the arguement of the non-perturbative function through

$$k' = k \, h\Big(\Phi_d, \frac{m}{Q}\Big), \tag{5.86}$$

in order to absorb all the dependence on decay-products variables. After this change of variable the Φ_d integration only acts on the non-perturbative function, convolving

it with the perturbatively calculable functions d_t and h to give

$$\tilde{F}_C\Big(k', 1, \frac{m}{Q}\Big) = \int d\Phi_d \, \frac{d_t\Big(\Phi_d, \frac{m}{Q}\Big)}{h(\Phi_d, \frac{m}{Q})} F_C\Big(\frac{k'}{h(\Phi_d, \frac{m}{Q})}, 1\Big) \,, \qquad . \tag{5.87}$$

This allows us to write

$$\begin{aligned} \frac{\mathrm{d}\sigma^{\text{decay}}}{\mathrm{d}M_t} &= N(Q, m, z_{\text{cut}}, \Phi_J) \int \mathrm{d}l^+ J_B\Big(\hat{s}_t - \frac{Q}{m} l^+, \, \Gamma_t, \, \delta m, \, \mu\Big) \\ &\quad \times \int \mathrm{d}k' \, S_C^{\text{part}}\Big(l^+ - \frac{mk'}{Q}, Q_{\text{cut}}, \beta, \mu\Big) \, \tilde{F}_C\Big(k', 1, \frac{m}{Q}\Big) \end{aligned} \tag{5.88}$$

here the m_t/Q prefactor pulls out the dominant dependence on the boost. It cancels out the Q/m_t boost factor in the argument of J_B, which largely eliminates the Q dependence of the peak position observed in the ungroomed case. If we take the n-th moment then

$$\Omega_n^{(1)\text{eff}} = \int dk' \, k'^n \tilde{F}_C\Big(k', 1, \frac{m}{Q}\Big) = \Big[\int d\Phi_d \, d_t\Big(\Phi_d, \frac{m}{Q}\Big) h^n\Big(\Phi_d, \frac{m}{Q}\Big)\Big] \, \Omega_n^{(1)} \equiv \langle h^n \rangle \, \Omega_n^{(1)} \,, \tag{5.89}$$

so the $\langle h^n \rangle$ causes the effective moments to only have residual m_t/Q dependence. We implement Eq. (5.87) by computing $\langle h \rangle$ and $\langle h^2 \rangle$ exactly and using the resulting $\Omega_1^{(1)\text{eff}}$ and $\Omega_2^{(1)\text{eff}}$ to specify the function $\tilde{F}_C$. The fundamental non-perturbative parameters are still the $\Omega_n^{(1)}$ for the decay factorization theorem.

The exact form of F_C for our implementation for either the high-p_T or decay groomed top jet factorization is given in Sec. 5.5.1 below. It can be determined by fitting its first few moments defined by

$$\Omega_n^{(\beta)} = \int \mathrm{d}k \, k^n F_C(k, \beta) \,. \tag{5.90}$$

Once again the first moment $\Omega_1^{(\beta)}$ is the most important parameter as it determines the dimensional scale in this function. There is no reason to expect that this parameter is insensitive to β and indeed we find some evidence that the β dependence is significant.

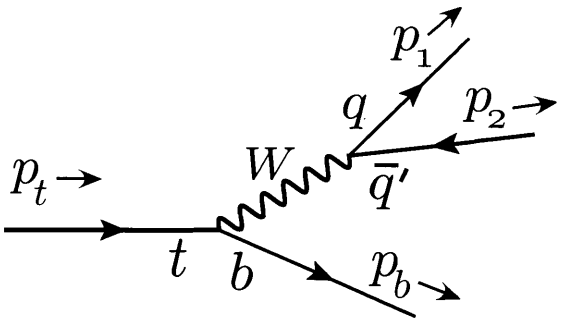

Figure 5-11: Top quark decay to three quarks, showing the notation used for their four-momenta.

The other parameter we keep in our analysis is related to the second moment, defined again with a dimensionless ratio

$$x_2^{(\beta)} = \frac{\Omega_2^{(\beta)} - \Omega_1^{(\beta)\,2}}{\Omega_1^{(\beta)\,2}}\,. \tag{5.91}$$

We explore the dependence of the soft drop cross section on $\Omega_1^{(\beta)}$ and $x_2^{(\beta)}$ in detail in Sec. 5.5.2.

5.3.5 Angular Distribution of Decay Products

We now have two different factorization formulas in Eqs. (5.70) and (5.88) that differ in their treatment of non-perturbative corrections. The choice between one or the other at a given p_T is dependent on the distribution of top decay products and is given by the condition in Eq. (5.28). In this section we calculate the functions $d_t(\Phi_d, m/Q)$ and $h(\Phi_d, m/Q)$, and then use the results to further explore the question of the regions where each of the decay and high-p_T factorization theorems are appropriate.

We perform the calculation of h using variables defined in the rest frame of top quark, and then apply a boost in the top jet direction to obtain the result in the pp center of mass frame. We start by simplifying the form of the phase space integration for the three body top decay shown in Fig. 5-11, using momenta for the quarks q, $\bar{q}'$,

and b as p_1, p_2, and p_b, respectively. The phase space integration measure is given by

$$\mathrm{PS} \equiv \int \mathrm{d}\Phi_d = \int \frac{\mathrm{d}^3 p_1}{(2\pi)^3 E_1} \int \frac{\mathrm{d}^3 p_2}{(2\pi)^3 E_2} \int \frac{\mathrm{d}^3 p_b}{(2\pi)^3 E_b} (2\pi)^4 \, \delta^{(4)}\left(p_t - p_1 - p_2 - p_b\right) . \tag{5.92}$$

Out of these nine variables for the momenta of three onshell particles, only five of them are independent after using the momentum conserving δ-function. Our choice of independent rest frame variables are as follows:

$$x_1 = \frac{2E_1}{mt} , \qquad \theta_1 , \qquad \theta_2 , \qquad \phi_S = \phi_1 + \phi_2 , \qquad \Delta\phi = \phi_1 - \phi_2 , \tag{5.93}$$

where θ_i and ϕ_i are the angles with the z axis and azimuthal angles in the rest frame of top quark. The angles in the boosted frame can be expressed in terms of these variables:

$$\tilde{\theta}_{1t} = \theta_{1t}\left(\frac{m}{Q}, \theta_1\right) , \qquad \tilde{\theta}_{2t} = \tilde{\theta}_{2t}\left(\frac{m}{Q}, \theta_2\right) , \qquad \tilde{\theta}_{bt} = \tilde{\theta}_{bt}\left(\frac{m}{Q}, \theta_1, \theta_2, \Delta\phi\right) . \tag{5.94}$$

Here $\tilde{\theta}_{it}$ refers to angle of the decay product i with respect to the top direction in the pp center-of-mass (or lab) frame. Thus in terms of these angles, the angle θ_d is defined as

$$\theta_d\left(\frac{m}{Q}, \theta_1, \theta_2, \Delta\phi\right) = \max(\tilde{\theta}_{it}, \tilde{\theta}_{jt}) , \qquad \tilde{\theta}_{ij} = \max(\tilde{\theta}_{12}, \tilde{\theta}_{1b}, \tilde{\theta}_{2b}) , \tag{5.95}$$

where the second condition determines the pair $ij = 12$, $1b$, or $2b$ that stops the groomer. We further note that due to the rotational symmetry about the boost axis ϕ_S is a cyclic coordinate and can be integrated over. Hence, expressed in the four remaining variables, the PS simplifies to

$$\begin{aligned} \mathrm{PS} = \frac{m_t^2}{64\pi^3} \int_{-1}^{1} \frac{\mathrm{d}\cos(\theta_1)}{4\pi} \int_{-1}^{1} \frac{\mathrm{d}\cos(\theta_2)}{4\pi} \int_0^{2\pi} \frac{\mathrm{d}\Delta\phi}{2\pi} \int_0^1 \mathrm{d}x_1 \\ \times \left(2 - \frac{\Delta\phi}{\pi}\right) \frac{2x_1(1-x_1)}{\Big[2 - x_1\Sigma(\theta_1, \theta_2, \Delta\phi)\Big]^2} , \end{aligned} \tag{5.96}$$

where

$$\Sigma(\theta_1, \theta_2, \Delta\phi) = 1 - \cos(\theta_{12}) = \big(1 - \cos(\theta_1)\cos(\theta_2) - \cos(\Delta\phi)\sin(\theta_1)\sin(\theta_2)\big)\,, \tag{5.97}$$

where θ_{12} is the angle between q_1 and $\bar{q}_2$. To ensure the top decay products lie in the jet of radius R we define a restricted PS with this constraint:

$$\begin{aligned}
\mathrm{PS}_R &\equiv \int \mathrm{d}\Phi_d^R = \int \mathrm{d}\Phi_d\, \theta\Big(R - \theta_d\Big(\frac{m}{Q}, \theta_1, \theta_2, \Delta\phi\Big)\Big) \\
&= \frac{m_t}{64\pi^3}\int_{-1}^{1}\frac{\mathrm{d}\cos(\theta_1)}{4\pi}\int_{-1}^{1}\frac{\mathrm{d}\cos(\theta_2)}{4\pi}\int_0^{2\pi}\frac{\mathrm{d}\Delta\phi}{2\pi}\int_0^1 \mathrm{d}x_1\,\theta\Big(R - \theta_d\Big(\frac{m}{Q}, \theta_1, \theta_2, \Delta\phi\Big)\Big) \\
&\quad \Big(2 - \frac{\Delta\phi}{\pi}\Big)\,\frac{2x_1(1-x_1)}{\Big[2 - x_1\Sigma(\theta_1, \theta_2, \Delta\phi)\Big]^2}\,.
\end{aligned} \tag{5.98}$$

This modified phase space is used both to calculate the moments $\langle h^n \rangle$ and to normalize d_t.

Now we state the result for $d_t(\Phi_d, m_t/Q)$ that is given by the resonant contribution of the bubble chain shown in Fig. 5-10:

$$d_t = \mathcal{N}_d \frac{p_2 \cdot p_t\, p_1 \cdot p_b}{\Big[\big(2\,p_1 \cdot p_2 - m_W^2\big)^2 + m_W^2\Gamma_W^2\big)\Big]}\,, \tag{5.99}$$

where $\mathcal{N}_d$ is a constant that fixes the normalization of d_t. We define

$$\tilde{s}(x_1, \theta_{12}) = 2\,p_1 \cdot p_2 = \frac{m_t^2 x_1(1-x_1)\Sigma(\theta_{12})}{2 - x_1\Sigma(\theta_{12})}\,, \tag{5.100}$$

which gives

$$d_t(x_1, \theta_{12}) = \frac{\mathcal{N}_d}{4}\frac{\big(x_1 - \tilde{s}\big)\big(1 - x_1 + \tilde{s}\big)}{\big[(\tilde{s} - \frac{m_W^2}{m^2})^2 + \frac{m_W^2\Gamma_W^2}{m^4}\big]}\,. \tag{5.101}$$

This now allows us to determine

$$\langle h^n \rangle = \int d\Phi_d^R\, d_t\Big(\Phi_d, \frac{m}{Q}\Big) h^n\Big(\Phi_d, \frac{m}{Q}\Big)$$

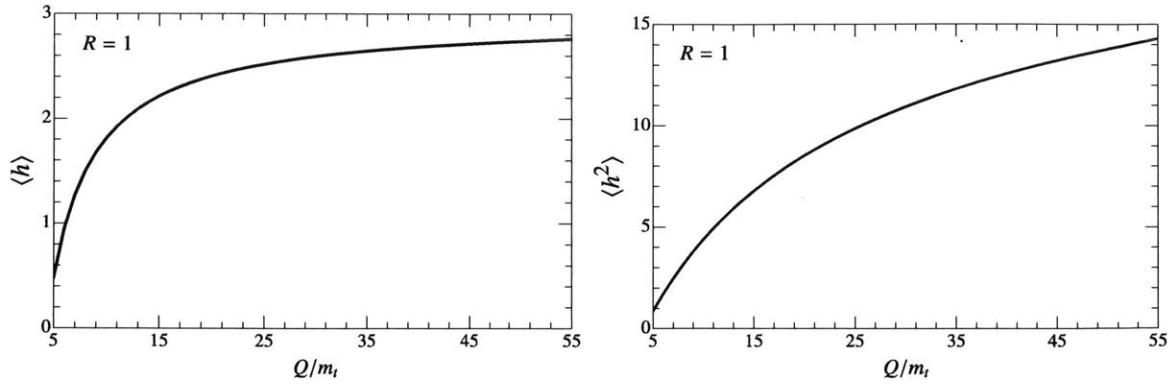

Figure 5-12: Here we show results for our calculation of $\langle h \rangle$ and $\langle h^2 \rangle$ as a function of the boost factor Q/m. Recalling that $Q = 2p_T \cosh(\eta)$, and to include also non-trivial rapidities, we show these results over an extended range.

$$= \frac{m_t^2}{64\pi^3} \int_{-1}^{1} \frac{\mathrm{d}\cos(\theta_1)}{4\pi} \int_{-1}^{1} \frac{\mathrm{d}\cos(\theta_2)}{4\pi} \int_0^{2\pi} \frac{\mathrm{d}\Delta\phi}{2\pi} \int_0^1 \mathrm{d}x_1 \, \theta\Big(R - \theta_d\Big(\frac{m}{Q}, \theta_1, \theta_2, \Delta\phi\Big)\Big) \Big(2 - \frac{\Delta\phi}{\pi}\Big) \frac{2x_1(1-x_1)}{\Big[2 - x_1\Sigma(\theta_{12})\Big]^2} d_t(x_1, \theta_{12}) \, \tan^n\left(\frac{1}{2}\theta_d\Big(\frac{m}{Q}, \theta_1, \theta_2, \Delta\phi\Big)\right) . \tag{5.102}$$

We compute the integrals in Eq. (5.102) with a Monte Carlo technique to obtain the result as a function of m/Q. In carrying out this analysis we fix the ratio m_W/m. The results for $\langle h \rangle$ and $\langle h^2 \rangle$ can be very well described by the ratio of two polynomials, leading to the following numerical fit results:

$$\langle h \rangle = \frac{17.05 \; - \; 3.96 \, Q/m_t}{1 \; - \; 1.34 \, Q/m_t} , \qquad \langle h^2 \rangle = \frac{-4.94 \; + \; 1.21 \, Q/m_t}{1 \; + \; 0.06 \, Q/m_t} , \tag{5.103}$$

where $Q = 2p_T \cosh(\eta_t)$. We show the actual numerical results for $\langle h \rangle$ and $\langle h^2 \rangle$ as a function of p_T with $\eta_t = 0$ in Fig. 5-12, where the red dots are exact calculations and the black solid lines are the fitting curves. We notice that $\langle h \rangle$ saturates to about 2.5 for high p_T, and $h \simeq 2$ for our dominant region of interest.

To determine which regime for non-perturbative corrections is dominant at a given p_T we compare the p_Λ^+ component of the modes for the high-p_T and decay cases in Fig. 5-13. Using our result for $\langle h \rangle$, Eqs. (5.68) and (5.76), and setting $\eta_t = 0$, $\beta = 2$,

and $z_{\rm cut} = 0.01$, we have

$$p^{+}_{\Lambda\,\text{high}p_T}(k,\, p_T;\, \beta = 2,\, z_{\rm cut} = 0.01,\, \eta_t = 0) = 2.3\, k \left(\frac{k}{p_T}\right)^{\frac{1}{3}}$$
$$p^{+}_{\Lambda\,\text{decay}}(k,\, p_T;\, \eta_t = 0) = \frac{(86.5\,\text{GeV})}{p_T}\, k\, \langle h \rangle (p_T/m)\,, \tag{5.104}$$

where k sets the scale for non-perturbative corrections. In the first figure we show the comparison where we set k in both the formulas to have the same value of 0.5 GeV. We observe from this plot that the two modes have similar contribution to the non-perturbative peak region for the range of p_T's of interest where constraints explored in Sec. 5.2 allow application of soft drop grooming. However, the comparison between the two cases is not straightforward since the non-perturbative functions are different, and hence there is no reason to take the same k in both formulas. For example, if we take $k_{\rm decay} = 2\, k_{\text{high}\,p_T} = 2$ GeV, then we get the result shown in the second figure, and here the "decay" factorization dominates. We will see later in our analysis of simulation data that both formulas actually work quite well, agreeing with PYTHIA8, and hence are both giving an accurate and fairly similar description of the physics in the regime of p_T that we explore. We do find that the "decay" factorization theorem generically gives smaller χ^2 values in our simple fits, and describes the p_T dependence of PYTHIA8 a bit better than the high-p_T factorization theorem. We will see that the fits to PYTHIA8 also supports the relation $k_{\rm decay} \sim 2\, k_{\text{high}\,p_T}$ at the level of the corresponding first moment parameters $\Omega_1^{(1)}$ and $\Omega_1^{(2)}$, which are obtained from the fits for $\beta = 2$.

5.4 PYTHIA Studies

In this section we explore various predictions of the peak region boosted soft-dropped top-jet factorization theorems by using Monte Carlo event simulation. This includes both exploring cases where the factorization theorems imply that the spectrum should be insensitive to certain variables, and cases where the factorization theorem's power counting and physical picture allow us to predict how the spectrum should behaves

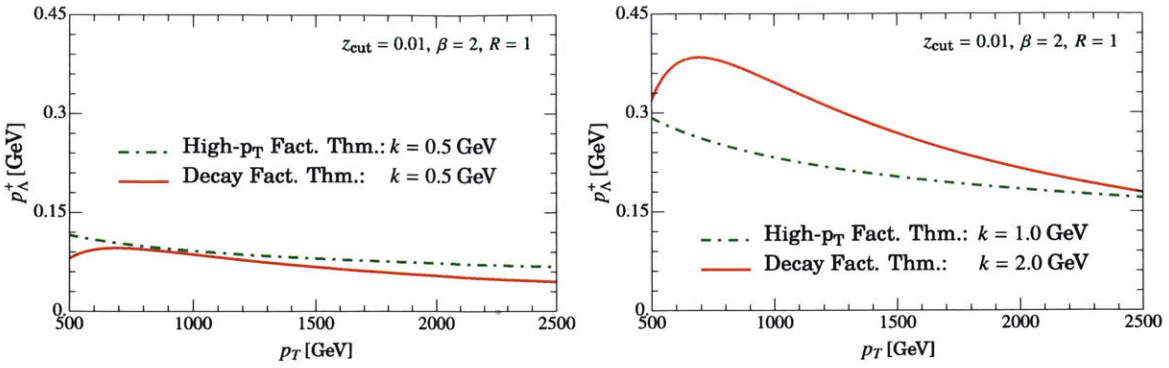

Figure 5-13: We compare p_Λ^+ for the two cases of non-perturbative corrections. In the first one we have $p^+_{\Lambda\,\mathrm{decay}} = p^+_{\Lambda\,\mathrm{high}p_T} = 0.5$ GeV. The second case we take $p^+_{\Lambda\,\mathrm{decay}} = 2p^+_{\Lambda\,\mathrm{high}p_T} = 2$ GeV

when changing certain variables.

For this analysis we generate events using PYTHIA 8.219 with a fixed input mass of $m_t^{\mathrm{MC}} = 173.1\,\mathrm{GeV}$ and by default both hadronization and MPI turned on with the default tune. As a default we also take jets in the bin $p_T \geq 750\,\mathrm{GeV}$, $|\eta| < 2.5$. The jet bins are determined from the partonic top momentum in PYTHIA to speed up the event generation. (We have confirmed that these variables are very close to the corresponding jet p_T and η, such that the difference for determining the events in our p_T and η bins is negligible for our analyses.) The jets are determined by the XCone algorithm with radius $R = 1$, and then the active t or $\bar{t}$ being considered is groomed with soft drop parameters $z_{\mathrm{cut}} = 0.01$ and $\beta = 2$. In addition as a default we take a very loose jet-veto of $p_T^{\mathrm{veto}} = 200\,\mathrm{GeV}$ which retains about 85% of the events. By default we always consider M_J spectra that are normalized over the full M_J range shown in the plot, unless otherwise noted. In our description of the plots we will for simplicity always refer to the M_J spectra as being obtained from the top quark jet, though in practice we obtain these spectra by independently combining results from both the top quark jets and anti-top jets in the events.

5.4.1 z_{cut} and β dependence

We start by considering the dependence on the soft drop parameters z_{cut} and β. Due to the constraints discussed above in Sec. 5.2 the factorization theorem is only valid

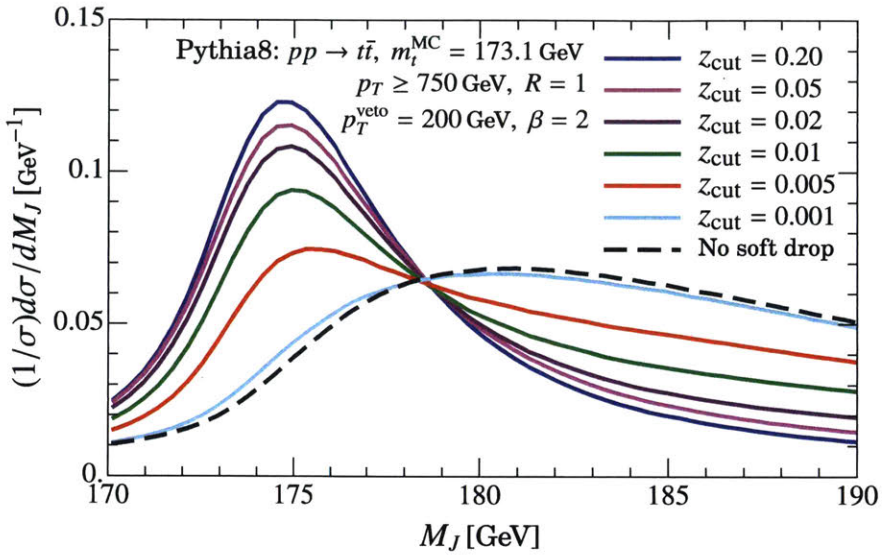

Figure 5-14: z_{cut} dependence of the normalized M_J spectrum from PYTHIA8, showing a transition at the predicted light soft drop values.

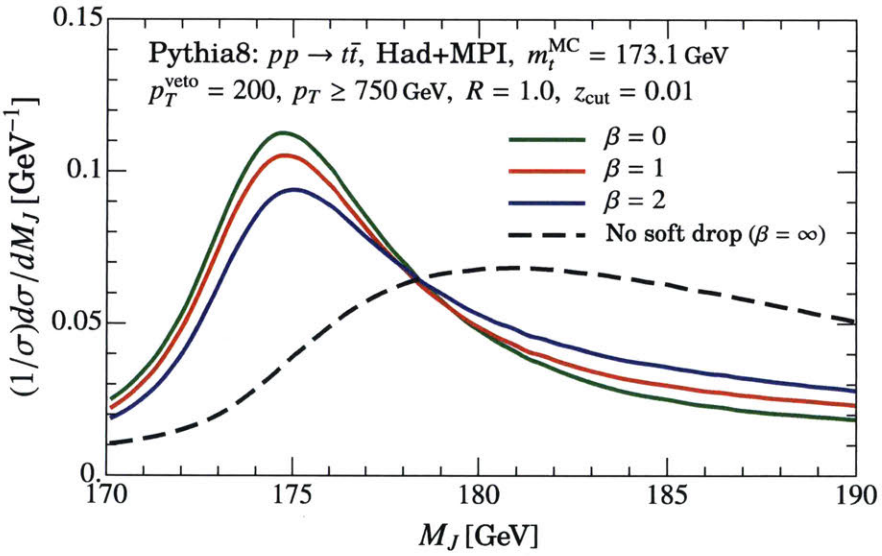

Figure 5-15: β dependence of the normalized M_J spectrum from PYTHIA8. We fix $z_{\mathrm{cut}} = 0.01$ so that there is still a fairly light soft drop being applied as we vary β.

for a limited range of z_{cut}. These restrictions were displayed in Fig. 5-8 for various values of p_T, M_J, and β, and generically require that z_{cut} is an order of magnitude smaller than the z_{cut} values being considered experimentally for other processes. We referred to this as a requirement of light soft drop grooming.

Nevertheless the factorization theorems imply that only this light grooming is

needed to make the top-jet insensitive to the wide angle ultra-soft radiation, and hence that there should be a visible transition when the light soft drop becomes active. To test this we plot in Fig. 5-14 the normalized jet mass spectrum from a PYTHIA8 simulation of $pp \to t\bar{t}$ while varying $z_{\rm cut}$. Prior to soft drop, or with very light grooming such as $z_{\rm cut} = 0.001$, the jet is contaminated with soft particles and hence we see a very broad M_J spectrum which peaks at values significantly higher than the input Monte Carlo top mass of $m_t^{\rm MC} = 173.1\,\text{GeV}$. The shift of the peak from the input mass is by about 7 GeV. When we increase $z_{\rm cut}$ towards the nominal $z_{\rm cut} = 0.01$ going through the transitional value of $z_{\rm cut} = 0.005$ we observe that the spectrum makes a rapid evolution, exhibiting a narrower width and peaking significantly closer to the input top-mass. Once the light soft drop is active the peak is at a value that is only $\simeq 1\,\text{GeV}$ higher than the input Monte Carlo top-mass.

As we increase $z_{\rm cut}$ further, to values > 0.01, the peak location in Fig. 5-14 remains stable. This demonstrates that stronger grooming is not actually removing additional soft particles that still contaminate the top resonance region. This occurs because the top-decay products are energetic and always pass the soft-drop condition even for this stronger grooming. The decay products set a minimum value for R_g determined by the angle θ_d discussed in Sec. 5.1.2, which means that soft particles inside the radius R_g are always retained.

We saw earlier in Fig. 5-8 that as we decrease β to apply a stronger grooming with soft drop, the expansions needed to derived the factorization formulae have larger expansion parameters. In particular a more limited range of $z_{\rm cut}$ is required to retain the same expansion, and smaller values should be considered. For this reason we focus our analysis on $\beta = 2$, while only giving a few M_J spectrum plots for smaller β. The β dependence predicted by PYTHIA8 is shown in Fig. 5-15 and turns out to actually be quite mild, with peaks of similar width, location, and height for $\beta = 2, 1, 0$. This provides an indication that the breakdown of the factorization theorem with changing β may be mild.

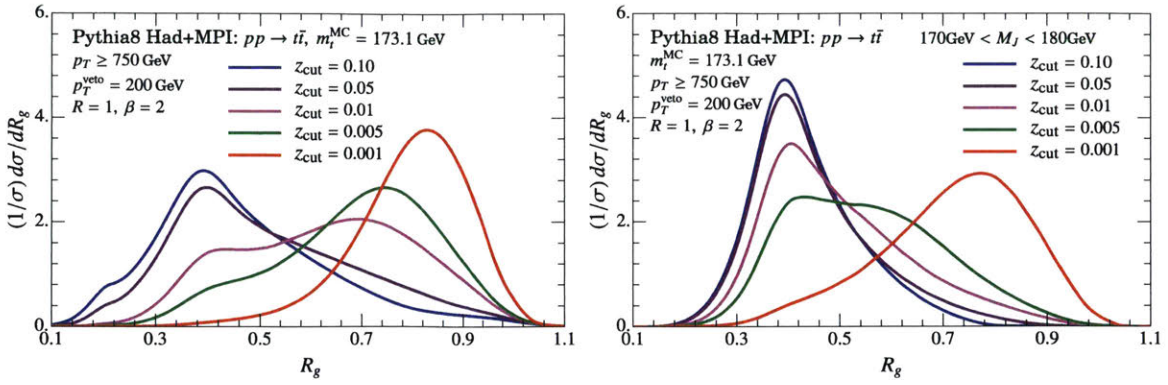

Figure 5-16: R_g spectrum as a function of the strength of the soft drop grooming parameter z_{cut}. The right panel imposes a constraint to take only events in the peak region 170 GeV $< M_J <$ 180 GeV, while the left panel is unconstrained.

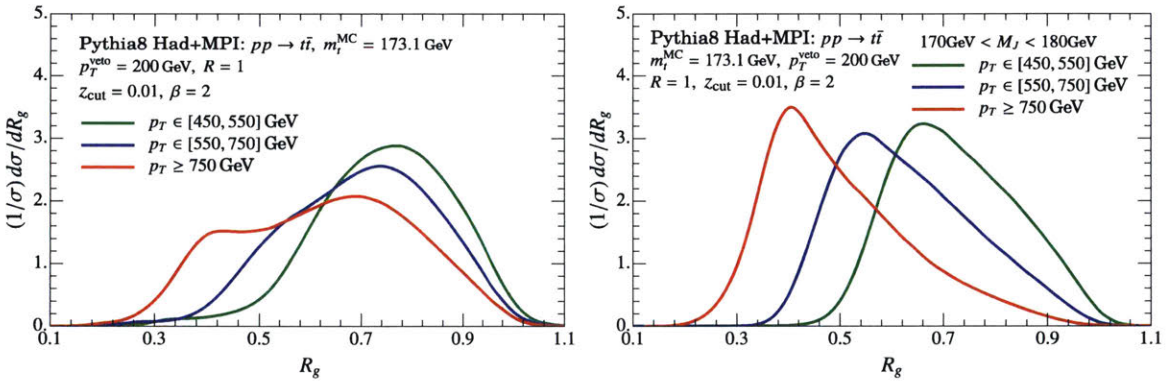

Figure 5-17: R_g spectrum as a function of p_T. The right panel imposes a constraint to take only events in the peak region 170 GeV $< M_J <$ 180 GeV, while the left panel is unconstrained.

5.4.2 R_g distributions

Another method for studying the light soft drop transition is by measurements of the spectrum of the soft dropped groomed jet radii R_g. Given an event with particles grouped into an initial jet of radius R, the soft drop procedure generates a radius R_g utilizing the angular distance of the pair of particles in the angular ordered cluster tree that first passes the soft drop criteria. Therefore R_g is an experimentally accessible variable which yields a distribution of values on given sample of events. In Fig. 5-16 we show the R_g spectrum as a function of z_{cut}, finding once again that there is a transition in the spectrum in the light grooming region of $z_{\text{cut}} \sim 0.01$. In the left panel of Fig. 5-16 both the peak and tail of the M_J spectrum are contributing, so

the light grooming transition is shown most clearly in the right panel of Fig. 5-16 where an additional constraint of $170\,\text{GeV} < M_J < 180\,\text{GeV}$ is imposed to ensure that only events in the peak region contribute. The transition of the R_g spectrum with changing z_{cut} shown in the right panel of Fig. 5-16 matches very closely with the transition observed above for the M_J spectrum in Fig. 5-14.

It is also interesting to look at the R_g spectrum as a function of the top jets p_T. Indeed we expect R_g to be influenced by the top decay products, and if the top quark decay products are playing an important role in the application of soft drop, to track the decay product derived angle θ_d which was introduced and discussed in Sec. **??**. If this is the case we would expect that the peak of the R_g spectrum would decrease as m/p_T with increasing p_T. In Fig. 5-17 we show the resulting R_g spectra for three different p_T bins, again without any M_J restriction in the left panel, and with a restriction to the peak region of M_J in the right panel. The peak position decreases with increasing p_T as expected, and actually fits very well to a m/p_T functional form with a coefficient that is in good numerical agreement with the approximate result $\tan(\theta_d/2) \simeq \langle h \rangle m/Q$ using our calculation for $\langle h \rangle$ from Sec. 5.3.5. This provides the first evidence that PYTHIA8 favors the decay form of the factorization theorem where the top decay products have an important influence on the behavior of the soft drop grooming.

5.4.3 Dependence on a p_T Veto of additional jets

The soft-drop procedure causes the factorization theorems to become independent of interactions other than those generated by the heavy top-quark producing the jet. In particular, after soft-drop the top-quark has ultra-collinear and collinear-soft radiation that only depends on variables associated to the top-jet such as its direction, but is independent of the other $\bar{t}$-jet and initial state radiation from the beams. One variable that probes the nature of the event outside the jet is a jet-veto, and so one may explore how the spectrum changes when varying the strength of such a jet-veto. The jet-veto for $pp \to t\bar{t}$ restricts the presence of jets beyond the boosted t and $\bar{t}$ jets by demanding that the p_T for any jet beyond these two satisfies $p_T < p_T^{\text{veto}}$. In the case

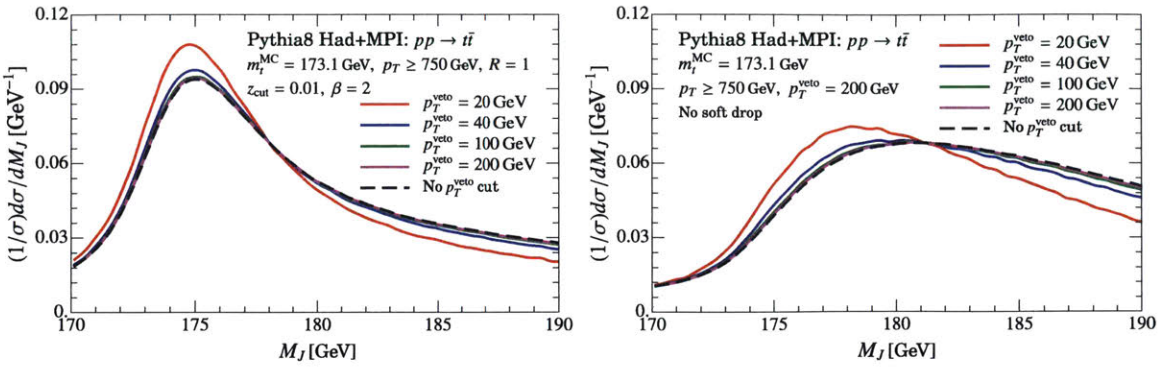

Figure 5-18: p_T^{veto} dependence for soft drop (left) and no soft drop (right)

of non-soft-dropped jets the jet-veto provides an important theoretical input which restricts the event to the exclusive jet category, but this veto is not required for the soft dropped factorization formulae. The only dependence on the veto occurs in the normalization factors N in Eqs. (5.70) and (5.85), which does not directly influence the M_J spectrum.[2] This is true as long as the jet veto's restriction on soft radiation in the event outside the jet is not stronger than that caused by soft drop for the soft particles in the jet since the distribution of soft radiation is fairly homogeneous and the amount of soft radiation inside and outside the jet is correlated. Hence the soft drop factorization theorem predicts that the spectrum should be insensitive to p_T^{veto} for a wide range of values.

In Fig. 5-18 (left panel) we show the M_J spectrum for various values of p_T^{veto}. To get a feeling for the strength of these vetoes we note that the fraction of events they retain are 12%, 33%, 65%, and 84% for $p_T^{\text{veto}} = 20, 40, 100, 200\,\text{GeV}$ respectively. We see that as predicted for $p_T^{\text{veto}} > 40\,\text{GeV}$ that there is very little sensitivity to the jet-veto, and that the spectrum is indistinguishable from having no-veto by the time we get to $p_T^{\text{veto}} = 100$. This implies that for an experimental analysis one may work with no veto, and hence not restrict the number of events by this cut. In our analyses we use the value of $p_T^{\text{veto}} = 200$ by default, simply as a reminder that our later theoretical calculation of the normalization factors N do technically implement

[2]There is a residual dependence on the jet-veto only because we bin the jets over p_T and η, which through the Q dependence couples N with the terms in the factorization theorem that are sensitive to M_J. However this is a small effect.

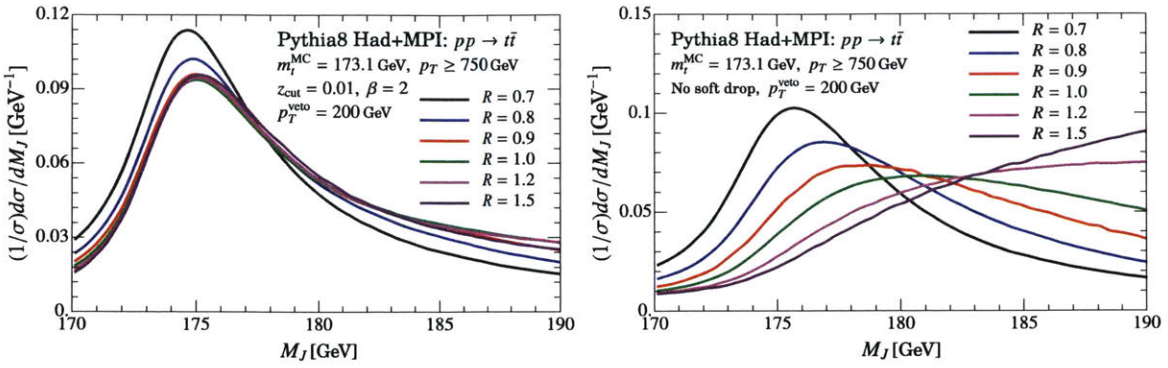

Figure 5-19: Dependence of the M_J spectrum on the jet radius R with soft drop (left) and without soft drop (right)

a loose jet-veto, though again we emphasize that this is a negligible effect at the desired level of precision.

For jets without soft drop it turns out that there is also insensitivity to the jet veto. As explained in Ref. [80], for jets produced by the hard scattering of massless quarks or gluons, this is predicted by the non-soft drop factorization theorem, because at NLL the dependence on the jet-veto factorizes from the M_J dependence, and hence mostly drops out of the normalized spectra. Furthermore it was found in [80] that the impact of the fixed order NLO corrections that might modify this picture, and which are included first at NNLL order, are very small. In Fig. 5-18 (right panel) we show that this is also the case for $pp \to t\bar{t}$ events simulated with PYTHIA8, validating the picture that even without the protection from soft drop that the jet veto dependence of the normalized M_J spectrum is small.

5.4.4 Jet radius dependence

After carrying out soft-drop the jet is groomed of soft radiation at larger angles, which reduces the radius from R down to the groomed radius $R_g < R$. The same R_g is obtained independent of the initial starting R, as long as R is large enough to not be considered a small parameter, namely $R/2 \sim 1$. This implies that the jet-mass spectrum will be independent of R. On the other hand, if we start with smaller $R/2$ then this may still influence the jet mass spectrum by cutting into the decay products.

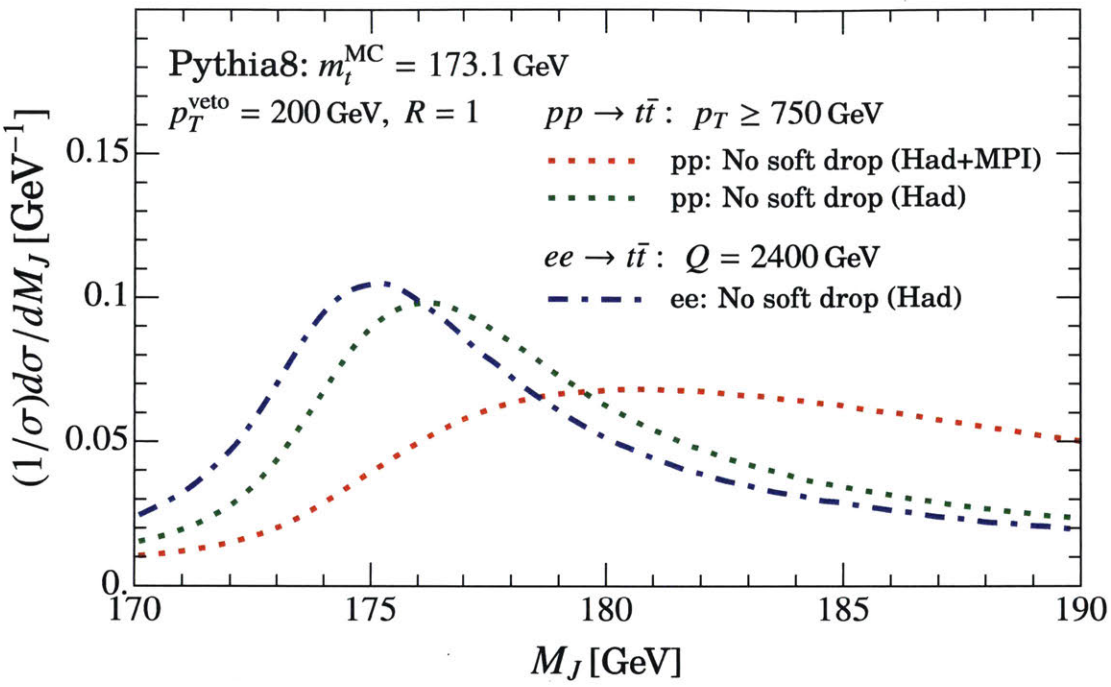

Figure 5-20: Comparison of top jets from e^+e^- and pp collisions in PYTHIA8 without soft drop.

This expectation is quite different from the predicted jet-radius dependence of the jet-mass spectrum of jets without soft drop, where the jet radius dependence modifies the shape in a linear fashion as R is varied.

In Fig. 5-19 (left panel) we show the M_J spectrum after soft drop for various values of R. For $R \gtrsim 0.9$ we observe that the spectrum is insensitive to the precise R value as predicted. In contrast, in Fig. 5-19 (right panel) we show the strong dependence on R of the M_J spectrum when considered prior to soft drop. Here the perturbative soft contamination brings in direct dependence on R in terms of the variable $m_J^2/(p_T R)$ which modifies the double Sudakov logarithms, and hence gives a strong dependence. (For further discussion of the ungroomed case see for example Ref. [80].)

5.4.5 Comparison of $e^+e^- \to t\bar{t}$ and $pp \to t\bar{t}$ results

The insensitivity of the soft dropped factorization theorem to outside interactions (interactions not associated with the heavy top-quark producing the jet) also predicts a correspondence between the M_J spectrum for top jets produced from $e^+e^- \to t\bar{t}$ and

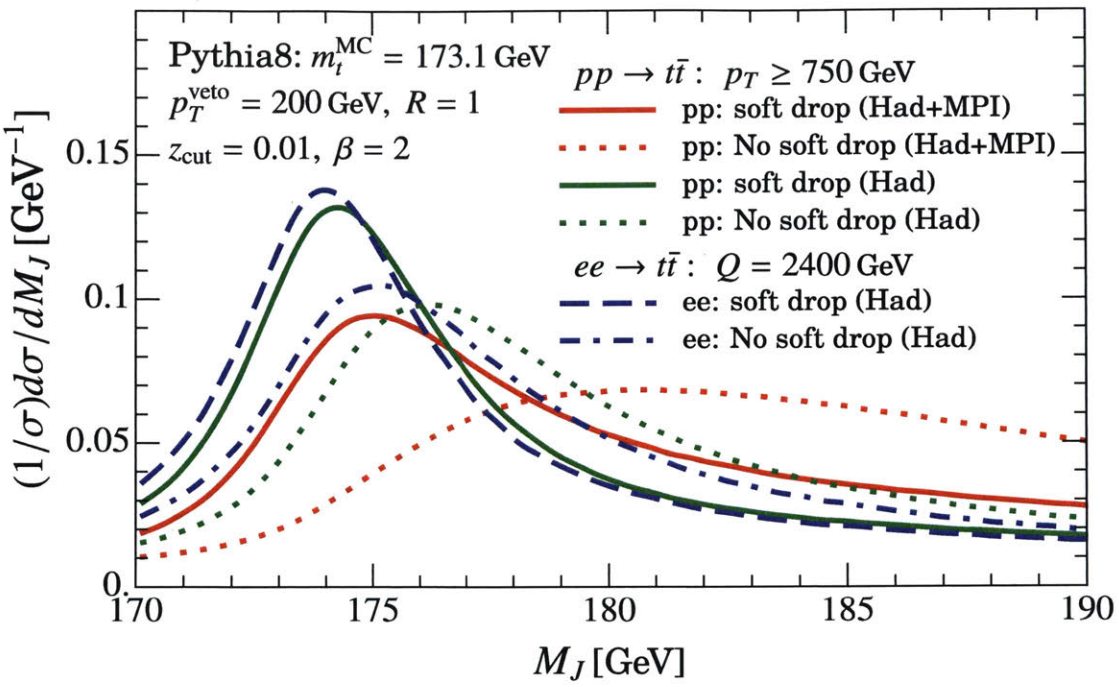

Figure 5-21: Comparison of top jets from e^+e^- and pp collisions in PYTHIA8 with and without soft drop.

$pp \to t\bar{t}$. These processes both obey the same factorization theorems in Eqs. (5.70) and (5.88). Indeed, the functions and variables in these formulae are the same for both processes except for the normalization factor N, and the definition of the variable Q. For pp collisions $Q = 2p_T \cosh(\eta)$, while for e^+e^- collisions Q is the center of mass energy of the e^+e^- collision. The other difference is that pp collisions can have additional contributions to the jet mass spectrum from the underlying event, which is absent in e^+e^-. This UE is not something that is rigorously predicted by the factorization theorems, though as described in Sec. 4.5 it can still be modeled fairly accurately in our theoretical calculations. As a result of Monte Carlo tuning it is also believed to be modeled fairly accurately by the MPI contributions included in PYTHIA8.

In Fig. 5-20 we show results for the M_J spectrum from e^+e^- and pp collisions without soft drop. As can be seen from the e^+e^- hadronized result (blue-dashed line) and pp hadronized result (green dotted line), the two spectra are noticeably different, with peak positions differing by $\simeq 1\,\text{GeV}$. With MPI turned on (broad red dotted

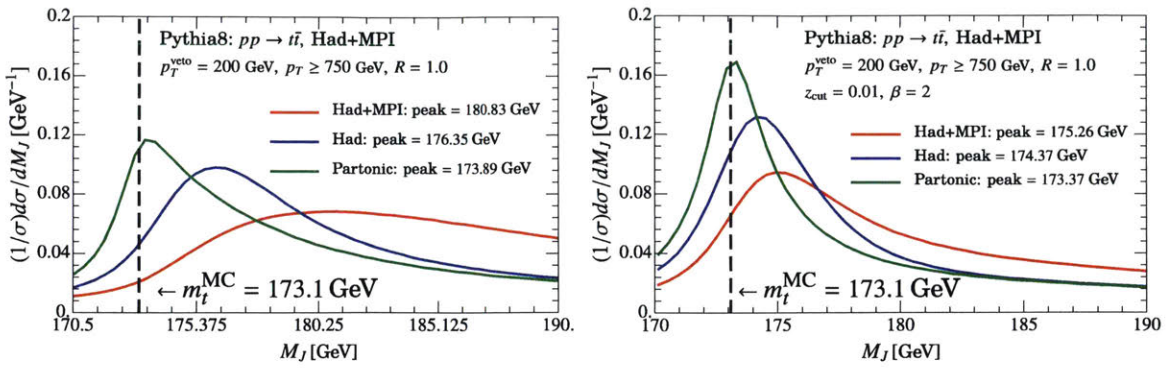

Figure 5-22: Effect of adding hadronization and MPI without (left) and with (right) soft drop grooming.

curve) the differences are significantly larger. In Fig. 5-21 we retain these curves and add the three analogous results after soft drop has been applied, shown as the dashed-blue line, solid green line, and solid red line for e^+e- with hadronization, pp with hadronization, and pp with hadronization and MPI, respectively. Here the dashed-blue and solid-green curves with hadronization agree quite well, as predicted by the factorization theorems. The peak positions for these curves differ by only $\simeq 0.24\,\text{GeV}$ which is within the expected accuracy of the accuracy of the approximations used to make a comparison with similar Q values. This factor of four improvement difference between the peak locations agrees with our theoretical expectations. Note that to obtain the corresponding center-of-mass energy Q for the e^+e^- result, we considered the range of p_T and η values for the default pp bin, computed the average p_T and η weighted by the corresponding cross section, and used these values to obtain an average value for $Q = 2p_T \cosh(\eta)$ for the pp bin, giving $Q \simeq 2460\,\text{GeV}$. Available simulation data with the nearby value of $Q = 2400\,\text{GeV}$ was then used for the comparison.

5.4.6 Hadronization and MPI

When MPI is added the soft drop pp result has a peak that is shifted by 4.5 GeV. This is shown most cleanly in Fig. 5-22 (left panel) where for pp collisions we display the no soft drop hadronization result (blue) and hadronization+MPI result (red), including

also here the purely partonic PYTHIA8 result (green), and listing the positions of the various peak locations in GeV. The shift from adding MPI to the hadronization result is about a factor of two larger than the $\simeq 2.5\,\text{GeV}$ shift between the partonic and hadronic peak positions.

After soft drop the analogous pp results are shown in Fig. 5-22 (right panel). Here we observe a significantly smaller shift between both the partonic and hadronization results, $\simeq 1.0\,\text{GeV}$ and between the hadronization and hadronization+MPI results, $\simeq 1.1\,\text{GeV}$. The latter result is quite important; since the UE / MPI effects must be modeled in a manner that goes beyond the factorization theorem this reduction in the magnitude of their contribution provides a significant decrease in the associated uncertainty. At the level of the analysis carried out here we make a rough estimate that the factorization based model for including UE effects, through modifying the moment parameters $\Omega_n \to \Omega_n^{\text{MPI}}$, has a 30% uncertainty. This approximation for the residual uncertainty may actually be somewhat conservative since this modeling agrees well with PYTHIA8's MPI model with much higher accuracy. Nevertheless we feel it is appropriate to be conservative when relying on model dependent methods. This rough estimate yields a 0.3 GeV uncertainty estimate for the modeling of MPI. With further dedicated studies of MPI in samples of top, massless quark or b-jets, we may gain the needed confidence to make this rough uncertainty estimate more precise in the future.

5.4.7 p_T dependence of the $pp \to t\bar{t}$ jet mass spectrum

In Fig. 5-23 we study the p_T dependence of the soft-dropped spectrum predicted by PYTHIA8, for four different p_T bins. In the first panel we see that there is essentially no p_T dependence of the spectrum in the partonic PYTHIA results. The second panel includes hadronization, and we begin to see p_T dependent shifts between the bins at a very small 0.1–0.2 GeV level. These small shifts are in agreement with the dramatically reduced p_T dependence predicted by the soft drop factorization theorems. Indeed, these small shifts are compatible with the lack of p_T dependence predicted by Eq. (5.128). They are also compatible with Eq. (5.129) if the Λ_{QCD} is replaced

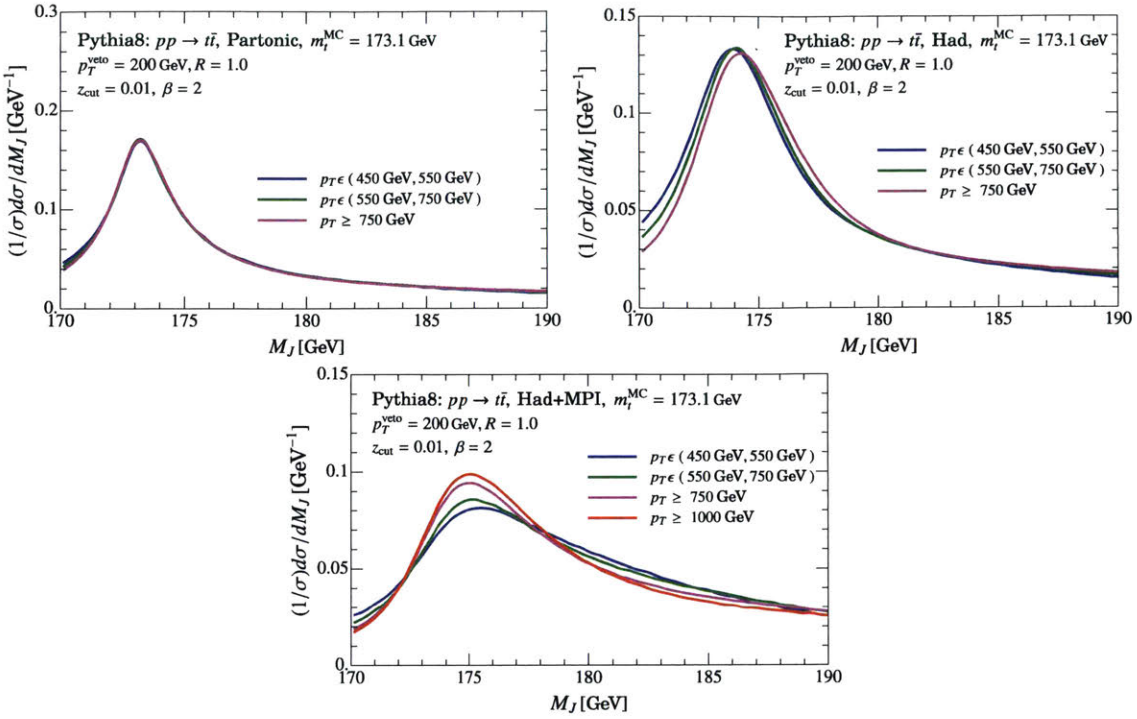

Figure 5-23: p_T dependence of the M_J spectrum with soft drop. The three panels are partonic PYTHIA8, PYTHIA8 with hadronization, and PYTHIA8 with hadronization and MPI, respectively.

by $\Omega_1^{(\beta)} \sim 1\,\text{GeV}$. Finally the third panel of Fig. 5-23 adds MPI effects. Once again the peak of the distribution remains quite stable, with variations of at most 0.25 GeV between neighboring p_T bins. Once MPI is included the top jet mass peak is broadened with increasing p_T by the additional soft radiation populating the groomed jet at angular distances $< R_g$. In the presence of MPI there is also a very small backward shift of the peak position with increasing p_T in PYTHIA8, which however is not significant at the expected level of our uncertainties.

Note that if the relatively mild dependence of the M_J spectrum on p_T is taken to hold at smaller p_T, below the region of validity of the factorization theorem, then one could attempt to extrapolate the theoretical predictions of the soft-drop factorization theorem even to smaller p_T (for example, by simply using the predictions at larger p_T and assigning an additional uncertainty). The existence of mild behavior is supported by Monte Carlo simulations in this region. Due to the inherent imprecision of such an extrapolation we do not favor it, and will not consider it further here, though it

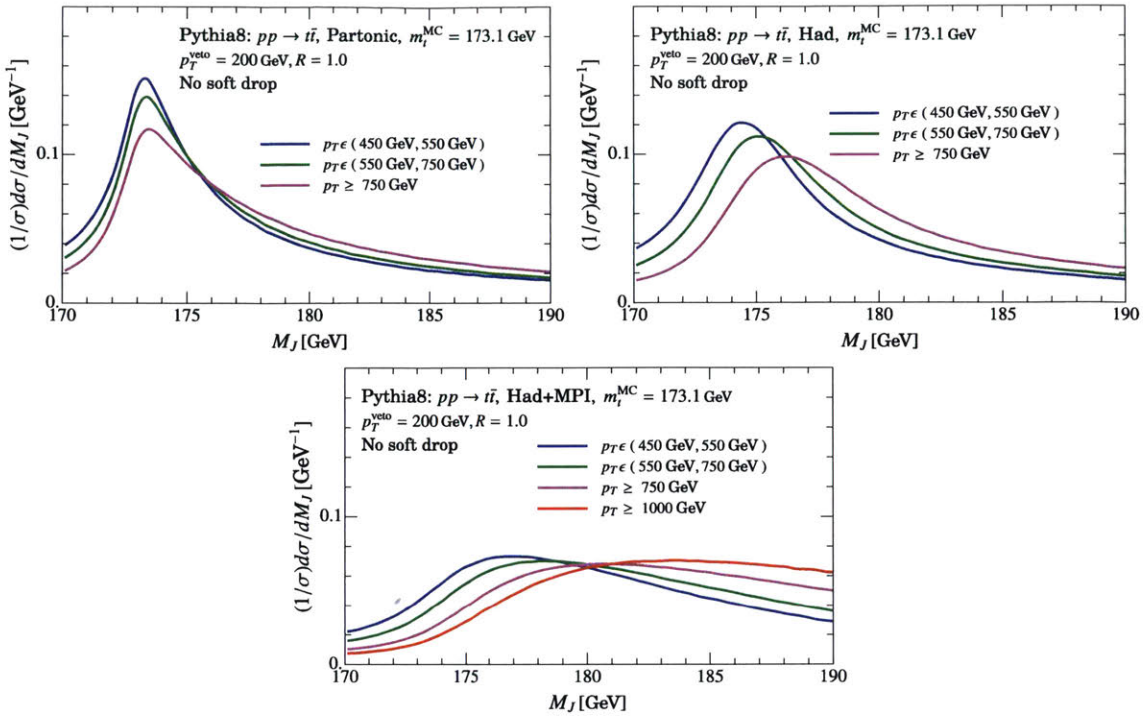

Figure 5-24: p_T dependence of the M_J spectrum without soft drop. The three panels are partonic, with hadronization, and with hadronization and MPI respectively.

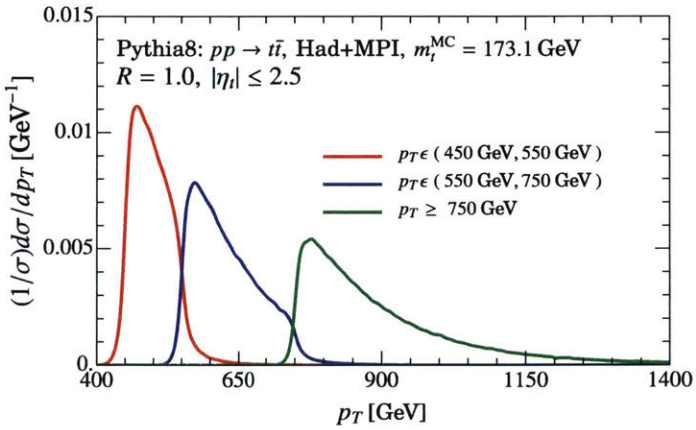

Figure 5-25: Spectrum of jet p_T values in three different p_T bins which are fixed by the parent top quarks p_T.

might be interesting to explore further in the future, particularly while size of the data sample for top quarks at larger p_T remains limited.

Note that our implementation of determining the events in a p_T bin in PYTHIA8 uses as a short cut the p_T of the parent top quark rather than the jet p_T. This is quite advantageous for collecting statistics in a given p_T bin since we do not need

to run a jet finding algorithm to determine the p_T. In Fig. 5-25 we show the actual spectrum of jet p_T values for each of these bins. This plot shows that the jet p_T tracks very closely with the parent top quarks p_T, with the anticipated sharp fall off at the edges of the bins (the difference in top quark and jet p_T values is formally power suppressed).

5.5 Factorization Theorem Results

In this section we discuss further our implementation of the decay and high-p_T soft drop factorization theorems in Eqs. (5.70) and (5.88) and the ungroomed factorization theorem in Eq. (4.51). In particular we discuss the profile functions used to sum large logarithms in the appropriate phase space regions and forms we use for the non-perturbative functions F and F_C. We then carry out a systematic exploration of how these factorization theorems depend on various variables, including the hadronic parameters Ω_1 and x_2, top mass m_t, jet p_T, z_{cut} and β. We also give a more sophisticated comparison between cross section predictions obtained from the high-p_T and decay factorization theorems, demonstrating that they are quite similar in the desired region of phase space.

5.5.1 Factorization Theorem Implementation

The various functions appearing in the ungroomed and groomed factorization theorems are each dominated by physics from a single physical scale, and also depend on a renormalization scale μ. This μ dependence is exploited to sum large logarithms using the renormalization group to evolve between the scales associated with the various jet, soft, and hard functions. After this evolution, there is still residual dependence on the boundary scale values μ_i that we use to specify the initial conditions for this evolution, but this dependence cancels out order by order in resummed perturbation theory. As we vary the physical observable M_J, encoded by $\hat{s}_t = (M_J^2 - m^2)/m$, the cross section goes through different regions, which are referred to as the peak, tail, and ultra-tail regions. Since the arguments of the logarithms in the initial conditions

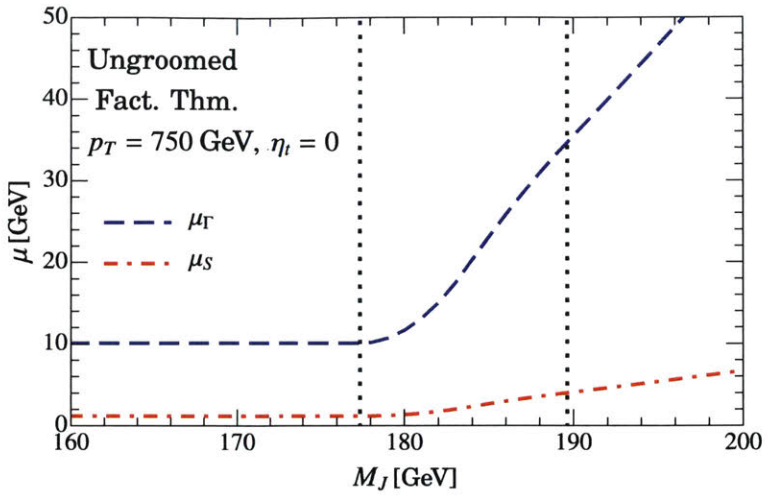

Figure 5-26: Profile functions for ungroomed top jet factorization theorm. The dotted vertical lines indicate the transition region that distinguishes the peak and tail regions.

depend on $\hat{s}_t$, the scales μ_i must also, in particular with increasing $\hat{s}_t$. This is encoded by the use of "profile scales" $\mu_i = \mu_i(\hat{s}_t)$ which satisfy the correct theoretical constraints in various regions, and provide a smooth interpolation in between [93, 5]. Our precise implementation follows results for profiles used in Refs. [80, 69]. In the following two subsections we discuss the profiles for the case of the ungroomed factorization thoerem, the soft drop groomed high-p_T factorization theorem, and the decay factorization theorem respectively. We then discuss our implementation of the non-perturbative hadronization functions F and F_C in Sec. 5.5.1.

Profile Functions for Ungroomed Top Jet Factorization

The factorization formula in Eq. (4.70) contains the following characteristic renormalization scales: the hard scale μ_Q, top mass scale μ_t, the bHQET heavy quark jet scale μ_Γ, beam scales $\mu_{B_{a,b}}$, and soft scales $\mu_{S_{t,\bar{t}}}$ for the top jets, and $\mu_{S_{a,b}}$ for the soft radiation in the jet vetoed beam region.

The regions relevant for the scales μ_t, $\mu_{S_{t,\bar{t}}}$, μ_{Γ_t} are *Peak*, *Tail* (bHQET resummation) region, and the *Ultra tail* (SCET resummation region). In order to avoid large logarithms, these scales must satisfy certain constraints in the different regions:

1. Peak (non-perturbative), $\hat{s} \sim \Gamma \ll m_t$:

   $\mu_t \sim m_t,\ \mu_\Gamma \sim \Gamma,\ \mu_{S_{t,\bar{t}}} \sim \Lambda_{\rm QCD}$,

2. Tail (bHQET Resummation), $\Gamma_t \ll \hat{s} \ll m_t$:

   $\mu_t \sim m_t,\ \mu_\Gamma \sim \hat{s},\ \Lambda_{\rm QCD} \ll \mu_{S_{t,\bar{t}}} \sim \frac{m_t}{Q_{t,\bar{t}}}\hat{s}$,

3. Ultra Tail (SCET resummation), $\Gamma_t \ll \hat{s} \sim m_t$:

   $\mu_t = \mu_\Gamma \sim m_t,\ \mu_{S_{t,\bar{t}}} = \frac{m_t^2}{Q_{t,\bar{t}}}$.

The profile function for $\mu_{S_{t,\bar{t}}}$ written in terms of dimensionless variables $\xi_{t,\bar{t}} = \frac{\hat{s}_{t,\bar{t}}}{m_t}$ are given by the following formula. For the soft scales associated with the jets we have:

$$\mu_{S_{t,\bar{t}}}(\xi, t_i) = \Big[1 + e_{S_{t,\bar{t}}} V(\xi, t_3)\Big] \begin{cases} \mu_\Lambda + \Gamma_t \frac{m_t}{Q_{t,\bar{t}}} & 0 \le \xi < t_0 \\ \zeta(\mu_\Lambda + \Gamma_t \frac{m_t}{Q_{t,\bar{t}}},\ 0,\ 0,\ r_s\ \mu_t\ \frac{m_t}{Q_{t,\bar{t}}},\ t_0,\ t_1,\ \xi) & t_0 \le \xi < t_1 \\ r_s\ \mu_t\ \frac{m_t}{Q_{t,\bar{t}}}\ \xi & t_1 \le \xi < t_2 \\ \zeta(0,\ r_s\ \mu_t\ \frac{m_t}{Q_{t,\bar{t}}},\ \mu_t\ \frac{m_t}{Q_{t,\bar{t}}}, 0,\ t_2,\ t_3,\ \xi) & t_2 \le \xi < t_3 \\ \frac{m_t}{Q_{t,\bar{t}}}\ \mu_t & t_3 \le \xi < 1 \end{cases} \tag{5.105}$$

Here $\zeta(a_1\ , b_1\ , a_2\ , b_2\ , t_1\ , t_2\ , t)$ has $t_t < t_2$ and is a piecewise quadratic function that smoothly connects two straight lines of the form $l_1(t) = a_1 + b_1\ t$ for $t < t_1$ and $l_2(t) = a_2 + b_2\ t$ for $t > t_2$ at the meeting points t_1 and t_2. The arguments of the ζ function in Eq. (5.105) are simply the coefficients of the equation of the straight lines that occur for the regions below and above where ζ appears. For our case where we focus on the peak region, the region where we transition from the tail to the ultra-tail region, $\xi > t_2$, is not relevant and hence we can take $t_2 = t_3 = 1$. We also always take the slope parameter to have it canonical value $r_s = 1$. Finally we take $\mu_\Lambda = 1$ GeV, noting that the flat region for small $\hat{s}_t$ freezes the scales of the perturbative

functions before they can get close to the Landau pole in the strong coupling where their perturbative expressions would no longer be valid. The parameters e_i take a default value of zero and are varied by ± 0.5 to carry out scale variation. The function $V(\tau, t_3)$ that always multiples the e_i parameters is defined as follows:

$$V(\xi, t_3) = \theta(t_3 - \xi)\left(1 - \frac{\xi}{t_3}\right)^2, \tag{5.106}$$

ensuring that variations of scales related to the resummation are turned off by the time we reach the fixed order region with $\xi > t_3$. Our choice for t_0 and t_1 are

$$t_0 = \frac{Q_{t,\bar{t}}\,\mu_\Lambda}{m_t^2}, \qquad t_1 = 4\,\frac{Q_{t,\bar{t}}\,\mu_\Lambda}{m_t^2}, \tag{5.107}$$

where this t_0 roughly defines the extent of the peak region, and taking $t_1 = 4\,t_0$ ensures that we have a smooth transition to the tail region. Different parameters t_0 and t_1 can in principal appear for the t and $\bar{t}$ case due to differences in Q_t and $Q_{\bar{t}}$.

We similarly define the profile for the bHQET jet scales for the two J_B functions as:

$$\mu_{\Gamma_{t,\bar{t}}}(\xi, t_i) = \Big[1 + e_{\Gamma_t} V(\xi, t_3)\Big] \begin{cases} \frac{Q_{t,\bar{t}}}{m_t}\,\mu_\Lambda + \Gamma_t & 0 \le \xi < t_0 \\ \zeta(\frac{Q_{t,\bar{t}}}{m_t}\mu_\Lambda + \Gamma_t,\, 0,\, 0,\, r_s\mu_t,\, t_0,\, t_1,\, \xi) & t_0 \le \xi < t_1 \\ r_s\mu_t\,\xi & t_1 \le \xi < t_2 \\ \zeta(0,\, r_s\mu_t,\, \mu_t, 0,\, t_2,\, t_3,\, \xi) & t_2 \le \xi < t_3 \\ \mu_t & t_3 \le \xi < 1 \end{cases} \tag{5.108}$$

These scales are consistent with the constraints for different regions stated above. They preserve the see-saw relation between the bHQET jet and soft scale: $\mu_{\Gamma_t} \sim \frac{Q}{m_t}\,\mu_{S_t}$.

For the hard scales we take $\mu_Q = Q$ and $\mu_m = m$, and vary these scale choices by a factor of two when estimating uncertainties. A plot of the various profile functions for the ungroomed factorization theorem is shown in Fig. 5-26.

For the choice of profile scales for the beam functions $\mu_{B_{a,b}}$ and the associated soft scales $\mu_{S_{a,b}}$ we follow Ref. [80] when we consider a SCET_I particle based beam thrust jet veto, and Ref. [112] for a jet based p_T^{veto}. Since our normalized results for the M_J spectra are essentially independent of the treatment of the beam related scales, and for that matter the jet-veto itself, we will not go into detail about these profile functions. Their treatment is also the same for the calculation of the normalization function N in the soft-drop factorization theorems. We discuss the profile scales that differ for the case of soft drop in the next subsection.

Profile Functions Soft Drop Groomed Top Jets

We now consider groomed top jets. Instead of the soft function we now have the global soft function and the collinear-soft function with corresponding scales μ_{S_G} and μ_{S_C}. We choose the global soft function scale μ_{S_G} as a constant for all the regions:

$$\mu_{S_G} = \left[1 + e_{S_G}\right]\left(2^\beta Q_t z_{\text{cut}}\right), \tag{5.109}$$

where the parameter e_{S_G} is used to vary this scale for estimating higher order perturbative uncertainties. The choice of the profile function for μ_{S_C} differs between the high-p_T and decay cases.

For the high-p_T soft drop factorization theorem the μ_Γ scale is taken to be:

$$\mu_\Gamma^{\rm I}(\xi,t_i) = \Big[1+e_{\Gamma_t}V(\xi,t_3)\Big]\begin{cases} \frac{Q_{t,\bar{t}}}{m_t}\,\mu_\Lambda\left(\frac{\mu_\Lambda}{Q_{\rm cut}}\right)^{\frac{1}{\beta+1}}+\Gamma_t & 0\le\xi<t_0^{\rm I} \\ \zeta\Big(\frac{Q_{t,\bar{t}}}{m_t}\mu_\Lambda\left(\frac{\mu_\Lambda}{Q_{\rm cut}}\right)^{\frac{1}{\beta+1}}+\Gamma_t,\,0,\,0,\,r_s\mu_t,\,t_0^{\rm I},\,t_1^{\rm I},\,\xi\Big) & t_0^{\rm I}\le\xi<t_1^{\rm I} \\ r_s\mu_t\xi & t_1^{\rm I}\le\xi<t_2 \\ \zeta(0,\,r_s\mu_t,\,\mu_t,0,\,t_2,\,t_3,\,\xi) & t_2\le\xi<t_3 \\ \mu_t & t_3\le\xi<1 \end{cases} \tag{5.110}$$

(If we chose to apply soft drop to both the t and $\bar{t}$ jets simultaneously then we would have two such scales with their own ξ parameters.) Here the result in the region $0\le\xi<t_0^{\rm I}$ is dictated by the scales appearing through the convolutions in the high-p_T factorization theorem. The parameter e_{Γ_t} is used to vary this scale for the perturbative uncertainty analysis. We define the μ_{SC} scale for the top jet using the corresponding μ_Γ profile and the μ_{S_G} scale via:

$$\mu_{SC}(\xi,t_i) = \Big[1+e_{S_t}V(\xi,t_3)\Big]\left[\mu_\Gamma^{\rm I}(\xi,t_i)\frac{m_t}{Q_t}\big(\mu_{S_G}\big)^{\frac{1}{1+\beta}}\right]^{\frac{1+\beta}{2+\beta}}. \tag{5.111}$$

This choice for μ_{SC} can be motivated by noting that from Eq. (5.16) we have

$$\begin{aligned}\mu_{SC}^2 &\simeq \left(\frac{2m_t\hat{s}_t}{Q_t}\right)^{\frac{2(1+\beta)}{2+\beta}}\left(\frac{Q_t z_{\rm cut}}{2}\right)^{\frac{2}{2+\beta}} \\ &\simeq \left[\hat{s}_t\,\frac{m_t}{Q_t}\big(2^\beta Q_t z_{\rm cut}\big)^{\frac{1}{1+\beta}}\right]^{\frac{2(1+\beta)}{2+\beta}},\end{aligned} \tag{5.112}$$

and that Eq. (5.111) enforces this see-saw relation, while allowing for a scale variation through the parameter e_{S_t}. The choice of transition points t_i appearing in the ultra-collinear function in Eq. (5.108) are based on the form of non perturbative convolution

structure in Eq. (5.70). We take $t_0^{\rm I}$ to correspond to the value of $\hat{s}_t$ that makes the soft-collinear mode non-perturbative. This is given by Eq. (5.23) as follows:

$$t_0^{\rm I} = \frac{1}{m_t}\frac{\mu_\Lambda Q_t}{m_t}\left(\frac{\mu_\Lambda}{2^\beta Q_t z_{\rm cut}}\right)^{\frac{1}{1+\beta}}. \tag{5.113}$$

We make a choice of t_1 such that we avoid any sharp transitions and kinks in the profile functions. For convenience, we define $t_{\rm mid}$ to be the point of the intersection of the two straight lines in regions $0 < \xi < t_0$ and $t_t < \xi < t_2$:

$$t_{\rm mid}^{\rm I} = \frac{Q_t\mu_\Lambda + \Gamma_t m_t}{r_s \mu_t m_t}. \tag{5.114}$$

Then we choose t_1 such that it symmetrically placed with respect to t_0 about $t_{\rm mid}$:

$$t_1^{\rm I} = 2\, t_{\rm mid}^{\rm I} - t_0^{\rm I}. \tag{5.115}$$

For the soft drop decay factorization theorem in Eq. (5.85) we modify the peak region profile for μ_Γ profile in Eq. (5.108) to account for the difference in the scaling of non-perturbative momentum:

$$\mu_{\Gamma_t}^{\rm II}(\xi, t_i) = \Big[1 + e_{\Gamma_t} V(\xi, t_3)\Big] \times \begin{cases} h\,\mu_\Lambda + \Gamma_t & 0 \le \xi < t_0^{\rm II} \\ \zeta(h\,\mu_\Lambda + \Gamma_t,\, 0,\, 0,\, r_s\mu_t,\, t_0^{\rm II},\, t_1^{\rm II},\, \xi) & t_0^{\rm II} \le \xi < t_1^{\rm II} \\ r_s\mu_t\xi & t_1^{\rm II} \le \xi < t_2 \\ \zeta(0,\, r_s\mu_t,\, \mu_t, 0,\, t_2,\, t_3,\, \xi) & t_2 \le \xi < t_3 \\ \mu_t & t_3 \le \xi < 1 \end{cases}. \tag{5.116}$$

Here we determine $t_0^{\rm II}$ by noting that this roughly corresponds to the value of $\hat{s}_t = \hat{s}_\Lambda^{\rm II}$ when θ_{SC} in Eq. (5.11) is the same as that of the top decay product at the

widest angle with respect to the jet axis:

$$\theta_{SC} \sim \frac{m_t}{Q_t} h \,, \tag{5.117}$$

which gives

$$t_0^{\rm II} = \frac{\hat{s}_\Lambda^{\rm II}}{m_t} = 2^{\beta-2} z_{\rm cut} \left(\frac{m_t}{Q_t}\right)^\beta h^{2+\beta} \,. \tag{5.118}$$

We have included an additional factor of $1/4$ here for convenience since it yields smoother profiles in the transtion region. As above we set $t_1^{\rm II}$ symmetrically with respect to $t_0^{\rm II}$ about the intersection point of the straight line profiles in the peak and tail regions:

$$t_{\rm mid}^{\rm II} = \frac{h\,\mu_\Lambda + \Gamma_t}{r_s\,\mu_t} \,, \tag{5.119}$$

and

$$t_1^{\rm II} = 2\,t_{\rm mid}^{\rm II} - t_0^{\rm II} \,. \tag{5.120}$$

The choice of scales that appear for the factorization based calculation of the normalization factors N in the soft drop cross section formulae, are taken to be the same as in the ungroomed case.

A plot of the various nontrivial profile functions for the two soft drop factorization theorems is shown in Fig. 5-26 for the choice $p_T = 750\,\text{GeV}$. Despite the differences in the functional forms in Eqs. (5.108) and (5.116), see that the μ_Γ and μ_{CS} scales are actually quite similar for high-p_T and decay for this value of p_T. Perturbatively these factorization theorems involve the same functions, so the logarithms they sum up are very similar, and the only difference appears from their treatment of non-perturbative corrections which has a mild impact on the choice of profile functions in the range of p_T we consider here.

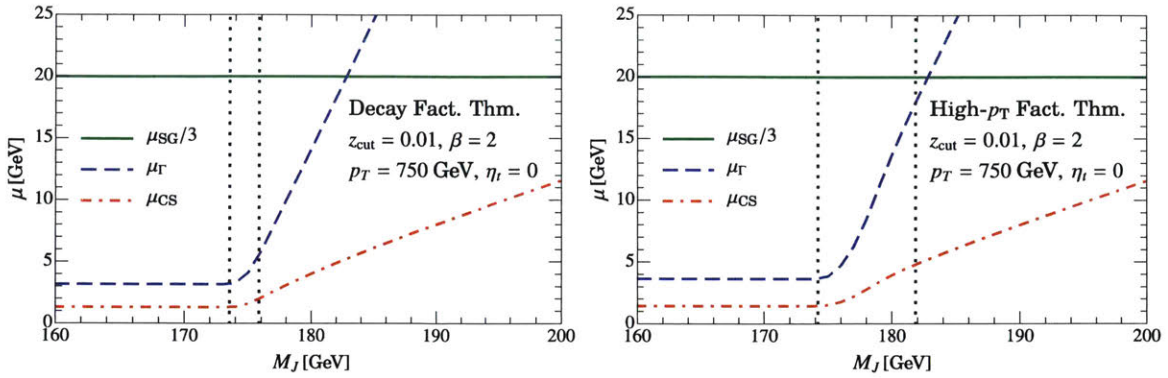

Figure 5-27: Profile Functions for the "decay" and "high-p_T" factorization theorem. The dotted vertical lines indicate the end and onset of peak and tail region respectively.

Parameterizing the Hadronization Functions

As discussed in Sec. 4.4 the effect of non-perturbative effects on the jet regions in the ungroomed factorization theorem are determined by a non-perturbative function $F(k, k')$:

$$S^\kappa_{IJ}(\ell_a, \ell_b, \ell_t, \ell_{\bar{t}}, \{\mu_{S_i}, \delta\}) \;=\; \int d\ell'_t \int d\ell'_{\bar{t}}\; S^\kappa_{IJ_{\rm part.}}(\ell_a, \ell_b, \ell_t - \ell'_t, \ell_{\bar{t}} - \ell'_{\bar{t}}, \{\mu_{S_i}, \delta\}) F(\ell'_t, \ell'_{\bar{t}}), \tag{5.121}$$

where the partonic soft function $S_{\rm part.}$ is convoluted with the non-perturbative function F which has the normalization

$$\int d\ell_t \int d\ell_{\bar{t}}\, F(\ell_t, \ell_{\bar{t}}) \;=\; 1. \tag{5.122}$$

In order to have an explicit functional form we parameterize the nonperturbative soft function for the ungroomed cross section using the Korchemsky-Tafat model [86]

$$F(\ell^+, \ell^-) \;=\; \theta(\ell^+)\theta(\ell^-) \frac{\mathcal{N}(a, b, \Lambda)}{\Lambda^2} \left(\frac{\ell^+\ell^-}{\Lambda^2}\right)^{a-1} \exp\left[\frac{-2\ell^+ - 2\ell^- - 2b\sqrt{\ell^+\ell^-}}{\Lambda}\right] \tag{5.123}$$

Here Λ, a, and b are parameters of the model and $\mathcal{N}(a, b, \Lambda)$ is a normalization factor that ensures the normalization condition in Eq. (5.122)..

In our analysis of the ungroomed jet mass spectra we always consider integrating fully over one jet mass, while studying the other. Since at NLL order there is no correlation between the two jet mass variables, so the only possible correlation occurs through F via the parameter b. Keeping b and integrating over ℓ^- only effectively results in a modified one-dimensional model function for the ℓ^+ depencence, whose parameters depend on b. Therefore for simplicity for our analysis of single jet mass spectra we take $b = 0$. The integral over ℓ^- then leads to the simple one-dimensional exponential model function modulated by a power,

$$F(\ell) \;=\; \theta(\ell)\frac{\mathcal{N}(a,\Lambda)}{\Lambda}\Big(\frac{\ell}{\Lambda}\Big)^{a-1}\exp\Big(\frac{-2\ell}{\Lambda}\Big)\,, \tag{5.124}$$

where again $\mathcal{N}(a,\Lambda)$ is fixed to ensure this function is normalized to 1 when integrated over ℓ. Computing the moment parameters for this function we find

$$\Omega_1 = \frac{a\Lambda}{2}\,, \qquad x_2 = \frac{1}{a}\,, \tag{5.125}$$

so that the parameters Λ and a are in 1-to-1 correspondence with the moment based parameters Ω_1 and x_2 that we wish to vary for our analysis. The parameter x_2 varies from $0 \leq x_2 \leq 1$ for any reasonable functional form, and we generally observe that this parameters impact on the cross section is subdominant to that of Ω_1, particularly for smaller x_2 values.

In the case of the soft drop factorization theorems we have a one-dimensional nonperturbative hadronization function, which is $F_C(k,\beta)$ for the high-p_T case, and $F_C(k,\beta=1)$ for the decay case. For these we choose to use the same model function given in Eq. (5.124), translating to the β dependent moment parameters $\Omega_1^{(\beta)}$ and $x_2^{(\beta)}$ using the direct analog of Eq. (5.125). While it would in interesting to explore the dependence on higher moment parameters beyond the $\Omega_2^{(\beta)}$ encoded in x_2, doing so is beyond the scope of this work.

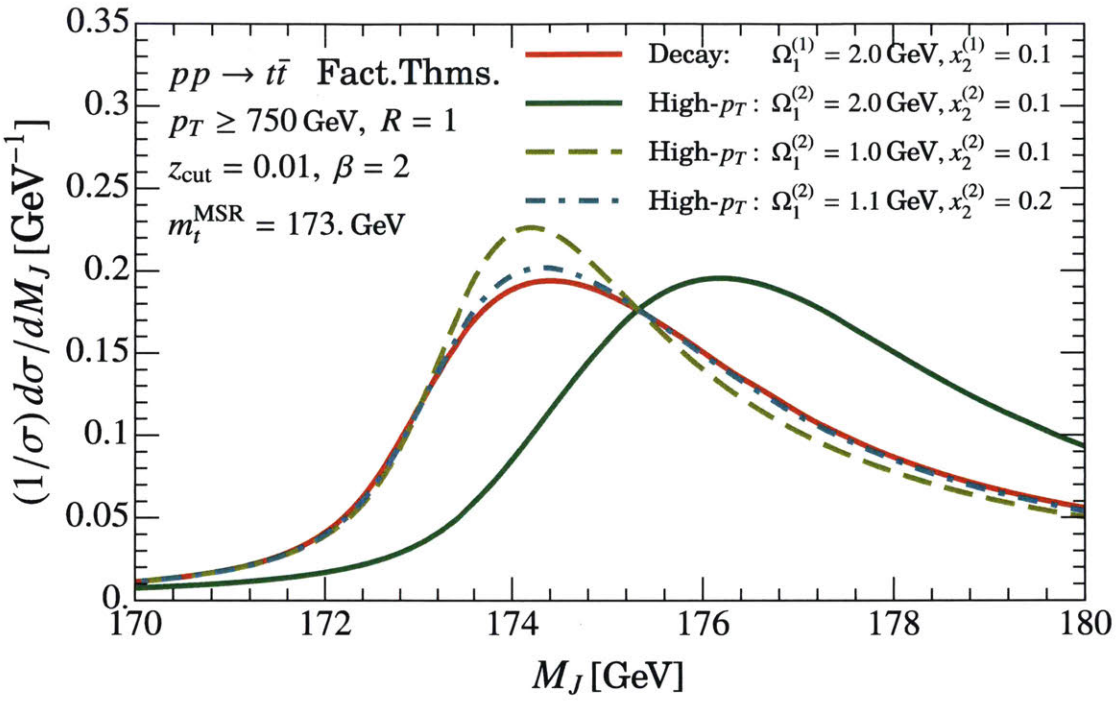

Figure 5-28: Results from the "decay" and "high-p_T" factorization formulae. For the high-p_T case we consider several different choices for the non-perturbative parameters, $\Omega_1^{(2)}$ and $x_2^{(2)}$, with the last choice made so that the cross section is similar to the decay result.

5.5.2 Factorization Theorems: Ω_1 and x_2 dependence

In this and the following sections we explore the dependence of the factorized cross sections on various parameters. For the soft drop factorization theorms the main difference between the decay and high-p_T cases are their predictions for how non-perturbative hadronization corrections precisely effect the M_J differential cross section. For example, in the decay case we have a non-perturbative function $F_C(k', 1)$ which is independent of β, while for the high-p_T case the non-perturbative function is β dependent. These functions are determined by two non-perturbative parameters, $\Omega_1^{(\beta)}$ and $x_2^{(\beta)}$, which may take different values for different values of β.

To explore the dependence on these parameters first consider the cross section results in Fig. 5-28. The solid red and solid green curves take the same values for the parameters, $\Omega_1^{(2)} = \Omega_1^{(1)}$ and $x_2^{(1)} = x_2^{(2)}$ ignoring their β dependence, and we see that this leads to quite different predictions for the jet mass spectrum, with a different peak position and width. If we instead decrease the value of $\Omega_1^{(2)}$ by a factor

of two, then this yields the yellow dashed curve for the high-p_T factorization theorem result, whose peak position, tails, and width are more much closer to the decay result. Changing in addition $x_2^{(2)}$ to 0.2 and increasing $\Omega_1^{(2)}$ slightly to 1.1 GeV yeilds the dot-dashed blue curve for the high-p_T result, which now matches the decay result very closely. This serves as an example of the fact that when we are considering a single p_T bin, that within the range of reasonable nonperturbative parameter variations in the factorization theorems the decay and high-p_T results are essentially equivalent. To explore the dependence on other parameters we therefore adopt the values given by the red solid curve and dot-dashed blue curve as our default values.

The variations in Fig. 5-28 also demonstrate that the cross section is fairly sensitive to non-perturbative corrections. This sensitivity is not unexpected from the structure of our factorization theorems where the entire functions F or F_C play a role in the peak region (this is in contrast to the tail region on the right of the M_J peak where only a single hadronic parameter Ω_1 or $\Omega_1^{(\beta)}$ is important). To explore this further we plot in Fig. 5-29 independent variations of the various Ω_1 and x_2 parameters for the decay, high-$p-T$ and ungroomed factorization theorems respectively. We see that the sensitivity to the Ω_1 parameter is largest in the ungroomed case (bottom-left panel), which occurs because in this case the non-perturbative corrections are enhanced by a factor of Q/m. They are smallest in the decay case (top-left panel) where this enhancement factor is absent, and are in between in the high-p_T case (middle-left panel). Note that we have considered slightly different variations of the parameters Ω_1, $\Omega_1^{(1)}$ and $\Omega_1^{(2)}$ to account for the fact that these parameters also do not have identical meanings. In the panels on the right of Fig. 5-29 we show the corresponding changes from varying x_2 which are always subdominant to the Ω_1 type variations. Again the impact of the x_2 parameters is somewhat different in the three cases, but always modifies the peak region and the tail to the left of the peak.

5.5.3 Factorization Theorem m_t dependence

A crucial dependence for the factorization theorems is that of the top mass parameter m_t that we wish to measure. This dependence turns out to be quite linear with a

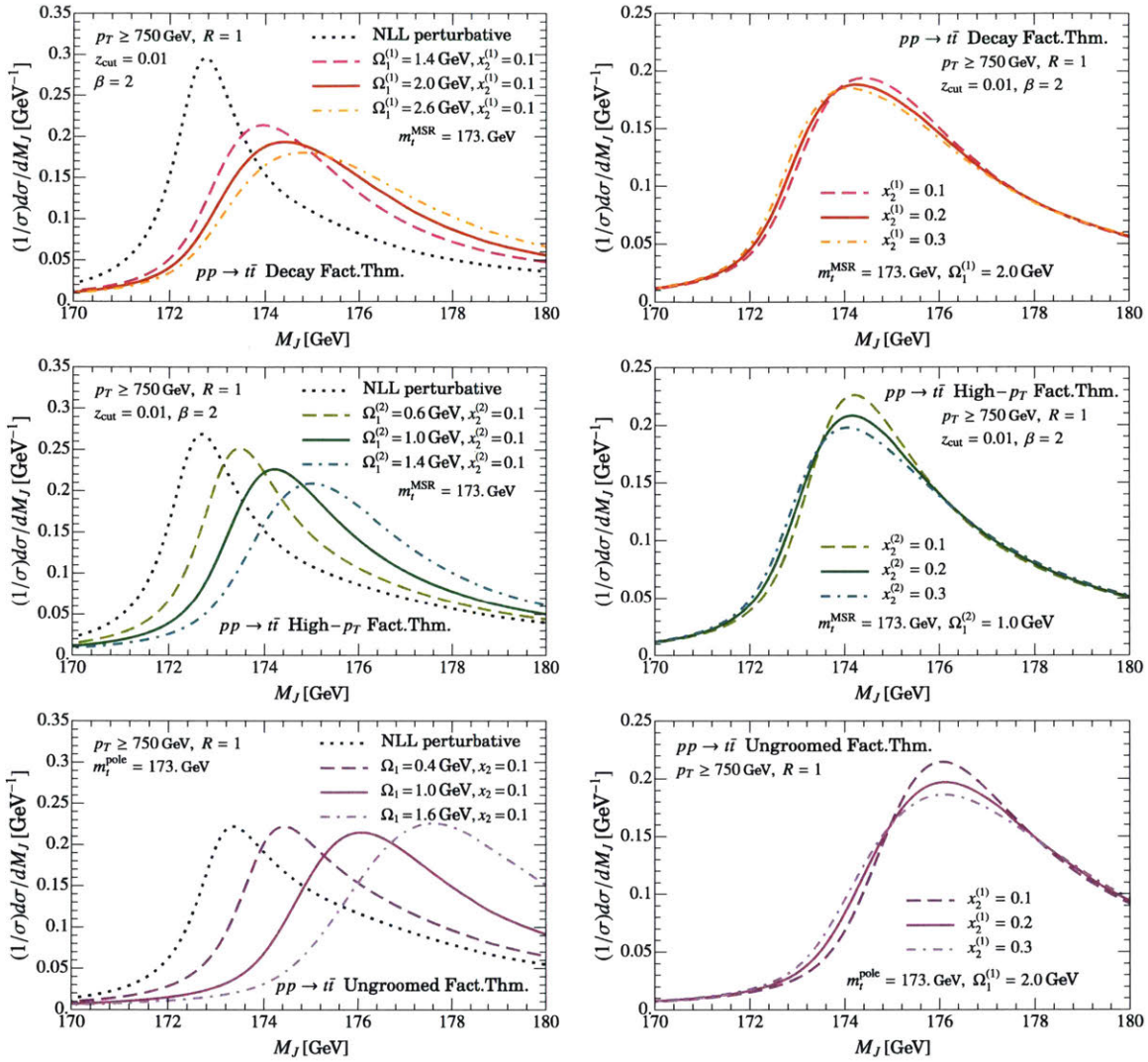

Figure 5-29: Effect of the nonperturbative parameters $\Omega_1^{(\beta)}$ (left panels) and $x_2^{(\beta)}$ (right panels) on the cross sections predicted by the factorization theorem. The top panels are the soft drop decay factorization theorem with $\Omega_1^{(1)}$ and $x_2^{(1)}$, the middle panels the soft drop high-p_T factorization theorem with $\Omega_1^{(2)}$ and $x_2^{(2)}$, and the bottom two panels use the ungroomed factorization theorems with Ω_1 and x_2. In the left panels we also include a dotted curve for the purely perturbative NLL result without hadronization.

change δm_t essentially shifting the peak in the M_J spectrum by the same amount δm_t. This is illustrated in the left panel of Fig. 5-30 using the decay factorization theorem and MSR mass scheme to define m_t, but is also true for the high-p_T and ungroomed versions and with the pole mass definition. For even smaller variations $\delta m_t \simeq 0.2\,\text{GeV}$ the dominant change to the entire M_J spectrum is actually given by

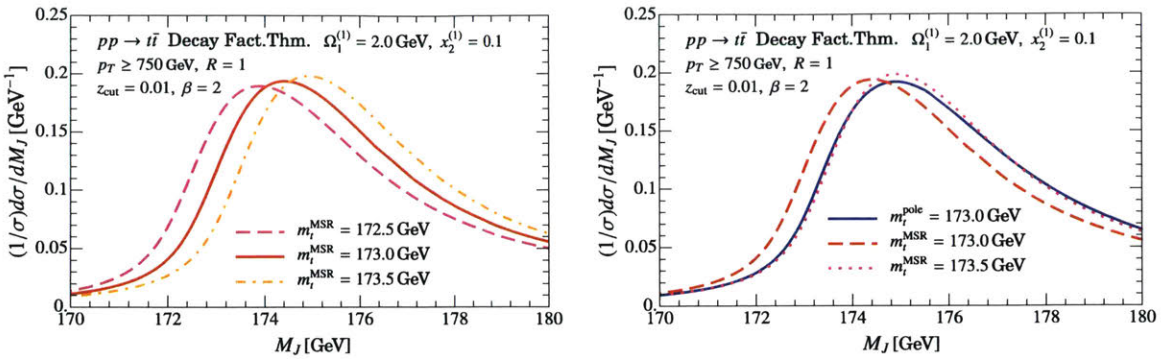

Figure 5-30: (left panel) Dependence on m_t^{MSR} for the decay soft drop factorization theorem, showing that the peak shifts in a manner directly proportional to the value of the top-mass. The dependence in the high-p_T factorization theorem, and ungroomed factorization theorem is very similar and hence not shown. (right panel) Comparison of results in the pole and MSR top mass schemes for the decay factorization theorem. For the reasons discussed in the text, the difference between schemes is primarily a shift, and hence similar spectra can be obtained by using different input masses in the two schemes as shown.

a simple shift.

In the right panel of Fig. 5-30 we compare the type of deviations that occur by changing the top mass scheme. We consider the pole mass m_t^{pole} and the MSR mass, which is scale dependent and hence defined at a reference scale of $R = 1\,\text{GeV}$,

$$m_t^{\text{MSR}} = m_t^{\text{MSR}}(R = 1\,\text{GeV})\,, \tag{5.126}$$

which in Ref. [75, 65] has been argued to be the right scale physically to obtain a value close to that of the Monte Carlo mass m_t^{MC}. The right panel of Fig. 5-30 gives results for the pole mass (blue solid curve) and the MSR mass parameter m_t^{MSR} (red dashed curve) both with a common input value of 173.0 GeV. The peak locations of these curves differ by 0.5 GeV, which is in agreement with the expected size of deviations caused by varying the mass scheme.

In contrast if we increase the MSR mass to 173.5 GeV, yielding the dotted red curve in Fig. 5-30, then we see that it agrees quite well with the pole mass result for 173.0 GeV. Because the jet scale profiles μ_Γ are flat or vary by a small amount in the peak region, the dominant effect of varying the mass scheme between pole and MSR

simply comes from the renormalization group evolution of the MSR mass, $m_t^{\rm MSR}(R)$ from the scale 1 GeV up to the scale μ_Γ of the bHQET jet function. At the NLL order we are working the input value of $m_t^{\rm pole}$ effectively corresponds to $m_t^{\rm MSR}(R)$ with the scale $R = \mu \simeq 5\,\text{GeV}$ as the typical scale μ_Γ appearing in $J_B(\hat{s}_t, \delta m, \Gamma_t, \mu_\Gamma)$. The observed difference in pole and MSR fit results is compatible with the result from evolving between these scales, $m_t^{\rm MSR}(1\,\text{GeV}) - m_t^{\rm MSR}(5\,\text{GeV}) = 0.53\,\text{GeV}$.

We point out that having a correspondence between $m_t^{\rm pole}$ and $m_t^{\rm MSR}$, with a value of $m_t^{\rm pole}$ that is 0.5 GeV smaller than the $m_t^{\rm MSR}$, is not compatible with the pole mass obtained from converting between schemes at one-loop order, $m_t^{\rm pole} = m_t^{\rm MSR}(1\,\text{GeV}) + 0.17\,\text{GeV}$, which has the opposite sign. However, it is known that the pole mass has a renormalon ambiguity of $\sim \Lambda_{\rm QCD}$, so that this conversion is not being carried out by a convergent series, and furthermore that the $m_t^{\rm pole}$ parameter is in general expected to be more unstable than that of the short-distance MSR mass. The fact that the pole mass is scale independent but ambiguous because of the $\sim \Lambda_{\rm QCD}$ renormalon can be directly attributed to the reason why the correspondence between the $m_t^{\rm pole}$ and $m_t^{\rm MSR}$ values that give equivalent cross sections does not agree with a direct conversion between these schemes.[3] In general this should be interpreted as additional uncertainty that is inherent to using the pole mass. For this reason we continue to take the MSR mass as our default for further plots in this section.

5.5.4 Factorization Theorem p_T dependence

For boosted top quarks we require $m/p_T \ll 1$, and as discussed in Sec. 5.2 the soft drop constraints also require a minimum p_T to in order to place us in the desired region for the various expansions. Within the region of validity, the three factorization theorems make somewhat different predictions for the p_T dependence. In both soft drop cases this dependence turns out to be much weaker than that in the non soft-dropped factorization theorem. For the discussion below recall that $Q = 2p_T \cosh(\eta)$.

In the non soft-dropped factorization theorem there is p_T dependence in the per-

[3]For example, if fits for m_t were made in two renormalon free short distance schemes, then one would expect that the perturbative relation between the schemes would be satisfied by the fit results.

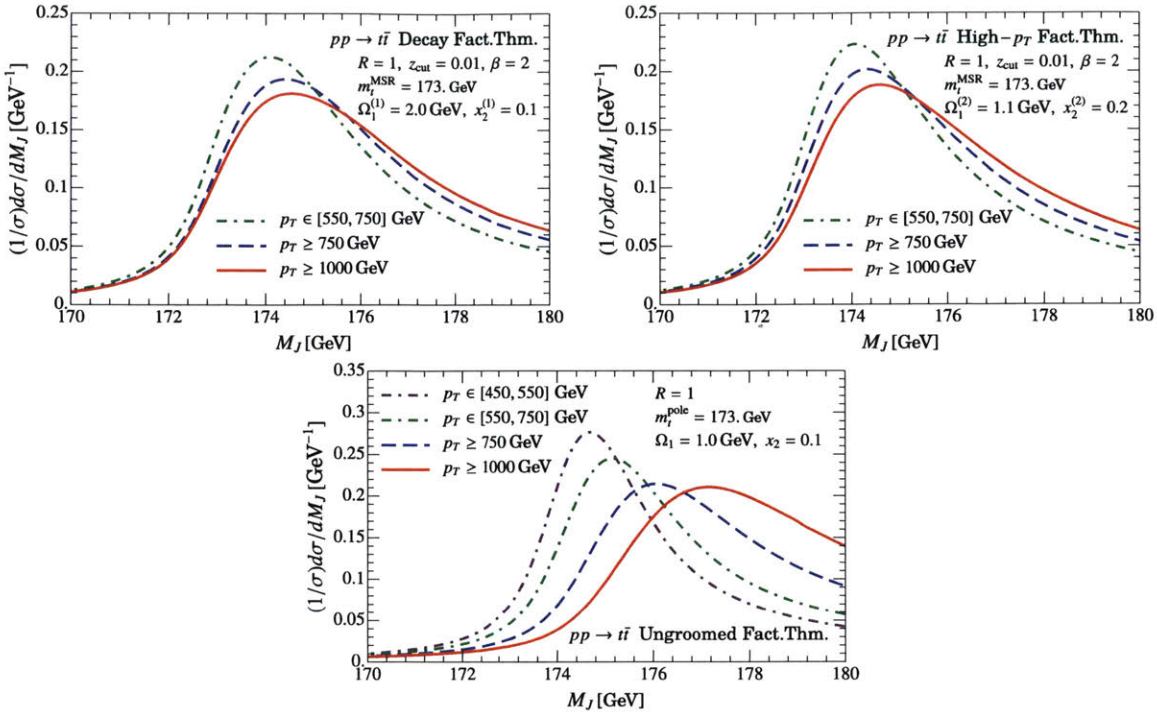

Figure 5-31: Dependence on p_T in the decay factorization theorem (top left panel), high-p_T factorization theorem (top right panel), and ungroomed factorization theorem (bottom panel). The decay and high-p_T variations are very similar but not identical, whereas the ungroomed variations are significantly different. Since the ungroomed factorization may apply at lower p_T, we show a fourth lower p_T bin.

turbative resummation of double logarithms, and from the boost factor Q/m which appears as a multiplicative factor on the momentum ℓ in the argument of the boosted jet function J_B in Eq. (4.51). Since the perturbative soft function $S(\ell - k, \ldots)$ and non-perturbative soft function $F(k, \ldots)$ have momentum appearing at the same level, $\ell - k$, the Q/m boost factor also causes a boost of the corrections from hadronization. For example the factorization theorem yields a peak position that behaves qualitatively as [49]

$$M_J^{\text{peak}}\Big|_{\text{noSD}} \simeq m + (\alpha_s \Gamma_t + \ldots) + \frac{Q\Lambda_{\text{QCD}}}{m}\,. \tag{5.127}$$

Here the second term includes perturbative corrections that depend on the mass scheme, and the last term is from the boosted hadronization effects.

For the decay factorization theorem in Eq. (5.88) there is still a p_T dependence

in the Sudakov logarithms that appear between the jet and collinear-soft scales, but these scales are numerically closer. In addition the impact of the non-perturbative soft function is modified by the presence of a m/Q factor appearing in the convolution between the perturbative collinear-soft function $S_C\big[(\ell - hkm/Q)Q_{\text{cut}}\big]$ and the non-perturbative collinear-soft function $F_C(k)$. This m/Q factor encodes the fact that the decay products approach the jet axis as the jet is boosted to larger Q values. When considering the impact of hadronization on the jet mass, this m/Q compensates the Q/m boost factor in J_B, leading for example to a stable peak position as p_T is varied,

$$M_J^{\text{peak}}\Big|_{\text{decay}} \simeq m + (\alpha_s\Gamma_t + \ldots) + \Lambda_{\text{QCD}} + \ldots\,. \tag{5.128}$$

Here the last displayed term is from the hadronization, and the final ellipses denote subleading m/Q dependent contributions.

In the case of the high-p_T factorization theorem there is the same p_T dependence in the Sudakov logarithms as the decay case, but a modified dependence in the hadronization corrections. Due to the form of Eq. (5.70) there is a reduced p_T dependence relative to the no soft drop case, but still more remaining p_T dependence than the decay factorization theorem case. In particular for the peak position we have

$$M_J^{\text{peak}}\Big|_{\text{high}-p_T} \simeq m + (\alpha_s\Gamma_t + \ldots) + \frac{Q^{\frac{\beta}{1+\beta}}\Lambda_{\text{QCD}}^{\frac{1}{1+\beta}}}{m(2^\beta z_{\text{cut}})^{\frac{1}{1+\beta}}}\,. \tag{5.129}$$

In our default boosted p_T region of $p_T \simeq 700$–1000 GeV the predictions from Eqs. (5.128) and (5.129) are hard to distinguish numerically (and indeed we have seen that the factorization theorems can give very similar spectra).

In Fig. 5-31 we show results for the p_T dependence of the three factorization theorems. As anticipated this dependence is largest for the ungroomed factorization theorem (bottom panel), which differs from the groomed cases. For the high-p_T and decay results (top panels) the p_T dependence is actually quite similar for the range of p_Ts we consider, further adding to evidence that both formulas will be able to give

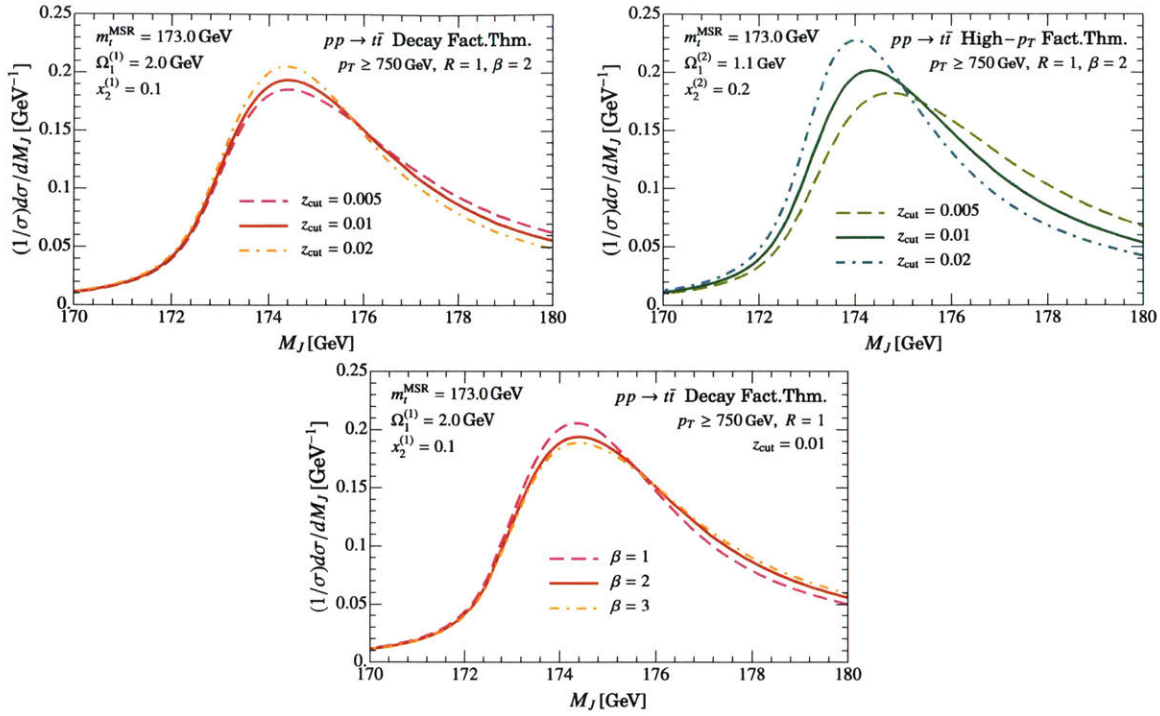

Figure 5-32: Dependence on $z_{\rm cut}$ in the decay factorization theorem (top left panel), $z_{\rm cut}$ in the high-p_T factorization theorem (top right panel), and β in the decay factorization theorem (top left panel). We do not show β dependence for high-p_T since its non-perturbative parameters depend on β. All results here are at NLL and may be modified by fixed order corrections that are not included here.

accurate predictions for the range of p_Ts we are interested in. For much higher p_T differences between the two soft drop factorization theorems would become evident.

5.5.5 Soft Drop Factorization Theorems: $z_{\rm cut}$ and β dependence

Finally, we turn to the dependence of the soft drop factorization theorems on the grooming parameters $z_{\rm cut}$ and β. Since the $z_{\rm cut}$ dependence only appears in perturbatively calculable functions it can be seen as a prediction of the factorization theorem. In Fig. 5-32 (top two panels) we plot the dependence on $z_{\rm cut}$ predicted by the decay and high-p_T factorization theorems. We see that this dependence is predicted to be more mild in the case of decay, than it is in the case of high-p_T. Thus varying $z_{\rm cut}$ can provide a handle on distinguishing between the two, as well as providing an additional

handle to help break potential degeneracies when fitting parameters like m_t, $\Omega_1^{(\beta)}$ and $x_2^{(\beta)}$.

In the decay case the β dependence is also perturbatively calculable just like $z_{\rm cut}$ since the non-perturbative function $F_C(k,1)$ is β independent. This is in contrast to the high-p_T case where the non-perturbative function $F_C(k,\beta)$ depends on β, and hence we can not make predictions for the β dependence without specifying $\Omega_1^{(\beta)}$ and $x_2^{(\beta)}$. Again this non-trivial difference occurs due to the treatment of non-perturbative corrections in the two factorization theorems and is an important distinction. In Fig. 5-32 (bottom panel) we plot the β dependence predicted by the decay factorization theorem. Interestingly we see that the variation from β is very degenerate with varying $z_{\rm cut}$ in the decay factorization theorem (compare the bottom and top-left panels).

It is important to realize that although the dominant factorization theorem depends to some extent on non-perturbative dynamics, that the preferred factorization theorem can actually be directly determined directly with data. This can be done simply by carrying out analyses on the same event sample but with grooming done using different parameter choices, including both choices for $z_{\rm cut}$, as well as for example using both $\beta = 1$ and $\beta = 2$.

5.6 Factorization Results versus Pythia

In this section we make direct comparisons between the factorization theorems and PYTHIA8 results. We focus on a comparison with the "decay" and "high-p_T" soft drop factorization formulae in Eqs. (5.70) and (5.88), but also consider the ungroomed factorization theorem in Eq. (4.51). As default soft drop parameters we take $z_{\rm cut} = 0.01$ and $\beta = 2$, and initial jets with a radius of $R = 1$. For this analysis all perturbative functions in the factorization theorems are taken at tree-level with next-to-leading-logarithmic (NLL) order resummation and an input value of the strong coupling as $\alpha_s(m_Z) = 0.118$. In the factorization theorems we use the MSR short distance top mass scheme $m_t^{\rm MSR}(R)$ [67, 66] and include it's leading logarithmic evolution from

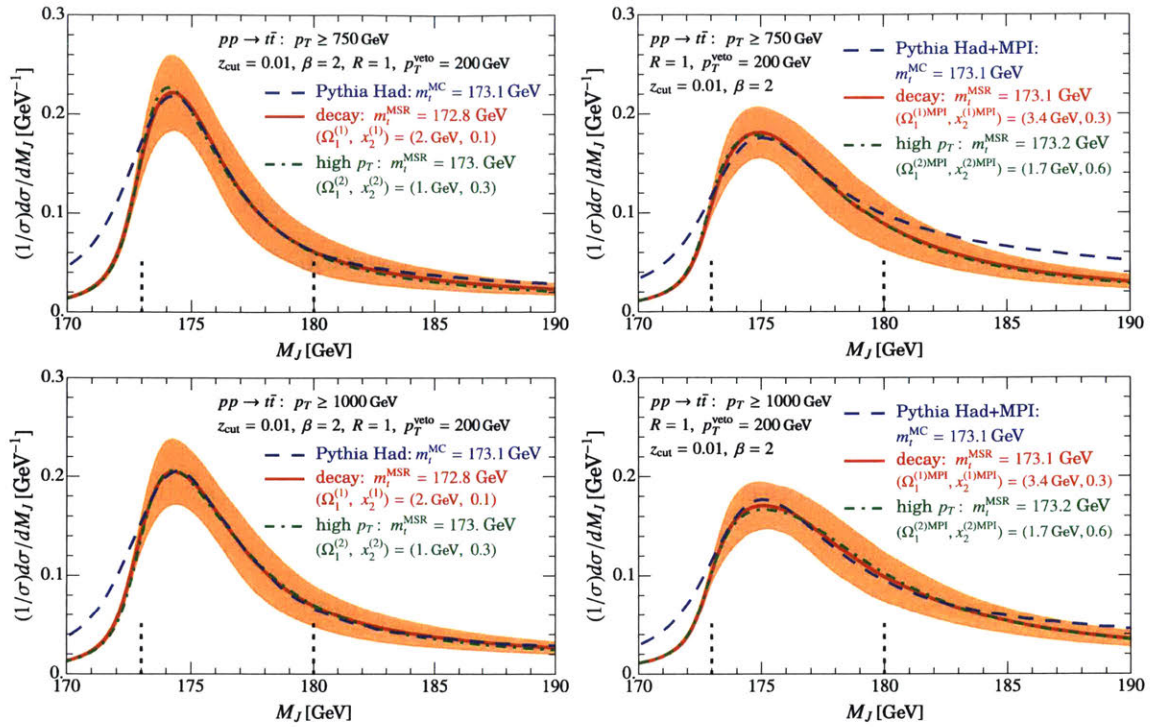

Figure 5-33: Comparison of PYTHIA8 without and with MPI to the "decay" and "high-p_T" factorization theorems at NLL. The m_t parameter is in the MSR mass scheme for the factorization theorems here. The top-mass parameter in PYTHIA8 is referred to as $m_t^{\rm MC}$.

a reference scale $R = 1\,\text{GeV}$ to the scale μ_Γ in J_B. We also consider results with the pole mass scheme. In PYTHIA8 we fix the top mass as $m_t^{\rm MC} = 173.1\,\text{GeV}$ where the MC reminds us that the mass definition depends on details of the Monte Carlo implementation including the shower cutoff and interface with hadronization.

The results in this section should be considered to be a first numerical calibration of the meaning of the $m_t^{\rm MC}$ parameter in simulations like PYTHIA8 by determining a direct correspondence to a Lagrangian mass parameter implemented through the hadron level factorization theorems. This approach was pioneered in Ref. [27] for $e^+e^- \to t\bar{t}$ and a measurement of 2-jettiness, where results up to next-to-next-to-leading-logarithmic order with NLO fixed order corrections are available. A key open question from this work was whether it could be extended to $pp \to t\bar{t}$ at hadron colliders, and our analysis here answers this question in the affirmative. Ref. [27] carried out a more sophisticated analysis of theoretical uncertainties, and correlations

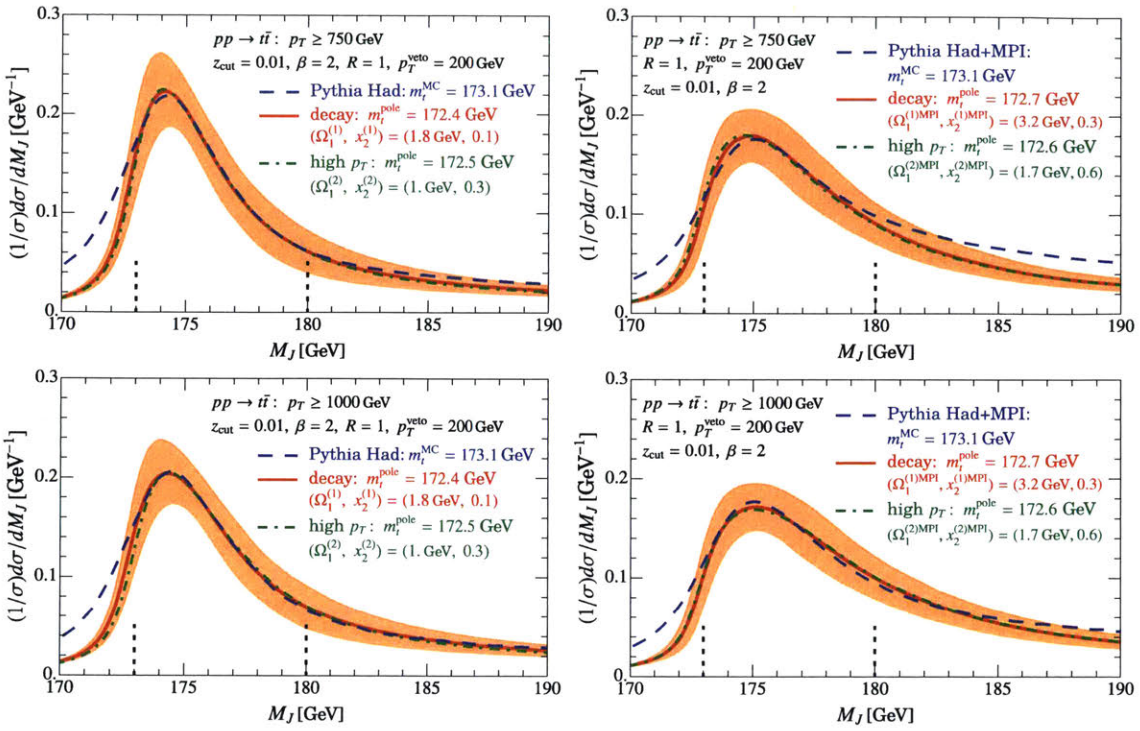

Figure 5-34: Comparison of PYTHIA8 without and with MPI to the "decay" and "high-p_T" factorization theorems at NLL. The m_t parameter is in the pole-mass scheme for the factorization theorems here. The top-mass parameter in PYTHIA8 is referred to as $m_t^{\rm MC}$.

between uncertainties than we will carry out here. (In the future our exploratory analysis should be extended to this level of analysis, in particular once full NNLL results for the soft drop top cross section are available.) In particular we do not intend to quote here the final uncertainties for the fit parameters, but will try to give some indication for what one may roughly anticipate the size of these uncertainties to be.

5.6.1 Soft Drop Pythia and Factorization Comparison

In Fig. 5-33 we show a comparison of PYTHIA8 results with the "decay" and "high-p_T" factorization formulae. As fit parameters in the factorization results we take the MSR mass $m_t^{\rm MSR} \equiv m_t^{\rm MSR}(R = 1\,\text{GeV})$, and the two non-perturbative parameters $\Omega_1^{(\beta)}$ and $x_2^{(\beta)}$. We do a simultaneous fit of these parameters to results for the $p_T \geq 750\,\text{GeV}$ and $p_T \geq 1000\,\text{GeV}$ bins. For the fit range we take $M_J \in [173, 180]\,\text{GeV}$, over which

the curves are also normalized. To maximize the use of shape information we compare cross sections for 10 bins in this range, using a χ^2 function that provides more weight to the peak of the distribution to simulate the fact that experimental uncertainties are expected to be smaller there. To obtain the best fit values we do a scan over values of the parameters with step size of 0.1 GeV for m_t and $\Omega_1^{(\beta)}$, and of step size of 0.1 for $x_2^{(\beta)}$ (also including the value $x_2^{(\beta)} = 0.05$).

In the upper two plots of Fig. 5-33 we include only hadronization in PYTHIA8, whereas the lower two plots also include MPI. The orange band shows the perturbative NLL uncertainty on the "decay" result, from varying scales in the factorization theorem through our profile functions. The values of p_T being considered are close to the upper limit of Eq. (5.29) (both above and below it), and our fits show that both factorization theorems actually reproduce the PYTHIA8 results quite accurately in the fit range.

The $m_t^{\rm MSR}$ fit values obtained from the fits in Fig. 5-33 are within 0.3 GeV of the input $m_t^{\rm MC}$. The variation between the five best fit values from the scan is $\Delta m_t^{\rm MSR} = \pm 0.3$ GeV for both the Had and Had+MPI fits, so we conclude that these values agree within the anticipated uncertainties. This is compatible with theoretical expectations for this mass parameter [75, 65], as well as results from the e^+e^- calibration analysis in [27]. We also observe that the fit values of $m_t^{\rm MSR}$ are compatible between the "decay" and "high-p_T" results (within 0.2 GeV), and between results with and without MPI effects (within 0.3 GeV). As anticipated, the dominant effect of adding MPI is to significantly increase the scale of the hadronization parameter, for example going from $\Omega_1^{(1)} = 2\,\text{GeV}$ to $\Omega_1^{(1)\rm MPI} = 3.4\,\text{GeV}$. Interestingly the fit values for $\Omega_1^{(2)}$ and $\Omega_1^{(2)\rm MPI}$ for the high-p_T factorization theorem give values that are half as large, in agreement with the rough comparisons of the theory results in Sec. 5.5.2. Adding MPI also modifies the fit results for $x_2^{(\beta)}$. The fact that $m_t^{\rm MSR}$ unchanged and only the hadronic parameters are modified is crucial, and validates that our approach to modeling the UE/MPI effects is working as anticipated. This fact is what enables a precision m_t to be obtained from this method.

In Fig. 5-33 and other fits given below there is a noticeable difference between the

factorization theorem results and PYTHIA8 for the tail on the left of the peak. For this reason we have purposely started the fit region at 173 GeV so that it includes less of the region on the left of the peak. We discuss this left of the peak region further in Sec. 5.6.5 below.

Since the soft drop factorization theorems provide control over the top mass scheme we can also repeat the analysis using the pole mass instead of the MSR mass. The analog of Fig. 5-33 showing the fit to PYTHIA8 with hadronization and hadronization+MPI is now given by Fig. 5-34. Summarizing and comparing the fit values with soft drop and PYTHIA8 with just Hadronization we have

$$\begin{aligned}
&\text{Had, decay, MSR :} && m_t^{\text{MSR}} = 172.8\,\text{GeV}, && \Omega_1^{(1)} = 2.0\,\text{GeV}, && x_2^{(1)} = 0.1\,, \\
&\text{Had, decay, pole:} && m_t^{\text{pole}} = 172.4\,\text{GeV}, && \Omega_1^{(1)} = 1.8\,\text{GeV}, && x_2^{(1)} = 0.1\,, \\
&\text{Had, high-}p_T\text{, MSR :} && m_t^{\text{MSR}} = 173.0\,\text{GeV}, && \Omega_1^{(1)} = 1.0\,\text{GeV}, && x_2^{(1)} = 0.3\,, \\
&\text{Had, high-}p_T\text{, pole:} && m_t^{\text{pole}} = 172.5\,\text{GeV}, && \Omega_1^{(1)} = 1.0\,\text{GeV}, && x_2^{(1)} = 0.3\,,
\end{aligned} \tag{5.130}$$

while the corresponding results including both Hadronization and MPI in PYTHIA8 are

$$\begin{aligned}
&\text{Had+MPI, decay, MSR:} && m_t^{\text{MSR}} = 173.1\,\text{GeV}, && \Omega_1^{(2)\text{MPI}} = 3.4\,\text{GeV}, && x_2^{(2)\text{MPI}} = 0.3\,, \\
&\text{Had+MPI, decay, pole:} && m_t^{\text{pole}} = 172.7\,\text{GeV}, && \Omega_1^{(2)\text{MPI}} = 3.2\,\text{GeV}, && x_2^{(2)\text{MPI}} = 0.3\,, \\
&\text{Had+MPI, high-}p_T\text{, MSR:} && m_t^{\text{MSR}} = 173.2\,\text{GeV}, && \Omega_1^{(2)\text{MPI}} = 1.7\,\text{GeV}, && x_2^{(2)\text{MPI}} = 0.6\,, \\
&\text{Had+MPI, high-}p_T\text{, pole:} && m_t^{\text{pole}} = 172.6\,\text{GeV}, && \Omega_1^{(2)\text{MPI}} = 1.7\,\text{GeV}, && x_2^{(2)\text{MPI}} = 0.6\,.
\end{aligned} \tag{5.131}$$

We observe that the m_t^{pole} values from the fit are 0.4–0.7 GeV smaller than the input m_t^{MC}. Again the variations between the five best fit values in the scan are at the $\Delta m_t^{\text{pole}} = \pm 0.3\,\text{GeV}$ level for both the Had and Had+MPI fits, so in this case the m_t^{pole} values are noticeably smaller than the input m_t^{MC} mass. This is compatible with the e^+e^- calibration result in [27]. These results show that the pole mass cannot be directly identified with the MC top mass. The obtained values of m_t^{pole} are

also compatible within uncertainties between the "decay" and "high-p_T" results, and between results with and without MPI effects, though in general we observe larger variations in the pole scheme than we do in MSR. Once again, the dominant effect of adding MPI is to significantly increase the scale of the hadronization parameters $\Omega_1^{(\beta)}$ and to modify $x_2^{(\beta)}$.

As can be seen from Eqs. (5.130) and (5.131) the values of the $\Omega_1^{(\beta)}$ and $x_2^{(\beta)}$ parameters remain very stable when comparing corresponding MSR and pole mass fits. For the top mass values the m_t^{pole} fit results give numbers that are 0.4–0.6 GeV smaller than the corresponding $m_t^{\text{MSR}}(1\,\text{GeV})$ fit results. At the NLL order we are working the difference between the fit in the two mass schemes comes from the evolution of $m_t^{\text{MSR}}(R)$. At this order the fit value of m_t^{pole} effectively corresponds to $m_t^{\text{MSR}}(R)$ with the scale $R = \mu \simeq 5\,\text{GeV}$ as the typical scale appearing in the $J_B(\hat{s}_t, \delta m, \Gamma_t, \mu)$ jet function. The observed difference in pole and MSR fit results is compatible with the result from evolving between these scales, $m_t^{\text{MSR}}(1\,\text{GeV}) - m_t^{\text{MSR}}(5\,\text{GeV}) = 0.53\,\text{GeV}$. This effect was also discussed above in Sec. 5.5.3, where we attributed it as being compatible with known deficiencies of the pole mass scheme. The determination of m_t^{pole} is expected to be more uncertain than that of the short-distance MSR mass. This is compatible with interpreting the difference between the results from directly fitting for m_t^{pole}, and obtaining m_t^{pole} via the MSR fit result, as an additional uncertainty in the pole mass.

5.6.2 Predictions for higher z_{cut} and lower β

Having determined the parameters of the soft drop factorization theorems we can now make predictions for other amounts of soft drop grooming. Here we consider predictions coming from the decay factorization theorem where both the z_{cut} and β dependence are calculable. In the left panels of Fig. 5-35 we show the factorization predictions (red curves) obtained when we double z_{cut} to $z_{\text{cut}} = 0.02$. The upper panel shows the parameters fixed from the Had fit, while the bottom panel shows those obtained from the Had+MPI fit. Also shown in the left panels of Fig. 5-35 are results from PYTHIA8 for this value of z_{cut} (dashed blue curves), which agree well

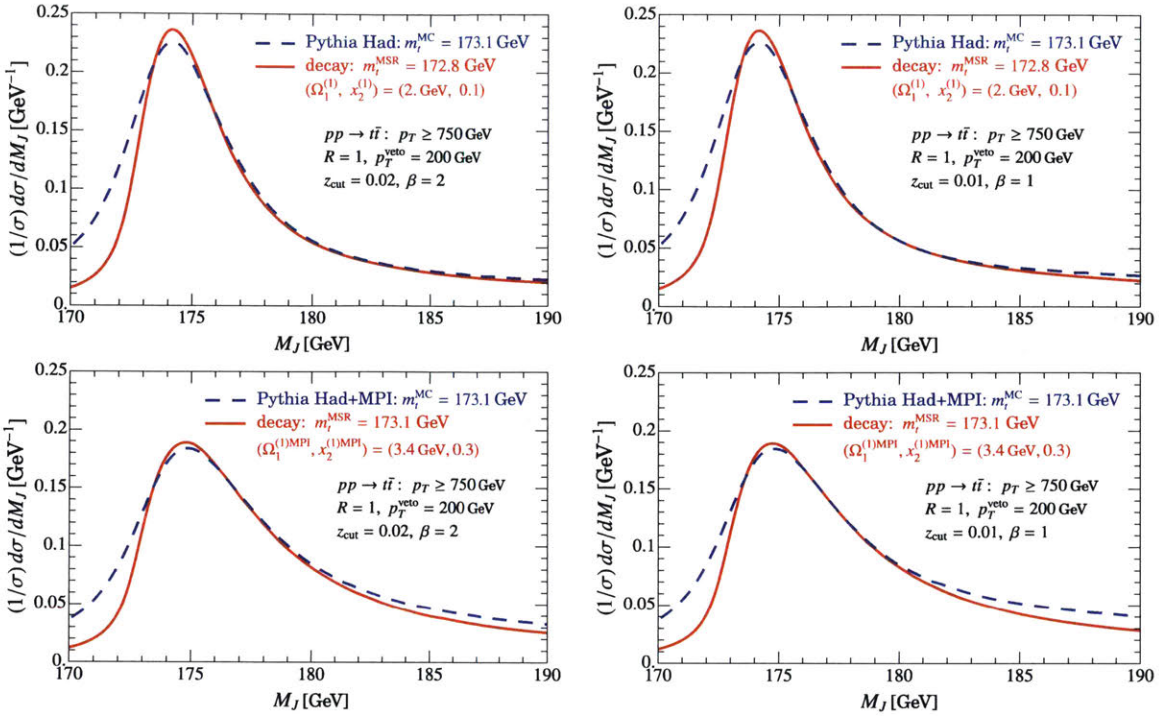

Figure 5-35: Predictions from the decay factorization theorem for values of the soft drop parameters other than the $z_{\text{cut}} = 0.01$ and $\beta = 2$ used for the fit. Results are compared to PYTHIA8 where the (left panel) varies to $z_{\text{cut}} = 0.02$ and the (right panel) varies to $\beta = 1$. These two variations are observed to yield very similar cross sections.

with the factorization results over a wide range of M_J values (an exception again being the region to the left of the peak). These results seem promising, showing that the fit results are pertinent, and can make meaningful predictions. Since the z_{cut} dependence of the high-p_T factorization theorem is stronger than that of decay, it fits the PYTHIA8 results from this variation less well. (This implies that PYTHIA8 agrees better with the decay factorization theorem, but does not necessarily answer the question as to which data prefers.)

Also shown in Fig. 5-35, in the two right panels, are predictions from varying β to $\beta = 1$ in the decay factorization theorem (red lines). These again agree well with the PYTHIA8 results (blue dashed curves). In fact we observe that the $z_{\text{cut}} = 0.01 \to 0.02$ variation and $beta = 2 \to 1$ variation are close to having degenerate effects on the cross section. The dependence on z_{cut} and β does not immediately provide a simple explanation for this degeneracy.

5.6.3 Soft Drop Results for Smaller p_T

Another possible variation that can be considered are different bins in p_T. While we leave a more detailed exploration of these variations to the future, a relevant question is whether the soft drop factorization theorem can be applied to smaller p_T values than those included in our fit, and where precisely do the predictions break down. This is particularly interesting since in the short term data from CMS and ATLAS will still be most statistically significant for smaller p_T.

In Fig. 5-36 we make predictions from both the decay and high-p_T factorization theorems for a bin with smaller p_T in the range $[550, 750]$ GeV. The left panel shows the results compared to PYTHIA8 with only hadronization, and still exhibit nice agreement within the theoretical uncertainty band, and in particular for the peak location. On the other hand in the right panel of Fig. 5-36 we show the prediction when MPI is included, and here theory and PYTHIA8 are no longer in agreement. In particular the peak positions now differ by 0.8 GeV and the shapes are quite different. We attribute this to the fact that $p_T \in [550, 750]$ GeV is becoming close to the boundary allowed by the expansions in our soft drop factorization theorem, and that the soft drop is no longer as effective for grooming the extra soft particles present with MPI turned on, and hence that higher order terms in the soft drop factorization expansions are becoming important. This initial exploration therefore appears to indicate that we should consider $p_T \gtrsim 700$ GeV to ensure the validity of the soft drop factorization theorems. It should be noted that adding this lower p_T bin in the soft drop based fit of Sec. 5.6 does not change this conclusion, since the results from this type of fit clearly exhibit tensions between the higher and lower p_T bins.

5.6.4 Comparison of Pythia and Factorization without grooming

In this section we repeat the comparison between factorization and PYTHIA8 but using the cross sections without jet grooming. While there are clear advantages to using

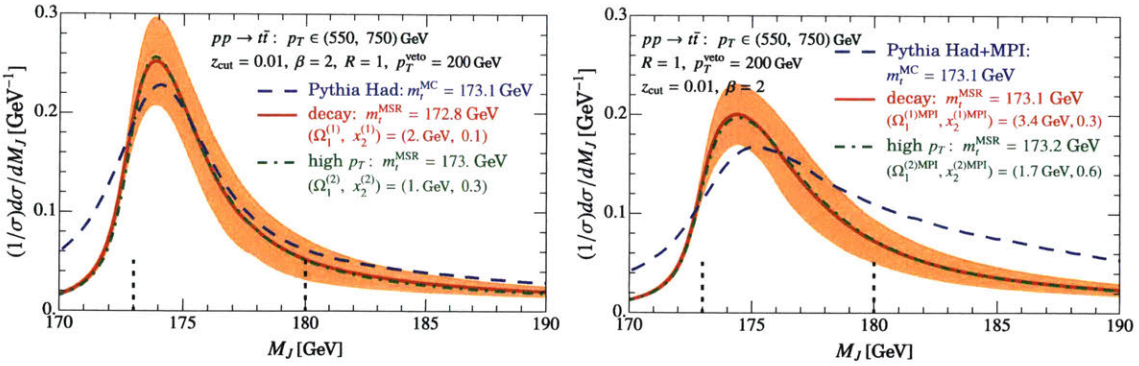

Figure 5-36: Comparison for a smaller p_T bin of PYTHIA8 without and with MPI to the "decay" and "high-p_T" factorization theorems at NLL. The factorization results use the values obtained from the fit to the higher p_T bins. Here m_t is in the MSR mass scheme, and the pole scheme results look very similar.

grooming, the extra theoretical expansions involved in deriving the soft drop factorization theorem also require jets with larger p_T than the ungroomed case. Indeed we have seen in Sec. 5.6.3 that the soft drop factorization predictions appear to be breaking down in the presence of MPI when considering a bin with $p_T \in [550, 750]$ GeV. It is therefore interesting to consider whether we could make predictions for smaller p_T if we considered the ungroomed cross section and use Eq. (4.51). This also will provide a test of whether we are able to handle the much larger amount of soft radiation from UE/MPI with the approach we have adopted that is based on using a modified parameters in the non-perturbative function F.

Much like our soft drop analysis, we carry out the fit using two bins in p_T, this time taking $p_T \in [550, 750]$ GeV and $p_T \geq 750$ GeV so as to focus on smaller p_T. Because of the larger peak shifts from both hadronization and MPI, we also adjust our fit windows, taking $M_J \in [173, 184]$ for the hadronization case and $M_J \in [173, 190]$ for the case including MPI. Other than these changes, the analysis stradegy is the same as for the fits done in Sec. 5.6, in particular the parameters are still $m_t^{\rm MSR}$, plus Ω_1, and x_2, which are now determining the function F.

The results of the fit are shown in Fig. 5-37 with solid magenta curves for the ungroomed factorization theorem, and dashed blue curves for the input PYTHIA8 results. We see that the factorization theorem results accurately reproduce PYTHIA8 both inside and above the fit window, even though we have included a lower p_T bin

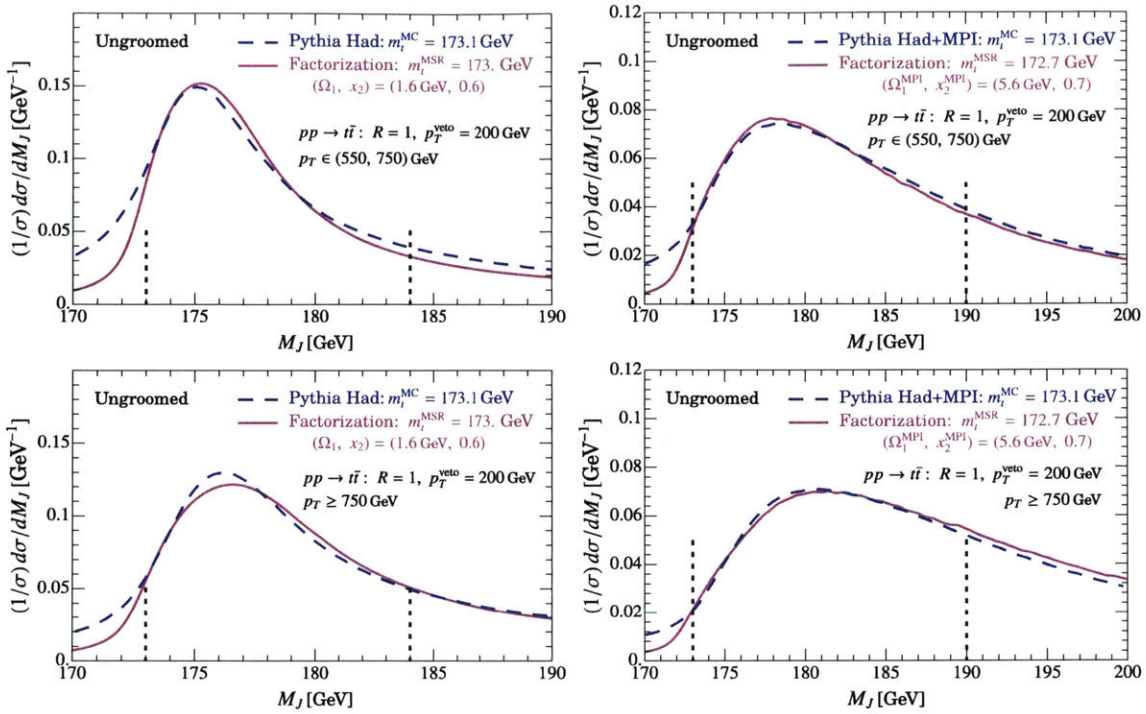

Figure 5-37: Comparison of PYTHIA8 and the fit with the factorization theorem at NLL for the case without grooming. The fit regions are shown by the vertical dashed lines. In the factorization theorem we take the m_t parameter in the MSR scheme.

than was done for the soft drop fit. Examining the values of the parameters obtained from the fit, we see that m_t^{MSR} is within 0.1 GeV of the input m_t^{MC} mass, is only modified by 0.3 GeV by the introduction of MPI. Comparing the best five fits we find variations of $\Delta m_t^{\text{MC}} = \pm 0.2\,\text{GeV}$, and again we conclude that these results for the masses are compatible within uncertainties. The dominant effect of adding MPI is to significantly modify the parameter Ω_1 which here goes from $\Omega_1 = 1.6\,\text{GeV}$ to the much larger value of $\Omega_1^{\text{MPI}} = 5.6\,\text{GeV}$. The larger value obtained for Ω_1^{MPI} is fully consistent with the larger amount of soft radiation present in the jet in this ungroomed study.

As a test of the quality of the fit we can also then make predictions for a smaller p_T bin. Considering a bin with $p_T \in [450, 550]\,\text{GeV}$ we obtain the predictions shown by the solid magenta curve in Fig. 5-38. The corresponding PYTHIA8 results are shown by the dashed blue curves. We see that the predictions agree quite well even for this small p_T, making it seem quite promising to apply the ungroomed factorization to analyze data at smaller p_T. Since this relies more heavily on the modeling of

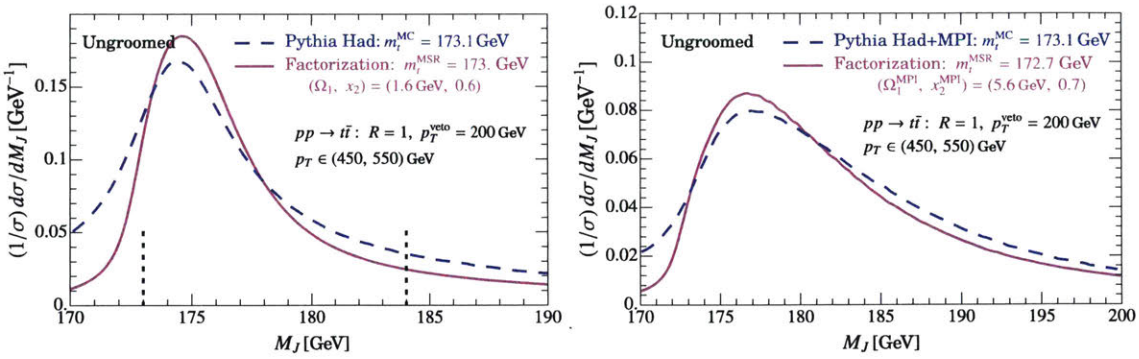

Figure 5-38: Predictions of the factorization theorem at NLL for the case without grooming compared to PYTHIA8 for a lower p_T bin. Parameters are taken from the fit to higher p_T bins, including m_t which is in the MSR scheme.

underlying event using the approach discussed in Sec. 4.5, there will be a larger theoretical uncertainty here. Using our earlier conservative 30% estimate would yield an uncertainty of $\sim 1.3\,\text{GeV}$, however the model does appear to work much better than that when comparing with PYTHIA8 and hence it is possible that this is an overestimate. Clearly this should be studied further in the near future by including more p_T bins, studying other values of the jet radius parameter R, and also providing profile variations to account for perturbative uncertainties.

It is also interesting to compare the results for the ungroomed factorization fit using the MSR mass scheme and pole mass scheme for m_t. The quality of the pole mass fits is very similar to that of the MSR mass fits shown in Fig. 5-37, and for that reason we do not display the plots here. A summary of the fit values for the various cases is given by

$$\begin{aligned}
&\text{Had, MSR mass:} && m_t^{\text{MSR}} = 173.0\,\text{GeV}, && \Omega_1 = 1.6\,\text{GeV}, && x_2 = 0.6\,, \\
&\text{Had, pole mass:} && m_t^{\text{pole}} = 172.1\,\text{GeV}, && \Omega_1 = 1.6\,\text{GeV}, && x_2 = 0.5\,, \\
&\text{Had+MPI, MSR mass:} && m_t^{\text{MSR}} = 172.7\,\text{GeV}, && \Omega_1^{\text{MPI}} = 5.6\,\text{GeV}, && x_2^{\text{MPI}} = 0.7\,, \\
&\text{Had+MPI, pole mass:} && m_t^{\text{pole}} = 172.3\,\text{GeV}, && \Omega_1^{\text{MPI}} = 5.4\,\text{GeV}, && x_2^{\text{MPI}} = 0.7\,.
\end{aligned} \tag{5.132}$$

Here we see significantly smaller values of m_t^{pole}, which are however still compatible

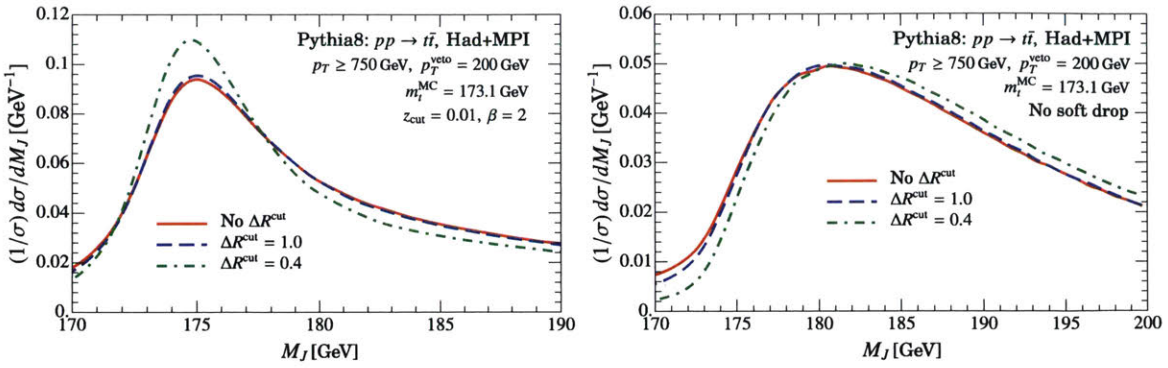

Figure 5-39: Comparing effect of ΔR cut on jets wit grooming (left panel) and without grooming (right panel).

with those obtained from the soft drop fits. We also see that in the pole scheme the value of m_t^{pole} remains stable when adding MPI, and the value of various hadronic parameters are very compatible with those obtained from the earlier fit in the MSR mass scheme.

5.6.5 ΔR cut on top decay products

Finally we return to the question of the disagreement between PYTHIA8 and factorization for the tail on the left of the peak in the M_J spectrum. Recall that in the factorization theorem the underlying contributions to the spectrum are a Breit-Wigner distribution that is dressed by perturbative Sudakov logarithms and soft perturbative and non-perturbative corrections. The Sudakov logarithms smear the spectrum above the physical threshold and hence have little effect in the offshell region to the left of the peak. Likewise the non-perturbative corrections tend to shift and broaden the entire spectrum. We do expect that the tail to the left of the peak will be affected by events where the decay products are outside the $R = 1$ jet cone, or are close to the boundary within the cone. It is also possible that the cross section in this region could be influenced by our use of the $\overline{\text{MS}}$ scheme when defining the Ω_1 and $\Omega_1^{(\beta)}$ parameters, since these are known to have an $\sim \Lambda_{\text{QCD}}$ renormalon themselves which can modify the spectrum near the threshold (see for example Ref. [74]). Another possible explanation is that PYTHIA8's description of the cross section in this region

may also be impacted by approximations used in the simulation of the top decay and associated shower dynamics. We leave exploration of the latter two possibilities to future work.

To test the impact of the first possibility we can compare the impact on the M_J spectra of making an angular cut to only keep events where each top decay product is within an angle ΔR^{cut} of the jet axis. In Fig. 5-39 we show the impact of this cut both with soft (left panel) and without soft drop (right panel). The curve without any such cut is solid red, while taking $\Delta R^{\text{cut}} = 1.0\,\text{GeV}$ gives the dashed blue curve. This imposes a restriction that all top decay products are within the jet, and as we can see this has a negligible effect on the M_J spectrum either with or without soft drop. The only visible effect is in the no soft drop case there is a small decrease to the cross section on the left of the peak, consistent with some of the out of cone decay products yielding contamination in this region. If we consider an even stronger $\Delta R^{\text{cut}} = 0.4\,\text{GeV}$ then the impact becomes visible for both the soft drop and no soft drop cases. Here we see a modification of the cross section on the left of the peak in both cases, indicating that events with decay products at wider angles are somewhat responsible for the behavior of the cross section to the left of the peak.

It is likely that both the factorization and PYTHIA8 predictions could be improved in this left of peak region, and we leave further exploration of this issue to the future.

5.7 Outlook for Utilizing Experimental Data

Above we have carried out an extensive analysis of predictions from our factorization formulae for the jet mass differential cross section. The main goal of using this cross section is to determine the top-mass in a short distance scheme. In this section we discuss the best short term method for combining our results with experimental data. Predictions from the decay and high-p_T versions of the factorization theorems are not distinguishable for the relevant range of p_Ts where there will be a statistically significant data set in the foreseeable future, so we will assume that soft drop based analyses are carried out with the decay version (which is slightly closer to the predictions of

PYTHIA8). An alternative is to make use of the factorization theorem without soft drop, since for smaller p_T values evidence was shown in Sec. 5.6.4 that it works better than the soft drop based results. As mentioned earlier, there are two basic methods to utilize our results: i) by making a direct comparison of the factorization based result to experimental data, fitting the top-mass m_t together with the hadronic parameters Ω_1 and x_2, and ii) by carrying out a calibration study fitting the same parameters in the factorization result to Monte Carlo predictions, thus determining a translation between $m_t^{\rm MC}$ and a top mass in a short distance scheme.

The major challenge for a direct comparison of the soft drop factorization theorem with data is the limited statistics at the higher p_T's that are required by our light grooming constraints. From the preliminary study in Sec. 5.6 it appears that a direct comparison with the soft drop groomed factorization theorem would require $p_T \gtrsim 700\,\text{GeV}$. There are much fewer top events at such large p_Ts, for example the number of events in the $p_T \in [700, 800]\,\text{GeV}$ bin is 4% of those in the $p_T \in [400, 500]\,\text{GeV}$ bin from the analysis of $19.7\,\text{fb}^{-1}$ of data in Ref. [40]. A recent study carried out a top-mass extraction from ungroomed jet-mass measurements by CMS in Ref. [107], using $p_T \geq 400\,\text{GeV}$ with cuts on ΔR and $p_T^{\rm veto}$. They found that the dominant uncertainties were the limited statistics for highly boosted tops, the unfolding of data to particle level, and Monte Carlo theory modeling, were quite significant $\Delta m_t^{\rm stat} = 6.0\,\text{GeV}$, $\Delta m_t^{\rm unfold} = 4.6\,\text{GeV}$, and $\Delta m_t^{\text{MC-theory}} = 4.0\,\text{GeV}$ using $19.7\,\text{fb}^{-1}$ of data at $\sqrt{s} = 8\,\text{TeV}$. We have seen in Sec. 5.6.4 that without grooming we are still able to predict the jet mass spectrum for $p_T \geq 450\,\text{GeV}$, where there are significantly more events. Thus for a direct comparison between the factorization spectrum and data the ungroomed factorization theorem is currently the most promising avenue, and it is possible that it may remain so in the near future. Both our soft drop and ungroomed studies also show that the extraction of the top mass can be done by fitting only three parameters: m_t, Ω_1, and x_2. The use of the ungroomed factorization theorem comes at a higher cost due to the larger impact of underlying event, and hence the associated larger uncertainty for the m_t extraction from modeling this effect. The results in Sec. 5.6.4 indicate that the simple model discussed in Sec. 4.5 works very

well, but this deserves further study, for example by testing results from Monte Carlos other than PYTHIA8. Although we obtain a good fit when the hadronic function F_C is parameterized by its first two moments, it would also be worth exploring the impact of the third and higher moments in a dedicated study (particularly given the large values of x_2 favored by some of our fits).

One important assumption we made was that pile-up can be handled experimentally in a way that does not significantly modify the interpretation of the jet-mass spectrum. While we have showed that light grooming at the level of $\sim 1\%$ is still very effective in reducing the effects of underlying event, it is not clear if it will provide the same level of effectiveness for removing pile-up in top-mass studies. The more typical stronger grooming, at the 10% level, modifies the spectrum of the original hard event in a manner that is beyond the range of validity of our soft drop factorization formulae. If direct comparison to data is carried out with our ungroomed factorization theorem then of course the use of grooming to handle pileup must be avoided. On the other hand, track based pileup methods such as charged-hadron subtraction or jet area subtractions [31] may well enable the jet mass spectrum of the primary hard collision to be reconstructed with a less dramatic impact on the spectrum. If the effects of such a method of handling pile-up are at worst similar to that of underlying event, that is to leave behind extra soft particles in the jet without disturbing the energetic decay products and associated radiation, then they can be handled by the same model that we have used for underlying event (see Sec. 4.5). This would mean simply modifying the interpretation of the same hadronic parameters which are being fit to the data

$$\Omega_1 \to \Omega_1^{\text{MPI+Pile up}}, \qquad x_2 \to x_1^{\text{MPI+Pile up}}. \tag{5.133}$$

Methods for treating pileup can be directly studied by comparing fits with these hadronic parameters to Monte Carlo simulations, which should determine whether this treatment will suffice at the desired level of precision. Such studies were beyond the scope of this work, but should be straightforward to carry out given the results

derived here.

In the second approach, using the factorization theorem to calibrate Monte Carlo, we are not directly constrained by the statistics of the high-p_T experimental datasets, since the Monte Carlo can be fit at multiple large p_T values and then used to extrapolate to lower p_T where the experimental analysis is carried out. In this case it is best to use the soft drop factorization theorem, both because of its simplicity in treating the isolated top jet, and because of its much reduced sensitivity to underlying event. We have shown through our NLL study in Sec. 5.6 that the MC top mass parameter $m_t^{\rm MC}$ can be calibrated by comparison with soft drop factorization results for a couple of p_T bins. This analysis can be further improved by considering simultaneous fits with more p_T bins, and other choices for $z_{\rm cut}$ and β. It can also be improved by increasing the perturbative order to NNLL, adding non-singular $\mathcal{O}(\alpha_s)$ corrections, and by analyzing perturbative uncertainties using a statistical method that carries out fits for many choices of profile parameters (all things that we intend to explore in the near future). One may also choose to use the MC to extrapolate in parameters other than p_T to go outside the range of the soft drop factorization theorem, such as in $z_{\rm cut}$, or by allowing the angular separation between decay products to increase to the point where they are reconstructed as separate jets. The main assumption here is that the meaning of the $m_t^{\rm MC}$ parameter is unchanged by these extrapolations. In general one expects that the closer the experimental analysis is to calibration study, and thus the fewer extrapolations used, that the more likely this is to be the case. Our results obtained in Sec. 5.6 for $pp \to t\bar{t}$ at NLL order with soft drop are in agreement with the more thorough e^+e^- calibration study at NNLL+$\mathcal{O}(\alpha_s)$ order without jet grooming presented in Ref. [27]. This agreement lends credibility to the fact that it may be safe to extrapolate the Monte Carlo away from the calibration region, in order to exploit experimentally favorable configurations.

The above considerations provide our best recommendation at this time, given our current state of theoretical knowledge: i) Prior to obtaining enough statistics at higher p_T, a direct comparison with experimental data with moderate boosts $p_T \gtrsim 450\,\text{GeV}$ should be carried out with the ungroomed factorization theorem. ii) Further

improvements to the Monte Carlo calibration study for $pp \to t\bar{t}$ should be carried out with the light soft drop factorization theorem and bins with $p_T \geq 700\,\text{GeV}$. To reduce extrapolation uncertainty the experimental analysis should still try to maintain similar choices for parameters, such as $z_{\text{cut}} = 0.01$.

There are also future avenues to explore theoretically, which may further improve the direct comparison to soft drop groomed jets. Given that light grooming and requirement of high p_T are both experimentally unfavorable, it would be interesting to explore whether top jets with more aggressive grooming and lower p_T can be described by effective field theory methods. One fact that makes this potentially possible is that the top-decay products can stop the soft drop groomer because of their commensurate energies, and thus protect the ultra-collinear radiation inside the groomed radius. We have seen from the PYTHIA8 study in Fig. 5-14 that the peak position actually remains quite stable even if we continue to increase z_{cut} beyond the range of validity of our light-grooming factorization. We provided a possible explanation in Sec. 5.1.3 that beyond the value of z_{cut} given by Eq. (5.33) the collinear-soft mode no longer moves with the soft drop curve but rather stays on the vertical line in Fig. 5-14. Exploring the feasibility of describing this new regime through factorization may allow us to go beyond the current constraint imposed by the light groomed factorization theorems.

Chapter 6

Hard Matching between SCET and bHQET

In this chapter we provide a result for the $\mathcal{O}(\alpha_s^2)$ correction to H_m at the scale $\mu \simeq m_t$ for the e^+e^--collider setup. This work is published in Ref. [72]. In Refs. [49, 50, 75] the hemisphere dijet invariant mass distribution in the peak region for the production of boosted tops in e^+e^- annihilation was suggested as an observable:

$$\begin{aligned}\frac{1}{\sigma_0}\frac{d\sigma}{\mathrm{d}M_t^2\,\mathrm{d}M_{\bar{t}}^2} &= H_Q\left(Q,\mu\right) H_m\left(m_t,\frac{Q}{m_t},\mu\right)\int d\ell^+ d\ell^- S(\ell^+,\ell^-,\mu) \\ &\quad\times J_B\left(\frac{M_t^2-m_t^2-Q\ell^+}{m_t},\Gamma_t,\delta m,\mu\right) J_B\left(\frac{M_{\bar{t}}^2-m_t^2-Q\ell^-}{m_t},\Gamma_t,\delta m,\mu\right) \\ &\quad\times\left[1+\mathcal{O}\left(\frac{m_t\alpha_s}{Q}\right)+\mathcal{O}\left(\frac{m_t^2}{Q^2}\right)+\mathcal{O}\left(\frac{\Gamma_t}{m_t}\right)+\mathcal{O}\left(\frac{\hat{s}_{t,\bar{t}}^2}{m_t^2}\right)\right]. \end{aligned} \tag{6.1}$$

We note that it is possible that the $\mathcal{O}(m_t\alpha_s/Q)$ power corrections indicated in Eq. (6.1) are absent, but we are not aware of a rigorous proof at this time.

The exact algorithm to determine the two jet regions and the precise form of the observable is irrelevant for the structure of Eq. (6.1) as long as parametrically $M_t \sim M_{\bar{t}}$, but does matter for the explicit perturbative expressions of its ingredients. The restriction $M_t \sim M_{\bar{t}}$ avoids large logarithms of the form $\ln(M_t/M_{\bar{t}})$, and is satisfied by variables designed to study the peak region of both jets, such as thrust. In the analysis of Ref. [50] all particles were assigned to either of the two top jets

depending on which hemisphere with respect to the thrust axis they enter. Thus the observable considered was physically close to event-shape distributions. The analysis of Ref. [50] for this inclusive jet observable was carried out at NLL′, i.e. including perturbative ingredients at $\mathcal{O}(\alpha_s)$ and NLL resummation. At the time of writing the hard function H_Q, the bHQET jet function and the soft function are already known up to $\mathcal{O}(\alpha_s^2)$ [98, 78, 83] or beyond, while resummation can be carried out to N^{3}LL. Thus, the only relevant correction missing to perform a N^{3}LL analysis for the double hemisphere invariant mass distribution and similar observables in the peak region is the hard function H_m at $\mathcal{O}(\alpha_s^2)$. This correction will affect the normalization of the differential cross section, while the shape of the cross section is determined mainly by the jet and soft functions.

The outline of the sections is as follows: In Sec. 6.1 we outline two methods to perform the computation. Instead of directly calculating the current matching factor between bHQET and SCET, we can also exploit the knowledge of the QCD heavy quark form factor calculated in Refs. [19, 59] and various properties of the EFT to extract the hard function. In Sec. 6.2 we carry out the computation at $\mathcal{O}(\alpha_s^2)$ using this method and show how to handle issues associated with the number of active quark flavors. This yields the result given in Eq. (6.34) in terms of the pole mass. In the two loop expression for H_m we find terms of the form

$$\alpha_s^2 C_F T_F \ln\left(\frac{Q^2}{m^2}\right) \ln^{0,1,2}\left(\frac{\mu^2}{m^2}\right). \tag{6.2}$$

The large logarithm $\ln(Q^2/m^2)$ is induced by the separation in rapidity of soft mass-shell fluctuations with the scaling $(p^+, p^-, p_\perp) \sim (m, m, m)$ from collinear mass-shell fluctuations with $(p^+, p^-, p_\perp) \sim (m^2/Q, Q, m)$. It can not be eliminated by a choice of μ or summed by the RGE in μ. This effect is directly related to virtual top quark loops which first appear at $\mathcal{O}(\alpha_s^2)$, and has been discussed in detail in Refs. [61, 103] together with other subtleties concerning the incorporation of a massive quark in primary massless jet production in SCET. In Sec. 6.3 we will explicitly carry out the matching calculation for the $\mathcal{O}(\alpha_s^2 C_F T_F)$ correction with primary massive top quarks,

and demonstrate how the amplitudes factorize into collinear and soft components which each involve a single rapidity scale. We show that this factorization is the same as that for massless external quarks, computed in Ref. [103], up to a different constant term that appears in the collinear corrections. The direct computation of the SCET soft and collinear diagrams at $\mathcal{O}(\alpha_s^2 C_F T_F)$ can be performed elegantly by first computing the virtual correction for the radiation of a "massive gluon" at one-loop and performing in a second step a dispersion integral. In Sec. 6.4 we show how to resum the type of rapidity logarithm in Eq. (6.2) using the framework of the rapidity renormalization group established in Refs. [38, 37]. We also demonstrate that the residual scale dependence of H_m on μ significantly decreases when employing the complete two-loop correction, and assess the impact of the rapidity logarithm.

6.1 Setup and Notation

As described in Refs. [49, 50] for the description of the peak region we first match QCD onto SCET, and then SCET onto bHQET. We stress that in SCET the top quark is considered as dynamical and hence the RGE takes place with six active flavors, while for the ingredients that arise in bHQET there are only five dynamical flavors in the evolution. The relevant current operators needed to define the hard functions in Eq. (6.1) are

$$\begin{aligned} \mathcal{J}_{\rm QCD} &= \bar\psi(x)\Gamma_i^\mu\psi(x)\,, \\ \mathcal{J}_{\rm SCET} &= \bar\chi_n S_n^\dagger \Gamma_i^\mu S_{\bar n}\chi_{\bar n}\,, \\ \mathcal{J}_{\rm bHQET} &= \bar h_{v_+} W_n Y_n^\dagger \Gamma_i^\mu Y_{\bar n} W_{\bar n}^\dagger h_{v_-}\,, \end{aligned} \tag{6.3}$$

where $\Gamma_v^\mu = \gamma^\mu$ and $\Gamma_a^\mu = \gamma^\mu\gamma_5$. The jet fields $\chi_n = W_n^\dagger\xi_n$ and $\chi_{\bar n} = W_{\bar n}^\dagger\xi_{\bar n}$ describe the collinear radiation in SCET, and contain the massive collinear quarks ξ_n and $\xi_{\bar n}$ [92, 106] and Wilson lines $W_{n,\bar n}$ where in position space $W_n^\dagger(x) = \mathrm{P}\exp\big(ig\int_0^\infty ds\,\bar n\cdot A_n(\bar n s + x)\big)$. The ultracollinear radiation in bHQET is described by the heavy quark fields $h_{v_{+,-}}$ and by $W_{n,\bar n}$. The wide-angle radiation in SCET is described by soft

Wilson lines $S_{n,\bar{n}}$, where in position space $S_n^\dagger(x) = \mathrm{P}\exp\left(ig\int_0^\infty ds\, n\cdot A_s(ns+x)\right)$, and ultrasoft Wilson lines $Y_{n,\bar{n}}$ are the analogs with ultrasoft gluon fields in bHQET. The difference between the SCET fields and bHQET fields is that SCET still contains soft and collinear fluctuations at the top mass scale, i.e. the SCET fields contain mass mode fluctuations which scale as $(p^+, p^-, p_\perp) \sim (m, m, m)$ and $(Q, m^2/Q, m)$ or $(m^2/Q, Q, m)$ which are absent in bHQET. This makes our EFT above the top mass scale an $\mathrm{SCET_{II}}$ type theory. There are six flavors in the $\overline{\mathrm{MS}}$ running coupling in QCD and SCET, and five flavors in bHQET.

The notation above differs from Ref. [50] which used a hybrid of $\mathrm{SCET_I}$ and $\mathrm{SCET_{II}}$, where the current operator was written as

$$\widetilde{\mathcal{J}}_{\mathrm{SCET}} = \bar{\chi}_n Y_n^\dagger S_n^\dagger \Gamma_i^\mu S_{\bar{n}} Y_{\bar{n}} \chi_{\bar{n}} \,. \tag{6.4}$$

Here the Wilson lines $S_{n,\bar{n}}$ describe exclusively soft mass mode fluctuations and have ultrasoft zero-bin subtractions. In Eq. (6.3) the SCET operator only describes soft fluctuations above and of order of the mass scale m, and not far below m. This simplifies the setup for the matching coefficient calculation, which in particular can be viewed as going from a six flavor theory to a five flavor theory.

The matching coefficients between these effective theories are defined by

$$\mathcal{J}_{\mathrm{QCD}}^{(n_l+1)} = C_Q^{(n_l+1)}\, \mathcal{J}_{\mathrm{SCET}}^{(n_l+1)} \big[1 + \mathcal{O}(m/Q)\big] \,, \tag{6.5}$$

$$\mathcal{J}_{\mathrm{SCET}}^{(n_l+1)} = C_m^{(n_f)}\, \mathcal{J}_{\mathrm{bHQET}}^{(n_l)} \big[1 + \mathcal{O}(\hat{s}/m)\big] \,. \tag{6.6}$$

Here both the currents and Wilson coefficients refer to the renormalized quantities. When we refer to the bare objects we will indicate this explicitly as e.g. in $\mathcal{J}_{\mathrm{SCET}}^{(\mathrm{bare},n_l+1)}$. For all quantities we consider we use the renormalized coupling constant. When we want to separate the color structures of the matching coefficients we will do so in the following way:

$$C_Q^{(n_l+1)} = 1 + C_Q^{(1,\,n_l+1)} + C_Q^{(C_F^2,\,n_l+1)} + C_Q^{(C_F C_A,\,n_l+1)} + C_m^{(C_F n_l T_F,\,n_l+1)} + C_Q^{(C_F T_F,\,n_l+1)} ,$$

$$C_m^{(n_f)} = 1 + \underbrace{C_m^{(1,n_f)}}_{\mathcal{O}(\alpha_s)} + \underbrace{C_m^{(C_F^2,n_f)} + C_m^{(C_F C_A,n_f)} + C_m^{(C_F n_l T_F,n_f)} + C_m^{(C_F T_F,n_f)}}_{\mathcal{O}(\alpha_s^2)} . \quad (6.7)$$

In all the objects above the coupling is renormalized in the $\overline{\text{MS}}$ scheme with the number of dynamical flavors, n_f, being either n_l or $(n_l + 1)$ as indicated by the superscript. Here n_l is the number of light quarks, and the additional flavor indicates the heavy quark (here the top quark). The choice for the number of flavors in each of the expressions above is motivated by the scales at which these objects live compared to the top mass. Note that we have kept the number of flavors appearing in C_m unspecified, as it can be expressed in either the n_l- or the $(n_l + 1)$-flavor scheme. We will be explicit about which scheme we are using in the equations below.

The hard functions in Eq. (6.1) are related to the Wilson coefficients via

$$H_Q(Q,\mu) = |C_Q|^2, \qquad H_m\left(m, \frac{Q}{m}, \mu\right) = |C_m|^2 . \quad (6.8)$$

Here the dependence on Q in the hard function H_m appears due to the boost factor Q/m.

In Eq. (6.1) all the functions live at their respective scales and are evolved to a common scale μ_{final} through renormalization group running. While the jet and the soft functions have convolution running [50], the large logarithms of the hard matching coefficients are summed by multiplicative evolution factors,

$$\begin{aligned} H_{\text{evol}}(Q, m, \mu_{\text{final}}; \mu_Q, \mu_m, \nu_Q, \nu_m) \equiv{}& H_Q^{(n_l+1)}(Q, \mu_Q)\, U_{H_Q}^{(n_l+1)}(Q, \mu_Q, \mu_m) \quad (6.9) \\ & \times H_m^{(n_l)}\left(m, \frac{Q}{m}, \mu_m; \nu_Q, \nu_m\right) U_v^{(n_l)}\left(\frac{Q}{m}, \mu_m, \mu_{\text{final}}\right), \end{aligned}$$

for $\mu_Q \simeq Q$, $\mu_m \simeq m$ and $\mu_{\text{final}} < \mu_m$. On the LHS the dependence on μ_Q and μ_m only comes from higher order corrections when the objects in Eq. (6.9) are truncated at a given order in resummed perturbation theory. The same is true for the rapidity scales ν_Q and ν_m, which are induced by the rapidity RGE that will be discussed further below and in Sec. 6.4.1. We will frequently drop these arguments that appear

after the semicolon. The evolution factors here obey the RG equations

$$\begin{aligned}
\mu\frac{\mathrm{d}}{\mathrm{d}\mu}U_{H_Q}^{(n_l+1)}(Q,\mu_Q,\mu) &= -\gamma_{H_Q}^{(n_l+1)}(Q,\mu)\,U_{H_Q}^{(n_l+1)}(Q,\mu_Q,\mu)\,,\\
\mu\frac{\mathrm{d}}{\mathrm{d}\mu}U_{v}^{(n_l)}\left(\frac{Q}{m},\mu,\mu_{\text{final}}\right) &= +\gamma_{v}^{(n_l)}\left(\frac{Q}{m},\mu\right)U_{v}^{(n_l)}\left(\frac{Q}{m},\mu,\mu_{\text{final}}\right),
\end{aligned} \tag{6.10}$$

where $\gamma_v^{(n_l)}$ is the anomalous dimension for the squared current in bHQET.

Eqs. (6.5) and (6.6) suggest two different methods that one can use to calculate the $\mathcal{O}(\alpha_s^2)$ piece of C_m or equivalently H_m:

1) *Indirect calculation using the known result for C_Q and the matrix elements for the QCD and bHQET current operators in pure dimensional regularization:*

Using Eq. (6.5) and (6.6), and taking matrix elements of the operators with onshell top-quark states as in [49], we have

$$\langle\mathcal{J}_{\text{QCD}}^{(n_l+1)}\rangle = C_Q^{(n_l+1)}\,C_m^{(n_l)}\,\langle\mathcal{J}_{\text{bHQET}}^{(n_l)}\rangle\,. \tag{6.11}$$

Using the relation between bare and renormalized bHQET currents

$$\langle\mathcal{J}_{\text{bHQET}}^{(n_l)}\rangle = Z_{\text{bHQET}}^{(n_l)}\,\langle\mathcal{J}_{\text{bHQET}}^{(\text{bare},\,n_l)}\rangle\,, \tag{6.12}$$

we get

$$C_m^{(n_l)} = \frac{\langle\mathcal{J}_{\text{QCD}}^{(n_l+1)}\rangle}{C_Q^{(n_l+1)}\,Z_{\text{bHQET}}^{(n_l)}\,\langle\mathcal{J}_{\text{bHQET}}^{(\text{bare},\,n_l)}\rangle}\,. \tag{6.13}$$

Note that the terms on the RHS involve objects with different flavor number schemes for the strong coupling, which must all be converted to n_l-flavors to get $C_m^{(n_l)}$. Here we work in dimensional regularization for both UV and IR divergences and renormalize the quantities in the $\overline{\text{MS}}$ scheme. With this regulator we can use the known two loop result for the heavy form factor $\langle\mathcal{J}_{\text{QCD}}\rangle$ given in Refs. [19, 59]. The result for C_Q is also known [98, 97] in $\overline{\text{MS}}$, and the result for $Z_{\text{bHQET}}^{(n_l)}$ can be determined by RG consistency

as discussed below. Loop graphs in bHQET factorize into ultrasoft and ultra-collinear contributions, and in general each involve at most a single dimensionful scale. The use of dimensional regularization for both the UV and IR, and employing onshell external quarks, imply that these loop corrections in bHQET are scaleless and vanish, such that $\langle \mathcal{J}^{(\text{bare},n_l)}_{\text{bHQET}} \rangle = 1$. In general, the IR divergences in the QCD and bHQET matrix elements will match up, and the UV divergences in $\langle \mathcal{J}^{(\text{bare},\,n_l)}_{\text{bHQET}} \rangle$ are eliminated by the counterterm $Z^{(n_l)}_{\text{bHQET}}$. In dimensional regularization with $1/\epsilon_{\text{IR}} = 1/\epsilon_{\text{UV}}$, this implies a cancellation of $1/\epsilon$ poles between $\langle \mathcal{J}^{(n_l+1)}_{\text{QCD}} \rangle$ and $Z^{(n_l)}_{\text{bHQET}}$. Thus we can use the simpler relation

$$C_m^{(n_l)} = \frac{\langle \mathcal{J}^{(n_l+1)}_{\text{QCD}} \rangle}{Z^{(n_l)}_{\text{bHQET}}\, C_Q^{(n_l+1)}} \,. \tag{6.14}$$

2) *Direct calculation by matching the SCET and bHQET current operators:*

Using Eq. (6.6) we can also just directly compute the Wilson coefficient from a matching calculation, computing partonic matrix elements using the same IR regulator in SCET and bHQET,

$$C_m^{(n_l)} = \frac{\langle \mathcal{J}^{(n_l+1)}_{\text{SCET}} \rangle}{\langle \mathcal{J}^{(n_l)}_{\text{bHQET}} \rangle} \equiv \frac{F^{(n_l+1)}_{\text{SCET}}}{F^{(n_l)}_{\text{bHQET}}} \,. \tag{6.15}$$

These matrix elements are form factors in the respective theories which we denote by F. We will use the same notation for the color structures in the perturbative expansion of F_{SCET} and F_{bHQET} as in Eq. (6.7). We define the relation between bare and renormalized SCET currents by

$$\langle \mathcal{J}^{(n_l+1)}_{\text{SCET}} \rangle = Z^{(n_l+1)}_{\text{SCET}}\, \langle \mathcal{J}^{(\text{bare},\,n_l+1)}_{\text{SCET}} \rangle \,. \tag{6.16}$$

As usual the bare currents are μ-independent, so from Eqs. (6.12), (6.15) and (6.16) the μ-RG equation for $C_m^{(n_l)}$ can be written as

$$\mu \frac{\mathrm{d}}{\mathrm{d}\mu} \ln C_m^{(n_l)} = \Big[\gamma^{(n_l+1)}_{\text{SCET}}(Q,\mu) - \gamma^{(n_l)}_{\text{bHQET}}\Big(\frac{Q}{m},\mu\Big) \Big](\alpha_s^{(n_l)}) \equiv \gamma_\mu^{C_m}(Q,m,\mu) \,, \tag{6.17}$$

where the current anomalous dimensions are computed order-by-order from the counterterms in the standard fashion

$$\gamma_{\rm SCET}^{(n_l+1)}(Q,\mu) = \mu\,\frac{\rm d}{{\rm d}\mu}\ln Z_{\rm SCET}^{(n_l+1)}\,, \qquad \gamma_{\rm bHQET}^{(n_l)}\Big(\frac{Q}{m},\mu\Big) = \mu\,\frac{\rm d}{{\rm d}\mu}\ln Z_{\rm bHQET}^{(n_l)}\,. \tag{6.18}$$

The anomalous dimension for the SCET current is known to 3-loop order [99]. Up to two loops the result reads

$$\begin{aligned}\gamma_{\rm SCET}^{(n_l+1)}(Q,\mu) = {}& \frac{\alpha_s^{(n_l+1)}(\mu)C_F}{4\pi}\big[-4L_Q+6\big] + \left(\frac{\alpha_s^{(n_l+1)}(\mu)}{4\pi}\right)^2\bigg\{C_F^2\big[3-4\pi^2+48\zeta_3\big] \\ & + C_FC_A\bigg[-\left(\frac{268}{9}-\frac{4\pi^2}{3}\right)L_Q+\frac{961}{27}+\frac{11\pi^2}{3}-52\zeta_3\bigg] \\ & + (n_l+1)C_FT_F\bigg[\frac{80}{9}L_Q-\frac{260}{27}-\frac{4\pi^2}{3}\bigg]\bigg\}\,,\end{aligned} \tag{6.19}$$

where $L_Q = \ln[(-Q^2-i0)/\mu^2]$. The bHQET anomalous dimension can be derived using one of the consistency relations [50] for the factorization theorem in Eq. (6.1):

$$\gamma_v = \gamma_{\rm bHQET} + \gamma_{\rm bHQET}^* = 2\gamma_{J_B} + 2\gamma_S\,, \tag{6.20}$$

where γ_S indicates the soft function anomalous dimension for one hemisphere. Using the results for γ_{J_B} given in Eq. (41) of Ref. [78] and for γ_S given in Eq. (19) of Ref. [68] (which can be derived via consistency from the two-loop jet function anomalous dimension [17]) we find

$$\begin{aligned}\gamma_{\rm bHQET}\Big(\frac{Q}{m},\mu\Big) = {}& \frac{\alpha_s^{(n_l)}(\mu)C_F}{4\pi}\big[-4L+4\big] + \left(\frac{\alpha_s^{(n_l)}(\mu)}{4\pi}\right)^2\bigg\{n_lC_FT_F\bigg[\frac{80}{9}L-\frac{80}{9}\bigg] \\ & + C_FC_A\bigg[-\left(\frac{268}{9}-\frac{4\pi^2}{3}\right)L+\frac{196}{9}-\frac{4\pi^2}{3}+8\zeta_3\bigg]\bigg\} + \mathcal{O}(\alpha_s^3)\,,\end{aligned} \tag{6.21}$$

where $L = \ln[(-Q^2-i0)/m^2]$. Expanding the recently calculated anomalous dimension in HQET at $\mathcal{O}(\alpha_s^3)$ [63, 64] we extract in appendix B also the three-loop coefficient, which has – to our knowledge – not yet been displayed in literature.

As mentioned above, the two-loop expression of C_m contains large logarithms of the form $\alpha_s^2 C_F T_F \ln(-m^2/Q^2) \sim \mathcal{O}(\alpha_s)$ which cannot be resummed using the RGE in μ. They are rapidity logarithms and originate from a separation of the soft and collinear mass modes which have the same invariant mass but different rapidity. These rapidity logarithms only appear inside H_m, and not for the other soft, jet, and hard functions in Eq. (6.1). Our focus here will be on the leading rapidity logarithms, which start contributing with the $\mathcal{O}(\alpha_s^2 C_F T_F)$ piece. The latter comes from virtual top quark loops, and hence we only need to compute the correction $F_{\rm SCET}^{(C_F T_F, n_l+1)}$, while the bHQET graphs give no contribution for this color structure, i.e. $F_{\rm bHQET}^{(C_F T_F, n_l)} = 0$.

To set up the stage for rapidity resummation we can factorize the current operators and its matrix elements into products of soft and collinear diagrams,

$$\begin{aligned}
\langle \mathcal{J}_{\rm SCET}^{(n_l+1)} \rangle &= \langle \mathcal{J}_{\rm SCET}^{(n_l+1)} \rangle_n \, \langle \mathcal{J}_{\rm SCET}^{(n_l+1)} \rangle_s \, \langle \mathcal{J}_{\rm SCET}^{(n_l+1)} \rangle_{\bar n} \,, \\
\langle \mathcal{J}_{\rm bHQET}^{(n_l+1)} \rangle &= \langle \mathcal{J}_{\rm bHQET}^{(n_l+1)} \rangle_n \, \langle \mathcal{J}_{\rm bHQET}^{(n_l+1)} \rangle_s \, \langle \mathcal{J}_{\rm bHQET}^{(n_l+1)} \rangle_{\bar n} \,,
\end{aligned} \tag{6.22}$$

where the $\{n, s, \bar n\}$ labels in bHQET indicate n-ucollinear, ultrasoft, and $\bar n$-ucollinear contributions respectively. Note that in order to split up these corrections we must choose an IR regulator which preserves the $\mathrm{SCET_{II}}$ nature of the theory. We will regulate the IR divergences using a gluon mass Λ, which thus differs from the use of pure dimensional regularization discussed above for method 1. In $\mathrm{SCET_{II}}$ the individual soft and collinear diagrams have rapidity divergences, and using the regulator of Refs. [38, 37] the coefficients will depend on a rapidity renormalization scale ν. Thus Eq. (6.15) can be decomposed into individual contributions involving n-collinear, $\bar n$-collinear, and soft amplitudes,

$$C_{m,i}^{(n_l)} = \frac{\langle \mathcal{J}_{\rm SCET}^{(n_l+1)} \rangle_i}{\langle \mathcal{J}_{\rm bHQET}^{(n_l)} \rangle_i} \,, \qquad i = n, \bar n, s \,. \tag{6.23}$$

This leads to

$$C_m^{(n_l)}\left(m, \frac{Q}{m}, \mu\right) = C_{m,n}^{(n_l)}\left(m, \mu, \frac{\nu}{Q}\right) C_{m,s}^{(n_l)}\left(m, \mu, \frac{\nu}{m}\right) C_{m,\bar n}^{(n_l)}\left(m, \mu, \frac{\nu}{Q}\right) , \tag{6.24}$$

where we included the dependence on scales and renormalization parameters. Thus we see that the logarithmic dependence on the Q/m boost variable is factorized by the rapidity regularization parameter ν into collinear factors that depend on Q and a soft factor which does not. To sum the rapidity logarithms we can follow the standard approach of matching and running.

We define hard functions $H_{m,i}^{(n_l)} = \left|C_{m,i}^{(n_l)}\right|^2$. The individual Wilson coefficient and hard functions obey related RG equations,

$$\nu\frac{\mathrm{d}}{\mathrm{d}\nu}C_{m,i}^{(n_l)} = \gamma_{\nu,i}^{C_m}\, C_{m,i}^{(n_l)}\,, \qquad \nu\frac{\mathrm{d}}{\mathrm{d}\nu}H_{m,i}^{(n_l)} = \gamma_{\nu,i}^{H_m}\, H_{m,i}^{(n_l)}\,, \qquad \gamma_{\nu,i}^{H_m} = \gamma_{\nu,i}^{C_m} + \left(\gamma_{\nu,i}^{C_m}\right)^*. \tag{6.25}$$

The ν-anomalous dimensions appearing here can be computed directly from the SCET and bHQET counterterms and depend only on m and μ. Taking Eqs. (6.12) and (6.16) and introducing individual counterterm factors for each of the collinear and soft component amplitudes, noting that the bare coefficients are ν-independent, and using Eq. (6.23) we get

$$\begin{aligned}\gamma_{\nu,i}^{C_m}(m,\mu) = \nu\frac{\mathrm{d}}{\mathrm{d}\nu}\ln C_{m,i}^{(n_l)} &= \nu\frac{\mathrm{d}}{\mathrm{d}\nu}\ln\langle\mathcal{J}_{\mathrm{SCET}}^{(n_l+1)}\rangle_i - \nu\frac{\mathrm{d}}{\mathrm{d}\nu}\ln\langle\mathcal{J}_{\mathrm{bHQET}}^{(n_l)}\rangle_i \\ &= \nu\frac{\mathrm{d}}{\mathrm{d}\nu}\ln Z_{\mathrm{SCET},i}^{(n_l+1)} - \nu\frac{\mathrm{d}}{\mathrm{d}\nu}\ln Z_{\mathrm{bHQET},i}^{(n_l)}\,, \qquad i = n,\bar{n},s\,. \end{aligned} \tag{6.26}$$

As we will see in detail below, individual contributions on the right hand side of Eq. (6.26) contain IR divergences, but they will always cancel to leave an IR finite result for the $\gamma_{\nu,i}^{C_m}$, when we fully expand in either the n_l-flavor or (n_l+1)-flavor scheme for the strong coupling.

6.2 Two Loop Determination of H_m from QCD heavy form factor

In this section we use the first method outlined in Sec. 6.1 to determine the bHQET matching coefficient, C_m at two loops. From Eq. (6.14) the ingredients we need are

the UV renormalized QCD two-loop heavy quark form factor, $\langle \mathcal{J}_{\rm QCD}^{(n_l+1)} \rangle$, in dimensional regularization and the SCET matching coefficient, $C_Q^{(n_l+1)}$. In the following we abbreviate the appearing logarithms as

$$L = \ln\left(\frac{-Q^2 - i0}{m^2}\right), \qquad L_m = \ln\left(\frac{m^2}{\mu^2}\right), \qquad L_Q = \ln\left(\frac{-Q^2 - i0}{\mu^2}\right). \tag{6.27}$$

From Refs. [19, 59] we extract the renormalized two loop QCD heavy quark form factor result in the high energy limit, $Q^2 \gg m^2$, evaluated at an arbitrary scale $\mu \gtrsim m$, abbreviating $\alpha_s^{(n_l+1)} \equiv \alpha_s^{(n_l+1)}(\mu)$, [1]

$$\begin{aligned}
F_{\rm QCD}^{(n_l+1)} &= 1 + \frac{\alpha_s^{(n_l+1)} C_F}{4\pi} \left\{ \frac{2L-2}{\epsilon} - L^2 - (2L_m - 3)L + 2L_m - 4 + \frac{\pi^2}{3} \right. \\
&\quad + \epsilon \left[\frac{L^3}{3} + \left(L_m - \frac{3}{2}\right)L^2 + \left(L_m^2 - 3L_m + 8 - \frac{\pi^2}{6}\right)L - L_m^2 + \left(4 - \frac{\pi^2}{3}\right)L_m \right. \\
&\quad \left. \left. - 8 + \frac{\pi^2}{3} + 4\zeta_3 \right] + \mathcal{O}(\epsilon^2) \right\} \\
&\quad + \left(\frac{\alpha_s^{(n_l+1)}}{4\pi}\right)^2 C_F^2 \left\{ \frac{1}{\epsilon^2}\left[2L^2 - 4L + 2\right] + \frac{1}{\epsilon}\left[-2L^3 - (4L_m - 8)L^2 + \left(8L_m - 14 + \frac{2\pi^2}{3}\right)L \right. \right. \\
&\quad \left. - 4L_m + 8 - \frac{2\pi^2}{3} \right] + \frac{7}{6}L^4 + \left(4L_m - \frac{20}{3}\right)L^3 + \left(4L_m^2 - 16L_m + \frac{55}{2} - \frac{2\pi^2}{3}\right)L^2 \\
&\quad - \left(8L_m^2 - \left(28 - \frac{4\pi^2}{3}\right)L_m + \frac{85}{2} - 32\zeta_3\right)L + 4L_m^2 - \left(16 - \frac{4\pi^2}{3}\right)L_m + 46 + \frac{13\pi^2}{2} \\
&\quad \left. - 44\zeta_3 - 8\pi^2 \ln 2 - \frac{59\pi^4}{90} + \mathcal{O}(\epsilon) \right\} \\
&\quad + \left(\frac{\alpha_s^{(n_l+1)}}{4\pi}\right)^2 C_F C_A \left\{ \frac{1}{\epsilon^2}\left[-\frac{11}{3}L + \frac{11}{3} \right] + \frac{1}{\epsilon}\left[\left(\frac{67}{9} - \frac{\pi^2}{3}\right)L - \frac{49}{9} + \frac{\pi^2}{3} - 2\zeta_3 \right] + \frac{11}{9}L^3 \right. \\
&\quad + \left(\frac{11}{3}L_m - \frac{233}{18} + \frac{\pi^2}{3}\right)L^2 + \left(\frac{11}{3}L_m^2 - \left(\frac{233}{9} - \frac{2\pi^2}{3}\right)L_m + \frac{2545}{54} + \frac{11\pi^2}{9} - 26\zeta_3\right)L \\
&\quad \left. - \frac{11}{3}L_m^2 + \left(\frac{230}{9} - \frac{17\pi^2}{9} + 4\zeta_3\right)L_m - \frac{1595}{27} - \frac{7\pi^2}{54} + \frac{134}{3}\zeta_3 + 4\pi^2 \ln 2 - \frac{\pi^4}{60} + \mathcal{O}(\epsilon) \right\} \\
&\quad + \left(\frac{\alpha_s^{(n_l+1)}}{4\pi}\right)^2 C_F n_l T_F \left\{ \frac{1}{\epsilon^2}\left[\frac{4}{3}L - \frac{4}{3}\right] + \frac{1}{\epsilon}\left[-\frac{20}{9}L + \frac{20}{9}\right] - \frac{4}{9}L^3 - \left(\frac{4}{3}L_m - \frac{38}{9}\right)L^2 \right. \\
&\quad \left. - \left(\frac{4}{3}L_m^2 - \frac{76}{9}L_m + \frac{418}{27} + \frac{4\pi^2}{9}\right)L + \frac{4}{3}L_m^2 - \left(\frac{88}{9} - \frac{4\pi^2}{9}\right)L_m + \frac{424}{27} - \frac{14\pi^2}{27} \right.
\end{aligned}$$

[1] Note that in Ref. [19] the counterterm for the renormalization of the coupling constant contains an extra factor $\Gamma(1+\epsilon)$, so that also additional finite terms are subtracted compared to the conventional $\overline{\rm MS}$ renormalization.

$$
\begin{aligned}
&\quad - \frac{16}{3}\zeta_3 + \mathcal{O}(\epsilon)\Big\} \\
&+ \left(\frac{\alpha_s^{(n_l+1)}}{4\pi}\right)^2 C_F T_F \left\{\frac{1}{\epsilon}\left[\frac{8}{3}L_m\, L - \frac{8}{3}L_m\right] - \frac{4}{9}L^3 - \left(\frac{4}{3}L_m - \frac{38}{9}\right)L^2 - \Big(4L_m^2 - 4L_m \right. \\
&\left. + \frac{530}{27} + \frac{2\pi^2}{3}\Big)L + 4L_m^2 - \left(\frac{16}{3} - \frac{4\pi^2}{9}\right)L_m + \frac{1532}{27} - \frac{4\pi^2}{9} + \mathcal{O}(\epsilon)\right\}.
\end{aligned}
\tag{6.28}
$$

Note that we keep the $\mathcal{O}(\epsilon)$ part of the one loop piece in $F_{\rm QCD}^{(1,n_l+1)}$ since it yields a contribution when considering the cross terms in the expansion of the ratio in Eq. (6.14). (One can avoid considering these cross terms and obtain the same answer by taking the logarithm of Eq. (6.14).) We remark that in these expressions the pole mass scheme has been used for the top quark mass m.

The other ingredient we need is the well known two-loop expression for C_Q, widely used in the SCET literature, and obtained with the aid of the massless form factor calculation of Refs. [98, 97],

$$
\begin{aligned}
C_Q^{(n_l+1)} &= 1 + \frac{\alpha_s^{(n_l+1)}(\mu) C_F}{4\pi}\left\{-L_Q^2 + 3L_Q - 8 + \frac{\pi^2}{6}\right\} \\
&+ \left(\frac{\alpha_s^{(n_l+1)}(\mu)}{4\pi}\right)^2 C_F^2 \left\{\frac{1}{2}L_Q^4 - 3L_Q^3 + \left(\frac{25}{2} - \frac{\pi^2}{6}\right)L_Q^2 - \left(\frac{45}{2} + \frac{3\pi^2}{2} - 24\zeta_3\right)L_Q \right. \\
&\qquad \left. + \frac{255}{8} + \frac{7\pi^2}{2} - 30\zeta_3 - \frac{83\pi^4}{360}\right\} \\
&+ \left(\frac{\alpha_s^{(n_l+1)}(\mu)}{4\pi}\right)^2 C_A C_F \left\{\frac{11}{9}L_Q^3 - \left(\frac{233}{18} - \frac{\pi^2}{3}\right)L_Q^2 + \left(\frac{2545}{54} + \frac{11\pi^2}{9} - 26\zeta_3\right)L_Q \right. \\
&\qquad \left. - \frac{51157}{648} - \frac{337\pi^2}{108} + \frac{313\zeta_3}{9} + \frac{11\pi^4}{45}\right\} \\
&+ \left(\frac{\alpha_s^{(n_l+1)}(\mu)}{4\pi}\right)^2 C_F T_F (n_l+1)\left\{-\frac{4}{9}L_Q^3 + \frac{38}{9}L_Q^2 - \left(\frac{418}{27} + \frac{4\pi^2}{9}\right)L_Q \right. \\
&\qquad \left. + \frac{4085}{162} + \frac{23\pi^2}{27} + \frac{4\zeta_3}{9}\right\}.
\end{aligned}
\tag{6.29}
$$

The remaining quantities in Eq. (6.14) are the coefficient $C_m^{(n_l)}$ we wish to determine, and the counterterm $Z_{\rm bHQET}^{(n_l)}$. The contributions to these two quantities can be easily distinguished since $Z_{\rm bHQET}^{(n_l)}$ only has terms with powers of $1/\epsilon$, whereas $C_m^{(n_l)}$ is

given by the finite $\mathcal{O}(\epsilon^0)$ contribution. Therefore, it is straightforward to distinguish these two quantities unambiguously. Since we wish to determine these with n_l active flavors, we must convert the strong coupling in $\langle \mathcal{J}_{\rm QCD}^{(n_l+1)} \rangle$ and $C_Q^{(n_l+1)}$ to the n_l-flavor scheme using the decoupling relation

$$\alpha_s^{(n_l+1)}(\mu) = \alpha_s^{(n_l)}(\mu)\left\{1 + \left[\Pi(m^2,0) - \frac{\alpha_s^{(n_l)}(\mu) T_F}{3\pi}\frac{1}{\epsilon}\right] + \mathcal{O}(\alpha_s^2)\right\}, \tag{6.30}$$

where the one-loop vacuum polarization at zero momentum transfer for a massive quark pair is given by

$$\Pi(m^2,0) = \frac{\alpha_s(\mu) T_F}{3\pi}\left(\frac{\mu^2 e^{\gamma_E}}{m^2}\right)^{\epsilon}\Gamma(\epsilon) = \frac{\alpha_s(\mu) T_F}{3\pi}\left[\frac{1}{\epsilon} - L_m + \epsilon\left(\frac{1}{2}L_m^2 + \frac{\pi^2}{12}\right) + \mathcal{O}(\epsilon^2)\right]. \tag{6.31}$$

We need to keep terms up to $\mathcal{O}(\epsilon)$ in Eq. (6.30) since they contribute in the dimensional regularization scheme we are using when multiplying $\mathcal{O}(\alpha_s/\epsilon)$ IR divergent terms in Eq. (6.14). Using these results in Eq. (6.14) we find the following expression for $Z_{\rm bHQET}^{(n_l)}$,

$$\begin{aligned} Z_{\rm bHQET}^{(n_l)} = 1 &+ \frac{\alpha_s^{(n_l)}(\mu) C_F}{4\pi}\frac{1}{\epsilon}\left(2L-2\right) + \left(\frac{\alpha_s^{(n_l)}(\mu)}{4\pi}\right)^2 C_F^2 \frac{1}{\epsilon^2}\left(2L^2 - 4L + 2\right) \\ &+ \left(\frac{\alpha_s^{(n_l)}(\mu)}{4\pi}\right)^2 C_F C_A\left\{\frac{1}{\epsilon^2}\left[-\frac{11}{3}L + \frac{11}{3}\right] + \frac{1}{\epsilon}\left[\left(\frac{67}{9} - \frac{\pi^2}{3}\right)L - \frac{49}{9} + \frac{\pi^2}{3} - 2\zeta_3\right]\right\} \\ &+ \left(\frac{\alpha_s^{(n_l)}(\mu)}{4\pi}\right)^2 C_F n_l T_F\left\{\frac{1}{\epsilon^2}\left[\frac{4}{3}L - \frac{4}{3}\right] + \frac{1}{\epsilon}\left[-\frac{20}{9}L + \frac{20}{9}\right]\right\}. \end{aligned} \tag{6.32}$$

This result can also be extracted from earlier literature using the consistency relation for RG running between H_m, and the soft and the jet functions in Eq. (6.1). In particular, the $1/\epsilon^2$ terms in Eq. (6.32) are given by a term involving the lowest order β-function, and the square of the one-loop result (due to non-abelian exponentiation), while the $1/\epsilon$ terms are directly related to the two-loop anomalous dimension given in Eq. (6.21). This provides a key cross-check for $Z_{\rm bHQET}^{(n_l)}$ and hence for our result below for $C_m^{(n_l)}$.

After cancellation of the $1/\epsilon$ and $1/\epsilon^2$ terms in Eq. (6.14) with the help of $Z_{\rm bHQET}^{(n_l)}$, the remaining $\mathcal{O}(\epsilon^0)$ terms give the desired result for $C_m^{(n_l)}$. With the top-mass in the pole scheme we find

$$
\begin{aligned}
C_m^{(n_l)}\Big(m,\frac{Q}{m},\mu\Big) &= 1+\frac{\alpha_s^{(n_l)}(\mu)C_F}{4\pi}\left(L_m^2-L_m+4+\frac{\pi^2}{6}\right)\\
&+\left(\frac{\alpha_s^{(n_l)}(\mu)}{4\pi}\right)^2 C_F^2\left\{\frac{1}{2}L_m^4-L_m^3+\left(\frac{9}{2}+\frac{\pi^2}{6}\right)L_m^2-\left(\frac{11}{2}-\frac{11\pi^2}{6}+24\zeta_3\right)L_m\right.\\
&\qquad\left.+\frac{241}{8}+\frac{13\pi^2}{3}-8\pi^2\log 2-6\zeta_3-\frac{163\pi^4}{360}\right\}\\
&+\left(\frac{\alpha_s^{(n_l)}(\mu)}{4\pi}\right)^2 C_A C_F\left\{-\frac{11}{9}L_m^3+\left(\frac{167}{18}-\frac{\pi^2}{3}\right)L_m^2-\left(\frac{1165}{54}+\frac{28\pi^2}{9}-30\zeta_3\right)L_m\right.\\
&\qquad\left.+\frac{12877}{648}+\frac{323\pi^2}{108}+4\pi^2\log 2+\frac{89\zeta_3}{9}-\frac{47\pi^4}{180}\right\}\\
&+\left(\frac{\alpha_s^{(n_l)}(\mu)}{4\pi}\right)^2 C_F n_l T_F\left\{\frac{4}{9}L_m^3-\frac{26}{9}L_m^2+\left(\frac{154}{27}+\frac{8\pi^2}{9}\right)L_m-\frac{1541}{162}-\frac{37\pi^2}{27}-\frac{52\zeta_3}{9}\right\}\\
&+\left(\frac{\alpha_s^{(n_l)}(\mu)}{4\pi}\right)^2 C_F T_F\left\{-\frac{8}{9}L_m^3-\frac{2}{9}L_m^2+\left(\frac{130}{27}+\frac{2\pi^2}{3}\right)L_m+\frac{5107}{162}-\frac{41\pi^2}{27}-\frac{4\zeta_3}{9}\right.\\
&\qquad\left.-\left(\frac{4}{3}L_m^2+\frac{40}{9}L_m+\frac{112}{27}\right)\ln\left(\frac{-Q^2-i0}{m^2}\right)\right\},
\end{aligned}
\tag{6.33}
$$

Finally we arrive at the main result of this section - the result for $H_m=|C_m|^2$ in the n_l-flavor scheme with the top-mass in the pole scheme ($\alpha_s^{(n_l)}\equiv\alpha_s^{(n_l)}(\mu)$)

$$
\begin{aligned}
H_m^{(n_l)}\Big(m,\frac{Q}{m},\mu\Big) &= 1+\frac{\alpha_s^{(n_l)}(\mu)}{4\pi}C_F\left(2L_m^2-2L_m+8+\frac{\pi^2}{3}\right)\\
&+\left(\frac{\alpha_s^{(n_l)}(\mu)}{4\pi}\right)^2 C_F^2\left\{2L_m^4-4L_m^3+\left(18+\frac{2\pi^2}{3}\right)L_m^2-\left(19-\frac{10\pi^2}{3}+48\zeta_3\right)L_m\right.\\
&\qquad\left.+\frac{305}{4}+10\pi^2-16\pi^2\log 2-12\zeta_3-\frac{79\pi^4}{90}\right\}\\
&+\left(\frac{\alpha_s^{(n_l)}(\mu)}{4\pi}\right)^2 C_A C_F\left\{-\frac{22}{9}L_m^3+\left(\frac{167}{9}-\frac{2\pi^2}{3}\right)L_m^2-\left(\frac{1165}{27}+\frac{56\pi^2}{9}-60\zeta_3\right)L_m\right.\\
&\qquad\left.+\frac{12877}{324}+\frac{323\pi^2}{54}+8\pi^2\log 2+\frac{178\zeta_3}{9}-\frac{47\pi^4}{90}\right\}\\
&+\left(\frac{\alpha_s^{(n_l)}(\mu)}{4\pi}\right)^2 C_F n_l T_F\left\{\frac{8}{9}L_m^3-\frac{52}{9}L_m^2+\left(\frac{308}{27}+\frac{16\pi^2}{9}\right)L_m-\frac{1541}{81}-\frac{74\pi^2}{27}-\frac{104\zeta_3}{9}\right\}
\end{aligned}
$$

$$+\left(\frac{\alpha_s^{(n_l)}(\mu)}{4\pi}\right)^2 C_F T_F \Bigg\{ -\frac{16}{9}L_m^3 - \frac{4}{9}L_m^2 + \left(\frac{260}{27}+\frac{4\pi^2}{3}\right)L_m + \frac{5107}{81} - \frac{82\pi^2}{27} - \frac{8\zeta_3}{9} - \left(\frac{8}{3}L_m^2 + \frac{80}{9}L_m + \frac{224}{27}\right)\ln\left(\frac{Q^2}{m^2}\right)\Bigg\}. \tag{6.34}$$

As anticipated, all of the logarithms in this expression are minimized for $\mu \simeq m$, except for the contributions in the last line that involve the rapidity logarithm $\alpha_s^2 C_F T_F \ln(Q^2/m^2)$. To understand the origin of this type of logarithm in the context of the renormalization group requires a further factorization of $H_m^{(n_l)}$ into soft and collinear pieces, as in Eq. (6.24). In the next section we will carry out an independent calculation of the $\mathcal{O}(\alpha_s^2 C_F T_F)$ terms in $H_m^{(n_l)}$. This sets up the rapidity renormalization group analysis of this term, which can be found in Sec. 6.4.1. In Sec. 6.4.2 we present the result for $H_m^{(n_l+1)}$ with the top mass renormalized in the $\overline{\text{MS}}$ scheme.

6.3 Direct Computation of the $\mathcal{O}(\alpha_s^2 C_F T_F)$ Result

6.3.1 Ingredients for the Calculation

In this section we perform a direct computation of the $\alpha_s^2 C_F T_F$ piece of the matching coefficient $C_m(m, Q/m, \mu)$ due to massive quark loops using the second method from Sec. 6.1. We carry out the calculation in analogy to Refs. [61, 103], where the corresponding contribution to the matching coefficient at the mass scale for massless external quarks (in the following called "primary") was computed. In this section we extend the calculation to the case of primary massive quarks.

Starting from Eq. (6.15) we note that for the $\alpha_s^2 C_F T_F$ massive quark term, the bHQET graphs expressed in the usual n_l-flavor scheme do not give any contribution. The SCET graphs do contribute, and should be expressed in the same scheme for the strong coupling. Using the decoupling relation in Eq. (6.30) we obtain in the notation of Eq. (6.7)

$$C_m^{(C_F T_F, n_l)}\left(m, \frac{Q}{m}, \mu\right) = \left[F_{\text{SCET}}^{(C_F T_F, n_l+1)}(Q, m, \Lambda, \mu)\right. \tag{6.35}$$

$$- \frac{\alpha_s^{(n_l)}(\mu) T_F}{3\pi} \ln\left(\frac{m^2}{\mu^2}\right) F_{\rm SCET}^{(1,n_l+1)}(Q, m, \Lambda, \mu)\Big]_{\alpha_s^{(n_l+1)} \to \alpha_s^{(n_l)}} .$$

The second term on the right hand side accounts for the coupling conversion of the SCET form factor from $(n_l + 1)$ to n_l flavors.[2] As discussed in detail below, we will use a massive gluon as an IR regulator Λ, such that $\mathcal{O}(\epsilon)$ terms in the coupling conversion in Eq. (6.30) can be dropped. For the remainder of this section we will drop the superscript $(n_l + 1)$ on the SCET form factors.

We adopt the calculational method of Refs. [61, 103], where the two loop graphs containing a "secondary" massive quark bubble are calculated by starting with one-loop graphs describing the radiation of a massive gluon with mass M and applying in a second step dispersion relations to account for the gluon splitting into a pair of secondary massive quarks with masses m. The corresponding relation can be written as

$$\begin{aligned}\frac{(-i)g^{\mu\rho}}{p^2 + i\epsilon} \Pi_{\rho\sigma}(m^2, p^2) \frac{(-i)g^{\sigma\nu}}{p^2 + i\epsilon} &= \frac{1}{\pi} \int \frac{{\rm d}M^2}{M^2} \frac{(-i)\left(g^{\mu\nu} - \frac{p^\mu p^\nu}{p^2}\right)}{p^2 - M^2 + i\epsilon} {\rm Im}\left[\Pi(m^2, M^2)\right] \\ &\quad - \frac{(-i)\left(g^{\mu\nu} - \frac{p^\mu p^\nu}{p^2}\right)}{p^2 + i\epsilon} \Pi(m^2, 0) . \end{aligned} \tag{6.36}$$

Here $\Pi(m^2, p^2)$ is the gluonic vacuum polarization due to the massive quark-antiquark bubble,

$$\Pi_{\mu\nu}^{AB}(m^2, p^2) = -i(p^2 g_{\mu\nu} - p_\mu p_\nu)\Pi(m^2, p^2)\delta^{AB} \equiv \int {\rm d}^4x \, e^{ipx} \langle 0|T J_\mu^A(x) J_\nu^B(0)|0\rangle , \tag{6.37}$$

[2]Note that the subscript "$\alpha_s^{(n_l+1)} \to \alpha_s^{(n_l)}$" used here and elsewhere stands for the plain replacement of the couplings and does not involve any expansion based on Eq. (6.30).

with the imaginary part in $d = 4 - 2\epsilon$ dimensions given by

$$\mathrm{Im}\big[\Pi(m^2,p^2)\big] = \theta(p^2-4m^2)\, g^2 T_F \left(\frac{p^2}{\tilde{\mu}^2}\right)^{-\epsilon} \frac{2^{3-2d}\pi^{(3-d)/2}}{\Gamma\left(\frac{d+1}{2}\right)} \left(d-2+\frac{4m^2}{p^2}\right)\left(1-\frac{4m^2}{p^2}\right)^{(d-3)/2} . \tag{6.38}$$

We note that the same method can be applied to account for any kind of secondary particles by a corresponding choice of the polarization function Π. Eq. (6.36) allows us to express the contribution to the SCET form factor due to the massive quark loops as

$$\begin{aligned} F_{\mathrm{SCET}}^{(C_F T_F,\,\mathrm{bare})}(Q,m,\Lambda) &= F_{\mathrm{SCET}}^{(\mathrm{OS},C_F T_F,\mathrm{bare})}(Q,m) \\ &\quad - \left(\Pi(m^2,0) - \frac{\alpha_s^{(n_l)}(\mu) T_F}{3\pi}\frac{1}{\epsilon}\right) F_{\mathrm{SCET}}^{(1,\,\mathrm{bare})}(Q,m,\Lambda)\,, \end{aligned} \tag{6.39}$$

where the "on-shell" form factor is

$$F_{\mathrm{SCET}}^{(\mathrm{OS},C_F T_F,\mathrm{bare})}(Q,m) = \frac{1}{\pi}\int \frac{\mathrm{d}M^2}{M^2}\, F_{\mathrm{SCET}}^{(1,\,\mathrm{bare})}(Q,m,M)\, \mathrm{Im}\big[\Pi(m^2,M^2)\big]\ . \tag{6.40}$$

In Eq. (6.39) Λ denotes the gluon mass acting as our IR regulator, which we distinguish from the gluon mass M used in the dispersion integration. Since total bare quantities are μ-independent, we do not add μ as an argument to the components of bare quantities at a specific order. In $F_{\mathrm{SCET}}^{(\mathrm{OS,bare})}$ the massive quark contributions to the coupling are renormalized with the onshell subtraction, i.e. $F_{\mathrm{SCET}}^{(\mathrm{OS,bare})}$ is given in the scheme with n_l dynamic flavors. In Eq. (6.39) the second term accounts for the change to $n_l + 1$ dynamic flavors. The form factor itself is still unrenormalized, as indicated by the (bare) superscript. We perform the $\overline{\mathrm{MS}}$ renormalization for the SCET current using Eq. (6.16). Incorporating Eqs. (6.39) and (6.16) into Eq. (6.35) the result for $C_m^{(C_F T_F, n_l)}$ can be written as

$$C_m^{(C_F T_F, n_l)}\Big(m, \frac{Q}{m}, \mu\Big) = F_{\rm SCET}^{(\rm OS, C_F T_F, bare)}(Q, m) \tag{6.41}$$
$$- \left(\Pi(m^2, 0) - \frac{\alpha_s^{(n_l)}(\mu) T_F}{3\pi} \frac{1}{\epsilon}\right) \Big(F_{\rm SCET}^{(1)}(Q, m, \Lambda, \mu) - Z_{\rm SCET}^{(1)}(Q, m, \mu)\Big)$$
$$+ Z_{\rm SCET}^{(C_F T_F)}(Q, m, \mu) - \frac{\alpha_s^{(n_l)}(\mu) T_F}{3\pi} \ln\left(\frac{m^2}{\mu^2}\right) F_{\rm SCET}^{(1)}(Q, m, \Lambda, \mu)\,.$$

Here the 1-loop form factor $F_{\rm SCET}^{(1,\rm bare)}$ is a UV and IR divergent amplitude, and $Z_{\rm SCET}^{(C_F T_F)}$ is the SCET current counterterm in the $(n_l + 1)$-flavor scheme. Using the explicit form of $\Pi(m^2, 0)$ in Eq. (6.31) one can rewrite Eq. (6.41) as

$$C_m^{(C_F T_F, n_l)}\Big(m, \frac{Q}{m}, \mu\Big) = F_{\rm SCET}^{(\rm OS, C_F T_F, bare)}(Q, m) + Z_{\rm SCET}^{(C_F T_F)}(Q, m, \mu) \tag{6.42}$$
$$+ \left(\Pi(m^2, 0) - \frac{\alpha_s^{(n_l)} T_F}{3\pi} \frac{1}{\epsilon}\right) Z_{\rm SCET}^{(1)}(Q, m, \mu)\,,$$

where we see explicitly that the dependence on the IR regulator is canceled. Note that we could have also carried out the computation employing the $(n_l + 1)$-flavor scheme to determine $C_m^{(C_F T_F, n_l+1)}$, which involves converting the bHQET form factor from the n_l to $(n_l + 1)$-flavor scheme. In this case the cancellation of IR divergences occurs in a different manner, and involves the $\mathcal{O}(\alpha_s)$ bHQET form factor. This approach is discussed in App. B.

Note that nothing in Eq. (6.42) depends on the low energy bHQET theory. Therefore the result applies equally well to the case where one integrates out the heavy quark loop without approaching the jet invariant mass threshold $s_t \to m^2$ and matches onto a n_l-flavor SCET theory instead of bHQET. In this case the matching coefficient only contains the contribution from the massive quark loop and receives corrections starting at $\mathcal{O}(\alpha_s^2 C_F T_F)$, so switching between the n_l and $(n_l + 1)$-flavor schemes only affects the corrections at $\mathcal{O}(\alpha_s^3)$ and beyond. This is in close analogy to the case of primary massless quarks discussed in detail in Refs. [61, 103].

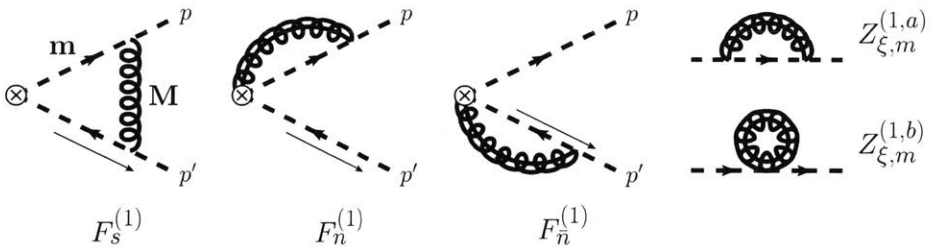

Figure 6-1: Non-vanishing EFT diagrams for the computation of the hard current at $\mathcal{O}(\alpha_s)$ with primary massive quarks and secondary massive gluons with masses m and M, respectively. Soft-bin subtractions are implied for the collinear diagrams.

6.3.2 One-loop computation for secondary massive gluons

Having laid out the basic framework in the previous section we now start with calculating the one loop SCET heavy quark form factors for a top-quark of mass m with a massive gluon of mass M to be used in the dispersion relation. The complete unrenormalized SCET result for the current form factor at $\mathcal{O}(\alpha_s)$ can be written as

$$F_{\text{SCET}}^{(1,\text{bare})}(Q,m,M) = F_{\text{SCET},m=0}^{(1,\text{bare})}(Q,M) + \underbrace{F_{\text{SCET}}^{(1,\text{bare})}(Q,m,M) - F_{\text{SCET},m=0}^{(1,\text{bare})}(Q,M)}_{=\delta F_{\text{SCET}}^{(1,\text{bare})}(m,M)} . \tag{6.43}$$

The correction with primary massless quarks $F_{\text{SCET,m=0}}^{(1,\text{bare})}$ has been already calculated in Refs. [36, 35, 34, 37, 61] and reads in $d = 4 - 2\epsilon$ dimensions

$$F_{\text{SCET},m=0}^{(1,\text{bare})} = \frac{\alpha_s(\mu)C_F}{4\pi}\left\{\frac{2}{\epsilon^2} + \frac{3}{\epsilon} - \frac{2}{\epsilon}L_Q + (2L_Q - 3)L_M - L_M^2 + \frac{9}{2} - \frac{5\pi^2}{6} + \mathcal{O}(\epsilon)\right\}, \tag{6.44}$$

where $L_Q = \ln\left(\frac{-Q^2-i0}{\mu^2}\right)$ and $L_M = \ln\left(\frac{M^2}{\mu^2}\right)$. The corresponding one-loop counterterm in $\overline{\text{MS}}$ reads

$$Z_{\text{SCET}}^{(1)} = \frac{\alpha_s(\mu)C_F}{4\pi}\left\{-\frac{2}{\epsilon^2} - \frac{3}{\epsilon} + \frac{2}{\epsilon}L_Q\right\}. \tag{6.45}$$

Fig. 6-1 illustrates the SCET graphs with massive gluons needed to compute $F_{\rm SCET}^{(1,\rm bare)}$. For the first three graphs in Fig. 6-1 the form factor contributions are defined as prefactors to the spinors, $F_i^{(1)}\,\bar{u}_{n,p}\gamma^\mu u_{\bar{n},p'}$ for $i = n, \bar{n}, s$ and are computed using the SCET Feynman rules for massive quarks given in Ref. [92].

Due to the eikonal structure the result for the soft diagram, $F_s^{(1,\rm bare)}$, is same as that for primary massless quarks [here $\tilde{\mu}^2 = \mu^2 e^{\gamma_E}/(4\pi)$],

$$F_s^{(1,\rm bare)} = -\,2ig^2 C_F \tilde{\mu}^{2\epsilon} \int \frac{\mathrm{d}^d k}{(2\pi)^d} \frac{1}{[k^- + i\epsilon]} \frac{1}{[k^+ - i\epsilon]} \frac{1}{[k^2 - M^2 + i\epsilon]}\,. \tag{6.46}$$

For the n-collinear diagram we get

$$F_n^{(1,\rm bare)} = 2ig^2 C_F \tilde{\mu}^{2\epsilon} \int \frac{\mathrm{d}^d k}{(2\pi)^d} \frac{Q - k^-}{[k^2 - Qk^+ - \frac{m^2}{Q}k^- + i\epsilon]} \frac{1}{[k^- + i\epsilon]} \frac{1}{[k^2 - M^2 + i\epsilon]}\,. \tag{6.47}$$

We can decompose this contribution into a correction corresponding to the diagram with primary massless quarks, and a UV and IR-finite difference of terms which can be computed in 4 dimensions,

$$F_n^{(1,\rm bare)} = F_{n,m=0}^{(1,\rm bare)} + \left(F_n^{(1,\rm bare)} - F_{n,m=0}^{(1,\rm bare)}\right). \tag{6.48}$$

After performing a contour integration in k^+, carrying out the $k_\perp$-integration and rescaling the label momentum as $k^- \equiv zQ$, the finite correction due to the mass of the primary quark yields

$$\begin{aligned} &F_n^{(1,\rm bare)} - F_{n,m=0}^{(1,\rm bare)} \qquad (6.49)\\ &= -\frac{\alpha_s C_F}{2\pi}\,\Gamma\left(2 - \frac{d}{2}\right)\left(\frac{\mu^2 e^{\gamma_E}}{M^2}\right)^{2-\frac{d}{2}} \int_0^1 \mathrm{d}z\,\frac{1-z}{z}\left[\left(1 - z + \frac{m^2}{M^2}z^2\right)^{\frac{d}{2}-2} - (1-z)^{\frac{d}{2}-2}\right]\\ &= \frac{\alpha_s C_F}{2\pi}\left[\ln\left(\frac{1+a}{2}\right)\ln\left(\frac{1-a}{2}\right) + \frac{1+a}{1-a}\ln\left(\frac{1+a}{2}\right) + \frac{1-a}{1+a}\ln\left(\frac{1-a}{2}\right) + 1 + \mathcal{O}(\epsilon)\right], \end{aligned}$$

with

$$a = \sqrt{1 - \frac{4m^2}{M^2}}\,. \tag{6.50}$$

In SCET loop graphs include soft 0-bin subtractions [96] which ensure that there is no double counting of infrared regions. For the soft 0-bin subtraction of $F_n^{(1,\text{bare})}$ the dependence on the primary quark mass drops out, and we obtain the same result as for primary massless quarks, which is therefore fully contained in $F_{n,m=0}^{(1,\text{bare})}$. Note that the result in Eq. (6.49) does not contain any rapidity divergences, so that rapidity logarithms arise only in the computation of $F_{n,m=0}^{(1)}$. This can be understood from the fact that the corrections due to soft modes are the same for massless and massive primary quarks, so that the rapidity divergences in the soft sector and, by consistency, also in the collinear sectors have to agree in both cases.

The $\bar{n}$-collinear diagram corresponds to switching k^- and k^+ in Eq. (6.47). We perform a decomposition analogous to Eq. (6.48),

$$F_{\bar{n}}^{(1,\text{bare})} = F_{\bar{n},m=0}^{(1,\text{bare})} + \left(F_{\bar{n}}^{(1,\text{bare})} - F_{\bar{n},m=0}^{(1,\text{bare})}\right). \tag{6.51}$$

The difference correction due to the primary quark mass is again UV and IR-finite and does not contain any rapidity divergences. Thus it yields for any choice of regulator the same result as the n-collinear correction, i.e.

$$F_{\bar{n}}^{(1,\text{bare})} - F_{\bar{n},m=0}^{(1,\text{bare})} = F_n^{(1,\text{bare})} - F_{n,m=0}^{(1,\text{bare})}\,. \tag{6.52}$$

Finally, we also have to consider the wave function corrections. In analogy to the computation in Ref. [50] we have

$$\Sigma^{(1)} = 2ig^2 C_F \tilde{\mu}^{2\epsilon} \frac{\not{n}}{2} \int \frac{\mathrm{d}^d k}{(2\pi)^d} \frac{Qm^2(3-\epsilon) - (Q^2 k^+ + Qp^2 + m^2 k^-)(1-\epsilon)}{Q^2[k^2 - M^2 + i\epsilon][(k+p)^2 - m^2 + i\epsilon]}\,. \tag{6.53}$$

Using $p^2 = m^2 + \Delta^2$ and decomposing the integrals into elementary one- and two-point

functions we obtain

$$\Sigma^{(1)} = ig^2 C_F \tilde{\mu}^{2\epsilon} \frac{\not{m}}{2} \frac{(1-\epsilon)}{Q(m^2+\Delta^2)} \Bigg\{ \left[A_0(m^2) - A_0(M^2)\right] \left[2m^2+\Delta^2\right] + B_0(m^2+\Delta^2, M^2, m^2) \left[\frac{4m^2(m^2+\Delta^2)}{1-\epsilon} + 2m^2M^2 + M^2\Delta^2 - \Delta^4\right] \Bigg\}, \tag{6.54}$$

which uses the loop integrals

$$\begin{aligned} A_0(m^2) &= \int \frac{\mathrm{d}^d k}{(2\pi)^d} \frac{1}{[k^2 - m^2 + i\epsilon]}, \\ B_0(p^2, M^2, m^2) &= \int \frac{\mathrm{d}^d k}{(2\pi)^d} \frac{1}{[k^2 - M^2 + i\epsilon]} \frac{1}{[(p-k)^2 - m^2 + i\epsilon]}. \end{aligned} \tag{6.55}$$

The wave function renormalization constant $Z_\xi^{(1)}$ is defined by taking the on-shell limit $\Delta \to 0$

$$\Sigma^{(1)} \overset{\Delta\to 0}{\longrightarrow} i\frac{\not{m}}{2}\frac{1}{Q}\left[2m\,\delta m_M^{(\mathrm{OS},1)} + \Delta^2 Z_\xi^{(1)} + \mathcal{O}(\Delta^4)\right], \tag{6.56}$$

where $\delta m_M^{(\mathrm{OS},1)}$ is the one-loop renormalization constant for the quark mass m in the pole mass scheme for the interaction with a massive gluon (with mass M). The wavefunction correction $Z_\xi^{(1)}$ can be written in terms of the wavefunction correction for primary massless quarks and a UV and IR finite remainder,

$$Z_\xi^{(1)} = Z_{\xi,m=0}^{(1)} + \left(Z_\xi^{(1)} - Z_{\xi,m=0}^{(1)}\right). \tag{6.57}$$

The remainder contribution in $d = 4$ dimensions reads

$$Z_\xi^{(1)} - Z_{\xi,m=0}^{(1)} = \frac{\alpha_s C_F}{4\pi} \frac{3}{2a(1-a^2)^2} \Bigg[2(1+a)^4(2-a)\ln\left(\frac{1+a}{2}\right) - 2(1-a)^4(2+a)\ln\left(\frac{1-a}{2}\right) + a\left(11 - 14a^2 + 3a^4\right) + \mathcal{O}(\epsilon)\Bigg], \tag{6.58}$$

where a was given above in Eq. (6.50).

The complete finite correction at one-loop, which accounts for the mass of the primary quark is given by the sum of the terms from Eqs. (6.49) and (6.58),

$$\delta F^{(1)}_{\rm SCET}(m,M) = 2\left(F^{(1,\rm bare)}_{n} - F^{(1,\rm bare)}_{n,m=0}\right)(m,M) - \left(Z^{(1)}_{\xi} - Z^{(1)}_{\xi,m=0}\right)(m,M)\,. \quad (6.59)$$

This result will be used for our two-loop computation in the next section.

6.3.3 Two-loop computation for secondary massive quarks

In this section we use the one-loop results from Sec. 6.3.2 to calculate the two-loop graph with the massive quark loop, and to determine the $C_F T_F$ contribution to C_m. First we compute $F^{(\rm OS, C_F T_F, bare)}_{\rm SCET}$ via Eq. (6.40) using the one-loop result in Eq. (6.43). Again we can decompose the two loop SCET form factor into a primary massless component and a correction for primary massive top quarks:

$$F^{(\rm OS, C_F T_F, bare)}_{\rm SCET} = F^{(\rm OS, C_F T_F, bare)}_{\rm SCET,\, m=0} + \delta F^{(C_F T_F)}_{m} \quad (6.60)$$

The calculation for primary massless quarks has already been performed in Ref. [103]. We display the result here for convenience:

$$\begin{aligned} F^{(\rm OS, C_F T_F, bare)}_{\rm SCET,\, m=0} = \left(\frac{\alpha_s^{(n_l)}(\mu)}{4\pi}\right)^2 C_F T_F \Bigg\{ &\frac{2}{\epsilon^3} + \frac{1}{\epsilon^2}\left[\frac{8}{3}L - 4L_Q + \frac{8}{9}\right] + \frac{1}{\epsilon}\left[\frac{4}{3}L^2 - \left(\frac{16}{3}L + \frac{16}{9}\right)L_Q \right. \\ &\left. + 4L_Q^2 + 4L - \frac{65}{27} - \frac{\pi^2}{9}\right] + \frac{56}{9}L^2 - \left[\frac{242}{27} + \frac{4\pi^2}{9}\right]L - \frac{8}{3}L_Q^3 + \left[\frac{16}{3}L + \frac{16}{9}\right]L_Q^2 \\ &- \left[\frac{8}{3}L^2 + 8L - \frac{130}{27} - \frac{2\pi^2}{9}\right]L_Q + \frac{875}{54} + \frac{8\pi^2}{9} - \frac{20\zeta_3}{3}\Bigg\}\,. \end{aligned} \quad (6.61)$$

The contribution from the two-loop $\overline{\rm MS}$ counterterm is known from the massless quark case and reads

$$Z^{(C_F T_F)}_{\rm SCET} = \left(\frac{\alpha_s^{(n_l+1)}(\mu)}{4\pi}\right)^2 C_F T_F \left\{ -\frac{2}{\epsilon^3} + \frac{1}{\epsilon^2}\left[\frac{4}{3}L_Q - \frac{8}{9}\right] + \frac{1}{\epsilon}\left[-\frac{20}{9}L_Q + \frac{65}{27} + \frac{\pi^2}{3}\right]\right\}, \quad (6.62)$$

where L and L_Q are defined in Eq. (6.27). The $1/\epsilon^n$ divergences in Eqs. (6.61) and (6.62) differ, and are reconciled only once we account for the additional scheme change correction in the last term of Eq. (6.39). The $\delta F_m^{(C_F T_F)}$ term can be computed by inserting the one-loop massive gluon correction term of Eq. (6.59) into the dispersive integral (6.40) which can be performed in four dimensions. The result reads

$$\delta F_m^{(C_F T_F)} = \left(\frac{\alpha_s^{(n_l)}(\mu)}{4\pi}\right)^2 C_F T_F \left\{\frac{1241}{81} - \frac{56\pi^2}{27} + \frac{16}{3}\zeta_3\right\}. \tag{6.63}$$

Thus the only modification in the massive quark loop contributions to the form factor for primary massive quarks with respect to primary massless quarks is a simple constant term. In particular no additional rapidity logarithm $\sim \ln(Q^2/m^2)$ appears, which can be again traced back to the universality of the soft corrections for massless and massive primary quarks.

Assembling all the pieces above in Eq. (6.42) we get the following result for $C_m^{(C_F T_F, n_l)}$:

$$\begin{aligned} C_m^{(C_F T_F, n_l)}\left(m, \frac{Q}{m}, \mu\right) = \left(\frac{\alpha_s^{(n_l)}(\mu)}{4\pi}\right)^2 C_F T_F \Bigg\{ &-\frac{8}{9}L_m^3 - \frac{2}{9}L_m^2 + \left(\frac{130}{27} + \frac{2\pi^2}{3}\right) L_m \\ &- \left(\frac{4}{3}L_m^2 + \frac{40}{9}L_m + \frac{112}{27}\right) \ln\left(\frac{-Q^2 - i0}{m^2}\right) + \frac{5107}{162} - \frac{41\pi^2}{27} - \frac{4\zeta_3}{9}\Bigg\}, \end{aligned} \tag{6.64}$$

which matches exactly with the $C_F T_F$ result we obtained above in Eq. (6.33). In the next section we decompose the SCET form factor result into soft and collinear pieces in order to find the terms needed for the rapidity RGE analysis.

6.3.4 Two Loop Ingredients for the Rapidity Renormalization Group

In order to determine the ingredients needed for the rapidity renormalization group analysis, we now calculate the $\mathcal{O}(\alpha_s^2 C_F T_F)$ SCET form factor contributions for the individual collinear and soft sectors using dispersion relations. We will employ the

symmetric η-regulator [38, 37] to regulate the rapidity divergences in the individual sectors. This corresponds to modifying the Wilson lines in the respective sectors according to

$$W_n : \frac{1}{\bar{n}\cdot\mathcal{P}} \to \frac{w^2(\nu)\,\nu^\eta}{(\bar{n}\cdot\mathcal{P})^{1+\eta}}, \qquad S_n : \frac{1}{n\cdot\mathcal{P}} \to \frac{1}{n\cdot\mathcal{P}}\,\frac{w(\nu)\,\nu^{\eta/2}}{|\bar{n}\cdot\mathcal{P}-n\cdot\mathcal{P}|^{\eta/2}}, \tag{6.65}$$

and similarly for $W_{\bar{n}}$ and $S_{\bar{n}}$. Here $\mathcal{P}^\mu$ denotes the label momentum operator and $w(\nu)$ is a dimensionless book keeping coupling parameter satisfying

$$\nu\frac{\mathrm{d}}{\mathrm{d}\nu}w(\nu) = -\frac{\eta}{2}\,w(\nu), \qquad \lim_{\eta\to 0} w(\nu) = 1. \tag{6.66}$$

The one-loop form factor corrections for the radiation of a massive gluon have been already calculated in Ref. [37] for massless quarks. Including the modification due to the quark mass in Eq. (6.59) they read after expanding in η

$$\begin{aligned}
F^{(1,\mathrm{bare})}_{\mathrm{SCET},\,n} &= F^{(1,\mathrm{bare})}_{\mathrm{SCET},\,\bar{n}} \qquad (6.67)\\
&= \frac{\alpha_s^{(n_l+1)}(\mu)w^2(\nu)C_F}{4\pi}\,\Gamma(\epsilon)e^{\gamma_E\epsilon}\left(\frac{\mu^2}{M^2}\right)^\epsilon\left\{\frac{2}{\eta}+\ln\left(\frac{\nu^2}{Q^2}\right)+2\psi(2-\epsilon)+2\gamma_E-\frac{1-\epsilon}{2-\epsilon}\right\}\\
&\quad+\frac{\delta F^{(1)}_{\mathrm{SCET}}(m,M)}{2},\\
F^{(1,\mathrm{bare})}_{\mathrm{SCET},\,s} &= \frac{\alpha_s^{(n_l+1)}(\mu)w^2(\nu)C_F}{4\pi}\,\Gamma(\epsilon)e^{\gamma_E\epsilon}\left(\frac{\mu^2}{M^2}\right)^\epsilon\left\{-\frac{4}{\eta}-2\ln\left(\frac{\nu^2}{-M^2+i0}\right)-2\psi(\epsilon)-2\gamma_E\right\}.
\end{aligned}$$

In the collinear results we have included the wave function contributions $Z_{\xi_n}/2$ and $Z_{\xi_{\bar{n}}}/2$. The soft-bin subtractions in the collinear diagrams vanish for the η-regulator.

In direct analogy to Eq. (6.39) the corresponding two-loop expressions for the individual soft and collinear sectors read

$$\begin{aligned}
F^{(C_FT_F,\mathrm{bare})}_{\mathrm{SCET},\,i}(Q,m) = \frac{1}{\pi}\int\frac{\mathrm{d}M^2}{M^2}\,F^{(1,\mathrm{bare})}_{\mathrm{SCET},\,i}(Q,m,M)\,\mathrm{Im}\left[\Pi(m^2,M^2)\right]\\
-\left(\Pi(m^2,0)-\frac{\alpha_sT_F}{3\pi}\,\frac{1}{\epsilon}\right)F^{(1,\mathrm{bare})}_{\mathrm{SCET},\,i}(Q,m,\Lambda).
\end{aligned} \tag{6.68}$$

for $i = n, \bar{n}, s$. Note that for this relation to make sense also the one-loop form factor

corrections with a massless gluon have to be decomposed according to Eq. (6.23). To achieve this goal we use a gluon mass $\Lambda \ll m$ as an infrared regulator which allows us to use the results in Eq. (6.67). As discussed in Sec. 6.1, we absorb all divergences of the form $1/\eta$, η^0/ϵ^n in the form factors into separate counterterms $Z^{(C_F T_F)}_{\mathrm{SCET},i}$ for each sector, so that

$$F^{(1)}_{\mathrm{SCET},i} = F^{(1,\mathrm{bare})}_{\mathrm{SCET},i} + Z^{(1)}_{\mathrm{SCET},i}\,, \qquad F^{(C_F T_F)}_{\mathrm{SCET},i} = F^{(C_F T_F,\mathrm{bare})}_{\mathrm{SCET},i} + Z^{(C_F T_F)}_{\mathrm{SCET},i}\,. \tag{6.69}$$

The explicit results for the counterterms at one-loop are given by[3]

$$\begin{aligned} Z^{(1)}_{\mathrm{SCET},n}(Q,m,\Lambda,\mu,\nu) &= Z^{(1)}_{\mathrm{SCET},\bar n}(Q,m,\Lambda,\mu,\nu)\,, \qquad (6.70)\\ &= \frac{\alpha_s^{(n_l+1)}(\mu)\,w^2(\nu)\,C_F}{4\pi}\left\{\frac{1}{\eta}\left[-\frac{2}{\epsilon}+2\ln\left(\frac{\Lambda^2}{\mu^2}\right)\right]+\frac{1}{\epsilon}\left[-\frac{3}{2}-\ln\left(\frac{\nu^2}{Q^2}\right)\right]\right\}\\ Z^{(1)}_{\mathrm{SCET},s}(Q,m,\Lambda,\mu,\nu) &= \frac{\alpha_s^{(n_l+1)}(\mu)\,w^2(\nu)\,C_F}{4\pi}\left\{\frac{1}{\eta}\left[\frac{4}{\epsilon}-4\ln\left(\frac{\Lambda^2}{\mu^2}\right)\right]-\frac{2}{\epsilon^2}+\frac{2}{\epsilon}\ln\left(\frac{\nu^2}{-\mu^2+i0}\right)\right\}, \end{aligned}$$

while at two-loop they read

$$\begin{aligned} &Z^{(C_F T_F)}_{\mathrm{SCET},n}(Q,m,\Lambda,\mu,\nu) = Z^{(C_F T_F)}_{\mathrm{SCET},\bar n}(Q,m,\Lambda,\mu,\nu)\\ &= \frac{\left[\alpha_s^{(n_l+1)}(\mu)\right]^2 w^2(\nu)\,C_F T_F}{16\pi^2}\left\{\frac{1}{\eta}\left[-\frac{4}{3\epsilon^2}+\frac{20}{9\epsilon}+\frac{8}{3}L_m\ln\left(\frac{\Lambda^2}{\mu^2}\right)-\frac{4}{3}L_m^2-\frac{40}{9}L_m-\frac{112}{27}+\mathcal{O}(\epsilon)\right]\right.\\ &\quad\left.+\frac{1}{\epsilon^2}\left[-\frac{2}{3}\ln\left(\frac{\nu^2}{Q^2}\right)-1\right]+\frac{1}{\epsilon}\left[\frac{10}{9}\ln\left(\frac{\nu^2}{Q^2}\right)+\frac{1}{6}+\frac{2\pi^2}{9}\right]\right\},\\ &Z^{(C_F T_F)}_{\mathrm{SCET},s}(Q,m,\Lambda,\mu,\nu)\\ &= \frac{\left[\alpha_s^{(n_l+1)}(\mu)\right]^2 w^2(\nu)\,C_F T_F}{16\pi^2}\left\{\frac{1}{\eta}\left[\frac{8}{3\epsilon^2}-\frac{40}{9\epsilon}-\frac{16}{3}L_m\ln\left(\frac{\Lambda^2}{\mu^2}\right)+\frac{8}{3}L_m^2+\frac{80}{9}L_m+\frac{224}{27}+\mathcal{O}(\epsilon)\right]\right.\\ &\quad\left.-\frac{2}{\epsilon^3}+\frac{1}{\epsilon^2}\left[\frac{4}{3}\ln\left(\frac{\nu^2}{-\mu^2+i0}\right)+\frac{10}{9}\right]+\frac{1}{\epsilon}\left[-\frac{20}{9}\ln\left(\frac{\nu^2}{-\mu^2+i0}\right)+\frac{56}{27}-\frac{\pi^2}{9}\right]\right\}. \end{aligned} \tag{6.71}$$

Note that the sum $Z^{(C_F T_F)}_{\mathrm{SCET},n} + Z^{(C_F T_F)}_{\mathrm{SCET},\bar n} + Z^{(C_F T_F)}_{\mathrm{SCET},s}$ reproduces the result for the SCET

[3]Although the full ϵ-dependence in the expression proportional to $1/\eta$ should be in principle kept unexpanded, this is only relevant to ensure that the coefficient of the $1/\eta$ pole is explicitly μ-independent, which is also true order by order in its ϵ expansion. Therefore we show here only the terms up to $\mathcal{O}(\epsilon^0)$ which contain the information we need later for the anomalous dimensions.

current counterterm $Z_{\rm SCET}^{(C_F T_F)}$ in Eq. (6.62). These results for the individual collinear and soft counterterms provide the necessary ingredients for determining the rapidity RGE for the collinear and soft sectors below in Sec. 6.4.1.

6.4 Rapidity Evolution and Numerical Results

6.4.1 Rapidity Renormalization Group Evolution

In our result for the matching coefficient between bHQET and SCET at $\mathcal{O}(\alpha_s^2)$, given above in Eq. (6.34), we encountered a large logarithm $\alpha_s^2 C_F T_F \ln(m^2/Q^2)$. We discussed the setup for the resummation of such logarithms above in Sec. 6.1. As shown in Sec. 6.3 these rapidity logarithms are only related to contributions of the virtual massive quarks that appear in the gluon vacuum polarization, and hence are the same as in the threshold corrections for massless primary quarks in Ref. [103]. There it was anticipated that they can be resummed by exponentiation, as is common for these kinds of logarithms. For example, for the radiation of a massive gauge boson the rapidity renormalization group implies that this exponentiation occurs to all orders in perturbation theory [36, 35, 37, 61]. The difference in our case is that the rapidity logarithms start at two-loops, and hence involve the additional issue of one-loop induced corrections due to the scheme change in the coupling constant.

Here we will show explicitly how to treat the rapidity logarithms at $\mathcal{O}(\alpha_s^2 C_F T_F)$ in a rapidity renormalization group framework, and subsequently demonstrate that they indeed exponentiate. We start from Eq. (6.26). Up to $\mathcal{O}(\alpha_s^2)$ we only have a contribution from the $C_F T_F$ dependent terms,

$$\begin{aligned}\gamma_{\nu,i}^{C_m}(m,\mu) &= \nu\frac{\mathrm{d}}{\mathrm{d}\nu}\ln Z_{\mathrm{SCET},i} - \nu\frac{\mathrm{d}}{\mathrm{d}\nu}\ln Z_{\mathrm{bHQET},i} \\ &= \nu\frac{\mathrm{d}}{\mathrm{d}\nu}Z_{\mathrm{SCET},i}^{(C_F T_F)} - \frac{\alpha_s^{(n_l)}(\mu) T_F}{3\pi}\ln\!\left(\frac{m^2}{\mu^2}\right)\nu\frac{\mathrm{d}}{\mathrm{d}\nu}Z_{\mathrm{SCET},i}^{(1)} + \mathcal{O}(\alpha_s^3)\,, \end{aligned} \tag{6.72}$$

where the second term accounts for coupling conversion from the (n_l+1)-flavor to n_l-flavor scheme. As before, in the n_l-flavor scheme the bHQET graphs give no con-

tribution. The results from Sec. 6.3.4 can now be used to compute this ν-anomalous dimension. Using Eq. (6.70) we can calculate the one-loop correction,

$$\nu\frac{\mathrm{d}}{\mathrm{d}\nu}\,Z^{(1)}_{\mathrm{SCET},\,n} = \nu\frac{\mathrm{d}}{\mathrm{d}\nu}\,Z^{(1)}_{\mathrm{SCET},\,\bar{n}} = -\frac{1}{2}\,\nu\frac{\mathrm{d}}{\mathrm{d}\nu}\,Z^{(1)}_{\mathrm{SCET},\,s} = -\frac{\alpha_s^{(n_l+1)}(\mu)\,C_F}{2\pi}\ln\left(\frac{\Lambda^2}{\mu^2}\right), \tag{6.73}$$

which exhibits dependence on the infrared gluon-mass regulator Λ. The two-loop term above can be calculated using Eq. (6.71) which gives

$$\begin{aligned}\nu\frac{\mathrm{d}}{\mathrm{d}\nu}\,Z^{(C_FT_F)}_{\mathrm{SCET},\,n} &= \nu\frac{\mathrm{d}}{\mathrm{d}\nu}\,Z^{(C_FT_F)}_{\mathrm{SCET},\,\bar{n}} = -\frac{1}{2}\,\nu\frac{\mathrm{d}}{\mathrm{d}\nu}\,Z^{(C_FT_F)}_{\mathrm{SCET},\,s} \\ &= \frac{[\alpha_s^{(n_l+1)}(\mu)]^2 C_F T_F}{16\pi^2}\left\{-\frac{8}{3}L_m\ln\left(\frac{\Lambda^2}{\mu^2}\right)+\frac{4}{3}L_m^2+\frac{40}{9}L_m+\frac{112}{27}\right\},\end{aligned} \tag{6.74}$$

where L_m is defined in Eq. (6.27). Together these results determine the ν-anomalous dimensions:

$$\begin{aligned}\gamma^{C_m,\,C_FT_F}_{\nu,\,n}(m,\mu) &= \gamma^{C_m,\,C_FT_F}_{\nu,\,\bar{n}}(m,\mu) = -\frac{1}{2}\,\gamma^{C_m,\,C_FT_F}_{\nu,\,s}(m,\mu) \\ &= \frac{[\alpha_s(\mu)]^2 C_F T_F}{16\pi^2}\left\{\frac{4}{3}L_m^2+\frac{40}{9}L_m+\frac{112}{27}\right\}.\end{aligned} \tag{6.75}$$

Note that the IR regulator has canceled out, and that here the coupling $[\alpha_s(\mu)]^2$ can be taken in either the n_l or (n_l+1)-flavor scheme since the anomalous dimension starts at $\mathcal{O}(\alpha_s^2)$ and the difference is higher order. This result suffices for solving the ν-RGE equations at NNLL order. Using Eq. (6.24) and Eq. (6.25) we can write an analog of Eq. (6.9) for the ν-evolution of H_m. From Eq. (6.24) we have

$$H_m^{(n_l)}\left(m,\frac{Q}{m},\mu\right) = H_{m,\,n}^{(n_l)}\left(m,\mu,\frac{\nu}{Q}\right)\,H_{m,\,\bar{n}}^{(n_l)}\left(m,\mu,\frac{\nu}{Q}\right)\,H_{m,\,s}^{(n_l)}\left(m,\mu,\frac{\nu}{m}\right). \tag{6.76}$$

With rapidity evolution this becomes

$$H_m^{(n_l)}\left(m, \frac{Q}{m}, \mu; \nu_Q, \nu_m\right) \tag{6.77}$$
$$= H_{m,n}^{(n_l)}\left(m, \mu, \frac{\nu_Q}{Q}\right) H_{m,\bar{n}}^{(n_l)}\left(m, \mu, \frac{\nu_Q}{Q}\right) V_{\rm RRG}(\nu_Q, \nu_m, \mu)\, H_{m,s}^{(n_l)}\left(m, \mu, \frac{\nu_m}{m}\right),$$

where on the LHS the dependence on ν_Q and ν_m comes from truncating the resummed perturbation theory for objects on the RHS. Here the functions $H_{m,n}^{(n_l)} = H_{m,\bar{n}}^{(n_l)}$ and $H_{m,s}^{(n_l)}$ are given up to $\mathcal{O}(\alpha_s^2)$ by

$$\begin{aligned}
H_{m,n}^{(n_l)}\left(m, \mu, \frac{\nu_Q}{Q}\right) &= 1 + \frac{\alpha_s^{(n_l)}(\mu) C_F}{4\pi}\left(L_m^2 - L_m + 4 + \frac{\pi^2}{6}\right) \\
&+ \left(\frac{\alpha_s^{(n_l)}(\mu)}{4\pi}\right)^2 C_F^2 \left\{\frac{1}{2}L_m^4 - L_m^3 + \left(\frac{9}{2} + \frac{\pi^2}{6}\right)L_m^2 - \left(\frac{11}{2} - \frac{11\pi^2}{6} + 24\zeta_3\right)L_m \right. \\
&\quad \left. + \frac{241}{8} + \frac{13\pi^2}{3} - 8\pi^2 \log 2 - 6\zeta_3 - \frac{163\pi^4}{360}\right\} \\
&+ \left(\frac{\alpha_s^{(n_l)}(\mu)}{4\pi}\right)^2 C_A C_F \left\{-\frac{11}{9}L_m^3 + \left(\frac{167}{18} - \frac{\pi^2}{3}\right)L_m^2 - \left(\frac{1165}{54} + \frac{28\pi^2}{9} - 30\zeta_3\right)L_m \right. \\
&\quad \left. + \frac{12877}{648} + \frac{323\pi^2}{108} + 4\pi^2 \log 2 + \frac{89\zeta_3}{9} - \frac{47\pi^4}{180}\right\} \\
&+ \left(\frac{\alpha_s^{(n_l)}(\mu)}{4\pi}\right)^2 C_F n_l T_F \left\{\frac{4}{9}L_m^3 - \frac{26}{9}L_m^2 + \left(\frac{154}{27} + \frac{8\pi^2}{9}\right)L_m - \frac{1541}{162} - \frac{37\pi^2}{27} - \frac{52\zeta_3}{9}\right\} \\
&+ \left(\frac{\alpha_s^{(n_l)}(\mu)}{4\pi}\right)^2 C_F T_F \left\{2L_m^2 + \left(\frac{2}{3} + \frac{8\pi^2}{9}\right)L_m + \frac{3139}{162} - \frac{4\pi^2}{3} + \frac{8\zeta_3}{3} \right. \\
&\quad \left. + \left(\frac{4}{3}L_m^2 + \frac{40}{9}L_m + \frac{112}{27}\right)\ln\left(\frac{\nu_Q^2}{Q^2}\right)\right\},
\end{aligned} \tag{6.78}$$

$$\begin{aligned}
H_{m,s}^{(n_l)}\left(m, \mu, \frac{\nu_m}{m}\right) &= 1 + \left(\frac{\alpha_s^{(n_l)}(\mu)}{4\pi}\right)^2 C_F T_F \left\{\frac{8}{9}L_m^3 + \frac{40}{9}L_m^2 + \left(\frac{448}{27} - \frac{4\pi^2}{9}\right)L_m \right. \\
&\quad \left. + \frac{656}{27} - \frac{10\pi^2}{27} - \frac{56\zeta_3}{9} - \left(\frac{8}{3}L_m^2 + \frac{80}{9}L_m + \frac{224}{27}\right)\ln\left(\frac{\nu_m^2}{\mu^2}\right)\right\},
\end{aligned} \tag{6.79}$$

and contain no large logarithms for $\mu \simeq m$, and for $\nu_Q \simeq Q$ and $\nu_m \simeq m$, respectively. The evolution factor $V_{\rm RRG}$ sums the rapidity logs between ν_m and ν_Q, and is defined

as follows

$$V_{\rm RRG}(\nu_f,\nu_i,\mu) = \exp\left\{\int_{\ln\nu_i}^{\ln\nu_f} \mathrm{d}\ln\nu \left[\gamma_{\nu,s}^{C_m} + (\gamma_{\nu,s}^{C_m})^*\right]\right\}. \tag{6.80}$$

The general result for $V_{\rm RRG}$, and the result at NNLL, will be given below.

Similarly to the ν-anomalous dimensions, we can also determine individual μ-anomalous dimensions for the collinear and soft sectors, $i = n, s, \bar{n}$,

$$\gamma_{\mu,i}^{C_m} = \mu\frac{\mathrm{d}}{\mathrm{d}\mu}\ln Z_{\mathrm{SCET},i} - \mu\frac{\mathrm{d}}{\mathrm{d}\mu}\ln Z_{\mathrm{bHQET},i}\,. \tag{6.81}$$

Repeating the steps below Eq. (6.72) we find

$$\begin{aligned}
\gamma_{\mu,n}^{C_m,C_FT_F}\Big(m,\mu,\frac{\nu}{Q}\Big) &= \frac{[\alpha_s^{(n_l)}(\mu)]^2 C_F T_F}{16\pi^2}\left\{-\left(\frac{8}{3}L_m+\frac{40}{9}\right)\ln\left(\frac{\nu^2}{Q^2}\right) - 4L_m - \frac{2}{3} - \frac{8\pi^2}{9}\right\} \\
&= \gamma_{\mu,\bar{n}}^{C_m(C_FT_F)}\Big(m,\mu,\frac{\nu}{Q}\Big), \\
\gamma_{\mu,s}^{C_m,C_FT_F}\Big(m,\mu,\frac{\nu}{m}\Big) &= \frac{[\alpha_s^{(n_l)}(\mu)]^2 C_F T_F}{16\pi^2}\left\{\left(\frac{16}{3}L_m+\frac{80}{9}\right)\ln\left(\frac{\nu^2}{-\mu^2+i0}\right) - \frac{224}{27} + \frac{4\pi^2}{9}\right\},
\end{aligned} \tag{6.82}$$

whose sum yields the same result for the $\mathcal{O}(\alpha_s^2 C_F T_F)$ μ-anomalous dimension of $C_m^{(n_l)}$ as the difference of Eqs. (6.21) and (6.19),

$$\begin{aligned}
&\gamma_{\mu,n}^{C_m,C_FT_F}\Big(m,\mu,\frac{\nu}{Q}\Big) + \gamma_{\mu,\bar{n}}^{C_m,C_FT_F}\Big(m,\mu,\frac{\nu}{Q}\Big) + \gamma_{\mu,s}^{C_m,C_FT_F}\Big(m,\mu,\frac{\nu}{m}\Big) \\
&\quad= \frac{\big[\alpha_s^{(n_l)}(\mu)\big]^2 C_F T_F}{16\pi^2}\left\{\left(\frac{16}{3}L_m+\frac{80}{9}\right)L_Q - 8L_m - \frac{260}{27} - \frac{4\pi^2}{3}\right\} \\
&\quad= \Big[\gamma_{\rm SCET}^{(n_l+1)} - \gamma_{\rm bHQET}^{(n_l)}\Big]^{(C_FT_F)} = \gamma_\mu^{C_m,C_FT_F}(Q,m,\mu)\,,
\end{aligned} \tag{6.83}$$

with L_m and L_Q defined in Eq. (6.27).

Eqs. (6.9) and (6.77) together include the evolution connected to H_m in the 2-dimensional μ-ν plane, including that from invariant mass scales μ_m to μ_Q, that from invariant mass scales μ_m to $\mu_{\rm final}$, and that from rapidity scales ν_Q to ν_m. As demonstrated in Ref. [37] the combined μ-ν evolution can be performed along any

path and the path independence implies the consistency equation:

$$\mu\frac{\mathrm{d}}{\mathrm{d}\mu}\gamma^{C_m}_{\nu,i} = \left(\frac{\partial}{\partial\mu} + \beta(g)\,\frac{\partial}{\partial g}\right)\gamma^{C_m}_{\nu,i} = \nu\frac{\mathrm{d}}{\mathrm{d}\nu}\gamma^{C_m}_{\mu,i}\,. \tag{6.84}$$

However, similar to the example of the massive Sudakov form factor considered in Ref. [37] we can see from Eq. (6.75) that $\gamma^{C_m}_{\nu,s}$ contains potentially large logarithms $\ln(\mu/m)$ for an arbitrary path in μ-ν-space. This is resolved by a prior resummation exploiting the fact that the derivatives in Eq. (6.84) are proportional to the cusp anomalous dimension. Since C_m is a matching coefficient between a (n_l+1)-flavor and n_l-flavor theory, we can express Eq. (6.84) in terms of the difference between the cusp anomalous dimensions $\Gamma_{\text{cusp}}[\alpha_s]$ in the (n_l+1) and n_l-flavor schemes. So for $\gamma^{C_m}_{\nu,s}$ we obtain

$$\begin{aligned}\mu\frac{\mathrm{d}}{\mathrm{d}\mu}\gamma^{C_m}_{\nu,s} &= \nu\frac{\mathrm{d}}{\mathrm{d}\nu}\gamma^{C_m}_{\mu,s} = -2\left(\Gamma_{\text{cusp}}[\alpha_s^{(n_l+1)}] - \Gamma_{\text{cusp}}[\alpha_s^{(n_l)}]\right)\\ &= \frac{\alpha_s^2 C_F T_F}{16\pi^2}\left(\frac{32}{3}L_m + \frac{160}{9}\right) + \mathcal{O}(\alpha_s^3)\,,\end{aligned} \tag{6.85}$$

which can be checked using the explicit perturbative expression of $\Gamma_{\text{cusp}}[\alpha_s]$ up to two loops,

$$\Gamma_{\text{cusp}}[\alpha_s^{(n_f)}] = \frac{\alpha_s^{(n_f)}}{4\pi}4C_F + \left(\frac{\alpha_s^{(n_f)}}{4\pi}\right)^2 4C_F\left[\left(\frac{67}{9} - \frac{\pi^2}{3}\right)C_A - \frac{20n_f}{9}T_F\right] + \mathcal{O}(\alpha_s^3)\,. \tag{6.86}$$

Integrating Eq. (6.85) in μ we obtain the resummed result for $\gamma^{C_m}_{\nu,s}$,

$$\begin{aligned}\gamma^{C_m}_{\nu,s}(m,\mu) &= -2\int_{\ln m}^{\ln\mu}\mathrm{d}\ln\mu'\left(\Gamma_{\text{cusp}}[\alpha_s^{(n_l+1)}(\mu')] - \Gamma_{\text{cusp}}[\alpha_s^{(n_l)}(\mu')]\right) + \gamma^{C_m}_{\nu,s}(m,m)\\ &= -\left(\omega^{(n_l+1)}(\mu,m) - \omega^{(n_l)}(\mu,m)\right) + \gamma^{C_m}_{\nu,s}(m,m)\,.\end{aligned} \tag{6.87}$$

Here the integration constant $\gamma^{C_m}_{\nu,s}(m,m)$ is the correction in the anomalous dimension $\gamma^{C_m}_{\nu,s}$ that does not multiply a logarithm $\ln(\mu^2/m^2)$. We are now in the position to write down a general expression for V_{RRG}. Using Eq. (6.80) we find the all orders

result

$$V_{\rm RRG}(\nu_Q,\nu_m,\mu)=\exp\left\{\left[\omega^{(n_l+1)}(\mu,m)-\omega^{(n_l)}(\mu,m)-\gamma^{C_m}_{\nu,s}(m,m)\right]\ln\left(\frac{\nu_m^2}{\nu_Q^2}\right)\right\}. \tag{6.88}$$

At NNLL order with the counting $\alpha_s(\mu)\ln(\nu_m/\nu_Q)\sim 1$, we can expand this exponential to the first non-trivial order. At the order we are working

$$\gamma^{C_m}_{\nu,s}(m,m)=-\frac{\left[\alpha_s^{(n_l+1)}(m)\right]^2 C_F T_F}{16\pi^2}\,\frac{224}{27}+\mathcal{O}(\alpha_s^3)\,, \tag{6.89}$$

as can be seen from Eq. (6.75), where we have for definiteness employed the (n_l+1)-flavor scheme. The evolution function ω at NNLL accuracy reads

$$\begin{aligned}\omega^{(n_f)}(\mu,\mu_0)=-\frac{\Gamma_0}{\beta_0}\Bigg\{&\ln r+\left(\frac{\Gamma_1}{\Gamma_0}-\frac{\beta_1}{\beta_0}\right)\frac{\alpha_s^{(n_f)}(\mu_0)}{4\pi}(r-1)\\&+\left(\frac{\Gamma_2}{\Gamma_0}-\frac{\beta_1\Gamma_1}{\beta_0\Gamma_0}-\frac{\beta_2}{\beta_0}+\frac{\beta_1^2}{\beta_0^2}\right)\frac{\left[\alpha_s^{(n_f)}(\mu_0)\right]^2}{32\pi^2}(r^2-1)\Bigg\},\end{aligned} \tag{6.90}$$

where $r=\alpha_s^{(n_f)}(\mu)/\alpha_s^{(n_f)}(\mu_0)$ and the coefficients β_i and Γ_i are evaluated with n_f flavors.

To extend the analysis to N^{3}LL resummation, one needs the result for the ν-anomalous dimension $\gamma^{C_m}_{\nu,s}(m,m)$ at $\mathcal{O}(\alpha_s^3)$, which can be inferred from the coefficient of the rapidity logarithm appearing in a related DIS calculation [6] due to consistency (see Ref. [73]).

6.4.2 Numerical Results

In this section we explore the impact of the two-loop correction to the hard function H_m on the differential cross section and the corresponding improvement to the perturbative uncertainties. To do this we examine the evolved hard function $H_{\rm evol}(Q,m,\mu_{\rm final};\mu_Q,\mu_m,\nu_Q,\nu_m)$ from Eq. (6.9). This function fully captures the multiplicative contributions for the differential cross section factorization theorem

in Eq. (6.1), including the matching at $\mu_Q \simeq Q$ in $H_Q^{(n_l+1)}$, the RG evolution from μ_Q down to $\mu_m \simeq m$ in $U_{H_Q}^{(n_l+1)}$, the matching at μ_m encoded in H_m, and through $U_v^{(n_l)}$ the RG evolution from μ_m down to a scale $\mu_{\rm final}$ where the soft and jet functions are evaluated.[4] Since the ingredient that has not been previously analyzed is H_m we focus our numerical study on the impact of this function and the associated reduction in the resulting μ_m dependence. For $H_m^{(n_l)}(m, Q/m, \mu_m; \nu_Q, \nu_m)$ we employ Eq. (6.77), which provides a decomposition of this function into collinear and soft components, $H_{m,i}^{(n_l)}$ with $i = n, \bar{n}, s$, plus a kernel $V_{\rm RRG}$ which carries out the RG evolution in rapidity from $\nu_Q \simeq Q$ to $\nu_m \simeq m$.

We begin by converting the result for the collinear and soft components $H_{m,i}^{(n_l)}$ in Eqs. (6.78) and (6.79) from the pole-mass scheme to the $\overline{\rm MS}$ mass scheme with n_l+1 dynamic flavors via

$$m_{\rm pole} = \bar{m}^{(n_l+1)}(\mu)\left(1 - \frac{\alpha_s^{(n_l+1)}(\mu) C_F}{4\pi}(3L_m - 4)\right) + \mathcal{O}(\alpha_s^2)\,. \tag{6.91}$$

The $\overline{\rm MS}$ scheme is an appropriate renormalon-free short distance mass scheme to be employed in the hard function H_m. For consistency we also convert the results in Eqs. (6.78) and (6.79) to the (n_l+1)-flavor scheme for the strong coupling. Together this yields up to $\mathcal{O}(\alpha_s^2)$

$$\begin{aligned}
H_{\bar{m},n}^{(n_l+1)}\Big(\bar{m}, \mu, \frac{\nu_Q}{Q}\Big) &= 1 + \frac{\alpha_s^{(n_l+1)}(\mu) C_F}{4\pi}\left(L_{\bar{m}}^2 - L_{\bar{m}} + 4 + \frac{\pi^2}{6}\right) \\
&+ \left(\frac{\alpha_s^{(n_l+1)}(\mu)}{4\pi}\right)^2 C_F^2 \left\{\frac{1}{2}L_{\bar{m}}^4 - L_{\bar{m}}^3 - \left(\frac{15}{2} - \frac{\pi^2}{6}\right)L_{\bar{m}}^2 + \left(\frac{33}{2} + \frac{11\pi^2}{6} - 24\zeta_3\right)L_{\bar{m}}\right. \\
&\quad \left. + \frac{177}{8} + \frac{13\pi^2}{3} - 8\pi^2\log 2 - 6\zeta_3 - \frac{163\pi^4}{360}\right\} \\
&+ \left(\frac{\alpha_s^{(n_l+1)}(\mu)}{4\pi}\right)^2 C_A C_F \left\{-\frac{11}{9}L_{\bar{m}}^3 + \left(\frac{167}{18} - \frac{\pi^2}{3}\right)L_{\bar{m}}^2 - \left(\frac{1165}{54} + \frac{28\pi^2}{9} - 30\zeta_3\right)L_{\bar{m}}\right. \\
&\quad \left. + \frac{12877}{648} + \frac{323\pi^2}{108} + 4\pi^2\log 2 + \frac{89\zeta_3}{9} - \frac{47\pi^4}{180}\right\}
\end{aligned}$$

[4]The soft or jet functions also contain an additional evolution which is not purely multiplicative [49]. This evolution affects the shape of the $\mathrm{d}\sigma/\mathrm{d}s_t\mathrm{d}s_{\bar{t}}$ distribution and was evaluated up to NNLL′ order in Ref. [78].

$$+\left(\frac{\alpha_s^{(n_l+1)}(\mu)}{4\pi}\right)^2 C_F n_l T_F \left\{\frac{4}{9}L_{\bar{m}}^3-\frac{26}{9}L_{\bar{m}}^2+\left(\frac{154}{27}+\frac{8\pi^2}{9}\right)L_{\bar{m}}-\frac{1541}{162}-\frac{37\pi^2}{27}-\frac{52\zeta_3}{9}\right\}$$
$$+\left(\frac{\alpha_s^{(n_l+1)}(\mu)}{4\pi}\right)^2 C_F T_F \left\{\frac{4}{3}L_{\bar{m}}^3+\frac{2}{3}L_{\bar{m}}^2+\left(6+\frac{10\pi^2}{9}\right)L_{\bar{m}}+\frac{3139}{162}-\frac{4\pi^2}{3}+\frac{8\zeta_3}{3}\right.$$
$$\left.+\left(\frac{4}{3}L_{\bar{m}}^2+\frac{40}{9}L_{\bar{m}}+\frac{112}{27}\right)\ln\left(\frac{\nu_Q^2}{Q^2}\right)\right\}=H_{\bar{m},\bar{n}}^{(n_l+1)}\left(\bar{m},\mu,\frac{\nu_Q}{Q}\right), \tag{6.92}$$

$$H_{\bar{m},s}^{(n_l+1)}\left(\bar{m},\mu,\frac{\nu_m}{m}\right)=1+\left(\frac{\alpha_s^{(n_l+1)}(\mu)}{4\pi}\right)^2 C_F T_F \left\{\frac{8}{9}L_{\bar{m}}^3+\frac{40}{9}L_{\bar{m}}^2+\left(\frac{448}{27}-\frac{4\pi^2}{9}\right)L_{\bar{m}}\right.$$
$$\left.+\frac{656}{27}-\frac{10\pi^2}{27}-\frac{56\zeta_3}{9}-\left(\frac{8}{3}L_{\bar{m}}^2+\frac{80}{9}L_{\bar{m}}+\frac{224}{27}\right)\ln\left(\frac{\nu_m^2}{\mu^2}\right)\right\}, \tag{6.93}$$

where $L_{\bar{m}}=\ln(\bar{m}^2/\mu^2)$ and $\bar{m}=\bar{m}^{(n_l+1)}(\mu)$ is the $\overline{\rm MS}$ mass for n_l+1 active flavors. For the bHQET evolution function $U_v^{(n_l)}$, when using the $\overline{\rm MS}$ mass scheme, we expand the pole mass appearing in the anomalous dimension in Eq. (6.21) in terms of $\bar{m}_t(\bar{m}_t)$ to obtain

$$\gamma_{\rm bHQET}\left(\frac{Q}{\bar{m}},\mu\right)=\frac{\alpha_s^{(n_l)}(\mu)C_F}{4\pi}\left[-4L+4\right]+\left(\frac{\alpha_s^{(n_l)}(\mu)}{4\pi}\right)^2\left\{n_l C_F T_F\left[\frac{80}{9}\bar{L}-\frac{80}{9}\right]\right.$$
$$\left.+C_F C_A\left[-\left(\frac{268}{9}-\frac{4\pi^2}{3}\right)\bar{L}+\frac{196}{9}-\frac{4\pi^2}{3}+8\zeta_3\right]\right\}$$
$$+\frac{32\,\alpha_s^{(n_l)}(\mu)\alpha_s^{(n_l)}(\bar{m})C_F^2}{(4\pi)^2}+\mathcal{O}(\alpha_s^3), \tag{6.94}$$

where $\bar{L}=\ln[(-Q^2-i0)/\bar{m}^2]$. For the ν-anomalous dimensions the $\overline{\rm MS}$ results are obtained by the simple replacement $m\to\bar{m}$, since they start at two-loops. For our central results below we use $\mu_m=\nu_m=\bar{m}_t$ and $\mu_Q=\nu_Q=Q$.

For our numerical analysis of $H_{\rm evol}$ we employ scale choices that are appropriate to the peak region of the differential cross section within bHQET. We fix $Q=\mu_Q=1\,\text{TeV}$, which is a possible c.m. energy for a future linear collider, and $\mu_{\rm final}=5\,\text{GeV}$ corresponding to the scale of the soft radiation. We do not vary these two scales here since their impact and associated uncertainties have been analyzed elsewhere [50]. They matter only for the overall normalization and thus cancel in the normalized spectrum. In addition we use the $\overline{\rm MS}$ mass $\bar{m}_t(\bar{m}_t)=163\,\text{GeV}$ or pole mass $m_t=171.8\,\text{GeV}$ using the two-loop conversion, and $\alpha_s^{(5)}(m_Z)=0.114$ [22, 5] and using

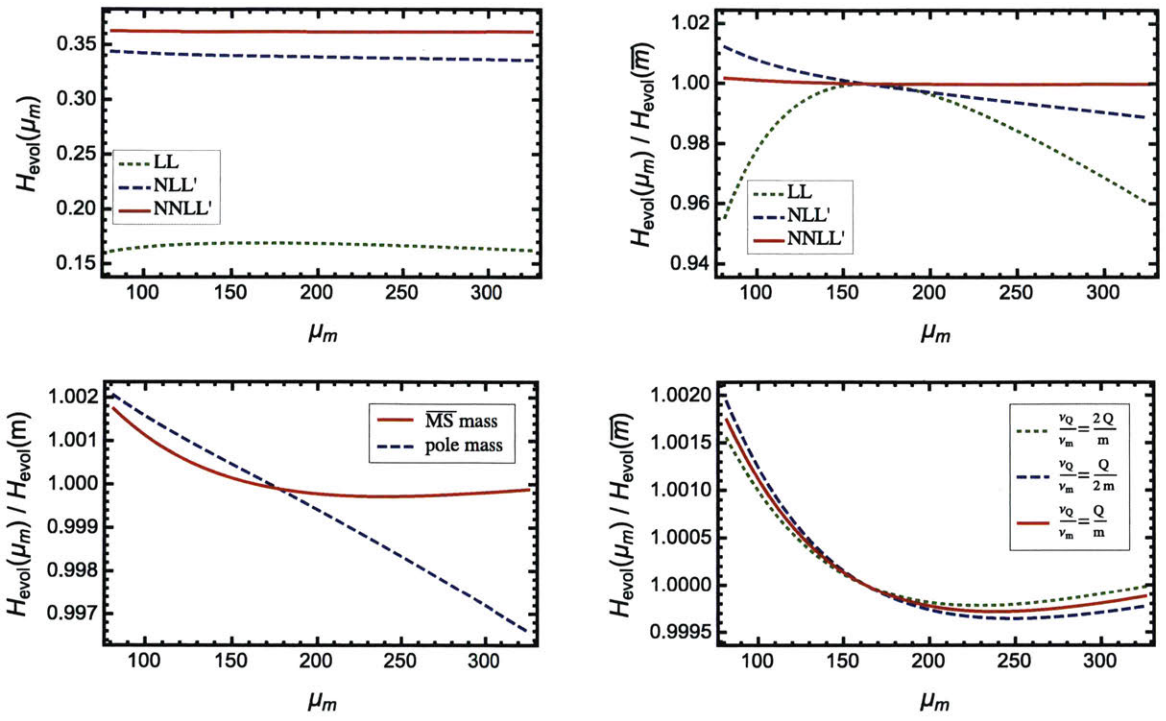

Figure 6-2: Upper panels: Plots of the residual dependence on the matching scale μ_m for the unnormalized (left) and normalized (right) evolved hard function $H_{\rm evol}$ at three different orders in the evolution, using the $\overline{\rm MS}$ mass. Lower left panel: Comparison of the scale dependence at NNLL$'$ for the $\overline{\rm MS}$ mass and the pole mass. Lower right panel: Impact of varying the ratio of rapidity scales ν_Q/ν_m by a factor of two at NNLL$'$ as a function of μ_m, with the $\overline{\rm MS}$ mass.

two-loop conversion at $\mu = \bar{m}_t$ to obtain $\alpha_s^{(6)}(\mu)$. For results with RG evolution that sums large logarithms we use the so called primed counting, i.e. our results at NLL$'$ and NNLL$'$ include NLL and NNLL evolution kernels together with the hard function boundary conditions at $\mathcal{O}(\alpha_s)$ and $\mathcal{O}(\alpha_s^2)$, respectively. [5] For the rapidity evolution we use the expression in Eq. (6.88), and the default rapidity scales $\nu_Q = Q$ and $\nu_m = m_t$, where m_t is either the $\overline{\rm MS}$ mass $\bar{m}_t(\bar{m}_t)$ or the pole mass.

To determine the impact on the normalization we first note that the two-loop fixed order corrections to $H_{\bar{m}}^{(n_l+1)}$ turn out to be small, giving at the central scale

[5] Going from NNLL$'$ to an even higher order in the resummation, N^{3}LL, does not affect any of the conclusions in this section, and therefore, for convenience, we carry out our numerical analysis at NNLL$'$.

$\mu_m = \bar{m}_t(\bar{m}_t)$ a 2% correction and the fixed-order series

$$H_{\bar{m}}^{(n_l+1)}\Big(\bar{m}_t, \frac{Q}{\bar{m}_t}, \mu_m = \bar{m}_t\Big) = 1 + 0.126(\text{1-loop}) + 0.015(\text{2-loop}) = 1.141\,. \qquad (6.95)$$

In the top-left panel of Fig. 6-2 we display the evolved hard function H_{evol} at the first three orders in resummed perturbation theory for values of μ_m in the range $\bar{m}_t/2 < \mu_m < 2\bar{m}_t$. We use the $\overline{\text{MS}}$ mass scheme and the expressions for $H_{\bar{m},n}^{(n_l+1)}$, $H_{\bar{m},\bar{n}}^{(n_l+1)}$ and $H_{\bar{m},s}^{(n_l+1)}$ from Eqs. (6.92) and (6.93). As already observed in Ref. [50], there is a significant correction when going from LL to NLL′ order which more than doubles H_{evol}. From NLL′ to NNLL′ we observe that the correction is notably smaller, indicating that the series has stabilized. Although the magnitude of these corrections is not captured by the μ_m variation, it is of the size expected from studying the uncertainty associated to the μ_{final} variation. The complete study of the μ_{final} variation requires including the jet and soft functions, which cancel the μ_{final} dependence of H_{evol} to the order one is working. We leave this for future work rather than taking it up here. We observe that the μ_m dependence significantly decreases as we go to higher order. This behavior is shown best in the top-right panel of Fig. 6-2, where the same curves are plotted, but now normalized to $H_{\text{evol}}(\mu_m = \bar{m}_t)$ at the respective order. The two-loop result for the hard function $H_{\bar{m}}^{(n_l+1)}$ plays a key role in this reduction of the scale dependence at NNLL′. Note that the size of the μ_m variation of the blue dashed curve at 2% correlates well with the size of the NNLO fixed order correction in Eq. (6.95), which gives a +2% correction. Therefore it is reasonable to take the μ_m variation of the solid red curve in this figure as an estimate of the $\mathcal{O}(\alpha_s^3)$ correction in Eq. (6.95), which we take to be $\pm 0.2\%$.

In the lower-left panel of Fig. 6-2 we compare the dependence on μ_m at NNLL′ for the $\overline{\text{MS}}$ mass with the corresponding result for the pole mass. In the pole mass case we employ Eqs. (6.78) and (6.79) for $H_{m,n}^{(n_l)}$, $H_{m,\bar{n}}^{(n_l)}$ and $H_{m,s}^{(n_l)}$. We see that the pole mass exhibits a larger sensitivity to the renormalization scale μ_m implying a slightly slower convergence of the perturbative series, potentially related to IR renormalon effects.

Finally, we can analyze the impact of the terms related to rapidity logarithms. For $\mu_m = \bar{m}_t(\bar{m}_t)$, these terms yield a numerical contribution of -0.0014 in the fixed-order full hard function $H_{\bar{m}}^{(n_l+1)}(\bar{m}_t, Q/\bar{m}_t, \mu_m = \bar{m}_t)$ in Eq. (6.95). Due to a relatively small coefficient, they do not give a significant correction in comparison with the remaining two-loop contributions which give a numerical correction of 0.0166. Therefore, we anticipate the dependence on the rapidity scales ν_Q and ν_m to be rather mild. In the lower-right panel of Fig. 6-2 we plot $H_{\rm evol}$ at NNLL$'$ for the $\overline{\rm MS}$ mass as a function of μ_m, but now with three choices for ν_Q/ν_m. To obtain these results we varied ν_Q up and down by a factor of two, but we note that equivalent results are obtained by instead varying ν_m by a factor of two. We see that varying ν_Q/ν_m by a factor of 2 gives a negligible effect compared to the residual μ_m dependence at this order. Therefore, we conclude that including an uncertainty from ν-variation is not necessary to obtain an estimate of the overall perturbative uncertainty of the cross section.

Now we summarize the results of this chapter. In the context of EFT factorization for boosted top quark production, we have extracted the hard function $H_m = |C_m|^2$ describing virtual fluctuations at the top-mass scale, completely at two-loop order using earlier results from Refs. [19, 59]. This result provides the last missing ingredient needed to make N^{3}LL resummed predictions (up to the 4-loop cusp anomalous dimension) for the invariant mass distribution of top-jets in the peak region using the factorization theorem of Refs. [49, 50] given in Eq. (6.1). Particular focus was given to the contributions to H_m from heavy quark loops, which induce terms with a large logarithm $\alpha_s^2 C_F T_F \ln(Q^2/m^2)$ that can not be treated with standard RG evolution in μ. These terms were computed once more directly using collinear and soft matrix elements in SCET, and we have shown how they can be factorized using a rapidity cutoff ν, and RG evolved using rapidity renormalization group equations. Interestingly, this factorization and RG evolution occurs within the Wilson coefficient C_m and hence at the amplitude level. Using our result for H_m we have assessed the remaining perturbative uncertainty associated to the top-mass scale, $\mu_m \simeq m$, and estimate it to be very small, $\pm 0.2\%$, predicting that the two-loop result for H_m provides a very accurate result for this function. The total normalization uncertainty in the differen-

tial cross section is expected to now be dominated by that from $\mathcal{O}(\alpha_s^3)$ perturbative corrections to the low-scale soft and jet functions, which could be estimated by a dedicated study of the residual μ_{final} dependence at NNLL$'$ order.

Chapter 7

Conclusion

In this thesis we have considered the application of effective field theories (EFT) for precision determinations of the mass of the top quark, m_t. We have shown that effective field theories provide the needed sophistication to describe the multi-scale process of the top production, decay, and hadronization at a hadron collider. EFTs provide a practical framework for carrying out calculations that are otherwise quite challenging in QCD. Using EFT methods we can accurately predict top-mass sensitive kinematic observables such as a simple hemisphere mass measurement at a lepton collider or more complex jet-mass measurements, with or without grooming, at hadron colliders. A key feature of the first principles theory calculations presented here is that they enable the top mass to be determined in a field theoretically well defined scheme, a major shortcoming of more well-established Monte Carlo (MC) based methods.

By matching QCD successively onto SCET and then bHQET we can describe the decay of boosted top quarks close to mass shell through a factorized formula for the corresponding peaked cross section. By factorizing the cross section into separate hard, soft and collinear components we are able to provide a description for the physics at different scales. These energy scales are related to the top production process and subsequent measurements on the final state particles. Through the bHQET jet functions that encode physics of collinear particles of virtuality of the order the width of the top quark (Γ_t) we are able to specify the top mass scheme.

Starting with the existing theory framework for describing top jets at lepton col-

liders, we extended this to extend it to the hadron collider case. We make use of the 2-jettiness measurement as a top-mass sensitive observable for the $pp \to t\bar{t}$ process. The 2-jettiness cross section has the same bHQET jet functions as in the lepton collider case, but now has a more sophisticated structure due to multiple color channels, PDFs, and jet-based measurement. The initial state radiation and PDFs are described through beam functions. We derive the form for hard matching between QCD and SCET, and between SCET and bHQET that is now a matrix in color space.

While most calculations are carried out in perturbation theory, we are also able to account for non-perturbative effects in the peak region by factorizing the soft function into perturbative and non-perturbative functions. The scale of non-perturbative corrections to the mass-spectrum is predominantly governed by the first moment Ω_1 of the non-perturbative function. The higher moments, when parameterized in terms of dimensionless numbers scaled with powers of the first moment, only have subleading effect on the peak position. We primarily considered $x_2 = \Omega_2/\Omega_q^2 - 1$. We further showed through studies comparing factorization and PYTHIA that one can account for dominant effects of the underlying event in addition to hadronization by simply increasing Ω_1 and modifying x_2. This allows for top mass extraction by fitting the factorized formula with only three unknown parameters.

We noted that the effects of UE can significantly affect the top-mass spectrum. While these effects can be modeled through the non-perturbative function, it is preferable like to work with observables that are less sensitive to this contamination. We therefore took another step and added jet grooming to our set of tools. In particular, we made use of the soft drop grooming procedure to drop wide angle radiation based on the soft drop criteria that depends on two parameters z_{cut} and β that specify the minimum energy fraction of the particles kept in the groomed jet and sensitivity to the angle between them respectively. This requires a more sophisticated setup in EFT.

Building upon the studies for jets from massless quarks we derived the factorization formula for soft drop groomed top jets. There is a more rich phenomenology for groomed top jets compared to jets from massless quarks due to interesting effects

from the top-decay products. The top-decay products, being commensurate in their energies, can stop the soft drop groomer in certain kinematic situations. This also changes the way non-perturbative corrections enter the cross section. As a result we have two different versions of factorized formulas: the "decay" factorization theorem where soft drop predominantly stops by comparing top decay products and the result depends on their angular distribution, and the "high-p_T" factorization which is a more direct generalization of the result for jets initiated by lighter quarks. Both the forms, however, are quite similar in their perturbative content, and, for the range of p_Ts that are experimentally possible, effectively only change the meaning of the non-perturbative scale set by Ω_1.

Soft drop grooming places non trivial restrictions on the range of groomer parameters for a given p_T of the top jet. In order to have a simple effective theory treatment for top mass measurements we find that we are restricted to a "light grooming" region. Light grooming limits us to $\sim 1\%$ level of grooming, which is much weaker than more typical 10% level of grooming that is being employed currently at the LHC. We further note that the light grooming is allowed only on top jets with $p_T \gtrsim 500$ GeV. However, we show that even when restricted to the light grooming region the groomed jet-mass distribution is quite robust to effects of underlying event, the activity in the beam region, and the jet-radius. Furthermore, the groomed jet-mass distribution is very similar to that of e^+e^- for similar kinematics.

We compare the results of factorization for groomed and ungroomed top jets with PYTHIA simulations. Our preliminary study allows us to calibrate the MC top mass parameter, $m_t^{\rm MC}$, and we find that it's definition is close to the MSR top mass with $R = 1$, $m_t^{\rm MSR}(R = 1{\rm GeV})$. Our calibration results for pole mass give $m_t^{\rm pole}$ that is about 0.5 - 1.0 GeV smaller than $m_t^{\rm MC}$.

The factorization theorems derived here allow for improvement in theoretical accuracy by incorporating higher order matrix elements as they become available. By also calculating of two-loop matching coefficient between SCET and bHQET at the top mass scale we have now made available all the ingredients needed to evaluate the dijet invariant mass cross section for the $e^+e^- \to t\bar{t}$ process at N^{3}LL accuracy.

Appendix A

Phase Space Integrations

The factorization formula in Eq. (4.70) is differential in $\eta_t, \eta_{\bar{t}}$, and p_T of the top and anti-top jets. This final form is obtained by performing the phase space integrals over the top and anti-top jet momenta using constraints from momentum conservation which we evaluate here. The differential momentum phase space for the top and anti-top jets is given by

$$d\Phi_{t,\bar{t}} = \frac{d^3 p_{t,\bar{t}}}{(2\pi)^3 2E_{t,\bar{t}}}, \tag{A.1}$$

and their four-momenta are parametrized as

$$p_{t,\bar{t}} = (E_T^{t,\bar{t}} \cosh\eta_{t,\bar{t}},\ p_T^{t,\bar{t}} \cos\phi_{t,\bar{t}},\ p_T^{t,\bar{t}} \sin\phi_{t,\bar{t}},\ E_T^{t,\bar{t}} \sinh\eta_{t,\bar{t}}), \tag{A.2}$$

where the jet energies are

$$E_T^{t,\bar{t}} \equiv \sqrt{(p_T^{t,\bar{t}})^2 + m_t^2}. \tag{A.3}$$

Using this parameterization of the jet momenta and working in the limit $p_T^{t,\bar{t}} \gg m_t$, the jets differential phase space can be brought into the form

$$d\Phi_{t,\bar{t}} = \frac{1}{2(2\pi)^3} p_{t,\bar{t}}^T dp_T^{t,\bar{t}} d\eta_{t,\bar{t}} d\phi_{t,\bar{t}}. \tag{A.4}$$

Thus, the jet phase space integrals take the form

$$\int d\Phi_t \int d\Phi_{\bar{t}} = \frac{1}{4(2\pi)^6} \int d\eta_t \int d\eta_{\bar{t}} \int d\phi_t \int d\phi_{\bar{t}} \int dp_T^t \int dp_T^{\bar{t}} (p_T^t p_T^{\bar{t}}), \tag{A.5}$$

and are performed using the momentum conservation delta function constraint:

$$\begin{aligned} \delta^{(4)}(p_a + p_b - p_t - p_{\bar{t}}) = & \delta\Big(\frac{Q(x_a + x_b)}{2} - E_T^t \cosh\eta_t - E_T^{\bar{t}} \cosh\eta_{\bar{t}}\Big) \\ & \delta\Big(\frac{Q(x_a - x_b)}{2} - E_T^t \sinh\eta_t - E_T^{\bar{t}} \sinh\eta_{\bar{t}}\Big) \\ & \delta\Big(p_T^t \cos\phi_t + p_T^{\bar{t}} \cos\phi_{\bar{t}}\Big) \delta\Big(p_T^t \sin\phi_t + p_T^{\bar{t}} \sin\phi_{\bar{t}}\Big) \end{aligned} \tag{A.6}$$

The azimuthal symmetry if the process allows us to choose a coordinate system where $\phi_t = 0$. This allows us to set $\phi_t = 0$ in the integrand and then integrate over all directions so that $\int d\phi_t = 2\pi$. The delta function constraint can now be written as

$$\begin{aligned} \delta^{(4)}(p_a + p_b - p_t - p_{\bar{t}}) = & \delta\Big(\frac{Q(x_a + x_b)}{2} - E_T^t \cosh\eta_t - E_T^{\bar{t}} \cosh\eta_{\bar{t}}\Big) \\ & \delta\Big(\frac{Q(x_a - x_b)}{2} - E_T^t \sinh\eta_t - E_T^{\bar{t}} \sinh\eta_{\bar{t}}\Big) \\ & \delta\Big(p_T^t + p_T^{\bar{t}} \cos\phi_{\bar{t}}\Big) \delta\Big(p_T^{\bar{t}} \sin\phi_{\bar{t}}\Big), \end{aligned} \tag{A.7}$$

which can be brought into the form:

$$\begin{aligned} \delta^{(4)}(p_a + p_b - p_t - p_{\bar{t}}) = & \delta\Big(\frac{Q(x_a + x_b)}{2} - E_T^t \cosh\eta_t - E_T^{\bar{t}} \cosh\eta_{\bar{t}}\Big) \\ & \delta\Big(\frac{Q(x_a - x_b)}{2} - E_T^t \sinh\eta_t - E_T^{\bar{t}} \sinh\eta_{\bar{t}}\Big) \\ & \delta\Big(p_T^t + p_T^{\bar{t}} \cos\phi_{\bar{t}}\Big) \\ & \frac{1}{p_T^{\bar{t}}} \Big[\delta(\phi_{\bar{t}}) + \delta(\phi_{\bar{t}} - \pi)\Big]. \end{aligned} \tag{A.8}$$

Since we have set $\phi_t = 0$, for a non-zero value of $p_T^t + p_T^{\bar{t}}$ only the $\phi_{\bar{t}} = \pi$ ($\phi_{\bar{t}} \neq \phi_t = 0$) point in phase space will contribute in the last line of Eq. (A.8), which gives $p_T^t = p_T^{\bar{t}} = p_T$. Performing the phase space integrals in Eq. (A.5) using the constraints in Eq. (A.8), we are left with the useful result:

$$\begin{aligned}\int d\Phi_t \int d\Phi_{\bar{t}}\,(2\pi)^4 \delta^{(4)}(p_a + p_b - p_t - p_{\bar{t}}) \;=\; & \frac{1}{8\pi}\int d\eta_t \int d\eta_{\bar{t}} \int dp_T\, p_T^t \\ & \delta\Big(\frac{Q(x_a + x_b)}{2} - p_T \cosh\eta_t - p_T \cosh\eta_{\bar{t}}\Big) \\ & \delta\Big(\frac{Q(x_a - x_b)}{2} - p_T \sinh\eta_t - p_T \sinh\eta_{\bar{t}}\Big),\end{aligned} \tag{A.9}$$

which used in deriving the final form of the factorization formula in Eq. (4.70) that is differential in $\eta_t, \eta_{\bar{t}}$, and p_T of the top and anti-top jets.

Appendix B

Direct Calculation of C_m in the $(n_l + 1)$-flavor scheme

In Sec. 6.3 we directly computed the $\mathcal{O}(\alpha_s^2 C_F T_F)$ massive quark correction to $C_m^{(n_l)}$ by using form factors in the n_l-flavor scheme. Since this coefficient lives at the border between the $(n_l + 1)$ and n_l-flavor theories, we could just as well have carried out the calculation for C_m by using form factors in the $(n_l + 1)$-flavor scheme, and then converted to an n_l-flavor coupling at the very end. Of course the same result is obtained in this approach, but there are a few subtle differences in the calculation, which we discuss here.

In particular, in Sec. 6.3 we noted that for the $\mathcal{O}(\alpha_s^2 C_F T_F)$ correction in the n_l-flavor scheme, the bHQET graphs give no contribution. However, using the $(n_l + 1)$-flavor scheme for the strong coupling this is no longer the case. To see this, consider the ratio in Eq. (6.15) and express the denominator in the $(n_l + 1)$-flavor scheme by inverting the decoupling relation given in Eq. (6.30):

$$\alpha_s^{(n_l)}(\mu) = \alpha_s^{(n_l+1)}(\mu)\left[1 + \frac{\alpha_s^{(n_l+1)}(\mu) T_F}{3\pi} \ln\left(\frac{m^2}{\mu^2}\right)\right]. \tag{B.1}$$

Expanding in α_s and using the notation in Eq. (6.7) we then get

$$C_m^{(C_F T_F, n_l+1)}\left(m, \frac{Q}{m}, \mu\right) = \left[F_{\text{SCET}}^{(C_F T_F, n_l+1)}(Q, m, \Lambda, \mu)\right. \tag{B.2}$$

$$- \frac{\alpha_s^{(n_l+1)}(\mu) T_F}{3\pi} \ln\left(\frac{m^2}{\mu^2}\right) F_{\rm bHQET}^{(1,n_l)}\left(\frac{Q}{m}, \Lambda, \mu\right)\Big]_{\alpha_s^{(n_l)} \to \alpha_s^{(n_l+1)}} .$$

Here the second term comes from converting the strong coupling constant to (n_l+1)-flavors in the one-loop bHQET graph. Below we drop the flavors superscript on the form factors. Here it should be understood that all the terms are now expressed in the (n_l+1)-flavor scheme. Then combining Eq. (B.2) and Eq. (6.39), and Eq. (6.16) we get

$$\begin{aligned} C_m^{(C_F T_F, n_l+1)}\left(m, \frac{Q}{m}, \mu\right) &= F_{\rm SCET}^{(\rm OS, C_F T_F, bare)}(Q, m) \\ &\quad - \left(\Pi(m^2, 0) - \frac{\alpha_s^{(n_l+1)}(\mu) T_F}{3\pi} \frac{1}{\epsilon}\right) F_{\rm SCET}^{(1,\rm bare)}\left(\frac{Q}{m}, \Lambda\right) \\ &\quad + Z_{\rm SCET}^{(C_F T_F)}(Q, \mu) - \frac{\alpha_s^{(n_l+1)}(\mu) T_F}{3\pi} \ln\left(\frac{m^2}{\mu^2}\right) F_{\rm bHQET}^{(1)}\left(\frac{Q}{m}, \Lambda, \mu\right) . \end{aligned} \tag{B.3}$$

Note that both $F_{\rm SCET}^{(1,\rm bare)}$ and $F_{\rm bHQET}^{(1)}$ are IR divergent. This result can be simplified by noting that in any flavor scheme the one-loop $C_m^{(1)}$ is given by the difference of one-loop renormalized SCET and bHQET amplitudes:

$$C_m^{(1)}\left(m, \frac{Q}{m}, \mu\right) = F_{\rm SCET}^{(1)}(Q, m, \Lambda, \mu) - F_{\rm bHQET}^{(1)}\left(\frac{Q}{m}, \Lambda, \mu\right) . \tag{B.4}$$

Using Eq. (B.4) in Eq. (B.3) we can then write down a simpler expression for $C_m^{(C_F T_F, n_l+1)}$:

$$\begin{aligned} C_m^{(C_F T_F, n_l+1)} &= F_{\rm SCET}^{(\rm OS, C_F T_F, bare)}(Q, m) + Z_{\rm SCET}^{(C_F T_F)}(Q, \mu) \\ &\quad - \left(\Pi(m^2, 0) - \frac{\alpha_s^{(n_l+1)}(\mu) T_F}{3\pi} \frac{1}{\epsilon}\right)\left(F_{\rm SCET}^{(1)}(Q, m, \Lambda, \mu) - Z_{\rm SCET}^{(1)}(Q, \mu)\right) \\ &\quad - \frac{\alpha_s^{(n_l+1)}(\mu) T_F}{3\pi} \ln\left(\frac{m^2}{\mu^2}\right) F_{\rm bHQET}^{(1)}\left(\frac{Q}{m}, \Lambda, \mu\right) \\ &= F_{\rm SCET}^{(\rm OS, C_F T_F, bare)}(Q, m) + Z_{\rm SCET}^{(C_F T_F)}(Q, \mu) \\ &\quad + \left(\Pi(m^2, 0) - \frac{\alpha_s^{(n_l+1)}(\mu) T_F}{3\pi} \frac{1}{\epsilon}\right) Z_{\rm SCET}^{(1)}(Q, \mu) \\ &\quad + \frac{\alpha_s^{(n_l+1)}(\mu) T_F}{3\pi} \ln\left(\frac{m^2}{\mu^2}\right) C_m^{(1)}\left(m, \frac{Q}{m}, \mu\right) . \end{aligned} \tag{B.5}$$

This result can be used to compute $C_m^{(C_F T_F, n_l+1)}$. Comparing it with Eq. (6.42) we see that it can be rewritten as

$$C_m^{(C_F T_F, n_l+1)} = C_m^{(C_F T_F, n_l)} + \frac{\alpha_s^{(n_l+1)}(\mu) T_F}{3\pi} \ln\left(\frac{m^2}{\mu^2}\right) C_m^{(1)}\,, \tag{B.6}$$

and hence is fully consistent with determining $C_m^{(C_F T_F, n_l+1)}$ from Eq. (6.42) and then simply applying the coupling conversion in Eq. (B.1) in the result. Note that in this (n_l+1)-flavor scheme approach the bHQET one-loop amplitude contributes and plays an important role in obtaining the scheme conversion term involving $C_m^{(1)}$ in the last line of Eq. (B.6).

Appendix C

bHQET current anomalous dimension at $\mathcal{O}(\alpha_s^3)$

To extent the resummation of large logarithms in the factorization theorem in Eq. (6.1) from NNLL to N^{3}LL the only missing ingredient – besides the cusp anomalous dimension at four-loops – is the $\mathcal{O}(\alpha_s^3)$ noncusp anomalous dimension of the bHQET jet function or equivalently of the bHQET current (which are related to each other via Eq. (6.20) with the known three loop result for γ_S). The latter has not been so far given in the literature, but can be extracted from a recent result for the three-loop anomalous dimension of a cusped Wilson loop [63, 64], which is equivalent to the full anomalous dimension in HQET. Expanding their result in the lightlike limit $x \sim m/Q \to 0$, we obtain with the help of the Mathematica package HPL [?]

$$\begin{aligned}\gamma_{\text{bHQET}}\Big(\frac{Q}{m},\mu\Big)\Big|_{\mathcal{O}(\alpha_s^3)} &= \left(\frac{\alpha_s^{(n_l)}(\mu)}{4\pi}\right)^3\Bigg\{C_F C_A^2\Bigg[\left(-\frac{490}{3}+\frac{536\pi^2}{27}-\frac{88}{3}\zeta_3-\frac{44\pi^4}{45}\right)L \\ &\quad +\frac{686}{9}-\frac{608\pi^2}{27}+\frac{1480}{9}\zeta_3+\frac{44\pi^4}{45}+\frac{8\pi^2}{3}\zeta_3-72\zeta_5\Bigg] \\ &\quad + C_F C_A T_F n_l\Bigg[\left(\frac{1672}{27}-\frac{160\pi^2}{27}+\frac{224}{3}\zeta_3\right)L-\frac{712}{27}+\frac{160\pi^2}{27}-\frac{992}{9}\zeta_3\Bigg] \\ &\quad + C_F^2 T_F n_l\Bigg[\left(\frac{220}{3}-64\zeta_3\right)L-\frac{220}{3}+64\zeta_3\Bigg]+C_F(T_F n_l)^2\Bigg[\frac{64}{27}L-\frac{64}{27}\Bigg]\Bigg\},\end{aligned} \tag{C.1}$$

where $L = \ln[(-Q^2 - i0)/m^2]$. The coefficient of this logarithm is proportional to the well-known lightlike cusp anomalous dimension at three loops, $\Gamma^{(3)}_{\text{cusp}}$, while the non-logarithmic ingredient of Eq. (C.1) represents the noncusp part. Together with the corresponding anomalous dimension of the SCET current this enables one to predict the logarithmic structure of H_m at three loops by solving Eq. (6.17). Furthermore it allows one to extract the last missing ingredient to predict the full IR-divergent structure of the three-loop full QCD form factor for massive quarks for $m \ll Q$, which is for example in Ref. [59] the coefficient $K^{(3)}$ in Eq. (63).

Bibliography

[1] Morad Aaboud et al. Measurement of the top quark mass in the $t\bar{t} \to$ dilepton channel from $\sqrt{s} = 8$ TeV ATLAS data. *Phys. Lett.*, B761:350–371, 2016.

[2] Georges Aad et al. Jet mass and substructure of inclusive jets in $\sqrt{s} = 7$ TeV pp collisions with the ATLAS experiment. *JHEP*, 05:128, 2012.

[3] Roel Aaij et al. Observation of $J/\psi p$ Resonances Consistent with Pentaquark States in $\Lambda_b^0 \to J/\psi K^- p$ Decays. *Phys. Rev. Lett.*, 115:072001, 2015.

[4] S. Abachi et al. Observation of the top quark. *Phys. Rev. Lett.*, 74:2632–2637, 1995.

[5] Riccardo Abbate, Michael Fickinger, Andre H. Hoang, Vicent Mateu, and Iain W. Stewart. Thrust at N^{3}LL with Power Corrections and a Precision Global Fit for $\alpha_s(m_Z)$. *Phys. Rev.*, D83:074021, 2011.

[6] J. Ablinger, A. Behring, J. Blümlein, A. De Freitas, A. Hasselhuhn, et al. The 3-Loop Non-Singlet Heavy Flavor Contributions and Anomalous Dimensions for the Structure Function $F_2(x, Q^2)$ and Transversity. *Nucl. Phys.*, B886:733–823, 2014.

[7] S. Alekhin, A. Djouadi, and S. Moch. The top quark and Higgs boson masses and the stability of the electroweak vacuum. *Phys. Lett.*, B716:214–219, 2012.

[8] Anders Andreassen, William Frost, and Matthew D. Schwartz. Consistent Use of the Standard Model Effective Potential. *Phys. Rev. Lett.*, 113(24):241801, 2014.

[9] ATLAS/CERN. Available at `http://www.jetgoodson.com/images/thesisImages/theAtlasDetector.png`.

[10] Christian W. Bauer, Sean Fleming, and Michael E. Luke. Summing Sudakov logarithms in $B \to X_s\gamma$ in effective field theory. *Phys. Rev.*, D63:014006, 2001.

[11] Christian W. Bauer, Sean Fleming, Dan Pirjol, and Iain W. Stewart. An effective field theory for collinear and soft gluons: Heavy to light decays. *Phys. Rev. D*, 63:114020, 2001.

[12] Christian W. Bauer, Michael E. Luke, and Thomas Mannel. Light cone distribution functions for B decays at subleading order in 1 / m(b). *Phys. Rev.*, D68:094001, 2003.

[13] Christian W. Bauer and Aneesh V. Manohar. Shape function effects in B —> X(s) gamma and B —> X(u) l anti-nu decays. *Phys. Rev.*, D70:034024, 2004.

[14] Christian W. Bauer, Dan Pirjol, and Iain W. Stewart. Soft-Collinear Factorization in Effective Field Theory. *Phys. Rev.*, D65:054022, 2002.

[15] Christian W. Bauer and Iain W. Stewart. Invariant operators in collinear effective theory. *Phys. Lett. B*, 516:134–142, 2001.

[16] Christian W. Bauer, Frank J. Tackmann, Jonathan R. Walsh, and Saba Zuberi. Factorization and Resummation for Dijet Invariant Mass Spectra. *Phys. Rev.*, D85:074006, 2012.

[17] Thomas Becher and Matthias Neubert. Toward a NNLO calculation of the $\bar{B} \to X_s\gamma$ decay rate with a cut on photon energy. II: Two-loop result for the jet function. *Phys. Lett.*, B637:251–259, 2006.

[18] M. Beneke, P. Marquard, P. Nason, and M. Steinhauser. On the ultimate uncertainty of the top quark pole mass. 2016.

[19] W. Bernreuther, R. Bonciani, T. Gehrmann, R. Heinesch, T. Leineweber, et al. Two-loop QCD corrections to the heavy quark form-factors: The Vector contributions. *Nucl.Phys.*, B706:245–324, 2005.

[20] Daniele Bertolini, Daniel Kolodrubetz, Duff Neill, Piotr Pietrulewicz, Iain W. Stewart, Frank J. Tackmann, and Wouter J. Waalewijn. Soft Functions for Generic Jet Algorithms and Observables at Hadron Colliders. *JHEP*, 07:099, 2017.

[21] Ikaros I. Y. Bigi, Mikhail A. Shifman, N. G. Uraltsev, and A. I. Vainshtein. On the motion of heavy quarks inside hadrons: Universal distributions and inclusive decays. *Int. J. Mod. Phys.*, A9:2467–2504, 1994.

[22] Johannes Blumlein, Helmut Bottcher, and Alberto Guffanti. Non-singlet QCD analysis of deep inelastic world data at O(alpha(s)**3). *Nucl. Phys.*, B774:182–207, 2007.

[23] S. W. Bosch, B. O. Lange, M. Neubert, and Gil Paz. Factorization and shape function effects in inclusive B meson decays. *Nucl. Phys.*, B699:335–386, 2004.

[24] Vincenzo Branchina and Emanuele Messina. Stability, Higgs Boson Mass and New Physics. *Phys. Rev. Lett.*, 111:241801, 2013.

[25] Vincenzo Branchina, Emanuele Messina, and Alessia Platania. Top mass determination, Higgs inflation, and vacuum stability. *JHEP*, 09:182, 2014.

[26] M. Breidenbach, J. I. Friedman, H. W. Kendall, E. D. Bloom, D. H. Coward, H. DeStaebler, J. Drees, L. W. Mo, and R. E. Taylor. Observed behavior of highly inelastic electron-proton scattering. *Phys. Rev. Lett.*, 23:935–939, Oct 1969.

[27] Mathias Butenschoen, Bahman Dehnadi, Andre H. Hoang, Vicent Mateu, Moritz Preisser, and Iain W. Stewart. Top Quark Mass Calibration for Monte Carlo Event Generators. *Phys. Rev. Lett.*, 117(23):232001, 2016.

[28] Dario Buttazzo, Giuseppe Degrassi, Pier Paolo Giardino, Gian F. Giudice, Filippo Sala, et al. Investigating the near-criticality of the Higgs boson. *JHEP*, 1312:089, 2013.

[29] Jonathan M. Butterworth, Adam R. Davison, Mathieu Rubin, and Gavin P. Salam. Jet substructure as a new Higgs search channel at the LHC. *Phys. Rev. Lett.*, 100:242001, 2008.

[30] N. Cabibbo, L. Maiani, G. Parisi, and R. Petronzio. Bounds on the Fermions and Higgs Boson Masses in Grand Unified Theories. *Nucl. Phys.*, B158:295–305, 1979.

[31] Matteo Cacciari and Gavin P. Salam. Pileup subtraction using jet areas. *Phys. Lett.*, B659:119–126, 2008.

[32] Matteo Cacciari, Gavin P. Salam, and Gregory Soyez. The Anti-k(t) jet clustering algorithm. *JHEP*, 04:063, 2008.

[33] Serguei Chatrchyan et al. Measurement of the underlying event in the Drell-Yan process in proton-proton collisions at $\sqrt{s} = 7$ TeV. *Eur. Phys. J.*, C72:2080, 2012.

[34] Jui-Yu Chiu, Andreas Fuhrer, Andre H. Hoang, Randall Kelley, and Aneesh V. Manohar. Soft-Collinear Factorization and Zero-Bin Subtractions. *Phys. Rev.*, D79:053007, 2009.

[35] Jui-Yu Chiu, Frank Golf, Randall Kelley, and Aneesh V. Manohar. Electroweak Corrections in High Energy Processes using Effective Field Theory. *Phys. Rev.*, D77:053004, 2008.

[36] Jui-Yu Chiu, Frank Golf, Randall Kelley, and Aneesh V. Manohar. Electroweak Sudakov corrections using effective field theory. *Phys. Rev. Lett.*, 100:021802, 2008.

[37] Jui-Yu Chiu, Ambar Jain, Duff Neill, and Ira Z. Rothstein. A Formalism for the Systematic Treatment of Rapidity Logarithms in Quantum Field Theory. *JHEP*, 1205:084, 2012.

[38] Jui-yu Chiu, Ambar Jain, Duff Neill, and Ira Z. Rothstein. The Rapidity Renormalization Group. *Phys.Rev.Lett.*, 108:151601, 2012.

[39] CMS/CERN. Available at https://www.theguardian.com/science/life-and-physics/2015/sep/06/all.

[40] CMS Collaboration. Investigations of the impact of the parton shower tuning in Pythia 8 in the modelling of $t\bar{t}$ at $\sqrt{s} = 8$ and 13 TeV. 2016.

[41] MichaÅĆ Czakon, Paul Fiedler, and Alexander Mitov. Total Top-Quark Pair-Production Cross Section at Hadron Colliders Through $O(\frac{4}{S})$. *Phys. Rev. Lett.*, 110:252004, 2013.

[42] R. H. Dalitz and Gary R. Goldstein. The Decay and polarization properties of the top quark. *Phys. Rev.*, D45:1531–1543, 1992.

[43] Mrinal Dasgupta, Alessandro Fregoso, Simone Marzani, and Alexander Powling. Jet substructure with analytical methods. *Eur. Phys. J.*, C73(11):2623, 2013.

[44] Mrinal Dasgupta, Alessandro Fregoso, Simone Marzani, and Gavin P. Salam. Towards an understanding of jet substructure. *JHEP*, 09:029, 2013.

[45] Yuri L. Dokshitzer, G. D. Leder, S. Moretti, and B. R. Webber. Better jet clustering algorithms. *JHEP*, 08:001, 1997.

[46] Estia Eichten and Brian Russell Hill. An Effective Field Theory for the Calculation of Matrix Elements Involving Heavy Quarks. *Phys. Lett.*, B234:511–516, 1990.

[47] Stephen D. Ellis, Christopher K. Vermilion, and Jonathan R. Walsh. Recombination Algorithms and Jet Substructure: Pruning as a Tool for Heavy Particle Searches. *Phys. Rev.*, D81:094023, 2010.

[48] Henning Flacher et al. Gfitter - Revisiting the Global Electroweak Fit of the Standard Model and Beyond. *Eur. Phys. J.*, C60:543–583, 2009.

[49] Sean Fleming, Andre H. Hoang, Sonny Mantry, and Iain W. Stewart. Jets from massive unstable particles: Top-mass determination. *Phys. Rev.*, D77:074010, 2008.

[50] Sean Fleming, Andre H. Hoang, Sonny Mantry, and Iain W. Stewart. Top Jets in the Peak Region: Factorization Analysis with NLL Resummation. *Phys. Rev.*, D77:114003, 2008.

[51] Christopher Frye, Andrew J. Larkoski, Matthew D. Schwartz, and Kai Yan. Factorization for groomed jet substructure beyond the next-to-leading logarithm. *JHEP*, 07:064, 2016.

[52] Christopher Frye, Andrew J. Larkoski, Matthew D. Schwartz, and Kai Yan. Precision physics with pile-up insensitive observables. 2016.

[53] Shireen Gangal, Maximilian Stahlhofen, and Frank J. Tackmann. Rapidity-Dependent Jet Vetoes. *Phys. Rev.*, D91(5):054023, 2015.

[54] Einan Gardi. Perturbative and nonperturbative aspects of moments of the thrust distribution in e+ e- annihilation. *JHEP*, 04:030, 2000.

[55] Jonathan Gaunt, Maximilian Stahlhofen, and Frank J. Tackmann. The Gluon Beam Function at Two Loops. *JHEP*, 08:020, 2014.

[56] Jonathan R. Gaunt. Glauber Gluons and Multiple Parton Interactions. *JHEP*, 07:110, 2014.

[57] Jonathan R. Gaunt and Maximilian Stahlhofen. The Fully-Differential Quark Beam Function at NNLO. *JHEP*, 12:146, 2014.

[58] Howard Georgi. An Effective Field Theory for Heavy Quarks at Low-energies. *Phys. Lett.*, B240:447–450, 1990.

[59] J. Gluza, A. Mitov, S. Moch, and T. Riemann. The QCD form factor of heavy quarks at NNLO. *JHEP*, 0907:001, 2009.

[60] Benjamin Grinstein. The Static Quark Effective Theory. *Nucl. Phys.*, B339:253–268, 1990.

[61] Simon Gritschacher, Andre H. Hoang, Ilaria Jemos, and Piotr Pietrulewicz. Secondary Heavy Quark Production in Jets through Mass Modes. *Phys. Rev.*, D88:034021, 2013.

[62] Tevatron Electroweak Working Group. Combination of CDF and D0 results on the mass of the top quark using up to 9.7 fb^{-1} at the Tevatron. 2014.

[63] Andrey Grozin, Johannes M. Henn, Gregory P. Korchemsky, and Peter Marquard. Three Loop Cusp Anomalous Dimension in QCD. *Phys. Rev. Lett.*, 114(6):062006, 2015.

[64] Andrey Grozin, Johannes M. Henn, Gregory P. Korchemsky, and Peter Marquard. The three-loop cusp anomalous dimension in QCD and its supersymmetric extensions. *JHEP*, 01:140, 2016.

[65] André H. Hoang. The Top Mass: Interpretation and Theoretical Uncertainties. In *7th International Workshop on Top Quark Physics (TOP2014) Cannes, France, September 28-October 3, 2014*, 2014.

[66] Andre H. Hoang, Ambar Jain, Christopher Lepenik, Vicent Mateu, Moritz Preisser, Ignazio Scimemi, and Iain W. Stewart. The MSR Mass and the $\mathcal{O}(\Lambda_{\text{QCD}})$ Renormalon Sum Rule. 2017.

[67] Andre H. Hoang, Ambar Jain, Ignazio Scimemi, and Iain W. Stewart. Infrared Renormalization Group Flow for Heavy Quark Masses. *Phys. Rev. Lett.*, 101:151602, 2008.

[68] Andre H. Hoang and Stefan Kluth. Hemisphere Soft Function at $O(\alpha_s^2)$ for Dijet Production in e^+e^- Annihilation. 2008.

[69] Andre H. Hoang, Daniel W. Kolodrubetz, Vicent Mateu, and Iain W. Stewart. C-parameter Distribution at N^3LL including Power Corrections. *Work in progress*, 2014.

[70] Andre H. Hoang, Christopher Lepenik, and Moritz Preisser. On the Light Massive Flavor Dependence of the Large Order Asymptotic Behavior and the Ambiguity of the Pole Mass. 2017.

[71] Andre H. Hoang, Sonny Mantry, Aditya Pathak, and Iain W. Stewart. Extracting a Short Distance Top Mass with Light Grooming. 2017.

[72] Andre H. Hoang, Aditya Pathak, Piotr Pietrulewicz, and Iain W. Stewart. Hard Matching for Boosted Tops at Two Loops. *JHEP*, 12:059, 2015.

[73] Andre H. Hoang, Piotr Pietrulewicz, and Daniel Samitz. Variable Flavor Number Scheme for Final State Jets in DIS. *DESY 15-098, UWThPh 2015-19*, 2015.

[74] Andre H. Hoang and Iain W. Stewart. Designing Gapped Soft Functions for Jet Production. *Phys. Lett.*, B660:483–493, 2008.

[75] Andre H. Hoang and Iain W. Stewart. Top Mass Measurements from Jets and the Tevatron Top-Quark Mass. *Nucl. Phys. Proc. Suppl.*, 185:220–226, 2008.

[76] Nathan Isgur and Mark B. Wise. Weak Decays of Heavy Mesons in the Static Quark Approximation. *Phys. Lett.*, B232:113–117, 1989.

[77] Nathan Isgur and Mark B. Wise. WEAK TRANSITION FORM-FACTORS BETWEEN HEAVY MESONS. *Phys. Lett.*, B237:527–530, 1990.

[78] Ambar Jain, Ignazio Scimemi, and Iain W. Stewart. Two-loop Jet-Function and Jet-Mass for Top Quarks. *Phys. Rev.*, D77:094008, 2008.

[79] Teppo T. Jouttenus, Iain W. Stewart, Frank J. Tackmann, and Wouter J. Waalewijn. The Soft Function for Exclusive N-Jet Production at Hadron Colliders. *Phys. Rev.*, D83:114030, 2011.

[80] Teppo T. Jouttenus, Iain W. Stewart, Frank J. Tackmann, and Wouter J. Waalewijn. Jet mass spectra in Higgs boson plus one jet at next-to-next-to-leading logarithmic order. *Phys. Rev.*, D88(5):054031, 2013.

[81] Gordon Kane. Scientific American, May 2003, Available at `http://scienceblogs.com/startswithabang/files/2013/08/particle_masses.png`.

[82] Randall Kelley and Matthew D. Schwartz. 1-loop matching and NNLL resummation for all partonic 2 to 2 processes in QCD. *Phys. Rev.*, D83:045022, 2011.

[83] Randall Kelley, Matthew D. Schwartz, Robert M. Schabinger, and Hua Xing Zhu. The two-loop hemisphere soft function. *Phys. Rev.*, D84:045022, 2011.

[84] Vardan Khachatryan et al. Measurement of the top quark mass using proton-proton data at $\sqrt{(s)} = 7$ and 8 TeV. *Phys. Rev.*, D93(7):072004, 2016.

[85] K. Kondo. Dynamical likelihood method for reconstruction of events with missing momentum. 2: Mass spectra for 2 —> 2 processes. *J. Phys. Soc. Jap.*, 60:836–844, 1991.

[86] G. P. Korchemsky and S. Tafat. On power corrections to the event shape distributions in QCD. *JHEP*, 10:010, 2000.

[87] F. Krauss. (Sherpa Collaboration), "Sketch of a $t\bar{t}h$ event". Available at `https://www.opensciencegrid.org/wp-content/uploads/2014/05/event.jpg`.

[88] David Krohn, Jesse Thaler, and Lian-Tao Wang. Jet Trimming. *JHEP*, 02:084, 2010.

[89] S. K. Lamoreaux. Demonstration of the casimir force in the 0.6 to $6\mu m$ range. *Phys. Rev. Lett.*, 78:5–8, Jan 1997.

[90] Andrew J. Larkoski, Simone Marzani, Gregory Soyez, and Jesse Thaler. Soft Drop. *JHEP*, 05:146, 2014.

[91] Andrew J. Larkoski, Ian Moult, and Duff Neill. Non-Global Logarithms, Factorization, and the Soft Substructure of Jets. *JHEP*, 09:143, 2015.

[92] Adam K. Leibovich, Zoltan Ligeti, and Mark B. Wise. Comment on quark masses in SCET. *Phys.Lett.*, B564:231–234, 2003.

[93] Zoltan Ligeti, Iain W. Stewart, and Frank J. Tackmann. Treating the b quark distribution function with reliable uncertainties. *Phys. Rev.*, D78:114014, 2008.

[94] Thomas Mannel and Matthias Neubert. Resummation of nonperturbative corrections to the lepton spectrum in inclusive B —> X lepton anti-neutrino decays. *Phys. Rev.*, D50:2037–2047, 1994.

[95] Aneesh V. Manohar, Thomas Mehen, Dan Pirjol, and Iain W. Stewart. Reparameterization invariance for collinear operators. *Phys. Lett.*, B539:59–66, 2002.

[96] Aneesh V. Manohar and Iain W. Stewart. The zero-bin and mode factorization in quantum field theory. *Phys. Rev.*, D76:074002, 2007.

[97] T. Matsuura, S. C. van der Marck, and W. L. van Neerven. The Calculation of the Second Order Soft and Virtual Contributions to the Drell-Yan Cross-Section. *Nucl. Phys.*, B319:570, 1989.

[98] T. Matsuura and W. L. van Neerven. Second Order Logarithmic Corrections to the Drell-Yan Cross-Section. *Z. Phys.*, C38:623, 1988.

[99] S. Moch, J. A. M. Vermaseren, and A. Vogt. The quark form factor at higher orders. *JHEP*, 08:049, 2005.

[100] S. Moch, S. Weinzierl, S. Alekhin, J. Blumlein, L. de la Cruz, et al. High precision fundamental constants at the TeV scale. 2014.

[101] David C. Moore, Alexander D. Rider, and Giorgio Gratta. Search for Millicharged Particles Using Optically Levitated Microspheres. *Phys. Rev. Lett.*, 113(25):251801, 2014.

[102] Ian Moult, Iain W. Stewart, Frank J. Tackmann, and Wouter J. Waalewijn. Employing Helicity Amplitudes for Resummation. *Phys. Rev.*, D93(9):094003, 2016.

[103] Piotr Pietrulewicz, Simon Gritschacher, Andre H. Hoang, Ilaria Jemos, and Vicent Mateu. Variable Flavor Number Scheme for Final State Jets in Thrust. 2014.

[104] Piotr Pietrulewicz, Frank J. Tackmann, and Wouter J. Waalewijn. Factorization and Resummation for Generic Hierarchies between Jets. *JHEP*, 08:002, 2016.

[105] Massimiliano Procura, Wouter J. Waalewijn, and Lisa Zeune. Resummation of Double-Differential Cross Sections and Fully-Unintegrated Parton Distribution Functions. *JHEP*, 02:117, 2015.

[106] Ira Z. Rothstein. Factorization, power corrections, and the pion form-factor. *Phys. Rev.*, D70:054024, 2004.

[107] Albert M Sirunyan et al. Measurement of the jet mass in highly boosted $\mathrm{t\bar{t}}$ events from pp collisions at $\sqrt{s} = 8$ TeV. *Eur. Phys. J.*, C77(7):467, 2017.

[108] Iain W. Stewart, Frank J. Tackmann, Jesse Thaler, Christopher K. Vermilion, and Thomas F. Wilkason. XCone: N-jettiness as an Exclusive Cone Jet Algorithm. *JHEP*, 11:072, 2015.

[109] Iain W. Stewart, Frank J. Tackmann, and Wouter J. Waalewijn. N-Jettiness: An Inclusive Event Shape to Veto Jets. *Phys.Rev.Lett.*, 105:092002, 2010.

[110] Iain W. Stewart, Frank J. Tackmann, and Wouter J. Waalewijn. The Beam Thrust Cross Section for Drell-Yan at NNLL Order. *Phys. Rev. Lett.*, 106:032001, 2011.

[111] Iain W. Stewart, Frank J. Tackmann, and Wouter J. Waalewijn. Dissecting Soft Radiation with Factorization. *Phys. Rev. Lett.*, 114(9):092001, 2015.

[112] Iain W. Stewart, Frank J. Tackmann, Jonathan R. Walsh, and Saba Zuberi. Jet p_T resummation in Higgs production at $NNLL' + NNLO$. *Phys. Rev.*, D89(5):054001, 2014.

[113] Frank J. Tackmann, Jonathan R. Walsh, and Saba Zuberi. Resummation Properties of Jet Vetoes at the LHC. *Phys. Rev.*, D86:053011, 2012.

[114] Jesse Thaler and Ken Van Tilburg. Maximizing Boosted Top Identification by Minimizing N-subjettiness. *JHEP*, 1202:093, 2012.

[115] Jesse Thaler and Thomas F. Wilkason. Resolving Boosted Jets with XCone. *JHEP*, 12:051, 2015.

[116] Jonathan R. Walsh and Saba Zuberi. Factorization Constraints on Jet Substructure. 2011.

[117] M. Wobisch and T. Wengler. Hadronization corrections to jet cross-sections in deep inelastic scattering. In *Monte Carlo generators for HERA physics. Proceedings, Workshop, Hamburg, Germany, 1998-1999*, pages 270–279, 1998.